CRANFIELD UNIVERSITY

YING HUI ZHOU

EXPERIMENTAL & SIMULATION STUDIES ON PERFORMANCE OF A COMPACT GAS/LIQUID SEPARATION SYSTEM

SCHOOL OF ENGINEERING
PROCESS SYSTEM ENGINEERING

PhD THESIS

Academic year: 2009-2013

Supervisor: Yi Cao

January 2013

CRANFIELD UNIVERSITY

SCHOOL OF ENGINEERING
PROCESS SYSTEM ENGINEERING

PhD THESIS

Academic Year 2009-2013

YINGHUI ZHOU

EXPERIMENTAL & SIMULATION STUDIES ON PERFORMANCE OF A COMPACT GAS/LIQUID SEPARATION SYSTEM

Supervisor: Yi Cao

January 2013

This thesis is submitted in partial fulfilment of the requirements for the degree of Doctor of Philosophy

ABSTRACT

The need of exploiting the offshore oil reserves and reducing the equipment costs becomes the motivation for developing new compact separation techniques. In the past years, the development of compact separators has almost solely focused on the cyclonic type separators made of pipes, because of their simple construction, relatively low cost of manufacturing and being able to withstand high pressures. Considerable effort has been put into the separator test program and qualification, and consequently notable advances in the compact separation technique have been made. However the application has been held back due to lacking of reliable predicting and design tools.

The objectives of this study were threefold. Firstly, an experimental study was carried out aiming at understanding the separation process and flow behaviours in a compact separator, named Pipe-SEP, operating at high inlet gas volume fraction (GVF). Secondly it is to gain insight of the gas and liquid droplet flow in the compact separator by means of Computational Fluid Dynamics (CFD) simulations. Last but not least, the understanding and insight gained above were used to develop a comprehensive performance predictive model, based on which, a reliable optimizing design procedure is suggested.

An experimental study was carried out to test a 150-mm Pipe-SEP prototype with a water-air mixture. Three distinct flow regimes inside the Pipe-SEP were identified, namely swirled, agitated, and gas blow-by. The transition of the flow regimes was found to be affected by inlet flow characteristics, mixture properties, geometry of the separator, and downstream conditions. A predictive model capable of predicting the transition of flow regimes and the separation efficiency was developed. A comparison between the predicted result and experiment data demonstrated that the model could serve as a design tool to support decision-making in early design stages.

The numerical simulations of gas and droplet flow in the Pipe-SEP were carried out by means of CFD. The gas flow simulation results showed that the swirl velocity profile was characterised by a forced vortex, where a uniform angular velocity is present at all radii. The axial velocity was discovered to be characterised by a slightly reverse flow

pattern, where near the wall the flow was directed upward, while in the centre region the flow was directed downward. The Discrete Phase Model (DPM) model was used to predict the cut size and the grade efficiency curve of the Pipe-SEP, where a large number of particles with different diameters were tracked. A comparison of Pipe-SEP with and without an 'L' gas outlet section showed that the gas outlet section had insignificant effect on the velocity profile, but an increase of the separation efficiency and the total pressure drop was observed. The effect of inlet gas velocity and separator diameter on the grade efficiency was studied, and it was concluded that the inlet gas velocity affected the grade efficiency, when the droplet had a diameter larger than the cut size. On the contrary the separator diameter affected the grade efficiency when the droplet had a size smaller than the cut size. The classic cyclone model was found to be able to predict a close cut size, and the scaling rules were applicable of capturing the performance trend of 'commercial separators' from the model tested.

The design problem of a standard two stage Pipe-SEP system, named Pipe-Hi-SEP, was formulated as a mathematical program, which combined the existing conventional separator design procedure, the unique fluid dynamic and mechanical constrains of a compact separator. By applying a non-linear optimisation procedure, an optimal Pipe-Hi-SEP system could be obtained that yields the lowest weight at required flow rate and separation efficiency. The application of this optimisation program for practical engineering design was illustrated by a case study. Using the formulated mathematical program, the optimum design could be carried out through a simultaneous search of all design variables. Moreover, the solution was able to provide an insight into what constrain the design, and the program has the flexibility suitable for various applications.

The thesis successfully demonstrated a new simulation method for predicting the performance of a compact separator, an improved understanding of the phase separation processes and flow hydrodynamic behaviour in the compact separator and it also developed an optimised program which can significantly improve the efficiency and effectiveness of the compact separation system design.

ACKNOWLEDGEMENTS

This thesis and its relative project is generous financial sponsored by the Knowledge Transfer Partnerships (KTP), Cranfield University and CALTEC Ltd. The KTP is a partially UK government sponsored programme for inspire collaboration between industries and universities in Britain.

I would like to offer my gratefulness to my PhD supervisor, Dr. Yi Cao, whose professional advice, has directed me finishing the PhD project and writing. This thesis can hardly be accomplished without his precise and careful corrections. Furthermore he has given me numerous suggestions and information regarding to the industry.

I would honestly thanks to Prof. Hoi Yeung for the extremely supportive academic supervision. Special thanks to the excellent technical support from Dr. Liyun Lao at Cranfield University and Mr. Sacha Sarshar, Dr. Najam Beg and Dr. Carl Wordsworth at CALTEC. Also thanks to Stan Collins, David Whittington, Kelvin White and John Knopp for their help with the lab technical work. Special thanks to Sam Skears for her supportive office activities. Last but not least is my great gratitude to my friends and colleagues in the PSE group of Cranfield University.

My personal special thanks to my husband Dr. Hua Wang for assisting me with his earnest love. Finally, I would like to thank my parents and my sister for their great love and unlimited encouragements.

TABLE OF CONTENTS

LIST OF FIGURES

LIST OF TABLES

NOMENCLATURE

A_d	Droplet area	m^2
A_{Hi-SEP}	Cross sectional area of Hi-SEP	m^2
A_{in}	Cross sectional area at inlet	m^2
$A_{Pipe-SEP}$	Cross sectional area of Pipe-SEP	m^2
A_s	The cross area of mesh pad	m^2
a	Cyclone inlet height	m
a_c	Acceleration due to the centripetal force	$m\,s^{-2}$
a_m	The surface area of the mesh pad	m^2
b	Cyclone inlet width	m
C_D	Drag coefficient	
c_o	The mass percentage of mist entering the cyclone	
C_{oL}	The limit-loading	
D	The cyclone body diameter	m
D_d	Droplet diameter	m
$D_{T,ij}$	The turbulent diffusion	
D_x	Vortex finder diameter	m
D_{50}	Cyclone's cut size	m
Eu	Euler number	
F_G	Gravity force	
F_B	Buoyancy force	
F_c	Centrifugal force	
F_D	Drag force	
F_σ	The retaining force	
f	The friction factor	
f_{air}	The gas only friction factor	
f_D	The drag coefficient of a single plate	
f_{mist}	The friction factor accounting for the effect of the mist	
G_k	The turbulence kinetic energy	
g	Gravitational constant	$m\,s^{-2}$

H_{CS}	The height of CS	m
H_m	The thickness of the mesh pad	m
K	Souders-Brown coefficient	$m\ s^{-1}$
K_{ij}	The sensitivity	
k	The turbulent kinetic energy	
k_s	Separator wall roughness	
L	The path length of particle travelling	
m_l	Liquid mass flow rate	$kg\ s^{-1}$
m_g	Gas mass flow rate	$kg\ s^{-1}$
N_s	The number of spiral turns	
N_μ	The viscosity number	
n	The number of bends	
P_w	The wetted perimeter	m^2
Q_g	Gas volumetric flow rate	$m^3\ h^{-1}$
Q_{Lin}	Liquid flow rate entering Pipe-SEP	$m^3 h^{-1}$
Q_{Lout2}	Liquid flow rate leaving Hi-SEP	$m^3 h^{-1}$
Q_l	Liquid volumetric flow rate	$m^3\ h^{-1}$
R	Pipe radius	m
r	The radial position of pipe	m
Re_d	Reynolds number of droplet	
Re_f	The Reynolds number of the wall film	
U	The mean axial velocity	$m\ s^{-1}$
U_m	The bulk velocity	$m\ s^{-1}$
U_i	The time averaged velocity in the direction x_i	
u_f	The liquid film mean velocity	$m\ s^{-1}$
u_i'	The ith fluctuating component of velocity	
v_{ch}	The characteristic velocity	$m\ s^{-1}$
v_{in}	Inlet velocity	
V_{l-SEP}	Volume of the liquid storage in the vessel	m^3
v_r'	The particle terminal velocity in the radial direction in the centrifugal field	$m\ s^{-1}$

v_{rCS}	Radial velocity in the CS	$m\,s^{-1}$
v_{θ}	Tangential velocity	$m\,s^{-1}$
$v_{\theta CS}$	Tangential velocity in the CS	$m\,s^{-1}$
$v_{\theta,l}$	The tangential film velocity	$m\,s^{-1}$
v_t	Terminal settling velocity of droplet	$m\,s^{-1}$
W	The mean tangential velocity	$m\,s^{-1}$
S	Swirl intensity	
Stk_{50}	Stokes number related to cut-size	
T	Temperature,	K
T_0	Room temperature	K
t_{cyc}	Residence time of cyclone	s
t_{mig}	The migration time	s
t_R	Retention time	s
$t_{63\%}$	The times at which the output reaches 63% of its final value	s
$t_{28\%}$	The times at which the output reaches 28% of its final value	s
$Y(s)$	The output	
$X(s)$	The input	

Greek and other

α_k	The inverse effective Prandtl number for k
α_ϵ	The inverse effective Prandtl number for ϵ
α_s	Swirl constant
β	Swirl decay coefficient
Δ	The magnitude of the steady-state change in the output
Δh_{2max}	The maximum Hi-SEP level deviation
ΔMF_i	The i^{th} mass fraction
ΔP_{dry}	“dry” pressure drop across mesh pad
ΔP_{wet}	“wet” pressure drop across mesh pad

ϵ	Dissipation rate	
ε	The porosity of mesh pad	
ε_{ij}	The dissipation tensor	
Γ	The liquid loading	
η_i	The separation efficiency of the i^{th} segment	
λ_{ij}	The relative gain	
ρ_l	Density of liquid	$kg\ m^{-3}$
ρ_g	Density of gas	$kg\ m^{-3}$
$\emptyset_{ij}$	The pressure strain	
μ_{eff}	The effective viscosity	
μ_g	Gas viscosity	$kgm^{-1}s^{-1}$
μ_l	Liquid viscosity	$kgm^{-1}s^{-1}$
μ_t	Turbulent viscosity	$kgm^{-1}s^{-1}$
δ	The magnitude of the input change	
δ	The film thickness	mm
δ_{ij}	The Kroneker delta	
Ω	Swirl number	

Abbreviations

ASB	Anti-Swirl Blades
AFC	Axial-Flow Cyclone
BRGL	Bottom-Riser-Gas-Lift
CFD	Computational Fluid Dynamics
CS	Cyclone Separator
CS	Cylindrical Surface
CV	Concentrated Vortex
DAS	Data Acquisition System
DPM	Discrete Phase Model
ESP	Electric Subsea Pump
FAD	Free Air Delivery

FER	Film Elimination Ring
FPSO	Floating Production Storage and Offloading
FV-LES	Finite volume LES
FV-RANS	Finite volume RANS model
GCU	Gas Carry Under
GCV	Gas control valve
GEC	Grade Efficiency Curve
GLCC	Gas-Liquid Cylindrical Cyclone
GLR	Gas Liquid Ratio
GOR	Gas Oil Ratio
GPSA	Gas Processors Suppliers Association
GVF	Gas Volume Fraction
HIS	Information Handling Services
HP	High Pressure
I-SEP	I Separator
LB-LES	Lattice-Boltzmann LES
LCO	Liquid Carry Over
LCV	Liquid control valve
LDA	Laser Doppler Anemometry
LES	Large Eddy Simulation
LP	Low Pressure
J-PUMP	Jet Pump
KTP	Knowledge Transfer Partnership
Pipe-Hi-SEP	Pipe separator and Hi separator
RANS	Reynolds-averaged Navier-Stokes
RFC	Reverse-Flow Cyclone
RGA	Relative gain array
RNG	Renormalization group
RSM	Reynolds Stress Model
PSE	Process System Engineering
PTV	Particle Tracking Velocimetry
PVC	Processing Vortex Core

SB	Solid Body
SEC	Screw Engineering Compressor
SGLSB	Subsea Gas Liquid Separation and Boosting
SSU	Subsea Separation Unit
TUSTP	Tulsa University Separation Technology Projects
UF KOV	Under Flow Knock-Out Vessel
VOF	Volume of Fluid
VSD	Variable Speed Drive
WJ	Wall Jet

1 INTRODUCTION

1.1 Background

In recent years, the offshore activities in the oil and gas industry have grown strongly. The Information Handling Services (HIS) data indicates that more than half of new discoveries of oil and gas reservoirs were offshore, especially in deep-water (Alex, 2010). Traditionally, an offshore reservoir can be explored by using conventional subsea technology. However as the exploration and development goes into the deep-water area, even with a technically successful exploration, the high costs of production based on conventional development schemes normally make these fields non-profitable. This is often the case for small reservoirs with complex geology and limited production potential. As a consequence the demand for developing innovative and low-cost facilities has increased rapidly.

One popular way of reducing the facility costs, is to reduce the size of key equipment-separators. Traditionally, oil, gas and water have been separated in large, heavy gravity settling vessels on the surface. However, more compact separation-units are preferred in offshore and subsea due to manufacturing cost and installation cost.

The term compact separation is commonly used to describe the separation-units which do not rely on gravity settling but use centrifugal force to enhance gravitational separation beyond 1 ‘g’ (one unit of standard gravity equalling to 9.80665 m/s^2). Due to the high ‘g’ force, the size of the separators can be reduced greatly. The importance of the compact separator has led to many investigations aimed at understanding and improving its performance in the past few years. Several types of compact separators have been developed with an impressive track record in metering loop, gas knockout and liquid knockout applications. However, reducing the size of separators will reduces the separation performance and the ability to handle fluctuations in flow rate and composition (Hannisdal *et al*., 2012). For offshore and subsea applications, an accuracy and robustness model should be able to predict the separation efficiency and it is crucial, since the failure of achieving this objective is severe in such applications. In addition, quantitative descriptions of the performance of compact separators are still deficient.

Most of the designs depend on empirical values from field experience. Such empirical knowledge is not much useful for design optimization.

The difficulties in quantifying performance of compact separators are mainly due to the complex flow behaviours in separators and uncertainties in upstream and downstream operating conditions. Extensive researches of compact separators have been conducted both with a mixture of air-water under ambient conditions and with hydrocarbon fluids under high pressure, even though the behaviour of hydrocarbon fluids under high pressure differs considerably from the low pressure experiment. Nevertheless, the experiments under ambient conditions together with advanced numerical simulations can provide a valuable insight into the phenomena that restrict the capacity and efficiency of compact separators.

In the present study, the performance of a new compact gas/liquid separation system, namely the Pipe-Hi-SEP, was investigated through experimental and modelling studies. The Pipe-Hi-SEP is a two-stage pipe separator, which consists of a Pipe-SEP and a Hi-SEP, as shown in Figure 1-1. The Pipe-SEP and Hi-SEP are geometrical similar, they are vertically installed pipe separator mounted with specific inlet and outlet arrangements. The main features of the Pipe-Hi-SEP system are:

- Tangential inlet to spin the fluid
- 'L'-shaped outlet sections to enhance the separation efficiency
- Film Elimination Ring (FER) to prevent creep of the liquid film into the gas outlet
- Anti-Swirl Blades (ASB) in the liquid and gas outlets to prevent vortexing
- Flexibility to be arranged in series and in parallel to improve capacity and performance

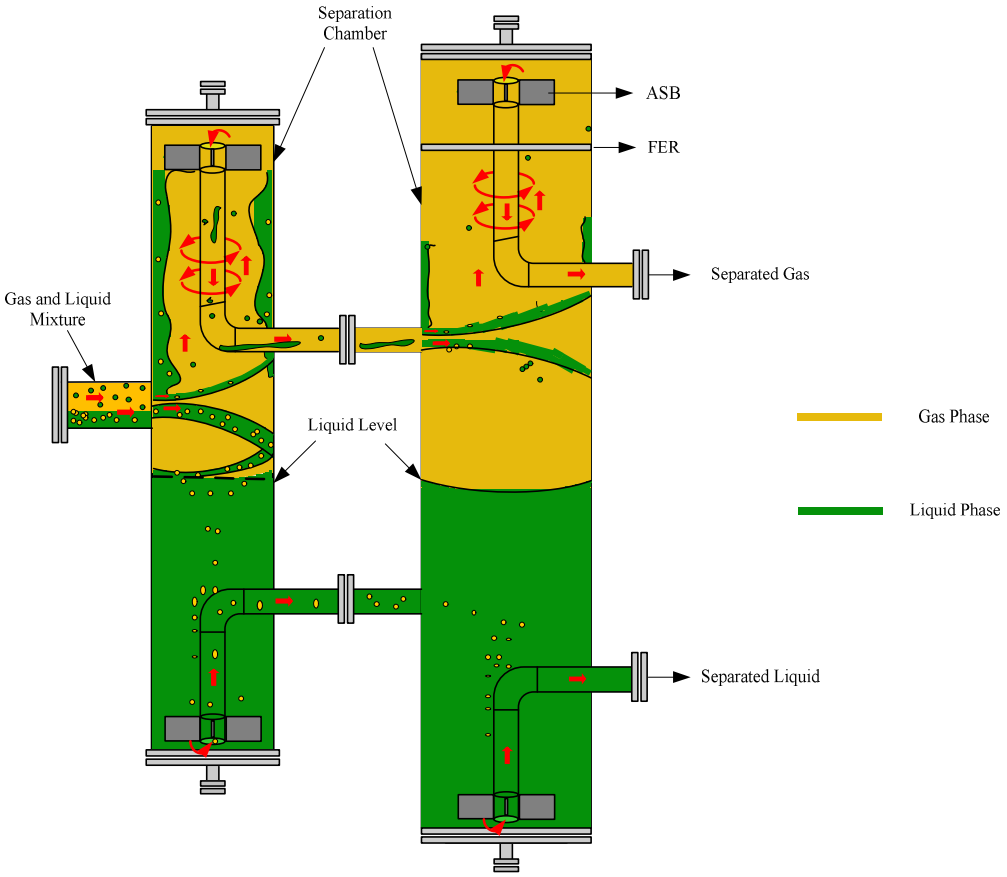

Figure 1-1 Schematic of the Pipe-Hi-SEP system

A scaled-down prototype was built in Cranfield University's Process System Engineering Flow Laboratory. The details of the experimental set up are presented in Chapter 3. The rig can handle gas/liquid flow with medium to high Gas Volume Fraction (GVF). This study was limited to Pipe-Hi-SEP operating at high (>85 Vol %) GVF.

1.2 Study Objectives

This study is aimed at gaining insight of the phase separation and flow hydrodynamic processes in the Pipe-Hi-SEP system to develop performance predictive models. The objectives include the following tasks:

- Experimentally investigate the flow behaviours and performance of Pipe-SEP separator at full range of flow rate.

- Develop numerical simulation models using a commercial Computational Fluid Dynamics (CFD) software package to obtain the flow profile within the phase separation process in the Pipe-SEP separator.
- Develop and validate the Pipe-SEP separator models for predicting the separation performance.
- Develop engineering design and optimizing tools of the two stage Pipe-Hi-SEP separation system for offshore and subsea applications.

1.3 Thesis Outline

The thesis is organised as follows:

Chapter 2 presents an overview of the present gas/liquid separation technology. Firstly, attention is paid to the different conditions that practical separators have to operate under. This will help in specifying the tasks of a separator. Secondly, three widely applied separation methods are described briefly in terms of operating principles, characteristics as well as their suitability for offshore and subsea applications. Furthermore, conventional guidelines for design of these separators were studied. At the end, an evaluation of the present compact separation technology is included. This point of view can highlight some specific differences between the conventional and compact separators.

In Chapter 3, the basic concepts and models of gas/liquid separator are discussed. A number of concepts relating to swirling flows, particle motion in a fluid, and unique problems posed by liquids in separator are discussed. Several (semi-)empirical models for predicting the flow pattern and separation efficiency are presented. In addition, an overview of the applications of CFD in separator modelling is presented.

Chapter 4 deals with the experimental investigations that have been carried out in order to gather the information necessary to reach the aforementioned objectives. Experiments are carried out in a 150-mm Pipe-SEP prototype operating with a water/air mixture. On the basis of extensive visual observation of flow behaviours and identification of the operational constraints, an explicit algorithm is proposed to predict flow regime transitions in the Pipe-SEP. The flow regime transitions will form the basis of the predictive model.

Chapter 5 is dedicated to a numerical study of Pipe-SEP. For Pipe-SEP operating at high GVF, predicting the separation efficiency involves predicting the droplets trajectory in the separation chamber. In order to achieve this, the gas velocity profile is simulated and compared with models in chapter 3. Separation efficiency is predicted by means of tracking droplets trajectories. Results of this CFD simulation are used to assess the suitability of using the classic cyclone separator model for the prediction of Pipe-Hi-SEP performance.

In chapter 6, experimental and numerical results are formulated into practical terms. Optimum design procedures that are suited for offshore and subsea application are proposed. These combine the advantages of several existing separator designs. Finally, the application of this optimisation procedure is illustrated by a case study.

The thesis is concluded by Chapter 7, which summarises the conclusions and provides recommendations for future work.

2 REVIEW OF PRESENT GAS-LIQUID SEPARATION TECHNOLOGY

This chapter gives a review of present gas/liquid separation technologies in oil and gas industry. First, the review focuses on the frequently encountered applications of oil and gas separators in onshore and offshore systems. Operating conditions and required properties of separators are discussed to highlight the specific differences between on-/off-shore and subsea applications. Next, a review is presented on three widely applied separation methods. Attention is paid to operating principles and characteristics as well as their suitability to subsea applications. Furthermore, since this research project is to develop improved criteria for designing compact separators, the standard methodologies of designing separators are studied, to provide an overall understanding of this knowledge field. Finally, recent advances in compact separator technology are summarised.

2.1 Classification of Gas/Liquid Separation Applications

In the oil and gas industry, the fluids produced are normally complex mixtures including water, crude oil, gas, condensates, and/or other impurities. In order to separate and condition these fluids to stable marketable products for storage and transportation, various process equipment are needed to be combined into a processing facility. Separation of oil and gas is a basic and crucial process operation to ensure the entire plant operation stable and profitable. For instance, a pump needs to work with gas-free liquid otherwise it would have cavitation, while a compressor requires the gas to be liquid-free in order to prevent breakdown. The limits on impurities in oil and gas products are strictly set, for example the final oil product normally consists of less than 1% of sediment and water, and the final gas usually requires no free liquid (Stewart and Arnold, 2008).

Traditionally, a separator is called a “two-phase separator”, if it is used to separate gas from the liquid, while a “three-phase separator” means it separates the mixture into gas, oil and water respectively. This section will give an introduction on the “two-phase separator” with various applications. Also, the term “gas/liquid separator” will be used to replace “two-phase separator” in the following sections.

When classifying the application of gas/liquid separator, an important distinction must be made depending on where the separator is used. When a separator is used in a producing train or on a platform near the wellhead, it is called a “stage separator”. In gas gathering, sales and distribution lines, a “gas scrubber” often handles fluid with a high gas to liquid ratio (GLR). The term “slug catcher” refers to a special type of separators with large capacities; it is often designed to handle gas and liquid slugs. In any case, they all separate a hydrocarbon stream into gaseous and liquid components at a specific condition. As concluded by Sarshar and Beg (2001), the applications of separators range from stage separation, partial separation, knockout of liquid from wet gas to testing and cleaning out of wells, multiphase metering and slug mitigation, among others. In the following section, the conventional on/off-shore applications and innovative subsea applications are reviewed.

2.1.1 On/Off-Shore Applications

A stage (or production) separator is the first vessel that the fluid flows through after it leaves the producing well. Normally, separation is performed sequentially in three to four stages, where fluid pressure is successively reduced in each stage. As illustrated in Figure 2-1, the production choke will reduce the well pressure to 3-5 MPa. The inlet temperature to the High Pressure (HP) separator often ranges from 100 to 150℃. Within the HP separator, the liquid is first flashed, and the light hydrocarbons are removed. The HP separators can be ‘two-phase’ or ‘three-phase’ depending on the well’s flowing characteristics. If there is a large portion of water, selecting a three-phase separator as the HP separator could decrease other separator sizes (Stewart and Arnold, 2008).

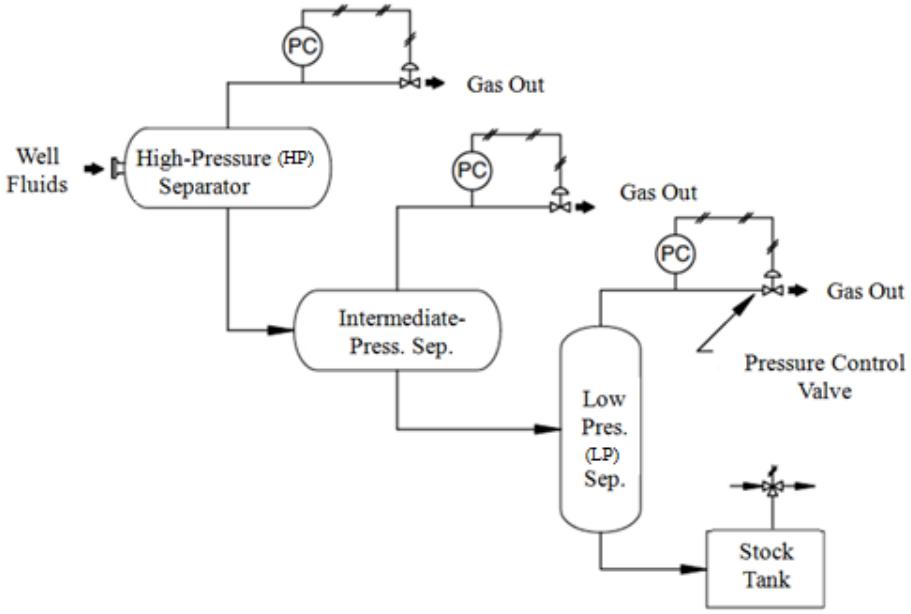

Figure 2-1 Schematic of a three-stages separation process (Stewart and Arnold, 2008)

The configuration of the second stage separator is the same as the first stage HP separator. Apart from processing the output from the first stage separator, it is also connected to the Low Pressure (LP) manifold and processes its output, in which the pressure is approximately 1MPa and the temperature is below 100℃ (Stewart and Arnold, 2008).

The final stage separator is also called flash drum or knock-out drum. Normally it is operated at atmospheric pressure (0.1MPa), under which the liquid would be “flashed” due to the large pressure differences. The liquid from the flash drum will be discharged to storage.

A “gas scrubber” can refer to a vessel used upstream from any processing vessel or unit to protect the downstream vessel or unit from liquid hydrocarbons and /or water. Compared to the stage separator, the liquid loading that enters a scrubber is much lower. Currently most of the gas scrubbers work with less than 4vol% liquid; the operational pressure ranges from atmospheric to more than 10Mpa, and the temperature can be from -170℃ in liquefied natural gas plants to 100℃ downstream of stripping columns. Vertical separators are commonly used as scrubbers (Bradley, 1992).

A “slug catcher” is commonly installed between the product pipeline and the processing equipment, and performs as a unique type of gas/liquid separator which can deal with large gas surges and liquid slugs regularly. Figure 2-2 shows a schematic of a typical finger type slug catcher. Due to these long pieces of pipes, a slug catcher has a sufficient buffer volume for holding the largest slugs that may come from upstream. This design works extremely well as sometimes it is hard to predict the slugging behaviour, particularly in some cases such as the terrain, hydrodynamic or riser-based slugging (Stewart and Arnold, 2008).

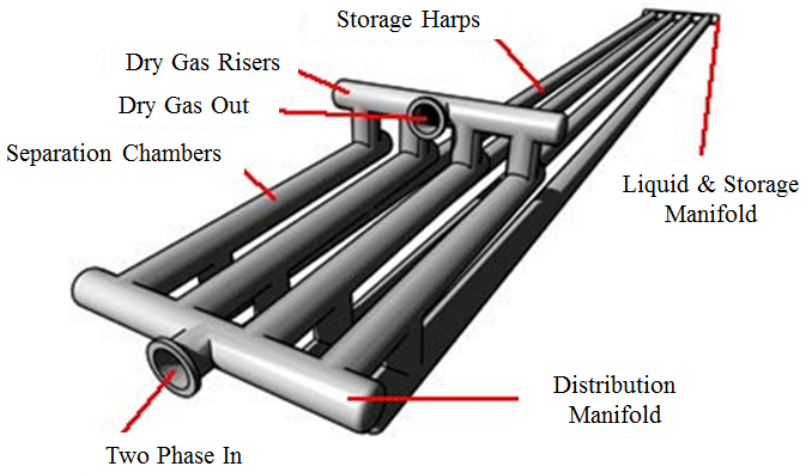

Figure 2-2 Schematic of a slug catcher with liquid “fingers” (Courtesy of Forge)

A “test separator” is designed to facilitate multiphase measurement in order to quantify and characteristics production from individual wells. A test separator normally can work as a two-phase and/or three-phase one. Different meters are equipped to determine oil, water and gas rates after separation (Bradley, 1992).

2.1.2 Subsea Applications

In recent years, subsea processing has become the most promising technology in developing marginal and deep-water fields. The potential benefits of subsea processing include increasing productivity, reducing flow assurance risk, and reducing the requirements for the topside processing equipment. Subsea processing consists of a series of technologies including separation, boosting, re-injection, compression and metering of reservoir fluids in the subsea environment. A logical approach is to

marinise topsides technology in order to take advantage of existing design and operational experiences. However, the current subsea technology is still not mature. There is plenty of room for research and developments of the subsea technology. Mentioned below are a few of the subsea technologies which involve gas/liquid separation.

The functionality of a Subsea Gas/Liquid Separation and Boosting (SGLSB) system is to separate gas and liquid at seafloor before the liquid is boosted. Then the separated gas and liquid are transported in different flowlines and risers to the same host. As shown in Figure 2-3, the SGLSB system includes a gas/liquid separator and a liquid booster. The separator separates the incoming well fluid with a specific efficiency. The separated gas flows up to the topside due to its natural pressure, and the separated liquid is pumped by a liquid booster. Differential pressure for the liquid booster is determined by the required topside delivery pressure, friction loss in the liquid riser and the weight of the liquid column. A single phase centrifugal pump could be used very effectively in the system, in a condition of less than 5% gas volume fraction (GVF); otherwise a multiphase pump is needed to boost the liquid (Birkeland *et al*., 2004).

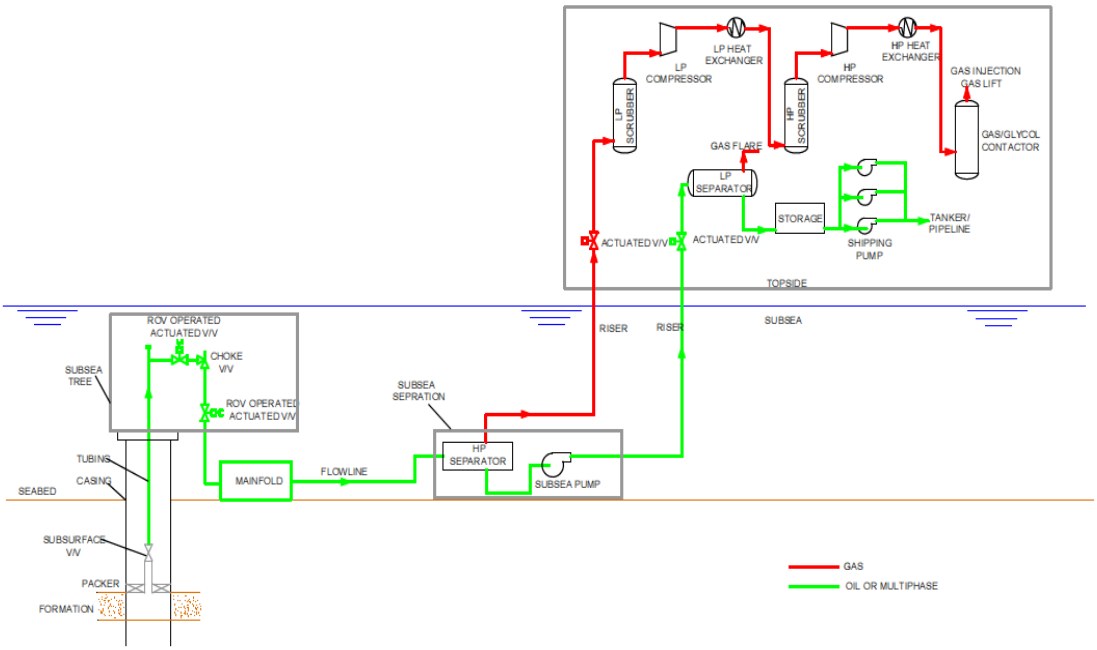

Figure 2-3 Schematic of a gas/liquid separation and boosting unit at riser base (Saint-marcoux and Fontfreyde, 2008)

A gas/liquid separation and boosting unit is shown in Figure 2-4, in which the separator level is kept within certain boundaries in case of extreme conditions such as being drained or overflowed. Draining the separator will result in poor performance or failure of the mechanical integrity of the pump. Overflowing the separator will lead to undesirable liquid entering the gas riser, consequently rising up the pressure drop, and possibly slug flow.

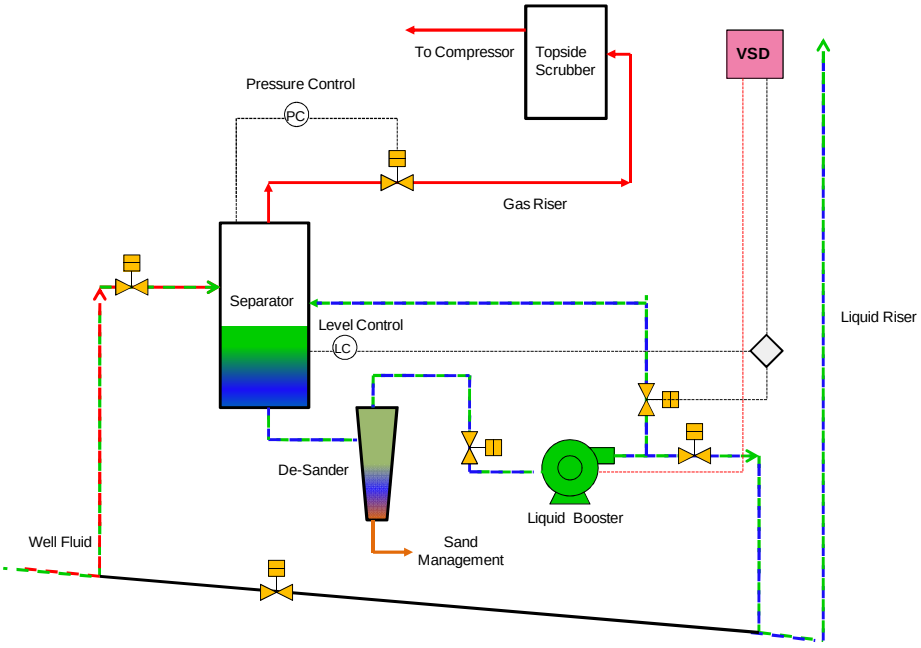

Figure 2-4 Schematic of the overall SGLSB system

The separator level is controlled by adjusting the pump speed, and it is achieved via a Variable Speed Drive (VSD) assembled at the topside. A local control loop with a recirculation line will compensate for rapid changes in the liquid level. Small transients will be handled by the separator itself as it has a liquid surge volume (Håheim and Gaillard, 2009).

The on-going Pazflor project is the pioneer of the SGLSB technology (Bon, 2009). The Pazflor project confronts the difficulty of producing distinctive types of oil from different reservoirs. Approximately two-thirds of oil is heavy crude which has 17–22° American Petroleum Institute (API), and the rest is lighter crude which has 35–38° API. The light oil is produced using the traditional production-loop system. Subsea

Separation Units (SSUs) were built-up to produce the heavy oil. As shown in Figure 2-5, each SSU includes one vertical gas/liquid separator and two hybrid pumps.

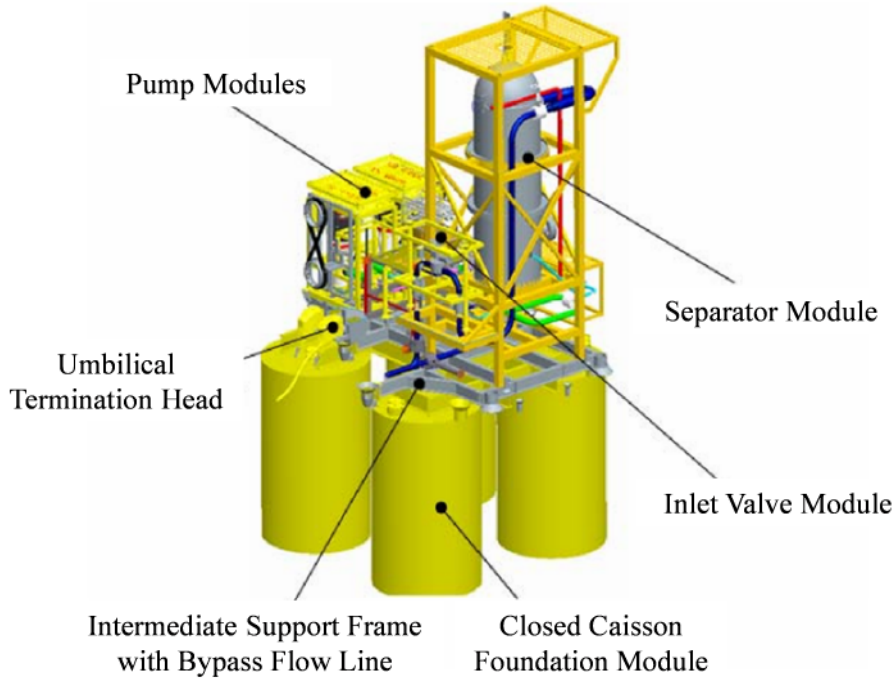

Figure 2-5 Overview of SSUs within the production of the Pazflor project (Gruehagen and Lim, 2009)

The SSU modules use large separation vessels operating at pressure of 2.3 MPa. A bottom-riser-gas-lift (BRGL) device combined with multiphase pumps is applied to provide sufficient differential pressure (ΔP), for producing the heavy fluid requested in the Pazflor project. Multiphase pumps would need to accommodate 15% GVF at normal operation, and up to 40% in case of unexpected fluid behaviour.

Another subsea separation and boosting system applied in deep-water is the ESP/Caisson technology (Vu *et al*., 2008). A special caisson separator with boosting device is mounted in a dummy well, which is located beneath the seabed in order to accommodate the separator and the Electric Subsea Pump (ESP). As seen from Figure 2-6 and Figure 2-7, the well fluid enters the caisson separator from its top end assembly. Within the caisson separator, the heavier liquid is separated due to centrifuging, and it flows downward to the ESP. The gas flows upwards due to its own pressure into a dedicated gas flowline. The ESP pumps those liquids toward the Floating Production

Storage and Offloading (FPSO) through a dedicated oil flowline. Therefore, the risks of hydrate and slugging often related to deep-water conditions, can be minimized by applying liquid-gas separation. Also, the single liquid phase can be boosted efficiently by means of industry proven ESP technology.

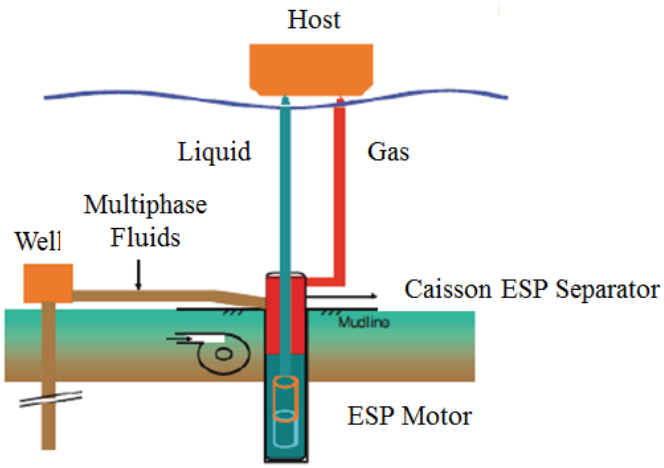

Figure 2-6 Schematic of production well and ESP/Caisson separator system (Deuel *et al.*, 2011)

Three down-hole pressure gauges are used for measuring the liquid level in the ESP/Caisson system. They are located from top to bottom along the depth of the separator. From the bottom two gauges, the density of the liquid is obtained. The liquid level is determined by the density and the pressure drop between the top and bottom gauges. A process control PID loop which is capable of offering feedback control and adjusting the pump speed is used to keep the liquid level in the caisson (Deuel *et al.*, 2011).

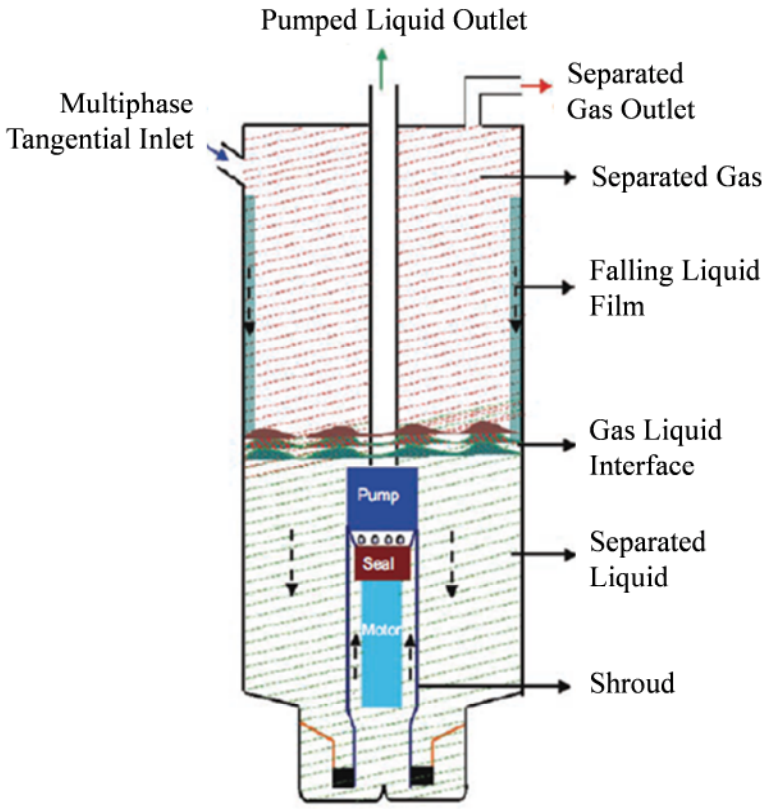

Figure 2-7 Detailed flow schematic of ESP/Caisson separator (Ju *et al.*, 2010)

The ESP/Caisson technology has been applied in Perdido and BC-10 projects at water depths about 2380 m and 1800 m, respectively. Due to the relatively low reservoir pressure and large water depths, artificial lift is required to make these field development economically (Vu *et al*., 2008).

As in the Perdido project, a 105m long, 35”x 16” OD vertical caisson separator is selected. Figure 2-8 shows an overview of the caisson separator. It is critical to have an efficient separation in the separator. A specially designed inlet, shown in Figure 2-9Figure 2-9, guides and partially separates the incoming fluids before the caisson separator. The lower part of the caisson length is designed to submerge the tall motor in the liquid phase so as to reduce the temperature of the motor. Additionally, the liquid slug initialized from the production well will be eliminated within the long caisson separator. The Gas Carry Under (GCU) of the separator is expected to be less than 10%. However, there are potential drawbacks for the ESP/Caisson technology, in terms of capital and intervention cost.

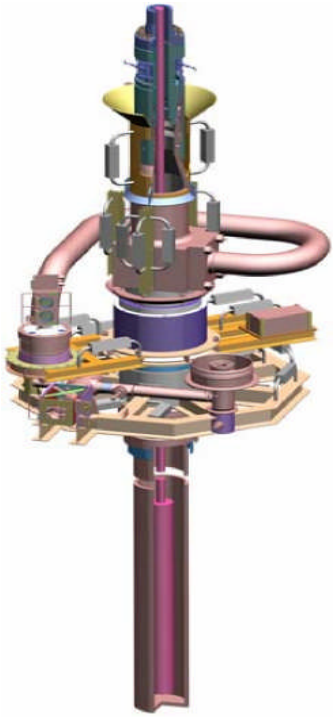

Figure 2-8 Diagram of the Caisson separator, (note it is in a vertical view) (Gruehagen and Lim, 2009)

Figure 2-9 Photo including the inlet part of the Caisson separator used in the Perdido project (Vu *et al*., 2008)

It can be seen from the above sections the current subsea separation technologies either need large separation vessels or complex building blocks. A state of art comparison of the subsea separation technologies is given in Table 2-1.

Table 2-1 Overall comparison of the state of art subsea separation technologies

Concepts	Pros & Cons & Comments
Gravity separation	**Pros:** - Simple concept, gravity separators installed on topside. **Cons:** - Due to subsea conditions, the experiences of topside installation would be less useful. - Units have larger diameters resulting in being complicated to produce and setup. - The cost is high. **Comments:** - Being used in some projects, however the industry expects a smaller but efficient technology for replacement.
Caisson separation	**Pros:** - Being used in subsea, including mechanical packaging and combination with the ESP pumps. Being found to be applicable to deep-water conditions. **Cons:** - Difficult to be applied to conditions with high levels of sand in the produced fluid. - The system performance is found to be limited and also the capacity is limited under the concept. - The total budget will increase due to spending on drilling and preparation of the dummy well. **Comments:** - The retrieving of the ESP needs to be developed for a more convenient method.

Overall, the total cost of using the above separation technologies is high. Secondly, if the production well is under excessive deep water, it would be difficult to manufacture and install those large vessels. Based on these, a cost effective technology which is efficient and robust under deep water conditions is highly demanded by the industry.

2.2 Present Industrial Gas/Liquid Separation Technologies

There are many technologies in terms of separating the gas and liquid. A brief overview of the most commonly used industrial gas/liquid separation technologies will be presented in this section. Three methods often used to achieve physical separation are gravity settling, inertia forces, and coalescing. These three separation methods are applied for distinctly different purposes. The gravity settling is achieved by decreasing the fluid velocity to allow the liquid droplets settle out in the separation space, and it is mainly applied to (pre-) separate large volume of coarse liquid. This method is hardly useful for mist separation. The inertial force is to alter the flow direction suddenly and is usually used as the inlet internal for bulk separation or in the situation of separating droplets. Separators based on this principle are not suitable for processing high liquid loading. Coalescing separation is applied when it is necessary to collect finest droplets to achieve very high separation efficiency. It is not suited to handle high liquid loadings. Each type of separation devices can either be used alone or in combination. The choice of a proper technology for separating gas/liquid production needs both a comprehensive understanding of the process conditions, and the knowledge of the impurities in the fluid (Stewart and Arnold, 2008).

In this section, the practical applications of these three separation methods are reviewed according to Figure 2-10. Attentions are paid to the principles governing the separation process, the operating characteristics and presently available practical design procedures. After a characterization of all listed separation devices, section 2.2.4 evaluates their suitability to subsea applications.

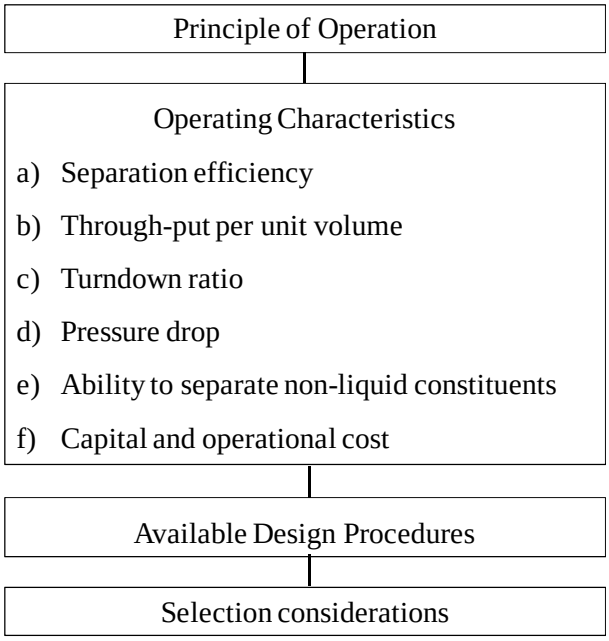

Figure 2-10 Diagram of the characterization of the separation devices presented in sections 2.2.1-2.2.3

2.2.1 Gravity Settling

Gravity settling is the conventional form of gas/liquid separation. It is often achieved in large pressure vessels. If the velocity of the gas/liquid mixture is sufficiently slow, large droplets will settle out in the separation space and gas bubbles will emerge to the gas/liquid surface. Two basic types of separators are widely used: horizontal and vertical. Horizontal separators are usually used for high gas-liquid flow rate, while vertical separators are commonly used on low to intermediate gas-liquid flow rate (Stewart and Arnold, 2008).

2.2.1.1 Principle of operation

Figure 2-11 and Figure 2-12 are typical schemes of horizontal and vertical gas/liquid separators, respectively. Despite the difference in orientation or size, all gravity separators consist of four main sections, as follows:

- The inlet diverter section
- The gravity settling section
- The mist extractor section
- The liquid collection section

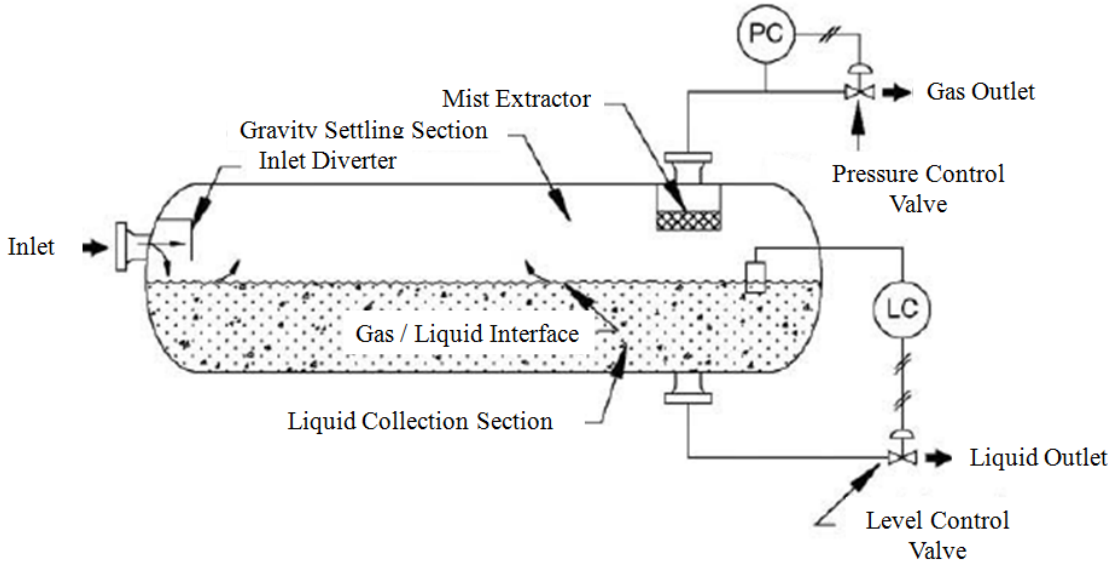

Figure 2-11 A typical schematic of a horizontal gas/liquid separator (Stewart and Arnold, 2008)

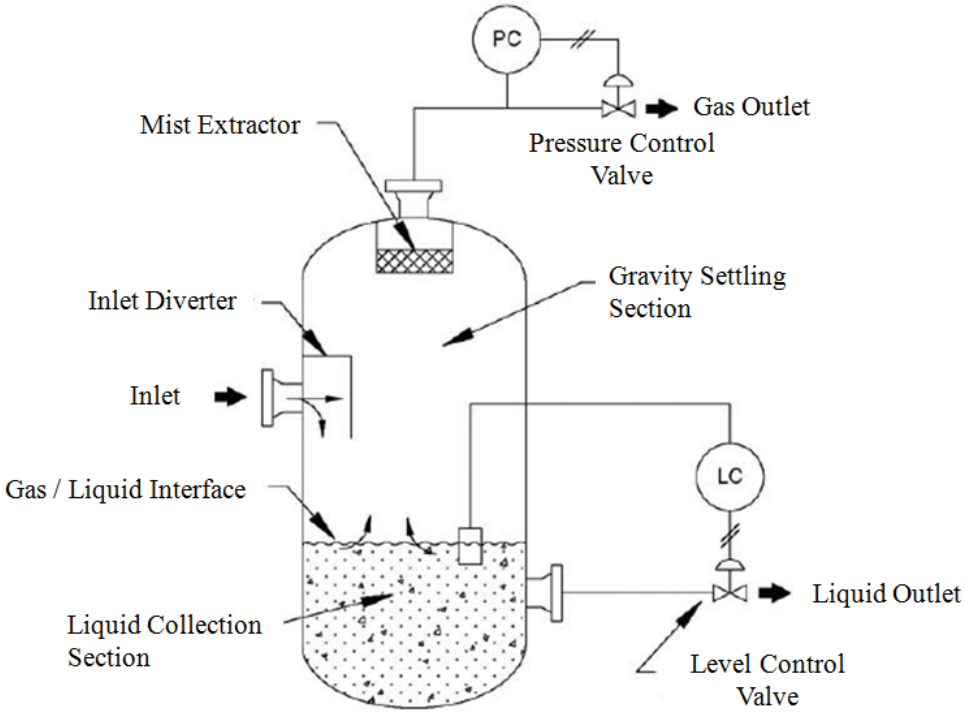

Figure 2-12 A typical schematic of a vertical gas/liquid separator (Stewart and Arnold, 2008)

The inlet diverter directs flow at the entrance of the fluid and performs the bulk separation of gas/liquid flow. The design of an inlet diverter is very important, as the diverter should generate minimum disturbances to avoid the re-entrainment problem. To meet these purposes a large variety of inlet devices exists, such as baffle plates, centrifugal diverter and inlet distributor, shown in Figure 2-13.

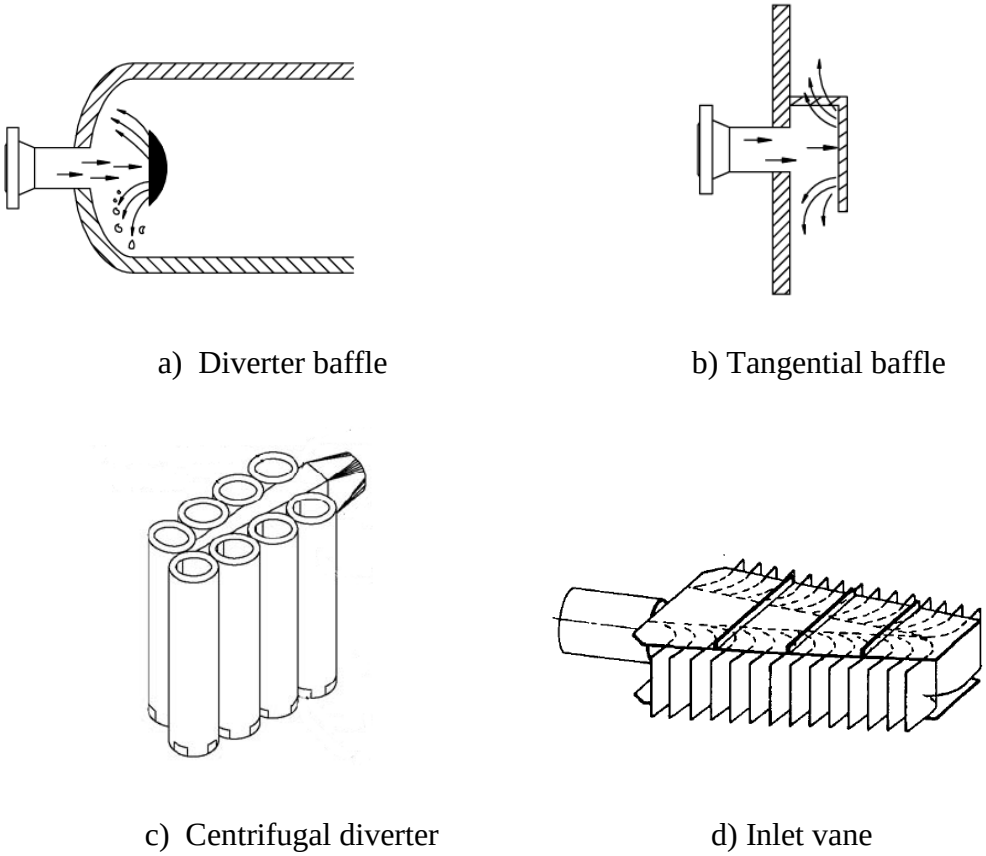

a) Diverter baffle b) Tangential baffle

c) Centrifugal diverter d) Inlet vane

Figure 2-13 Schematic of inlet diverters (Stewart and Arnold, 2008, Swanborn, 1988)

The baffle plate can take advantage of inertia as liquid and gas hit it. Liquid falls downward to section where the liquid exists of the vessel, while gas tends to move around the plate. The baffle plate can be designed as a half sphere, cone, flat plate and angled iron, etc. The baffle can be designed in any way as long as its structural support can bear the momentum impact on it. The diverter baffle shown in Figure 2-13 a) is for a horizontal separator. The tangential baffle shown in Figure 2-13 b) is usually applied in a vertical separator (Stewart and Arnold, 2008).

The centrifugal inlet diverters, as shown in Figure 2-13 c) use the centrifugal force to separate the incoming fluid. A cyclonic chimney or a tangential inlet is normally used to guide the fluid to flow around the wall of the devices. The centrifugal diverters can be very effective in terms of bulk separation, which also works well with foaming or emulsifying crudes. On the other hand the drawback of the centrifugal inlet diverters is that they are sensitive to the flow rate. At a lower flow rate, the system cannot perform properly. Due to this reason, centrifugal inlet diverters are not applied to conditions where flow rates are unsteady.

Inlet vanes are usually applied in scrubbing operations, where the inlet flow is expected to be distributed evenly across the separator. A half pipe arrangement was used frequently in the past. Today, the most commonly used inlet is the vane type, which includes a number of vanes that gradually release the gas and liquid into the scrubber, as shown in Figure 2-13 d).

The liquid droplets which were not separated at the inlet are expected to be separated in the gravity settling section, where liquid droplets larger than 140 μm were separated (Stewart and Arnold, 2008).

The liquid collecting section provides a retention time, which allows the entrained gas bubbles to escape. Moreover, this section provides a surge volume, which is capable of handling the slugs. The liquid separation quality is often dependent on the liquid retention time. The longer the retention time the better the separation. However, a longer retention time requires a larger vessel and/or an extension of the liquid depth of the separator. Most common retention times vary from 30s to 20 min depending on the fluid properties and other considerations (Stewart and Arnold, 2008).

The liquid level is maintained by a level control system. The signal is sent from the controller to control the liquid outlet valve, in order to keep the liquid level at the designed height. The level control is less important in a vertical separator, because the small fluctuations (several inches) of the liquid level will not influence the separator operating efficiency. However, for the horizontal separator, the liquid level is more critical, as it can affect the droplet settling space, therefore affecting separation efficiency. A pressure controller installed on the gas outlet is used to maintain the

pressure at a certain value, and the pressure relief devices are installed to control or limit the pressure build up in the separator in case of a process upset, instrument or equipment failure, or fire (Stewart and Arnold, 2008).

The gas flows out through mist extractors, where suspended liquid droplets are removed from the gas. Special coalescing elements are contained within the mist extractors, which can provide a large surface area in order to allow coalescence and eliminate the small droplets. Mist extractors can be very efficient in separating droplets smaller than 140μm. More details of the widely used wire meshes and vanes type will be discussed later in section 2.2.3.

Overall, the principles of operating the horizontal and vertical separator are quite similar. The only difference is that horizontal separators achieve separation tangentially to the flow and the vertical ones do it parallel to the flow. The selection of separator is often decided on a basis of economic consideration.

2.2.1.2 Operating characteristics

The operating characteristics of gravity settling separator can be summarized as following (Swanborn, 1988)

Table 2-2 The operating characteristics of gravity settling separator

a) Separation efficiency	:	Droplets with diameter of 140 μm and larger will settle out of the gas in most average-sized separators
b) Through-put per unit volume , K-value*	:	Low; $K < 0.1$ m/s for low-pressure applications
c) Turndown ratio	:	No theoretical lower limit to gas velocity
d) Pressure drop	:	Low; determined mainly by size and shape of in and outlet nozzles
e) Ability to separate non-liquid constituents:		Medium
f) Installation and operational costs	:	Strongly increases with increasing pressure

** K-value is Souders-Brown coefficient; it will be discussed in section2.2.1.3.*

2.2.1.3 Available design procedures

Rules of thumb have been established to improve the design of the gravity separator. The size of a gravity separator is usually decided by the gas settling velocity and the liquid retention time theory. The most comprehensive method was presented by Svrcek and Monnery (1993). The detail of the design procedures is included in Appendix A.

Settling theory

The settling theory is a simplification of the actual process taking place in the separators. Liquid droplets in a gas flow are acted on by three forces: gravity, buoyancy, and drag force, as illustrated in Figure 2-14.

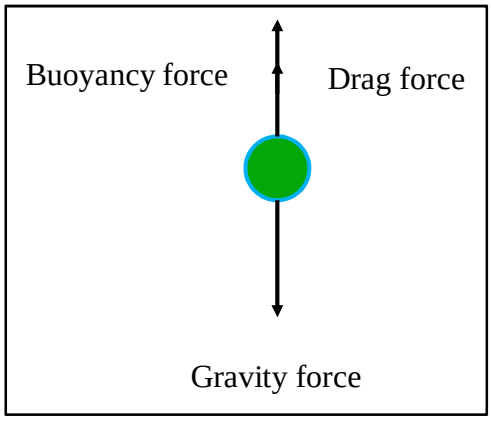

Figure 2-14 Schematic diagram indicating the forces of on a liquid droplet, note it is in an upwards-flowing gas field

The gravity force is always directed downward and is given by

$$F_G = \frac{\pi D_d^3}{6} \cdot \rho_l \cdot g \tag{2-1}$$

where F_G is the gravity force; D_d is the droplet diameter; ρ_l is liquid density; g is the gravitational constant.

Under the assumption that the droplet is in the gas, the buoyancy force is opposite the gravity force and is given by

$$F_B = -\frac{\pi D_d^3}{6} \cdot \rho_g \cdot g \tag{2-2}$$

where F_B is the buoyancy force; ρ_g is gas density.

The drag force is opposite the direction of droplet velocity and is determined from

$$F_D = -C_D \cdot A_d \cdot \rho_g \cdot \frac{v_t^2}{2} \tag{2-3}$$

where C_D is the drag coefficient, dimensionless; A_d is the droplet cross-section area and v_t is the terminal settling velocity of droplet.

Theoretically, if the gravity force is over the force caused by the droplets' motion relative to the gas phase, droplets will settle out of a gas flow. Therefore, balancing the net drag force and gravity force results in

$$v_t = \sqrt{\frac{4g}{3}\left(\frac{\rho_l - \rho_g}{\rho_g}\right)\frac{D_d}{C_D}} \tag{2-4}$$

Several correlations have been developed to estimate the drag coefficient C_D. In order to simplify the calculation, the droplet has been assumed as a solid, rigid sphere. Table 2-3 summarize the most widely used correlations.

Table 2-3 Correlations of drag coefficient C_D (Rhodes, 2008, Gibilaro *et al.*, 1985)

Literature	Correlation
Stoke's Law	$C_D = \frac{24}{Re_d}$ $Re_d < 2$
Intermediate Law	$C_D = \frac{18.5}{Re_d^{3/5}}$ $2 < Re_d < 500$
Newton's Law	$C_D \approx 0.44$ $500 < Re_d < 2 \times 10^5$
Bird	$C_D = \frac{24}{Re_d} + \frac{3}{Re_d^{1/2}} + 0.34$
Gerhart	$C_D = \frac{24}{Re_d} + \frac{6}{1 + Re_d^{1/2}} + 0.4$
Magnaudet	$C_D = \frac{24}{Re_d}(1 + 0.15Re_d^{0.687})$

where the droplet Reynolds number Re_d is defined as $Re_d = \frac{\rho_g \cdot D_d \cdot v_t}{\mu_g}$; μ_g is the gas viscosity. The terminal velocity v_t can be solved by an iterative process. Svrcek and Monnery (1993) also suggested correlation for calculating C_D without trial and error. The correlation is given in Appendix A.

The difficulty of applying the settling theory lies in finding out which minimum droplet size will give the desired separation efficiency. Walas (1990) suggested a value of 200 μm droplet diameter in terms of the design of a separator. Stewart and Arnold (2008) illustrated that the gravity separating space can remove droplets with sizes larger than 140 μm, while the demister can eliminate remaining droplets between 10 and 140 μm. Therefore, they suggested that droplet size can be taken as 140 μm for a separator design. They also recommended a 500 μm size for gas scrubbers and 300-500 μm for flare or vent scrubbers.

Eq. (2-4) can also be rearranged as Sauders and Brown equation as follows

$$v_t = K\sqrt{\frac{\rho_l - \rho_g}{\rho_g}} \tag{2-5}$$

where $K = \sqrt{\frac{4g}{3}\frac{D_d}{C_D}}$ is the settling velocity coefficient or Sauders and Brown coefficient, depending on design and operating conditions. K has the unit of m/s.

Usually, the K-value can be taken as an indication of separator's compactness. The bigger the K-value is the more compact the separator is. Gerunda (1981) suggested that the K-value was between 0.03 and 0.107 m/s. Smith (1987) recommended a K -value varying between 0.03 and 0.051m/s but suggested the use of conservative values in order to account for uncertainties in the conditions. In practical low pressure applications, the K-value recommended is no more than 0.1 m/s, and normally a 50% safety margin is applied for vessels without internals. The K-value declines as pressure increases, because increasing pressure often results in an interfacial tension reduction and thereby the droplets sizes are reduced as well. The Gas Processors Suppliers Association (GPSA, 1998)suggested to reduce the K-value to 75% for 8.5 MPa pressure for separators with a mist eliminator.

It is clear that separator designs based on the K-value do not fully account for the changing of the droplet sizes, which can be affected by changing of interfacial tension, fluid properties or composition. Also, the K-value does not consider the effect of liquid loading which may significantly affects separation efficiency.

Retention time theory

In order to make sure both gas and liquid can reach equilibrium in the separator, there is a need to maintain some liquid inside the vessel. The retention time is used to measure the liquid storage and is defined as

$$t_R = \frac{V_{l-SEP}}{Q_l} \tag{2-6}$$

where t_R is the retention time; V_{l-SEP} is the liquid storage volume in the vessel and Q_l is the liquid flow rate.

The liquid retention time is either selected from empirical data, or based on the requirement of ensuring a reliable and stable operation of the separator and downstream process. Generally, retention times are range from 30 to 180 seconds, which are found to be sufficient for most cases. However for foaming crude, the retention time may need to be extended from 120 to 720 seconds (Stewart and Arnold, 2008).

2.2.1.4 Selection considerations

Each type of gravity settling separator has specific advantages and limitations. In a vertical separator, the liquid droplets which need to be removed from the gas phase must settle downward against the up flowing gas. Conversely, in the horizontal separator, the movement of the liquid droplet is vertical to the gas flow; in this case it is much easier to be settled. Therefore, the difference in the flow pattern of the separated liquid droplets indicates that for a given gas loading, the horizontal separator is smaller and more cost effective. On the other hand a vertical separator occupies less floor space, which is an important consideration on an offshore platform and subsea block building (Stewart and Arnold, 2008).

Manning *et al*., (1991) compared the advantages and disadvantages of horizontal and vertical separators as shown in Table 2-4. It shows that horizontal separators are more effective and more economical in terms of separating normal gas-oil production, especially when there might be issues such as foam, emulsions or high GOR involved. However vertical separators are more effectively in the applications of high GOR, where only mists are need to be eliminated from the gas phase. As mentioned before,

the selection of separator is usually based on which one will accomplish the separation requirement at the lowest “life-cycle” cost.

Table 2-4 Comparison of horizontal and vertical separator

Type	Pros & Cons & Applications
Horizontal separator	**Pros:** - Requires smaller diameter for the same capacity - Larger surge volume - Large liquid surface area for foam dispersion **Cons:** - Occupies more space - Difficult to handle impurities **Applications:** - Large volume of gas/liquids separations - GOR is high or medium - Foaming crudes present
Vertical separator	**Pros:** - Can handle impurities - Less tendency for re-entrainment - Occupies less space **Cons:** - Difficult to maintain the instruments and safety devices, which are usually mounted on the top **Applications:** - Small flow rates of gas and /or liquids - Very high GOR or very low GOR or scrubber applications - When the application space is restricted to a certain size - When the controlling system needs to be easily handled

2.2.2 Cyclone Type

A cyclone separator mainly uses centrifugal forces, and they are used widely for de-dusting and de-misting. In a cyclone, the gas-particles (solids/droplets) mixture performs a swirling motion inside a cylindrical body, where the particles are flung outward and collected on the inner wall of the cyclone. The gas leaves either reversely or flow through the vortex finder. Based on the gas flow pattern inside cyclone, a cyclone can be classified as “Reverse-Flow Cyclone” (RFC), and “Axial-Flow Cyclone” (AFC). By far the majority of experimental and theoretical studies of cyclones have been reported relating with the separation between the solid particles and gas phase. However, the principles of separating liquid droplets from gas are the same, and it is the subject of the following section. Due to the geometry difference, the RFC and AFC are described separately.

2.2.2.1 Reverse-Flow Cyclone

2.2.2.1.1 Principle of operation

Generally, an RFC consists of an inlet section, a separation chamber, a liquid discharge and a gas outlet section. As shown in Figure 2-15, the swirling flow is created by the tangential injection of the mixture or axially flow through a swirl element. Figure 2-15a) represents a cylinder-on-cone RFC and b) represents a cylindrical RFC. As the mixture swirls, the gas flows axially down along the wall of the RFC, and when the gas reaches the near bottom of the RFC, the gas gradually flow towards the inner space of the RFC, with an upward axial movement. A vortex finder is assembled on the top of RFC, extending downward from the roof centre, and the gas flows out from it. The liquid droplets are flung towards the inner walls and formed liquid wall film. The liquid film falls down along the inner wall of the RFC and is collected at the liquid discharge section (Hoffmann and Stein, 2008).

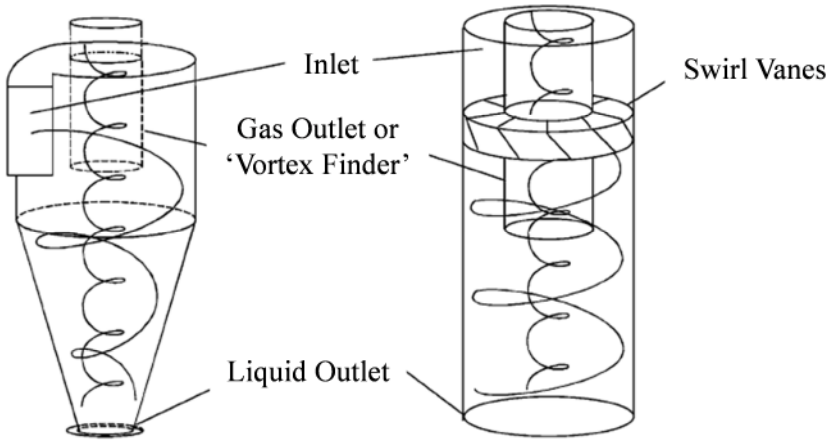

a) Cylinder-on-cone RFC b) Cylindrical RFC

Figure 2-15 Sketches of reverse flow cyclones (Peng *et al*., 2002)

Various inlet configurations are available for enhancing the separation efficiency of RFC. The four main types are: pipe inlet, rectangular inlet, wrap-around inlet, and swirl vanes, as shown in Figure 2-16. The pipe inlet is the simplest and cheapest one. The rectangular type generally provides good performances and is by far the most widely used inlet. However, a particular inlet transition part is required, named the round-to-rectangular section, and this transition section makes the manufacture of RFC more complicated. A large angular momentum is expected with the 'wrap-around' inlet, which will result in a greater swirl velocity at the vortex internal core. Because most of the inlet particle separation happens at the scroll section, it is more applicable to high particle load conditions. The swirl vane is often inserted in the cylindrical bodies and the gas phase enters cyclone parallel to its axis. Some operational benefits result from the axial symmetry, which is caused by this axial entry (Hoffmann and Stein, 2008).

Two types of configurations are generally used regarding the separator chamber shapes, one of which is cylinder-on-cone and another is cylindrical. Normally, the cylinder-on-cone one is called 'cyclone', whilst the cylindrical type is called 'swirl tubes (reversed)'. (In order to distinguish the swirl tube in section 2.2.2.2, the 'swirl tubes (reversed)' represents the swirl tube with reverse flow). The cyclone can be installed in a large vessel as the inlet device, which has been discussed in section 2.2.1. The cyclone is expected to handle large amounts of incoming liquid. The cyclone also can be designed as a standalone device, equipped with a liquid hold-up drum, which provides liquid

level control and liquid surge capacity. Swirl tubes (reversed) are usually applied in the high efficiency operations or final stage with medium or low particle loadings, and the most common configuration in the industry is a “swirl deck” or “multi-cyclone”, which consists of small tubes (Hoffmann and Stein, 2008).

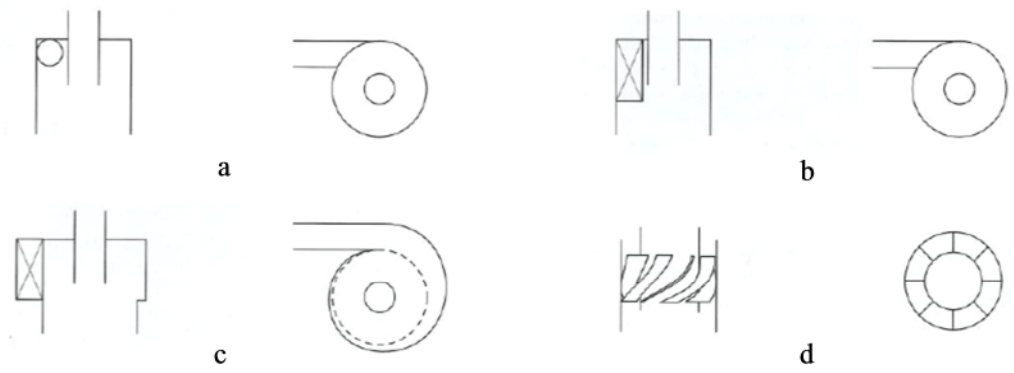

Figure 2-16 Four widely adopted inlet configurations (Hoffmann and Stein, 2008)
a) pipe inlet, b) rectangular inlet, c) wrap-around inlet, and d) swirl vanes, including their side (left) and top (right) views

2.2.2.1.2 Operating characteristics

The operating characteristics of reverse flow cyclone separator are summarized as follows (Swanborn, 1988)

Table 2-5 Operating characteristics of reverse flow cyclone separator

a)	Separation efficiency	:	Low for single cyclone; D_{50}~ 25-50μm High for multi-cyclone; D_{50}~ 5-7μm
b)	Through-put per unit volume , K-value	:	K~ 0.2-0.3m/s
c)	Turndown ratio	:	0.4, very sensitive to the flow rate
d)	Pressure drop	:	20-30mbar
e)	Ability to separate non-liquid constituents	:	Very good
f)	Installation and operational costs	:	Relate approximately inversely with K-value

2.2.2.1.3 Available design procedures

Various mathematical models have been proposed to estimate the velocity distributions and the performance of de-dusting cyclone in the literature. De-misting cyclones follow the same general sizing guidelines. In the following section, only the classic models available for computing cyclone grade efficiency and pressure loss will be briefly reviewed. More details will be discussed in Chapter 3.

Grade efficiency

Normally, the efficiency of a cyclone is characterized by the 'critical size' or the 'cut size' of particles. 'Critical size' is defined as the size of particles with a fractional efficiency of 1.0, while 'cut size' is the size of particles with a fractional efficiency of 0.5. A grade efficiency curve is sketched by plotting the particle diameter vs. separation efficiency (Hoffmann and Stein, 2008).

During the past few decades, different methods of theoretically evaluating the cyclone efficiency have been developed. The widely used 'equilibrium-orbit' model and 'time-of-flight' model are reviewed as follows. These two models were developed based on the standard reverse-flow, cylinder-on-cone cyclone with a tangential, slot type inlet (Hoffmann and Stein, 2008). A schematic of this type of cyclone is shown in Figure 2-17 to describe these models. The geometrical notations are indicated in the right-hand side.

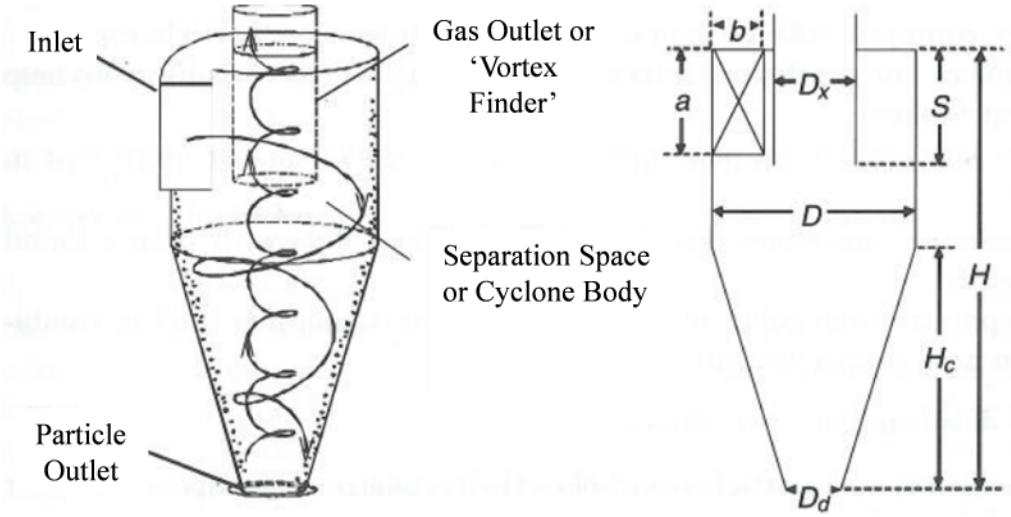

Figure 2-17 Schematic of a reverse-flow cyclone and geometrical notation (Hoffmann and Stein, 2008)

'Equilibrium-orbit' model

The 'equilibrium-orbit' model proposed by Barth (1956) is derived from a force balance on a particle rotating on the imaginary Cylindrical Surface (CS). The CS is defined as the interface between the outer and inner vortex, as shown in Figure 2-18. It is shaped by extending the vortex finder wall to the bottom of the cyclone.

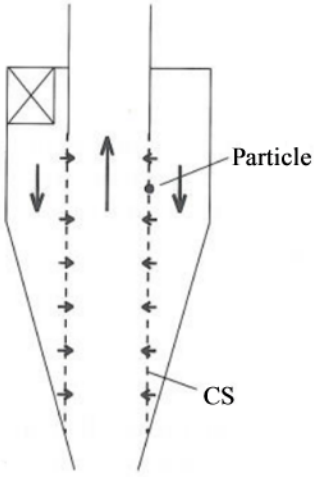

Figure 2-18 Schematic of the concept used in 'equilibrium-orbit' models (Hoffmann and Stein, 2008)

Over the CS, the gas velocity components are set to be constants. Because the gas phase flows from the outer part to the inner section of the vortex, there exists an inward drag, while a 'centrifugal force' acts outwardly. By balancing the two forces, the cyclone's cut size D_{50} indicates that there is 50% of chance that this particle will be captured. The cut size is an important parameter for measuring the separation capability of a cyclone.

The outward centrifugal force acting on the particle on the CS is given as

$$F_c = \frac{\pi D_d^3}{6}\rho_l\left(\frac{v_{\theta CS}^2}{D_x}\right) \tag{2-7}$$

where F_c is the centrifugal force; $v_{\theta CS}$ is the tangential velocity calculated in the CS. D_x is the vortex finder diameter.

The drag acting on the particles is inward and is given as

$$F_d = 3\pi D_d \mu_g v_{rCS} \tag{2-8}$$

where v_{rCS} is the radial velocity calculated in the CS.

Equating the centrifugal force and the drag force, the cut size D_{50} is determined as

$$D_{50} = \sqrt{\frac{v_{rCS} 9 \mu_g D_x}{\rho_l v_{\theta CS}^2}} \tag{2-9}$$

By assuming that the radial velocity is neglected near the cyclone wall and is uniform in the CS, the radial velocity v_{rCS} can be calculated as

$$v_{rCS} = \frac{Q_g}{\pi D_x H_{CS}} \tag{2-10}$$

where Q_g is the gas volumetric flow-rate, H_{CS} is the height of CS .

To obtain the tangential velocity in the CS, Alexander (1949) introduced the following correlations

$$v_{\theta CS} = \frac{C}{r^n} \tag{2-11}$$

$$n = 1 - (1 - 0.67D^{0.14})(\frac{T}{T_0})^{0.3} \tag{2-12}$$

where C is a constant; r is the radius of CS; D is the cyclone body diameter; T is the temperature and T_0 is room temperature (283K). In order to use the above correlations, the tangential velocity of the cyclone wall is assumed equal to the inlet velocity. Thus the tangential velocity in the CS can be calculated.

Muschelknautz (1972, 1980) further developed Barth's method, by accounting the effects of wall roughness and particle loading on the cyclone performance. Muschelknautz's model will be discussed in Chapter 3.

'Time-of-flight' model

Another classic model is the 'Time-of-flight' model, in which the time for the particle travelling within the cyclone is taken into account. The original method was introduced by Rosin *et al*., (1932). This model considers whether the particle will reach the radial wall before it reaches the bottom of the cyclone. The concept behind the 'time-of-flight' models is shown in Figure 2-19.

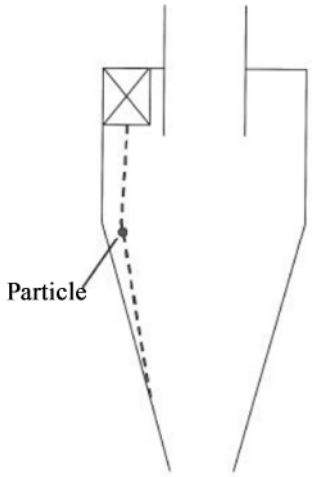

Figure 2-19 Schematic of the concept used in 'time-of-flight' models (Hoffmann and Stein, 2008)

In this approach, any radial gas velocity is neglected. The critical particle size is defined as the size of the particle which can migrate the radial distance across the cyclone within the residence time of the particle inside the cyclone. Correspondingly this path length for the particle travelling is given as

$$L = \pi D N_s \tag{2-13}$$

where N_s equals to the number of spiral turns that the particle encounters before reaching bottom. N_s can be calculated by fitting the graph provided by Zenz (2001).

$$N_s = 6.1(1 - e^{-0.066 v_{in}}) \tag{2-14}$$

where v_{in} is the inlet velocity. Assuming the tangential velocity equals the inlet velocity, then the residence time for a particle reaching bottom is given as

$$t_{cyc} = \frac{\pi D N_s}{v_{in}} \tag{2-15}$$

The final radial velocity of a particle is given by

$$v_r' = \frac{D_d^2(\rho_l - \rho_g)}{18\mu_g}\left(\frac{v_{in}^2}{D/2}\right) \tag{2-16}$$

The migration time required to strike the wall is given as

$$t_{mig} = \frac{b}{v_r'} \tag{2-17}$$

Equating the migration time to the residence time available, the critical particle size can be obtained:

$$D_{50} = \sqrt{\frac{9b\mu_g}{\pi N_s v_{in}(\rho_l - \rho_g)}} \tag{2-18}$$

From the 'equilibrium-orbit' model, it can be seen that an increase in D will lead to increasing of n. Consequently, $v_{\theta CS}$ will decrease and D_{50} will increase. This means the larger the cyclone is, the poorer the performance (bigger cut-size) will be. However, the 'time-of-flight' model indicates that the longer the cyclone is the better the efficiency will be (which is also known as smaller cut-size), because it allows a longer period for the particle to touch the wall within the longer cyclone. In general, the knowledge regarding the increase of the efficiency of a cyclone related to the following points (Hoffmann *et al*., 2001):

- Increasing the size and/or density of the particle traveling within the cyclone
- Increasing rotational speed of the vortex
- Reducing the diameter of the cyclone
- Extend the cyclone

Pressure drop

Three parts in general contribute to the overall cyclone pressure drop: 1) the entry part; 2) the main body, and 3) the vortex finder. The first one is normally negligible in terms of magnitude. The losses in the cyclone body are not in the dominated overall pressure loss either, but it is the main factor in controlling the swirl intensity within a cyclone. The largest pressure losses lie in the vortex finder. A dimensionless "Euler number" is often used for describing the pressure drop and it is given as

$$Eu = \frac{\Delta p}{\frac{1}{2}\rho v_{ch}^2} \tag{2-19}$$

where v_{ch} is the characteristic velocity, and it is often taken as the mean axial velocity in the cyclone. Δp is the pressure drop of a cyclone. Eq. (2-19) is normally used as the scaling rule to estimate the pressure drop of a geometrically similar cyclone.

Many models of estimating the pressure drop in a cyclone are empirical. These empirical models are sufficient for cyclones with smooth walls and where particle loading is low. Otherwise, models including the dissipative loss in the cyclone are more realistic such as the latest Muschelknautz model (Muschelknautz, 1972). Since pressure loss is not the main concern of this study, it will not be discussed in detail in this thesis.

Two of the most widely used empirical pressure drop models proposed for cyclone with slot-type inlets are (Hoffmann and Stein, 2008):

Shepherd and Lapple

$$Eu_{in} = \frac{16ab}{D_x^2} \tag{2-20}$$

Casal and Martinez-Benet

$$Eu_{in} = 3.33 + 11.3\left(\frac{ab}{D_x^2}\right)^2 \tag{2-21}$$

Scaling rules

There are some simple scaling rules derived to estimate the cut size in a cyclone and also the pressure drop based on the measured results from geometrically similar cyclones. Dimensional analysis showed that if geometrically similar cyclones have the same Re, then Stk_{50} and Eu will be the same. Then the cut size can be calculated from Stk_{50} and is given as

$$Stk_{50} = \frac{\Delta\rho D_{50}^2 v_{ch}}{18\mu_g D} \tag{2-22}$$

where $\Delta\rho$ is the density difference of gas and particles.

2.2.2.2 Axial-Flow Cyclones

In the Axial-Flow Cyclone (AFC), the gas enters along its cylindrical axis. Several sketches of AFC geometries are given in literatures. A schematic and a photograph of the typical AFC - Verlaan cyclone are shown in Figure 2-20. There is a 45° exit angle within the AFC at the vane blades (Jacobsson 2006). In order to assist the liquid separation, vertically slits with sharp inner edge are designed.

.

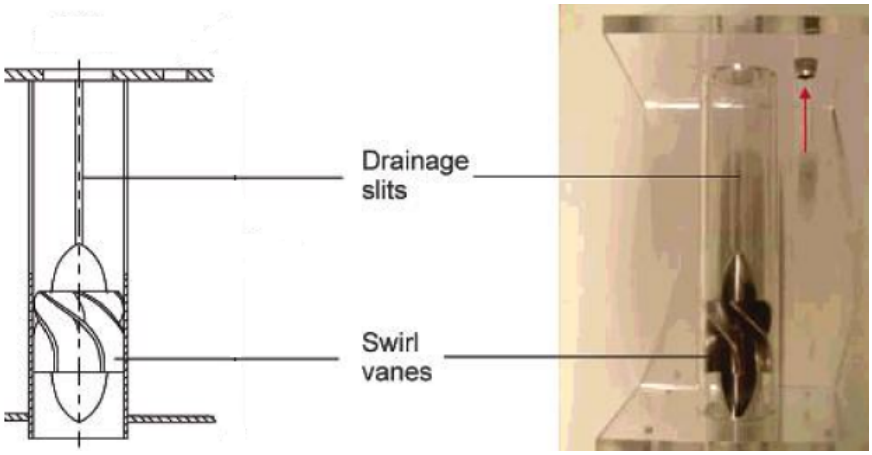

Figure 2-20 Schematic and photograph of Verlaan axial flow cyclone (Jacobsson 2006)

2.2.2.2.1 Principle of operation

The AFC is operated on a different principle to RFC. To create a swirling flow, the mixture is designed to enter the cyclone through a spinning part known as the swirl-vanes, which are located at the near bottom of AFC. After separation, the gas flow leaves from a vortex finder placed at the top centre.

It appears that the cyclone with smaller the radius has a higher separating efficiency. However, the radius for a single cyclone cannot be chosen as small as one would like for a given gas flow. One reason is that the spinning gas flow could gain so much velocity that the wall film would be re-entrained. Another reason is the pressure drop, which has been proved to increase with the square of the gas flow through a cyclone, could become excessive. So for a certain tube size a limit gas flow is set. In order to be able to process larger gas flows at the same separation efficiency a number of small swirl tubes are placed in parallel. The gases and liquids need to be distributed evenly between the various tubes (Austrheim *et al*., 2008).

2.2.2.2.2 Operating characteristics

The operating characteristics of multi axial flow cyclone separator are summarized as following (Swanborn, 1988)

Table 2-6 The operating characteristics of multi axial flow cyclone separator

a)	Separation efficiency	:	High; D_{50}~ 10μm
b)	Through-put per unit volume , K-value	:	K~ 0.4m/s
c)	Turndown ratio	:	0.2
d)	Pressure drop	:	< 10mbar
e)	Ability to separate non-liquid constituents	:	Depending on geometrical characteristics; some multi-cyclone installations experience plugging problems
f)	Installation and operational costs	:	Relate approximately inversely with K-value

2.2.2.2.3 Available design procedures

There is a lot of work published on design and operation of RFC, but less on AFC. Austrheim *et al*., (2007) investigated the performance of a deck of AFC with live natural gas fluids. They stated that the K-value is undesirable in terms of designing a cyclone deck. In the AFC, one decisive factor is the re-entrainment of liquid; the efficiency would drop off due to a greater volumetric gas flow and liquid loading.

2.2.2.3 Selection considerations

The cyclone can separate the droplets with diameter greater than 10um. Most cyclones have a cut size between about 3 to 15um. It is fairly easy to design a cyclone to satisfy the majority of de-misting processing, as droplets in the mist exhibit a much larger diameter. The biggest challenge is how to handle the liquid film once it is flung to the wall of the cyclone.

Normally swirl tubes are less effective than cyclones, while there are many situations where swirl tubes are preferable. In the first place, the axial inlets of swirl tubes occupy much less space than tangential inlets. In the second place, the cylindrical tubes are mechanically stronger than cylinder-on-cone cyclones. Finally, swirl tubes are more resistant to clogging (Austrheim *et al*., 2008) .

2.2.3 Mist Eliminator

To clean the gas flow with small droplets in the range of 5-100μm, which cannot be achieved economically by gravity settling, is subjected to a mist eliminator. The knitted-wire-mesh type and vane type are the two widely used mist eliminators. The following section presents an overview of these two types of eliminator.

2.2.3.1 Mesh type

A wire mesh eliminator consists of wire mesh pads and support grids, as shown in Figure 2-21. Wire mesh pads are made of stainless steel mats, which are knitted with wires with a diameter of 0.10 to 0.28mm. The void volume fraction of the mats is about 0.95 to 0.99 with high surface areas. The pads have a 100 to 150 mm thickness and 160 to 240 kg/m^3 density. In a gravity separator, they are normally placed near the gas outlet (Stewart and Arnold, 2008).

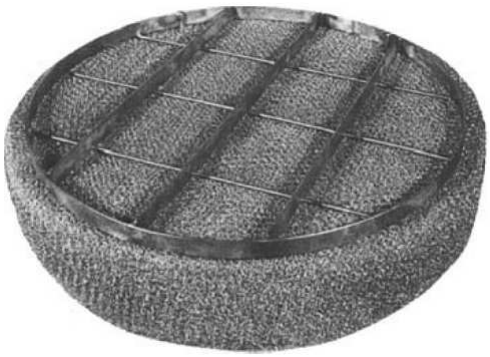

Figure 2-21 A sample of the wire mesh mist eliminator (Stewart and Arnold, 2008)

2.2.3.1.1 Principle of operation

In a wire mesh mist eliminator, direct interception causes droplets to impinge a wire when a gas flow passes very close to it. The separated liquid droplets coalesce and then fall down to the liquid section of gravity separator. Because mist eliminators are generally for gas which travels vertically upwards, the effectiveness mainly depends on the velocity range of the gas phase. A higher velocity will result in the liquids that have settled out to be re-entrained, and a lower velocity will make the gas pass through the mesh pad but the droplets would not be impinged and coalesced (Stewart and Arnold, 2008).

2.2.3.1.2 Operating characteristics

The operating characteristics of a mesh type eliminator are summarised as follows (Swanborn, 1988)

Table 2-7 The operating characteristics of a mesh type eliminator

a)	Separation efficiency	:	99% droplets with size no less than 10 μm can be removed as the mesh size is sufficient
b)	Through-put per unit volume , K-value	:	Low; up to 0.15
c)	Turndown ratio	:	Normally set of 30% of design gas velocity
d)	Pressure drop	:	Low; < 5 mbar
e)	Ability to separate non-liquid constituents	:	Very poor; plugging can occurred easily compared to the vane types of eliminator
f)	Installation and operational costs	:	Relatively high because of large required plan area

2.2.3.1.3 Available design procedures

As mentioned above, 99% of droplets with size no less than 10 μm can be removed, provided the mesh size is correct. The process is also determined by a prescribed velocity shown in Eq. (2-5). The K-value is determined experimentally. However, the theory behind the K-value is derived on basis of the maximum gas velocity in order for a droplet to settle out by gravity. By keeping the K-value constant the effect of droplet size and liquid load is ignored. Hence, it is not a consistent way of designing a mesh pad, but in practice the requirement ensures that the mesh is under a non-flooded situation.

Flooding point

If the gas velocity upstream of a mesh pad exceeds a certain limit, the droplets that have coalesced in the mesh pad, cannot be drained efficiently by gravity and therefore liquid begins to accumulate in the mesh. When this happened the point is called the flooding point and is accompanied by a sudden increasing of pressure drop over the mesh

(Austrheim *et al.*, 2007). Flooding conditions set the upper operation limit for mist eliminator.

In experiments of flooding velocities in packed columns, Sherwood *et al.*, (1938) found that the flooding velocity was dependent on the following factors: physical properties, liquid load, surface area of the mesh pad and void fraction of the mesh. They showed that the flooding point could be corrected by dimensionless quantities

$$\frac{A_s v_{g,s}^2}{g\varepsilon^3}\left(\frac{\rho_g}{\rho_l}\right)\mu_l^{0.2} = f\left(\frac{m_l}{m_g}\sqrt{\frac{\rho_g}{\rho_l}}\right) \tag{2-23}$$

where A_s is the cross area of mesh pad; $v_{g,s}$is the gas velocity pass the mesh pad; ε is porosity of packing; μ_l is liquid viscosity; m_l and m_g are the mass flow rate of liquid and gas, respectively.

Brunazzi (1998) found a good relation with the expression in (2-23), when analysing the flood point for two different mesh pads. Figure 2-22 shows that the flooding velocities decrease with increasing liquid load. Moreover, the operating pressure increases the density ratio, $\frac{\rho_g}{\rho_l}$, and flooding will occur at a lower superficial gas velocity.

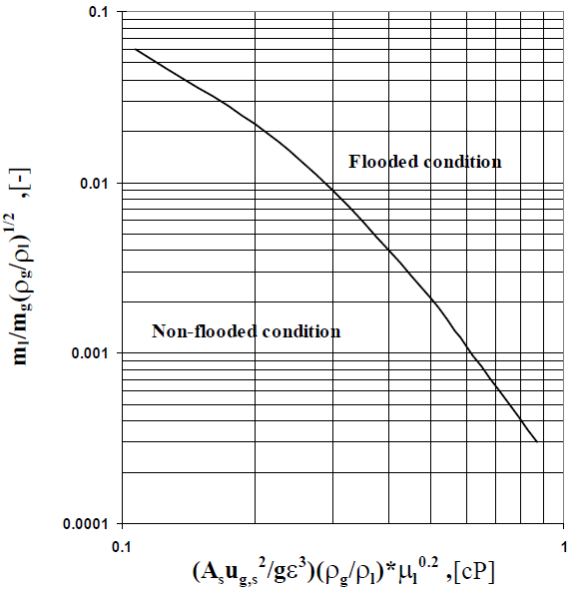

Figure 2-22 The correlation Burkholz found for the flooding point of two different mesh pads (Brunazzi, 1998)

Pressure drop

The pressure drop across a wire mesh pad ΔP_M consists of two parts, a "dry" pressure drop, ΔP_{dry} from gas flow, and a "wet" pressure drop, ΔP_{wet} from liquid holdup.

As the liquid holdup of the mesh pad is a function of liquid loading and gas velocity, ΔP_M increases strongly with the gas flow increasing. The "dry" pressure drop is given as:

$$\Delta P_{dry} = \frac{0.076 f H_m a_m \rho_g v_{g,s}^2}{981 \times 10^3} \tag{2-24}$$

where f is the friction factor from Figure 2-23; H_m is the thickness of the mesh pad and a_m is the surface area.

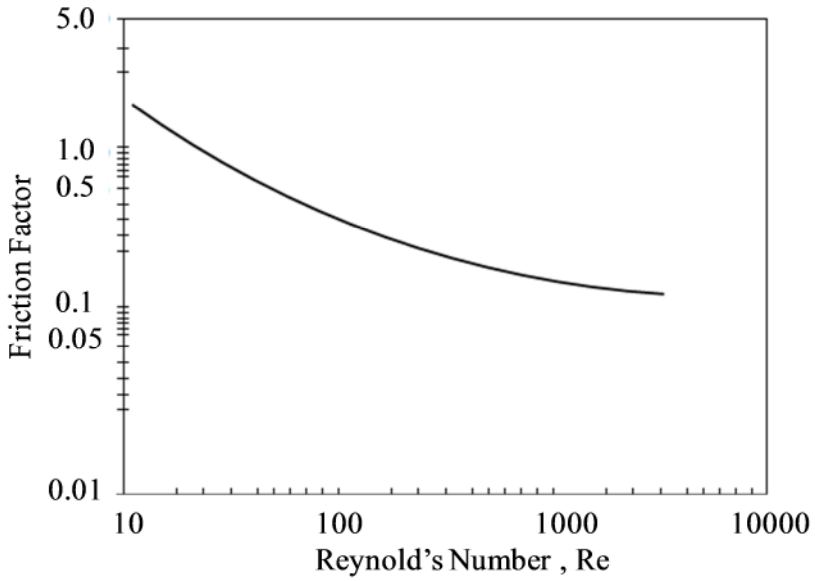

Figure 2-23 Plot of friction factor vs. Reynolds number within a dry eliminator (Stewart and Arnold, 2008)

The "wet" pressure drop is relative to both the liquid loading and the geometry of the mesh pad. The "wet" pressure drop is often obtained by experiment (Stewart and Arnold, 2008).

Another thing need to note here is that a uniform flow pattern is required in order to make the mesh eliminator working within the design capacity and the high efficiency. A

gas distributor is usually placed on the downstream of the mesh pad to distribute the flow evenly.

2.2.3.2 Vane type

The Vane type mist eliminator is made of several parallel vanes that contain directional changes, as shown in Figure 2-24. The vanes can condition the gas flow into a laminar flow. The droplets will be impinged and collect at the surface of the plates. The total depth of the flow direction varied from 150mm to 300mm, and the space between the vanes are 5mm to 75mm (Stewart and Arnold, 2008).

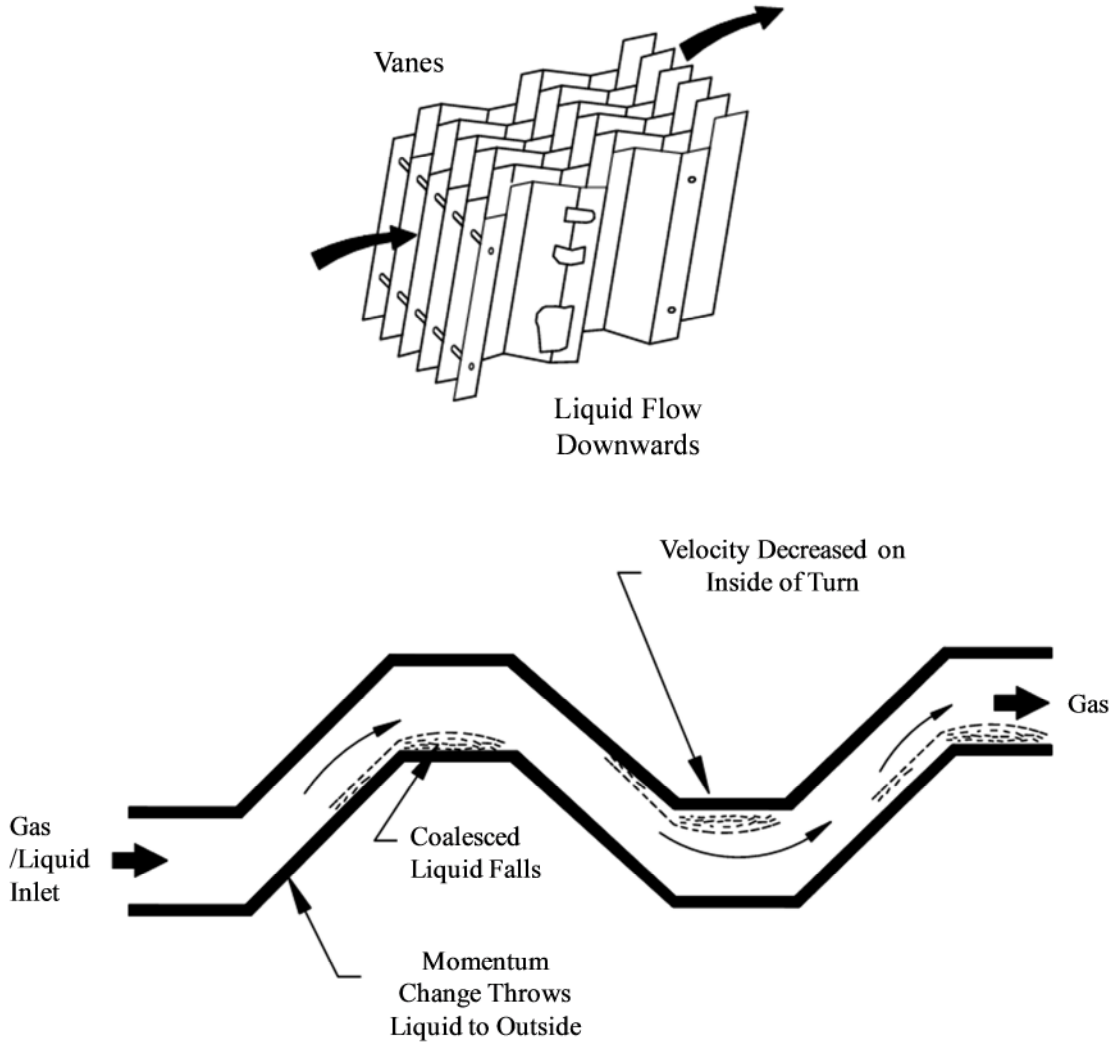

Figure 2-24 Typical vane-type mist eliminator (Stewart and Arnold, 2008)

2.2.3.2.1 Principle of operation

As the gas passes through a vane type mist eliminator, droplets strike on the vane surface and are separated out. A special designed drain pipe collects and reroutes the liquid to a section where collects liquid. The vane type mist eliminator can be installed in vessels either vertically or horizontally. In the horizontal vessels, the gravity is used to drain the liquid phase; therefore, the re-entrainment of the liquid will be minimized. As a consequence, the horizontally installed vane can handle higher through-put operation than in the vertical configuration (Stewart and Arnold, 2008).

2.2.3.2.2 Operating characteristics

The operating characteristics of a vane type mist eliminator can be summarised as follows (Swanborn, 1988)

Table 2-8 The operating characteristics of a vane type mist eliminator

a)	Separation efficiency	:	Good; droplets with diameter of 40μm and larger will be removed
b)	Through-put per unit volume , K-value	:	High; ranges from 0.09 to 0.3m/s in typical designs
c)	Turndown ratio	:	Approximately 25%; depending on liquid loading
d)	Pressure drop	:	Low; often <1.0-1.5 mbar
e)	Ability to separate non-liquid constituents	:	Poor; although danger of plugging is less than wire mesh eliminator
f)	Installation and operational costs	:	Relatively low; 2-3times of wire type

2.2.3.2.3 Available design procedures

The design of a vane type eliminator is usually dictated by Eq. (2-5). The K-value or Souder-Brown coefficient is determined experimentally, and ranges from 0.09m/s to 0.3m/s in typical designs. The maximum allowable velocity decreases with increasing pressure (Stewart and Arnold, 2008).

Similar to mesh type, the impaction is a major factor in separation. If the K-value is low the droplets will stay in the gas phase and will travel through the device but will not be collected. The upper boundary is needed to eliminate the re-entrainment. The maximal

gas velocity through a vane eliminator is normally determined at the beginning of re-entrainment of the liquid film on the vane blades.

Pressure drop

The correlation for calculating the pressure drop across a vane eliminator was provided by Calvert (1974)

$$\Delta P_V = n f_D \rho_g \frac{v_g^2}{2} \tag{2-25}$$

where n is the number of bends, and $f_D$is the drag coefficient of a single plate held at a certain angle to the flow.

2.2.3.2.4 Selection considerations

Knitted mesh eliminators are currently the primary method for gas demisting used in oil gas production facilities. A wire-mesh unit with correct size is effective to eliminate fine liquid droplets. The costs of wire-mesh extractors are low, however their use is limited to low gas velocities and comparing to other kinds they can be easily plugged. The wire-mesh pads are not suitable for the situation, where solids are present and can accumulate to plug the pad. The vane type is more expensive than the mesh type. The vane type is often used in process systems where there are solids, or there is a high liquid loading. The vane eliminator can also be used in operations with pressures of up to 10Mpa (Stewart and Arnold, 2008).

2.3 Evaluation of Present Compact Separators

An ever increasing quantity of gas and oil is produced from offshore. As a consequence, greater efforts are put into the corresponding facility designs. The majority of gas/liquid separations employed by the oil industry have been based on gravity settling and demisting meshes. The gravity separators are usually large and heavy vessels, which are expensive for offshore/subsea applications. On the other hand, demisting mats exhibits relatively high performance in droplet removal. However, for some conditions they are not appropriate, such as high liquid loading, foam tendency or impurity conditions, because the cost of intervention in offshore is extremely high. Therefore, the need of exploiting offshore oil reserves and cutting down equipment costs becomes the motivation of researching new compact separation techniques.

Cyclonic type separators have simple construction, they are relatively inexpensive to fabricate and operate with moderate pressure losses. Previously the R&D activities of compact separators have almost solely focused on cyclonic type separators. The earliest study of the cyclone separator for offshore production was from the 1980s. Davies and Watson (1983) showed several advantages of using a cyclone separator instead of a conventional separator. In recently years, intensive researches have been carried out to develop compact separators with various features. As examples of compact separators, the Gas/Liquid Cylindrical Cyclone (GLCC), the Cyclone Separator (CS), the Inline separator and the Multi-pipe separator will be introduced in the following section.

2.3.1 GLCC

The GLCC was first introduced by Tulsa University and Chevron Petroleum Technology (Arpandi *et al*., 1996). The GLCC is a type of cyclone separator, which applies a centrifugal force to enhance the separation process. Figure 2-25 illustrates the three main parts of the GLCC: the inclined tangential inlet, the tangential liquid outlet, and the axial gas outlet. The fluids enter the separator tangentially through an inclined feed pipe. Due to density differences, the highly swirling flow forces the gas spinning downward along the GLCC inner wall, then it is forced upward in the center. Initially, GLCC was designed to provide bulk gas/liquid separation as a part of a metering system. After extensive development, the GLCCs equipped with advanced control strategy have been applied widely in oil fields.

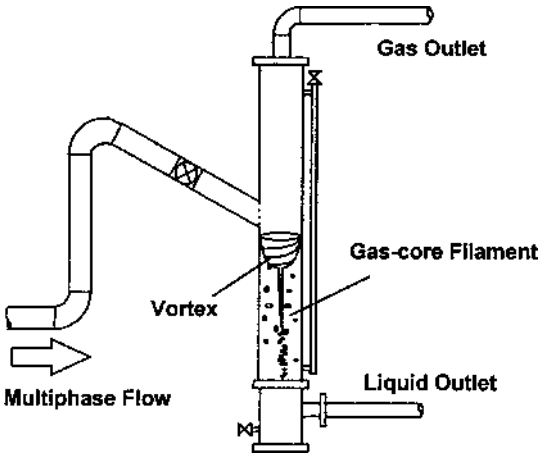

Figure 2-25 Schematic of the Gas/Liquid Cylindrical Cyclone (Arpandi *et al*., 1996)

Arpandi *et al*., (1996) proposed the conceptual design and applications of the GLCC. (Shoham and Kouba, 1998) reported field applications of the GLCC in relation to metering loops in Duri and Indonesia, gas knockout in China, and liquid knockout in Nigeria; the findings show that the GLCC can considerably improve metering accuracy and save significant costs. Due to the sensitivity of the designs to the flow rate, even though they are able to lead to really smaller sizes, they are rarely picked for production operations. But a GLCC is still very effective as a partial separator. In recent BC-10 and Perdido projects, as mentioned in section 2.1.2, the GLCC is deployed as the top assembly to promote the initial separation (Gruehagen and Lim, 2009).

2.3.2 Cyclone Separator (CS)

The CS was a joint development by Petrobras and the State University of Campinas (Franca *et al*., 1996) . The CS was primarily developed as part of a subsea boosting technology for oil production from deep-water fields. According to Franca *et al*., (1996), the CS can be described as a vertical case composed of three sub-separators, as shown in Figure 2-26. Primary separation occurs when the gas/liquid mixture leaves the inlet nozzle. The gas is mainly separated here. A liquid film with dispersed bubbles swirls along the inner wall due to tangential inertia, then liquid enters the helix channel, and the secondary separation happens. The gas that separates in this section flows through the existing holes into the inner pipe and then gets to the gas pipeline. The liquid and some dispersed bubbles plunge into the tertiary separator which acts as a gravitational separator for the residual gas, then directs the liquid to the pump suction line.

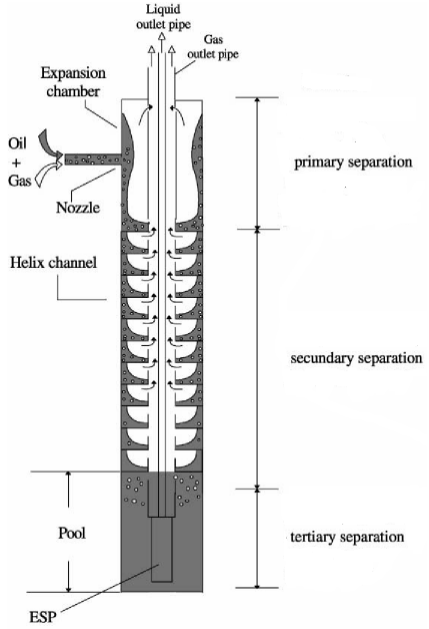

Figure 2-26 Schematic of the Cyclone Separator (Rosa *et al*., 2001)

Several research works were conducted to study the CS flow behaviours. Rosa *et al*., (1996) measured the thickness and flow direction of the liquid film on the chamber wall and the shape of the film cross-section in the helix channel by using electrical conductive and ultra-sound probes. Furthermore, a numerical simulation which assumes the flow is axis-symmetric was used to predict the average film quantities.

Rosa *et al*., (2001) tested three types of scaled-down CS models. In their study, three different liquid fluids were used during the tests with liquid viscosity from 1cP to 150 cP, at 25°C. As expected the capacity of the separator to handle the flow rate of liquid decreases as the liquid viscosity increases. They also found that the diameter of the critical gas bubble is proportional to the liquid viscosity.

2.3.3 Inline Separator

Inline separators were developed by Statoil and CDS (Schook and Asperen, 2005) . Inline separators apply cyclonic technology. Two kinds of devices exist: the Inline degasser and the Inline deliquidiser. The degasser is designed to separate the gas from the liquid dominated phase, while the deliquidiser does the opposite. Inline separators are often applied to de-bottleneck and upgrade existing facilities.

A schematic of the inline separator is shown in Figure 2-27 and Figure 2-28. The inline separators are equipped with mixing elements. The mixers are to ensure that a mixture is even distributed to avoid a stratified flow. Stationary swirl elements are placed in the downstream of mixing elements. Swirl elements create the rotational motion of the flow. Because of the differences in the density, the gas moves towards to the centre of separator chamber as the liquid spins along the chamber wall. For the degasser, the gas phase that exists the separator chamber from an annular part, which is linked to a vertical gas scrubber. In the vertical gas scrubber, the liquid phase which has been carried over will be separated and drained back to the main liquid stream. For the deliquidiser, gas is removed through a smaller pipe, which is inserted in the separator chamber. The liquid film is captured in a vertical boot part. Some gas that is trapped in the boot section is removed and injected back into device. At the downstream of inline separators, an anti-swirl element exists which can eliminate the motion of rotational flow and recovers some pressure (Schook and Asperen, 2005).

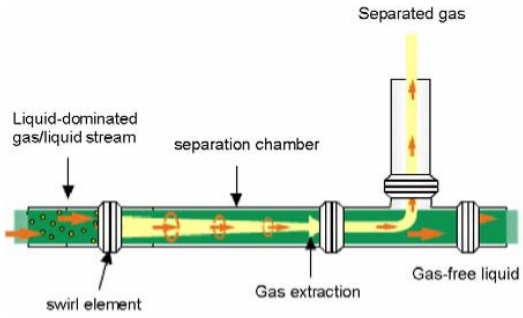

Figure 2-27 Schematic of an inline Degasser (Schook and Asperen, 2005)

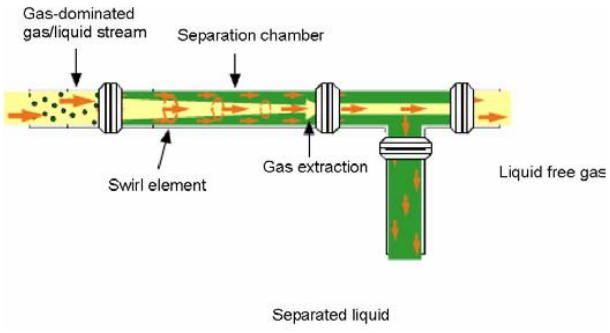

Figure 2-28 Schematic of an inline Deliquidiser (Schook and Asperen, 2005)

As reported by Fantoft *et al*., (2010), the degasser and deliquidiser can achieve 90-99.5% efficiency under optimal conditions and more than 80% efficiency under challenging conditions.

2.3.4 Multi-Pipe Separator

Roberto *et al*., (2011) reported that Saipem had developed a Vertical Multi-Pipe Separator made of several pipes within a vertical array. As a part of a SGLSB system, the purpose of such multi-pipe design is to fully utilize pipes to offer sufficient separation and liquid holdup volumes. Comparing with the conventional separation vessel, the vertical pipes have smaller diameter and thinner wall, and they especially designed for extreme conditions such as deep or ultra-deep water.

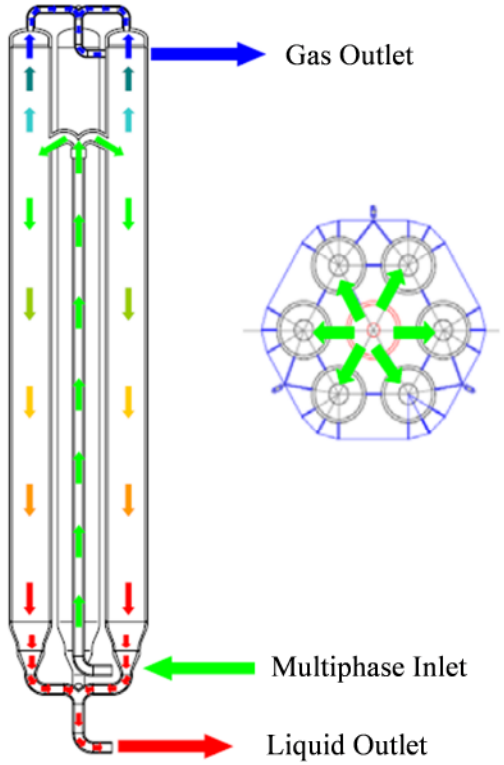

Figure 2-29 Multi-pipe separator principle Roberto *et al*., (2011)

Figure 2-30 Tangential inlet distributor Roberto *et al*., (2011)

The Vertical Multi-Pipe Separator, as illustrated in Figure 2-29, is designed similarly as a conventional vertical separator. Special designed inlet is to enhance the separation efficiency. The multiphase flow is expected to be evenly split into corresponding

separators. The distributor, as shown in Figure 2-30, is connected to a tangential inlet to avoid the high turbulences and smaller droplets which may generate by the splashing. The required slug handling capacity is achieved by extending the height of pipes appropriately. Separated liquids are commingled at the bottom and separated gases are collected above the pipe bundle. The separator will be included in the subsea station retrievable module.

Extensive qualification programs and validated simulations have been carried out to validate the effectiveness of the separator. According to the report of Roberto *et al*., (2011), under the design basis and extreme test conditions (125% of the design), the multi-pipe separator can deliver the required separation performance with the Liquid Carry Over (LCO) of less than 0.1% and Gas Carry Under (GCU) of less than 10%. Further qualification will be carried out before the multi-pipe separator can be implemented in subsea.

2.3.5 Pipe-Hi-SEP

The Pipe-Hi-SEP system developed within the present study is a type of compact cyclone separator. It achieves high efficiency separation in small diameter pipes, making the use of existing pipe code. The Pipe-Hi-SEP system was invented and patented by CALTEC Ltd (Arato *et al*., 2002). A Knowledge Transfer Partnership (KTP) project was set up between CALTEC Ltd and Cranfield University to explore the SGLSB technology. Integrating the compact Pipe-Hi-SEP system in the SGLSB system will make the overall subsea structure lighter and easier to manufacture.

As shown in Figure1-1 in Chapter 1, The Pipe-Hi-SEP system is a two stage separation system, which consists of a Pipe-SEP and a Hi-SEP. The Pipe-SEP and Hi-SEP have the same configuration but different in size. The Pipe-SEP is used primarily as a pre-separator. A gas liquid separation in the Pipe-SEP is accomplished in three stages. The bulk of gas/liquid separation happens when the flow enters tangential to the Pipe-SEP. The liquid swirls as a liquid film with dispersed bubbles over the inner wall of Pipe-SEP chamber. The liquid film encounters the FER, and then loses tangential inertia along the vertical direction and drops down the liquid chamber, from which it is discharged. The next stage is the disengagement of liquid droplets, during which the droplets flow with the bulk flows of gas and move in a radial outward direction towards the wall owing to

centrifugal force. The migration and residence times of the droplets would decide whether the droplets would strike the radial wall, or leave with the gas phase. The final stage is mist elimination, during which small droplets are captured by the ASB and coalesced into larger droplets, which are separated from the gas by gravity. The liquid outlet, besides acting as a liquid level maintainer, directs the liquid to the lower inlet of Hi-SEP. The entrained gas bubble in the liquid chamber of Pipe-SEP will be separated in the Hi-SEP, where the gas bubble moves towards the centre of the Hi-SEP and emerges at the gas/liquid interface. The gas that separated in the Pipe-SEP flows through the existing outlet into the upper part of Hi-SEP where the gas with entrained liquid droplets is separated.

The Hi-SEP has similar features as the Pipe-SEP. Due to the existence of Pipe-SEP, it makes the separation in the Hi-SEP much easier. The overall performance of Pipe-Hi-SEP depends on the performance of each separator.

2.4 Summary

The literature review presented in this chapter was intended to investigate the industry applications of gas/liquid separation and the concepts of compact separators. It reveals that advanced separators using high ‘g’ force and multiple pipes is the dominated configuration, which meets the increasing need of offshore and subsea separation. Over the past few years, considerable effort has been put into test programs and qualifications. However, the compact separators are not so widely used. The largest obstacle is the difficulty in predicting the performance or lack of reliable design tools. The compact Pipe-Hi-SEP system which is described in this study is relatively new, and for the assessment of separation performance, both experimental and numerical simulations are demanded.

3 REVIEW OF COMPACT SEPARATOR MODELLING THEORIES

This chapter gives a review of the general concepts related to cyclonic gas/liquid separator models. The focus will be on the models that deal with predicting cyclonic separator performance. First, the relevant theory and basic flow patterns in vortex flow field are discussed. Frequently used models for the efficiency of cyclonic separator are presented. Next, liquid creep and liquid re-entrainment problems posed by the liquids in the separator are discussed. Finally, recent advances in separator modelling by means of Computational Fluid Dynamics (CFD) are reviewed. It is my intent to explore which CFD model should be used to predict the Pipe-SEP performance.

3.1 Vortex Flow Characterisation

Vortex flow, sometimes called swirl flow, is generated by imparting a tangential velocity component on a flowing medium by means of a swirl generator. Vortex flow can be found in hydrocyclones, cyclones, swirl pipes, etc. Vortex flow is a complex turbulent flow and is very difficult to predict. Based on the early studies of gas cyclones conducted by Shepherd and Lapple (1939), the tangential velocity of a vortex flow is described as

$$v_\theta r^n = constannt \tag{3-1}$$

Where v_θ is tangential velocity; n stands for the vortex exponent, for which n=-1 indicates a forced vortex, whilst n=1 is for a free vortex.

In the forced case, the swirling fluid should have an infinite viscosity. There are no shearing motions among fluid layers with dissimilar radius, which results in a uniform angular velocity at all radii, like a rotating solid body. Meanwhile in a free vortex flow, the swirling fluid is assumed to have no viscosity. In such a fluid, the conservation part is the moment of momentum.

For real swirling flows, the tangential velocity profile is intermediate between forced vortex and free vortex. It normally consists of two parts: an inner central part with a nearly forced rotation and an outside one with a nearly free vortex motion. It is called a 'Rankine vortex'. The sketch in Figure 3-1 illustrates a real vortex of which the tangential velocity at a smaller radius is very close to a forced vortex while the tangential velocity at a larger radius is closer to a free vortex.

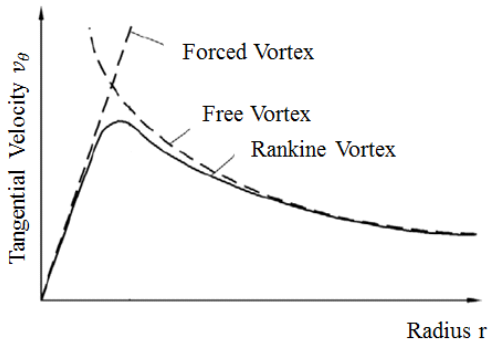

Figure 3-1 Schematic of two ideal vortex flows and a real vortex
(Hoffmann and Stein, 2008)

3.2 Swirl Flow in Pipe

In a survey of published experimental studies on swirling pipe flow conducted by Steenbergen and Voskamp (1998), they identified three types of swirl according to the radial distribution of tangential velocity components: 'Concentrated Vortex' (CV), 'Solid Body' (SB) and 'Wall Jet' (WJ). Figure 3-2 shows the three types of swirl.

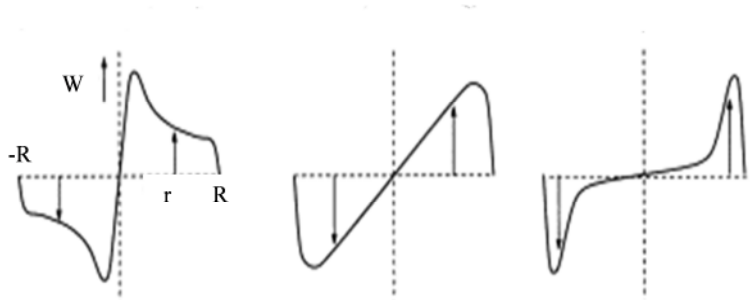

Concentrated Vortex (CV) Solid Body (SB) Wall Jet (WJ)

Figure 3-2 Schematic of three types of swirl in pipe flow
(Steenbergen and Voskamp, 1998)

In Figure 3-2, R is the radius of the pipe; W is the tangential velocity. The CV is characterized by a concentration of vortices in a region near the pipe centre, surrounded by an annulus of low vortices. The CV is found in cases where the fluid was set into rotation before entering the pipe in the radial direction. All fluid enters the pipe with an approximately equal angular momentum, and since during the deflection into the direction of the pipe axis the angular momentum of the fluid particles is largely conserved, the swirl more or less resembles the 'free vortex' type. The SB is usually created by guiding the fluid either through a pipe section containing a twisted tape or through a rotating pipe section filled with a honeycomb. The WJ is generated by allowing swirling fluid to enter the pipe in the inlet plane through an annular hole adjacent to the wall. Additionally, non-swirling fluid may enter the central region of the pipe.

The degree of swirl is usually characterised by the swirl intensity S. Kitoh (1991) defined the swirl intensity for axisymmetric flow as

$$S = \frac{2\pi\rho \int_0^R UWr^2 dr}{\rho\pi R^3 U_m^2} = 2\int_0^1 \left(\frac{r}{R}\right)^2 \frac{U}{U_m}\frac{W}{U_m} d\left(\frac{r}{R}\right) \tag{3-2}$$

where U is the mean axial velocity, U_m is the bulk velocity, r and R are radial position and pipe radius, ρ is fluid density, and W is the mean tangential velocity.

The swirl decays in the axial direction due to wall friction. According to Kitoh (1991), the swirl decays exponentially with a certain coefficient and the coefficient is related to the intensity. Steenbergen and Voskamp (1998) proposed the following equation describing the decay coefficient β in a fully developed pipe flow

$$\beta = (1.49 \pm 0.07)\lambda \tag{3-3}$$

where λ is the friction coefficient. They also stated that the swirl behaviour is related to the swirl intensity, the flow Reynolds numbers, and levels of wall roughness and the methods used to generate swirl.

3.3 Swirl Flow in Cyclones

The swirling flow in cyclones is generated by injecting the gas through a tangential inlet. The gas flows downward in the outer region and upward in the centre (Figure 2-15).

Figure 3-3 shows a sketch of the flow pattern in a standard Reversed Flow Cyclone, which was discussed in section 2.2.2.1.

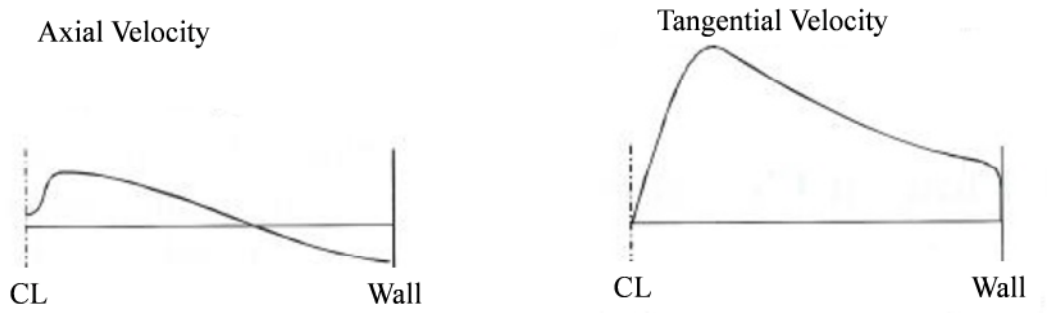

Figure 3-3 Schematic of the flow pattern in a tangential-inlet cyclone (Hoffmann and Stein, 2008)

The radial profile of the axial velocity is shown in the left of Figure 3-3. The downward axial flow at the outside area and the upward flow at the inner area are clearly shown. Also, a dip of the axial velocity exists around the centre line. The tangential velocity profile shown in the right is a typical Rankine type vortex: solid body rotation at the core region, followed by a near free vortex at the outside area and vanishing at a regime close to the wall. Usually Eq. (3-1) gives a description of the tangential velocity in the outside region, as n equals to 0.4-0.7 (Gupta *et al*., 1984).

The researches on the gas flow pattern in cyclones have mostly focused on the profile of axial and tangential velocity. Rare information about the radial velocity has been reported in the literature. The reason is that radial velocity is too small to preciously measure comparing to the bulk velocity.

All researches on cyclone show that understanding the velocity profile of the gas in cyclone is vital in order to predict the particle trajectories in the separation space, which provides a basis to model and predict the separation performance. As indicated in section 2.2.2.1.3, in the separation process, the tangential velocity profiles at the area close to the wall and in the CS are more important than the radial and axial velocities. The radial velocity near the wall is normally neglected, but considered to be evenly distributed within the CS, whilst the axial velocity is commonly assumed to be uniform in each region (inner region and outer region).

Unlike the axial and radial velocity, there are various mathematical models aimed at predicting cyclone tangential velocity profiles. Except the simple n-type model has been discussed in section 2.2.2.1.3 and section 3.1. Barth (1956) proposed another model, which firstly calculates the tangential gas velocity according to the inlet velocity, and then the tangential velocity within the CS is calculated from the wall velocity.

Barth's model assumed that the cyclone wall velocity is greater than the inlet velocity because of the constriction within inlet jet. As given by Figure 3-4, the inlet flow behaviours as a 'slot' inlet since when the gas comes in, it would be compressed against the cyclone wall, leading to an inlet area reduction and a velocity increase.

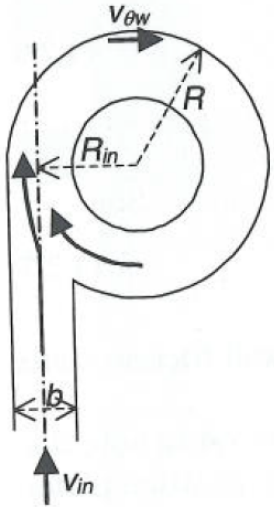

Figure 3-4 The inlet flow pattern of a 'slot' inlet (Hoffmann and Stein, 2008)

Barth (1956) introduced a factor α, which accounts for this inlet jet and is calculated from the following equation:

$$\alpha = \frac{v_{in} R_{in}}{v_{\theta w} R} \tag{3-4}$$

where R_{in} is the radial position of the inlet jet centre. If it is rectangular, it can assumed that $R_{in} = (R - \frac{b}{2})$, where b is the inlet width and R is the cyclone's radius.

Fitting the graph given by Barth (1956), Muschelknautz (1972, 1980) gave the following correlation for α

$$\alpha = 1 - 0.4(\frac{b}{R})^{0.5} \tag{3-5}$$

To get the tangential velocity at CS, $v_{\theta CS}$ from the tangential velocity at wall,$v_{\theta w}$, Barth derived the following equation

$$v_{\theta CS} = \frac{v_{\theta w}(\frac{R}{R_x})}{(1+\frac{H_{CS}R\pi f v_{\theta w}}{Q_g})} \tag{3-6}$$

where f is the wall friction factor. It can be seen that the core spin velocity $v_{\theta CS}$ is not only a function of cyclone geometry, but also a function of wall friction f. The friction factor in a demisting cyclone is usually expressed in two parts:

$$f = f_{air} + f_{mist} \tag{3-7}$$

where f_{air} is the gas only friction factor, f_{mist} is the friction factor accounting for the effect of the mist. f_{air} depends mainly on the relative wall roughness, k_s/D, and it can obtained from Table 3-1. k_s is the wall roughness and D is the diameter of separator.

Table 3-1 Value of f_{air} for three values of k_s/D

k_s/D(-)	f_{air}(-)
Hydraulically smooth	0.005
0.5×10^{-3}	0.010
3.0×10^{-3}	0.025

f_{mist} can be estimated as

$$f_{mist} = 0.4 f_{air} C_0^{0.1} \tag{3-8}$$

where c_o is the mass percentage of mist entering the cyclone, i.e. the percentage of liquid mass within the incoming gas.

Combining Eq. (3-7) and Eq. (3-8), the friction factor f can be expressed as

$$f = f_{air}(1 + 0.4 C_0^{0.1}) \tag{3-9}$$

The equation above indicates that increase of the cyclone length does not always resulting in a better performance of the cyclone. The wall friction increases based on the increasing of the cyclone length and wall surface area. The increased friction decreases

the core spin velocity. According to the Barth model, if the intensity in the vortex is smaller, consequently the centrifugal force applied to the particles in CS will be smaller, and similarly a longer CS will result in a smaller radial velocity. The inner drag force applied on the particles of CS will be smaller. Therefore it is difficult to deduce what the net effect will be. The liquid feeding the cyclone, assuming that most of it is spin and formed a liquid film on the wall, is an additional wall roughness, and its effect on the separation performance is discussed in the next section 3.4 (Hoffmann and Stein, 2008) .

3.4 Cyclone Efficiency

As discussed in section 2.2.3, the efficiency of a cyclone is usually characterised by the 'cut size', which can be either calculated with the 'equilibrium orbit model' or the 'time of flight' model. Once the cut size is known, a Grade Efficiency Curve (GEC) can be fitted. The GEC is the separation efficiency for a give particle size. Dirgo and Leith (1985) fitted a function in order to represent the GEC based on Barth's 'universal curve', and this method is shown in Figure 3-5. D_{50} is the cut size.

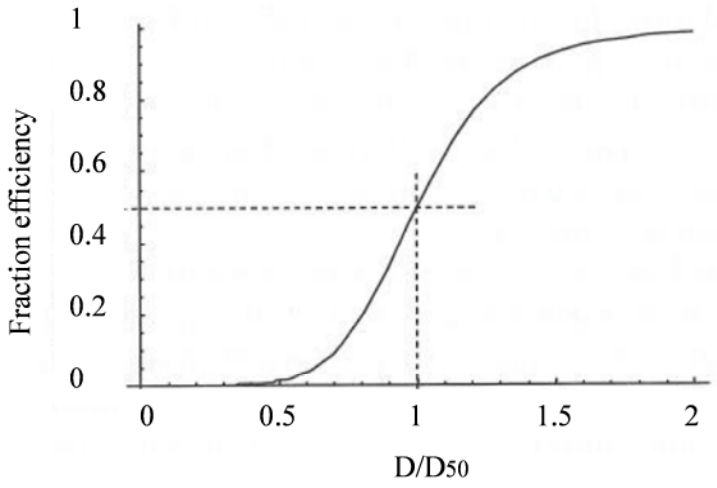

Figure 3-5 Fitted GEC around the cut size of Barth (Hoffmann and Stein, 2008)

The correlations is expressed as

$$\eta(D) = \frac{1}{1+(\frac{D_{50}}{D})^m} \tag{3-10}$$

For a given cyclone, the GEC data normally can be obtained from experiment, and then the exponent m can be obtained by curve fitting. m usually has a value between 2 and 7. A higher m value is associated with well-designed cyclones with smooth wall.

At low inlet liquid loading, the overall cyclone separation efficiency is calculated via the following equation

$$\eta = \sum_{i=1}^{N} \eta_i MF_i \tag{3-11}$$

In the equation the cyclone's incoming fluid is assumed to be divided into N segments evenly, with each segment comprising a known fraction of the total inlet liquid mass. For each segment, the mass fraction ΔMF_i (i^{th} mass fraction) is multiplied by the separation efficiency of the average droplet size of each segment, and an averaged droplet size is the averaged value of droplet sizes among all droplets in a segment. The separation efficiency is calculated from the GEC. The sum of all N segments is the overall efficiency (Hoffmann and Stein, 2008).

If the amount of liquid in the incoming fluid is high, then the mass loading effect on efficiency should be considered. The limit-loading, C_{oL}, which the gas phase can hold in turbulent suspension, is expressed by Muschelknautz and Dahl (1994) as

$$C_{oL} = 0.0078(\frac{D_{50}}{D_m})(10C_o)^k \quad \text{when} \quad 0.01 < C_o < 0.5 \tag{3-12}$$

$$\text{Where } k = 0.07 - 0.16 ln C_o \tag{3-13}$$

where C_o is the mass percentage of the liquid within in the inlet gas flow and D_m is the mean size of droplet in the incoming liquid.

If $C_o < C_{oL}$, the mass loading will not affect the efficiency. The simple method mentioned above can be used to calculate the cyclone's performance.

If $C_o > C_{oL}$, the mass loading will affect the efficiency. The cyclone works as a two-stage separator: the portion of liquid, which exceeds the limit-loading, will spin as 'wall flow' almost immediately upon entry. The remains in turbulent suspension will then be subject to normal separation at low mass loading conditions.

The overall separation efficiency accounting for the mass loading effect is expressed as

$$\eta = \left(1 - \frac{C_{oL}}{C_o}\right) + \left(\frac{C_{oL}}{C_o}\right) \sum_{i=1}^{N} \eta_i \Delta MF_i \quad (3\text{-}14)$$

3.5 Two Problems Related to Gas/Liquid Cyclones

Cyclones are usually very effective in separating gas and liquid, because the liquid droplets fed to cyclones generally have large size. Like Hoffmann and Stein (2008) states that designing cyclones to separate gas/liquid based on cut size are normally easy, the real challenge lies in how to deal with the separated liquid. Therefore this section will focus on the unique problems that are created by the liquid in gas/liquid cyclone.

3.5.1 Liquid Creep

In a gas/liquid cyclone, a certain amount of the inlet liquid phase will be centrifuged and a wall film will be formed due to this motion. It is transient and dragged by the upwardly gas flow. If not redirected, the wall film will easily creep to the roof and leave the cyclone with the gas phase. This phenomenon is named as the 'layer losses', which resulting in undesired liquid carry over.

If possible, the liquid creep should be avoided by appropriate designing of the cyclone. Some best practice has been suggested by Hoffmann and Stein (2008), which includes: the inlet pipe should not be too close to the cyclone roof, or the slightly downward inlet pipe may offer better performance; at high liquid loadings, devices such as 'inlet raceways', 'roof skinners' and 'anti-creep skirts' should be installed. The principle behind inlet raceways and roof skinners is to inhibit the liquid film arriving and leaving the cyclone upper regime. The saw-like edges are normally included in the anti-creep, which will help to redirect and dislodge the liquid film.

3.5.2 Liquid Re-entrainment

At severe conditions, liquid re-entrainment becomes the limiting factor for gas/liquid separator. Liquid re-entrainment will occur when the high gas velocity breaks droplets from liquid phase and consequently the droplets enter into the gas phase. For example, when the liquid loading increases, re-entrainment may happen due to droplet entrainment from the wall film. In such cases, the re-entrainment of droplet will mainly affect the performance of the separation process, rather than the droplet under the cut size of separator.

Ishii and Grolmes (1975) developed two mechanisms of entrainment, from the research of entraining the liquid film to a co-currently gas flow. Under higher liquid film Reynolds numbers, the liquid-entrainment is the roll wave entrainment and under lower liquid film Reynolds numbers, the liquid-entrainment is the undercut entrainment, as shown in Figure 3-6.

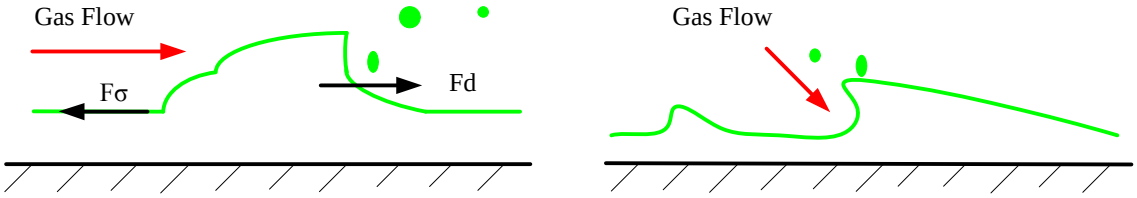

(a) Roll wave entrainment (b) Undercut entrainment

Figure 3-6 Mechanism for entrainment from a liquid film into a gas flow

The entrainment mechanism depends on the liquid film Reynolds number, which is expressed as

$$Re_f = \frac{\rho_l u_f \delta}{\mu_l} = \frac{\rho_l \Gamma}{\mu_l} \tag{3-15}$$

where δ is the thickness of film, u_f is the liquid film mean velocity, Γ is named as the liquid loading, defined as the liquid flow in the film per unit wetted perimeter.

In a separator, the Reynolds number of the wall film can be estimated as

$$Re_f = \frac{\rho_l u_f \delta}{\mu_l} = \frac{Q\eta\rho_l}{P_w \mu_l} \tag{3-16}$$

where P_w is the wetted perimeter and taken as πD, Q is the total liquid flow to the separator.

Ishii and Grolmes (1975) state that there exists a lower limit of Re_f, under which roll-wave entrainment will not take place no matter how high the gas velocity over the film. While at high Re_f, the film is fully turbulent, the gas velocity needed for the occurrence of entrainment becomes independent of Re_f.

The roll-wave entrainment is the result of droplets being sheared from the surface of a roll wave. The onset of roll-wave entrainment is derived by considering the force

balance between the drag force F_d and the retaining force F_σ. The drag force F_d is the result of gas acting on a wave crest on the film and the retaining force F_σ is the surface tension. Ishii and Grolmes (1975) assumed that roll wave entrainment would occur when the drag force, F_d exceeds the retaining force, F_σ

$$F_d \geq F_\sigma \tag{3-17}$$

The requirement of the inception for the liquid phase entrainment is given as

$$\begin{aligned} &\frac{\mu_l \mu_g}{\sigma}\sqrt{\frac{\rho_g}{\rho_l}} \geq 11.78 N_\mu^{0.8} Re_f^{-1/3} && \text{for } N_\mu \leq \frac{1}{15} \\ &\frac{\mu_l \mu_g}{\sigma}\sqrt{\frac{\rho_g}{\rho_l}} \geq 1.35 Re_f^{-1/3} && \text{for } N_\mu \geq \frac{1}{15} \end{aligned} \tag{3-18}$$

where N_μ is the viscosity number, defined as

$$N_\mu = \frac{\mu_l}{\sqrt{\rho_l \sigma \sqrt{\frac{\sigma}{g\Delta\rho}}}} \tag{3-19}$$

In a cyclonic separator, as the liquid film is spinning along the wall but not flowing due to the gravity, the gravity constant g in Eq. (3-19) needs to be replaced with the acceleration due to the centripetal force on the film, and it is given by

$$a = v_{\theta,l}^2 / R \tag{3-20}$$

where $v_{\theta,l}$ is the tangential film velocity.

The recent experiments conducted by Austrheim *et al.*, (2006, 2007, 2008) on a large scale scrubber equipped with a cyclone deck operating at high pressure show the performance to become worse as the gas flow increases, thus contradicting the theory. They concluded that the reason for the liquid loss could be the liquid re-entrainment. They also found that the re-entrainment number offers an analytical tool to quantify the separation efficiency. For a further understanding of the phenomena taking place, measurements of the droplet sizes throughout the separator and liquid film thickness are desirable, and achieving this will have a high priority in the future.

3.6 Numerical Modelling of Cyclonic Separators

The technique of CFD has been applied to improve the separator operation and to perfect the design for many years. However, CFD based simulations of two phase separators are mainly focused on the gas flow or gas flow with low particles loading. This section gives a brief review of relevant CFD modelling theory and analyses the recent CFD outcomes related to swirl flow and particle trajectories, illustrating the ability of CFD as a simulation tool and intending to find out the most suitable CFD models to be used in the following work.

3.6.1 CFD Modelling Theory

In CFD, the conservation equations governing the transport of mass and momentum in a flow is the Navier-Stokes equations in a 'finite difference' form. In principle, if the model mesh is well designed, the CFD is able solve the Navier-Stokes equations directly; however, in most of practice engineering calculations, this is too computationally expensive. The Reynolds-averaged Navier-Stokes (RANS) continuity and momentum equations are widely adopted to reduces the computational effort and resources, and RANS equations can be expressed as follows (ANSYS, 2012)

$$\frac{\partial(U_i)}{\partial x_i} = 0 \tag{3-21}$$

$$\frac{\partial(U_i)}{\partial t} + U_j \frac{\partial U_i}{\partial x_j} = -\frac{1}{\rho}\frac{\partial P}{\partial x_i} + \frac{\partial}{\partial x_j}[v\frac{\partial U_i}{\partial x_j} - \overline{u_i' u_j'}] \tag{3-22}$$

where U_i is the velocity component in the direction x_i; P is the pressure factor; ρ is the density of the fluid; v is the dynamic viscosity; $\overline{u_i' u_j'}$ is the Reynolds stress tensor and u_i' is the i^{th} fluctuating component of velocity.

As a result of the Reynolds-averaging, the Reynolds stresses terms $\overline{u_i' u_j'}$ must be modelled and appropriate turbulence models are required. The Boussinesq hypothesis can be used to link the Reynolds stresses to the mean velocity gradients, and it can be as expressed as follows

$$-\rho\overline{u_i' u_j'} = \mu_t\left(\frac{\partial U_i}{\partial x_j} + \frac{\partial U_j}{\partial x_i}\right) - \frac{2}{3}(\rho k + \mu_t \frac{\partial U_k}{\partial x_k})\delta_{ij} \tag{3-23}$$

where k is the turbulent kinetic energy, which is defined as $k = \frac{1}{2}\overline{u_i' u_j'}$, and δ_{ij} is the Kroneker delta. The Boussinesq approach is used in the Spalart-Allmaras models, the $k-\epsilon$ model and the $k-\omega$ model (ANSYS, 2012).

One classic model used the Boussinesq hypothesis is the $k-\epsilon$ model, in which transport equation for k is calculated from exact equation but ϵ is based on physical calculation. As an extensive model type from the standard $k-\epsilon$, the renormalization group RNG $k-\epsilon$ model is statistically derived from the instantaneous Navier-Stokes equations with the RNG method. It can provide more precise and consistent outcomes, and also suitable for more conditions such as the swirling flows.

The transport equations for the RNG $k-\epsilon$ model are expressed as below

$$\frac{\partial}{\partial t}(\rho k) + \frac{\partial}{\partial x_i}(\rho k U_i) = \frac{\partial}{\partial x_j}\left(\alpha_k \mu_{eff} \frac{\partial k}{\partial x_j}\right) + G_k - \rho\epsilon \qquad (3\text{-}24)$$

$$\frac{\partial}{\partial t}(\rho \epsilon) + \frac{\partial}{\partial x_i}(\rho \epsilon U_i) = \frac{\partial}{\partial x_j}\left(\alpha_\epsilon \mu_{eff} \frac{\partial \epsilon}{\partial x_j}\right) + C_{1\epsilon}\frac{\epsilon}{k} G_k - C_{2\varepsilon}\rho\frac{\epsilon^2}{k} - R_\epsilon \qquad (3\text{-}25)$$

where α_k and α_ϵ are the inverse effective Prandtl numbers for k and ϵ, respectively. In the high Reynolds number limit, $\alpha_k = \alpha_\epsilon \approx 1.393$, G_k is the turbulence kinetic energy due to the mean velocity gradients. $C_{1\epsilon}$ and $C_{2\epsilon}$ are constants where $C_{1\epsilon}$=1.42 and $C_{2\epsilon}$=1.68.

The effective viscosity μ_{eff} is expressed as

$$d\left(\frac{\rho^2 k}{\sqrt{\epsilon\mu}}\right) = 1.72\frac{\hat{v}}{\sqrt{\hat{v}^3 - 1 + C_v}} d\hat{v} \qquad (3\text{-}26)$$

where $\hat{v} = \mu_{eff}/\mu$, C_v ≈100. In the high Reynolds number limit, μ_{eff} can be expressed as

$$\mu_{eff} = \mu_t = \rho C_\mu \frac{k^2}{\varepsilon} \qquad (3\text{-}27)$$

where C_μ=0.0845

The RNG model has an additional term, R_ϵ, which can be expressed as

$$R_\epsilon = \frac{C_\mu \rho \eta^3 (1-\frac{\eta}{\eta_0})}{1+\beta\eta^3}\frac{\epsilon^2}{k} \tag{3-28}$$

where $\eta = Sk/\epsilon$ and C_μ = 0.0845 in the high Reynolds number limit. η_0=4.38 and β=0.012.

The modified turbulent viscosity is

$$\mu_t = \mu_{t0} f(\alpha_s, \Omega, \frac{k}{\epsilon}) \tag{3-29}$$

The alternative approach, known as the Reynolds stress model (RSM), by combing with the dissipation rate, is able to solve the transport equations the terms within the Reynolds stress tensor. It is given by

$$\underbrace{\frac{\partial}{\partial t}\left(\rho\overline{u_i'u_j'}\right)}_{Local\ time\ deivative} + \underbrace{\frac{\partial}{\partial x_k}\left(\rho u_k \overline{u_i'u_j'}\right)}_{C_{ij}=Convection} = \underbrace{-\frac{\partial}{\partial x_k}\left(\rho\overline{u_i'u_j'u_k'} + \overline{P\left(\delta_{kj}u_i' + \delta_{ik}u_j'\right)}\right)}_{D_{T,ij}=Turbulent\ diffusion}$$

$$+ \underbrace{\frac{\partial}{\partial x_k}\left[\mu\frac{\partial}{\partial x_k}\left(\overline{u_i'u_j'}\right)\right]}_{C_{ij}=Molecular\ diffusion} \underbrace{-\rho\left(\overline{u_i'u_k'}\frac{\partial u_j}{\partial x_k} + \overline{u_j'u_k'}\frac{\partial u_i}{\partial x_k}\right)}_{P_{ij}=Stress\ production} - \underbrace{\rho\beta\left(g_i\overline{u_j'\theta} + g_j\overline{u_i'\theta}\right)}_{G_{ij}=Buoyancy\ Production} +$$

$$\underbrace{\overline{P\left(\frac{\partial u_i'}{\partial x_j} + \frac{\partial u_j'}{\partial x_i}\right)}}_{\emptyset_{ij}=Pressure\ strain} - \underbrace{2\mu\overline{\frac{\partial u_i'}{\partial x_k}\frac{\partial u_j'}{\partial x_k}}}_{\varepsilon_{ij}=Dissipation} \tag{3-30}$$

The turbulent diffusion $D_{T,ij}$ is modelled using a simplified generalized gradient-diffusion model, as shown below

$$D_{T,ij} = \frac{\partial}{\partial x_k}\left(\frac{\mu_t}{\sigma_k}\frac{\partial\overline{u_i'u_j'}}{\partial x_k}\right) \tag{3-31}$$

where μ_t is the turbulent viscosity and σ_k =0.82.

The pressure strain term $\emptyset_{ij}$ is modelled by

$$\emptyset_{ij} = \emptyset_{ij,1} + \emptyset_{ij,2} \tag{3-32}$$

where $\emptyset_{ij,1}$ and $\emptyset_{ij,2}$ are the slow pressure–strain term and the rapid pressure strain term, respectively. $\emptyset_{ij,1}$ is modelled as

$$\emptyset_{ij,1} = -C_1\rho\frac{\epsilon}{k}[\overline{u_i'u_j'} - \frac{2}{3}\delta_{ij}k] \tag{3-33}$$

where C_1=0.18

$\emptyset_{ij,2}$ is modelled as

$$\emptyset_{ij,2} = -C_2\left[\left(P_{ij} + F_{ij} + 5/6G_{ij} - C_{ij}\right) - \frac{2}{3}\delta_{ij}(P + 5/6G - C)\right] \tag{3-34}$$

where C_2=0.60, $P = \frac{1}{2}P_{kk}$, $G = \frac{1}{2}G_{kk}$, $C = \frac{1}{2}C_{kk}$

For incompressible flows, the dissipation tensor ε_{ij} is expressed as

$$\varepsilon_{ij} = \frac{2}{3}\delta_{ij}\rho\epsilon \tag{3-35}$$

The scalar dissipation rate ε is solved via a transport equation

$$\frac{\partial}{\partial t}(\rho\epsilon) + \frac{\partial}{\partial x_i}(\rho\epsilon U_i) = \frac{\partial}{\partial x_j}\left[\left(\mu + \frac{\mu_t}{\sigma_\varepsilon}\right)\frac{\partial\epsilon}{\partial x_j}\right] + C_{\epsilon 1}\frac{1}{2}\frac{\epsilon}{k}P_{ii} - C_{\epsilon 2}\rho\frac{\epsilon^2}{k} \tag{3-36}$$

where σ_ϵ=1.0, $C_{\epsilon 1}$=1.44 and $C_{\epsilon 2}$=1.92.

An alternative approach to filter the Navier-Stokes equations is the large eddy simulation (LES) method, in which the eddies smaller than the filter size are removed and larger ones are solved directly. However, the computational resources required for LES to resolve the high Reynolds number industrial flows are significant. The detailed description of the LES model can be found in Fluent User Guide (ANSYS, 2012).

For the implementation of a CFD modelling of single phase using commercial software, such as FLUENT, the geometry of the object is first defined, and then the corresponding discretised grid is generated with a mesh tool. And then the initial, boundary conditions and the CFD parameters are defined. Finally, the CFD software solves the equations for fluid flow.

For the numerical simulation of multiphase flow, the Euler-Lagrange approach and the Euler-Euler approach are available. The Euler-Lagrange approach, which is sometimes named as Discrete Phase Model (DPM), is ideal for analysing the fluid flow with the volume fraction of the discrete phase being sufficiently low. Typically, the discrete

phase should not make up more than 10% of the total volumetric flow rate. Therefore, this approach works best with dispersed bubbly flows, droplet flows or granular flows. The primary phase is modelled by solving the RANS equations, meanwhile the solution for the dispersed phase is based on the tracking a huge number of particles, which were injected into the calculated primary phase. The force balance on the particle can be expressed as

$$\frac{du_p}{dt} = F_D(u - u_p) + \frac{g_x(\rho_p - \rho)}{\rho_p} + F_x \tag{3-37}$$

where $F_D(u - u_p)$ is the drag force per unit particle mass and F_D is given by

$$F_D = \frac{18\mu}{\rho_p d_p^2}\frac{C_D Re}{24} \tag{3-38}$$

where μ is the fluid phase viscosity, u_p is the particle velocity, μ is the fluid viscosity, ρ is the fluid density, ρ_p is the particle density, and d_p is the particle diameter. C_D is the drag coefficient. For spherical particles, the C_D can be estimated according to the Table in chapter 2. Re is the relative Reynolds number given by

$$Re = \frac{\rho d_p |u_p - u|}{\mu} \tag{3-39}$$

Generally, the phase coupling can be one-way or two-way, where the former one means that the effect from the primary phase to the discrete phase is modelled, but the effect from the discrete one is not considered. This is normally acceptable, although it is possible to couple the equations for the discrete and primary phases by introducing equations for the momentum and mass exchange between the phases. Thus, two-way coupling can be achieved by solving the equations for the two phases at the same time (ANSYS, 2012).

On the other hand, the Euler-Euler approach treats the multiphase problem as that of interpenetrating continua, in which the phases interact with each other. The phasic volume fraction idea is used in the approach, which assumes that a certain volume of a phase would not be taken by others, and it is also defined as continuous functions in terms of both space and time, in which the totality of phase volume fraction is equal to one. This approach is better when the two phases under consideration occupy similar

amounts of space and the study point is the interface of them. This approach is usually applied in stratified, free surface and slug flow. The commercial code ANSYS includes three types of Euler-Euler multiphase models: the volume of fluid (VOF) model, the mixture model and the Eulerian model. The guidelines for selecting the appropriate model to represent the multiphase flow of interested are introduced with more details in the ANSYS manual (ANSYS, 2012).

3.6.2 CFD Modelling of Cyclonic Separators

3.6.2.1 Gas flow in cyclone

Cyclone separators are widely used in processing industry. The flow fields inside cyclones are highly turbulent and very complex, and they are usually modelled in an Euler-Lagrangian approach. In such an approach, the basic requirement is to obtain an accurate gas velocity field for modelling the dispersed particles. In this section, the simulation of the swirling flow in cyclone is reviewed.

Kaya and Karagoz (2008) studied the swirling gas flow inside a cyclone with a tangential inlet. They investigated the performance of isotropic turbulence models, the standard $k-\varepsilon$ model, the RNG $k-\varepsilon$ model, the anisotropic model and the RSM when simulating the highly swirling flow. Figure 3-7 and Figure 3-8 show the comparison of the axial and tangential gas velocities computed by CFD with the experimental data. As it shows the RSM model yields a better prediction compared to the other two $k-\varepsilon$ turbulence models. It was concluded that the $k-\varepsilon$ models are not able to simulate the strongly swirling flows accurately, due to the strong anisotropy in the turbulent structure created by the highly swirling. Therefore, more sophisticated RSM models are more suitable for cyclone simulation.

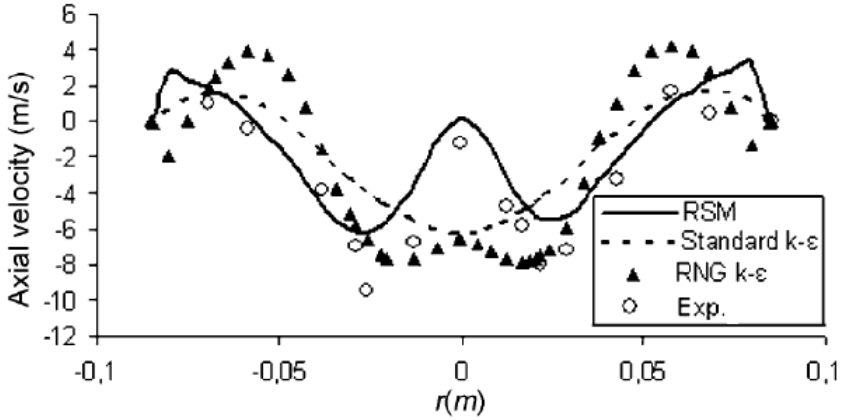

Figure 3-7 Comparison of the axial velocity profile computed by CFD and experimental data (Kaya and Karagoz, 2008)

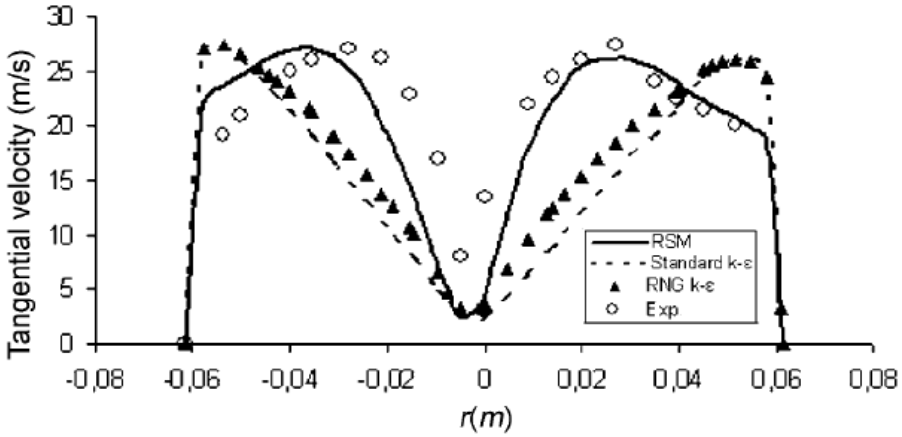

Figure 3-8 Comparison of the tangential velocity profile computed by CFD and experimental data (Kaya and Karagoz, 2008)

Kaya and Karagoz (2008) also assessed the performance of various pressure interpolation schemes. They found that the Presto scheme predicts well and they recommended using a SIMPLE algorithm for the coupling between the pressure and velocity coupling, QUICK algorithm for solving the momentum, and the second-order upwind method when solving the turbulence quantities.

Previous studies have dealt extensively not only with predicting the mean velocity profile of cyclone, but also with the inherent instability of cyclones: Processing Vortex Core (PVC) and its associated fluctuations have attracted a lot of interest from the CFD community. The steady RMS model has been reported to under-predict the fluctuating velocity, as discussed in Jiao *et al*., (2007). Shukla *et al*., (2011b) compared the static

and transient RSM models combined with different interpolation schemes. The simulation results showed that the transient RSM model can resolve PVC phenomenon in the cyclone core region. They also recommended second order upwind schemes for turbulence quantities, the first order upwind scheme for Reynolds stress equations, and the Presto scheme for pressure interpolation scheme.

With increasing computational power, Large Eddy Simulations (LES) are also available for cyclone simulations. Encouraging results have been reported and demonstrate the ability of LES to capture the PVC. Gronald and Derksen (2011) performed a gas cyclone simulation with a transient finite volume RANS model (FV-RANS), a finite volume LES (FV-LES) model and a lattice-Boltzmann LES (LB-LES) model.

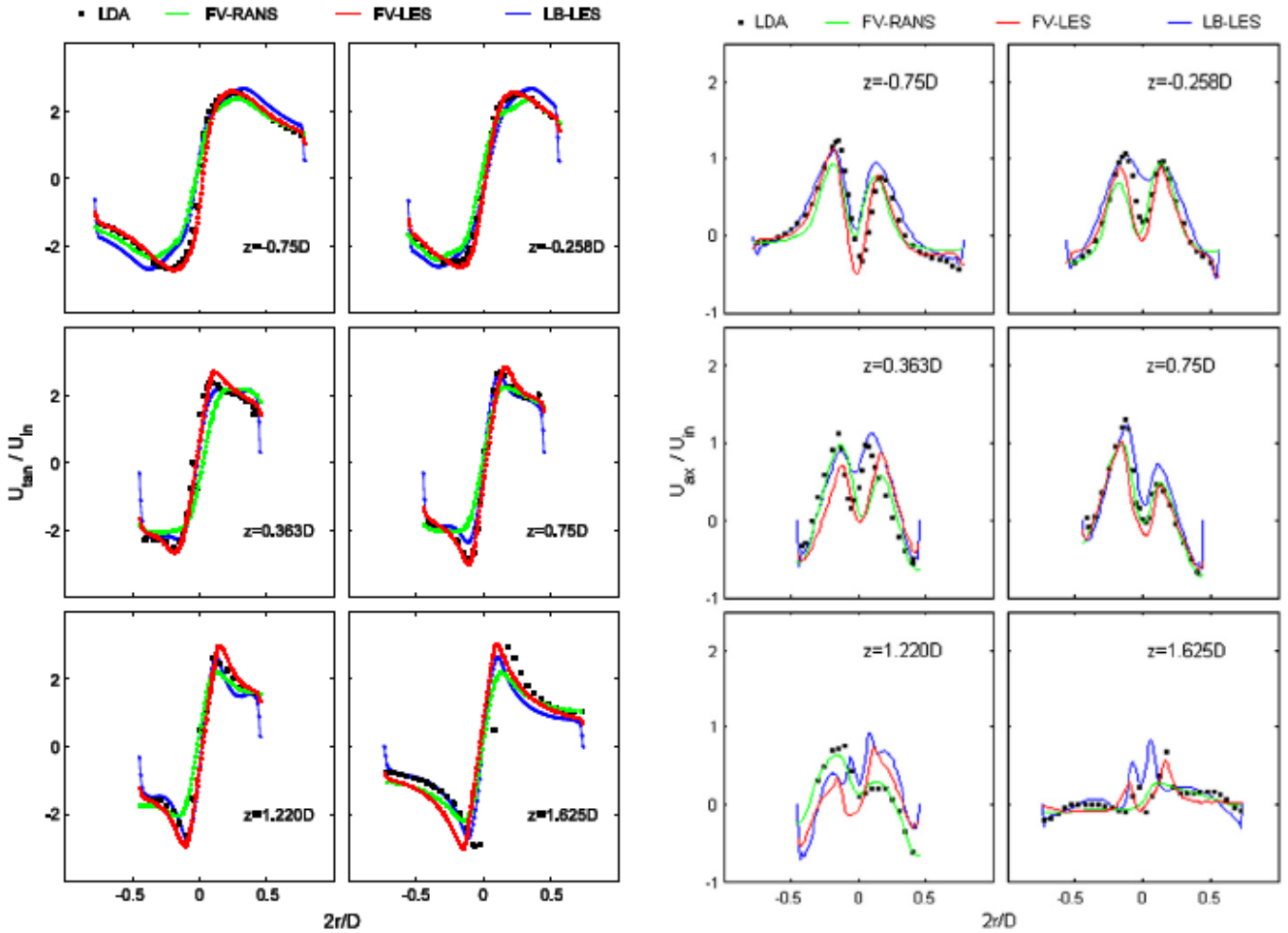

Figure 3-9 Comparison of the LDA measured results for the mean tangential and axial velocity with three simulation approaches (Gronald and Derksen, 2011)

The simulation results were compared to Laser Doppler Anemometry (LDA) velocity results obtained by Gronald and Derksen (2011). It is clear that the measured velocity results compared well with the simulation results. For the mean tangential velocity profile, the two LES models predict the maximum tangential velocities and the widths of the vortex cores very well; whereas results from the RANS model under-predict the widths of the vortex core. In terms of the axial velocity profile, the three models both offer good predictions. The asymmetry of the profiles is well represented in the simulations.

Gronald and Derksen (2011) concluded that a transient FV-RANS approach with a reasonable coarse mesh is able to offer the prediction results on an industrial level, and with acceptable computing recourse consumption. The FV-RANS cannot predict the high velocity fluctuation near the vortex centre, whereas LES approaches with finer meshes are able to simulate the flow field more precisely, but with more computational cost.

CFD simulations have been used not only to predict the flow profile as mentioned above but have also been used for designing cyclones. As mentioned in chapter 2, a cyclone includes seven parts. Any change of them will affect the flow pattern and performance. Numerous studies have been performed to explore the optimum design of cyclones.

Elsayed and Lacor (2011a) investigated the influence of the inlet parameters on the performance and the corresponding velocity field of a cyclone with a tangential rectangular inlet using the RSM model. Figure 3-10 shows the profile of the tangential and axial velocities lie at the area close to the cyclone inlet with different inlet width/height. The peak values of the velocities will increase as the width/height reduces. Because the centrifugal force is proportional to the tangential velocity, the decrease of this dimension will result in higher collection efficiency. The variation of axial velocity is not significant, except when b/D=0.375. With this configuration, the axial velocity profile is shown as an inverted ‘V’ rather than an inverted ‘W’. In this case, because the length of the inlet width is more than the length from the cyclone to the vortex finder wall, the inlet flow will partially strike the vortex finder instead of swirling around the vortex finder. Normally, this kind of design should be avoided in industrial applications.

Finally, they concluded that altering the inlet parameters such as the width/height will result in a change in pressure and collection efficiency. Based on the study, they suggested a width-to-height ratio 0.5 to 0.7.

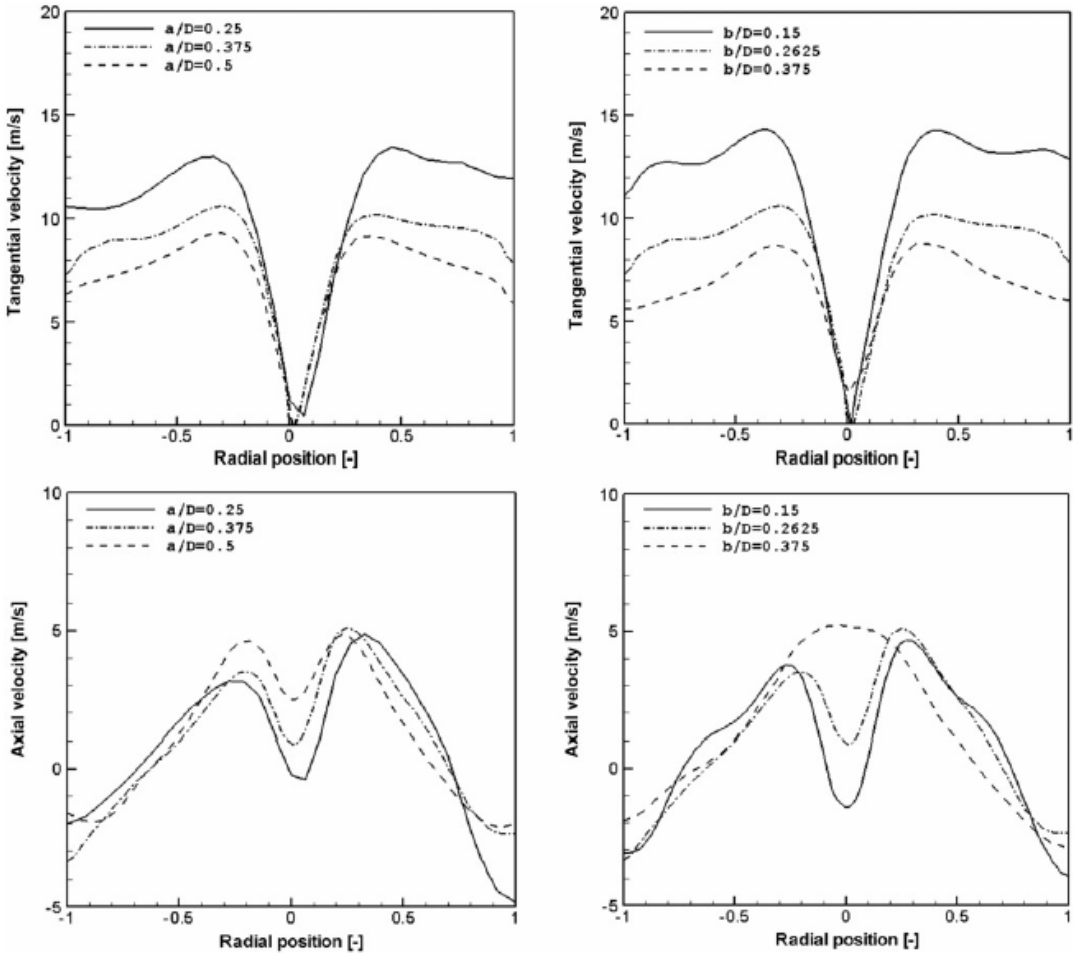

Figure 3-10 Comparison indicating the influence of altering the inlet parameters on the flow field (Elsayed and Lacor, 2011a)

In another work, Elsayed and Lacor (2011b) investigated the cone-tip diameter and the consequent effect of changing it, mainly regarding to the performance and flow profile of a cyclone with a tangential rectangular inlet using the LES model. The results show the cone-tip has very little influence.

Raoufi *et al.*, (2008) worked on the influence from the shape of the cyclone vortex finder. Figure 3-11 gives the pressure contours within 4 cyclones with different cone-shaped vortex finders (at the flow rate of 70 l/min). Each vortex finder has a different divergence angle, which indicates that the vortex core is twisting along the axis within

the cyclone. As the vortex finder divergence angle is decreased, the low-pressure zone at the cyclone centre expands. This pattern agrees with the experimental results from Lim *et al*. (2004).

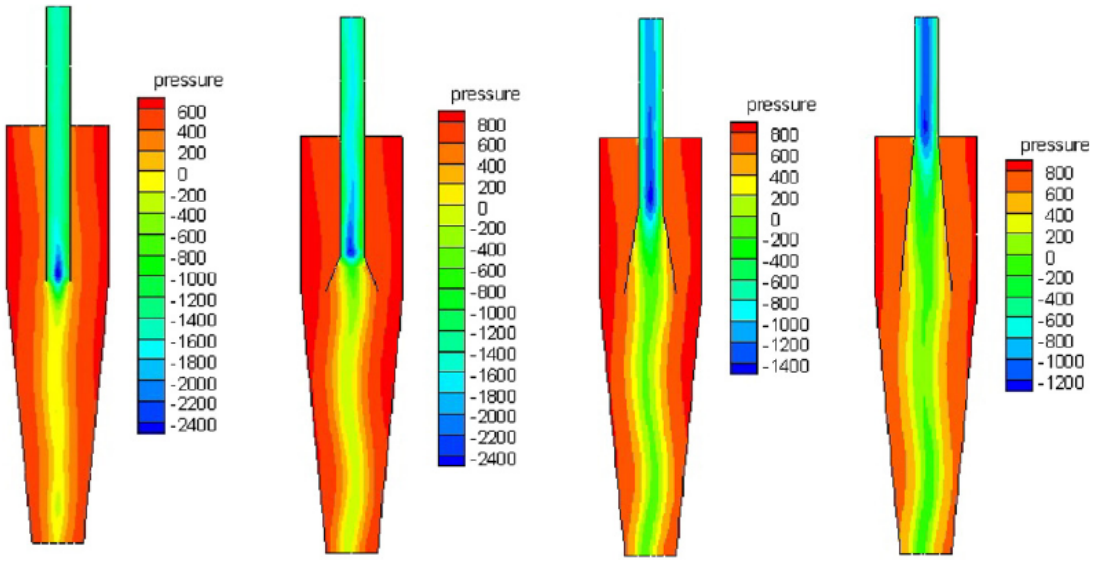

Figure 3-11 Pressure contours in cyclone with different cone-shaped vortex finders (Raoufi *et al*., 2008)

From the above cases, it can be seen that the major advantage in using a CFD simulation for cyclone design is due to the fact that it can offer a more precise flow field compared to other methods, and it can also offer suggestions regarding design optimisation.

3.6.2.2 Simulation of the particle flow in cyclone

In CFD, two methods are used to model the particle flow, namely the 'Eulerian-Eulerian' and the 'Eulerian-Lagrangian' approaches. The difference between the two methods is whether the particle is considered as an individual phase or not. In the former one, the particle is described as an individual phase within the gas phase, governed by Stokes' drag law. This approach can simulate the 'coupling' between the two phases relatively easily, but the disadvantage is this method is not able to study the flow any further. The latter method simulates the motion of particles within the gas phase, using their own governing equations. The advantage is that it can predict the influence of the gas on the particles. But the influence from the particles to the gas phase is hard to be included.

Extensive numerical simulations have been performed by Derksen *et al*., (2003, 2006) studying the solid particles interacting within the gas phase. The governing equations are Navier-Stokes equations, the solver used a lattice-Boltzmann discretization, and the Navier-Stokes equations are filtered with a Smagorinsky subgrid-scale model. Derksen (2003) studied the particle behaviour and the separation efficiency of the Stairmand cyclone. One-way coupling was used and the particles flow analysis was done with the Lagrangian method for the particle tracking process. The grade efficiency curve was obtained and compared with the Barth model. The simulation agreed well with the model prediction and also indicated that using particle tracking it is possible to obtain accurate calculations of the collection efficiencies, for certain situations such as when the mass loading is relatively low. In the work of Derksen *et al*., (2006), two-way coupling was used to simulate the same cyclone, and the influence of particle loading on the gas phase and its behaviour was studied. The presence of large amounts of solid reduces both the swirl intensity and the turbulence. The reduction of swirl and turbulence will increase the separation efficiency, while the loss of swirl reduces the centrifugal force, which drives the particles towards the wall, and consequently it reduces the efficiency, and the reduced turbulence will reduce the particle dispersion and will drive them more to the core than to the wall region, thus leading to a better performance.

3.6.2.3 Simulation of the liquid flow in cylindrical cyclones

The GLCC is a vertical cylindrical cyclone with a downward inclined tangential inlet. Extensive experimental investigations have been performed to develop the mechanistic models. Recent CFD studies of the GLCC can be found in Erdal and Shirazi (2001), Gupta and Kumar (2007) and Hreiz *et al*., (2011).

Erdal and Shirazi (2001) simulated the water flow in the GLCC using 3D steady-state models, including the standard $k-\varepsilon$ and the RSM models. The simulation outcomes showed neither of the models can predict flow field accurately, but the standard $k-\varepsilon$ model was better.

Gupta and Kumar (2007) obtained some experimental results of the tangential velocity from Particle Tracking Velocimetry (PTV). They used the RNG $k-\varepsilon$ model to

describe hydrodynamics, which offers an overall matching between the simulation and experimental outcomes.

Hreiz *et al*., (2011) performed CFD simulations and used the predicted velocity to compare with 2D LDV experiments from Erdal and Shirazi (2001). They applied the RANS, URANS and LES modelling in terms of different conditions, such as turbulence and near wall treatments. Figure 3-12 and Figure 3-13 give tangential and axial liquid velocity results within the GLCC, respectively. The velocities at four positions (marked as x values) below the inlet are shown in these figures. The profiles calculated by the high-Reynolds realizable $k-\varepsilon$ method. The results from LES model are validated against the profiles measured by LDA. It is clear that the tangential velocity simulations using high-Reynolds realizable $k-\varepsilon$ model globally agree well with the measurements, even though the size of the forced vortex is slightly over-predicted as the distance to the inlet increased. The high-Reynolds realizable $k-\varepsilon$ model predicts the axial velocity field closer to the pipe axis than the one shown in experimental measurements. The capture diameter is also studied within the simulation, which is the backflow zone width. The LES simulation presented better results than those obtained with the realizable model.

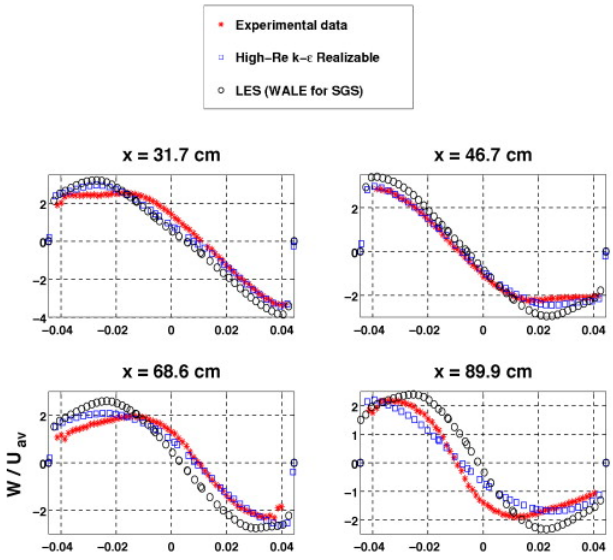

Figure 3-12 Comparison of CFD simulations of tangential velocity profiles with experimental results (Hreiz *et al*., 2011)

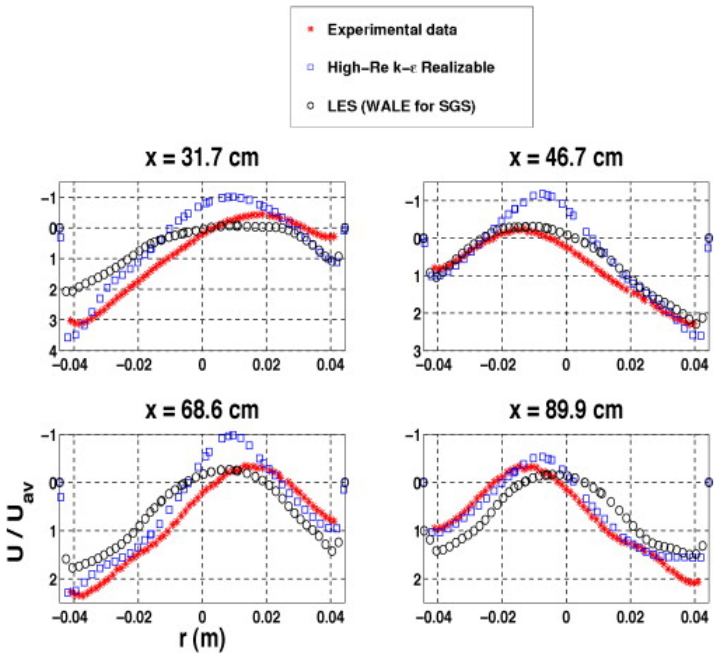

Figure 3-13 Comparison of CFD simulations of axial velocity profiles with experimental results (Hreiz *et al*., 2011)

In Figure 3-14 vortex helical pitch results from experiment and simulation are compared. The high-Reynolds realizable $k-\varepsilon$ model is used. The simulations agree well with the experiment, but there are some differences in the reverse flow width. Because the LDV measurement cannot work on flows close to the wall, the high axial velocity close to the wall is not appeared within the experiment.

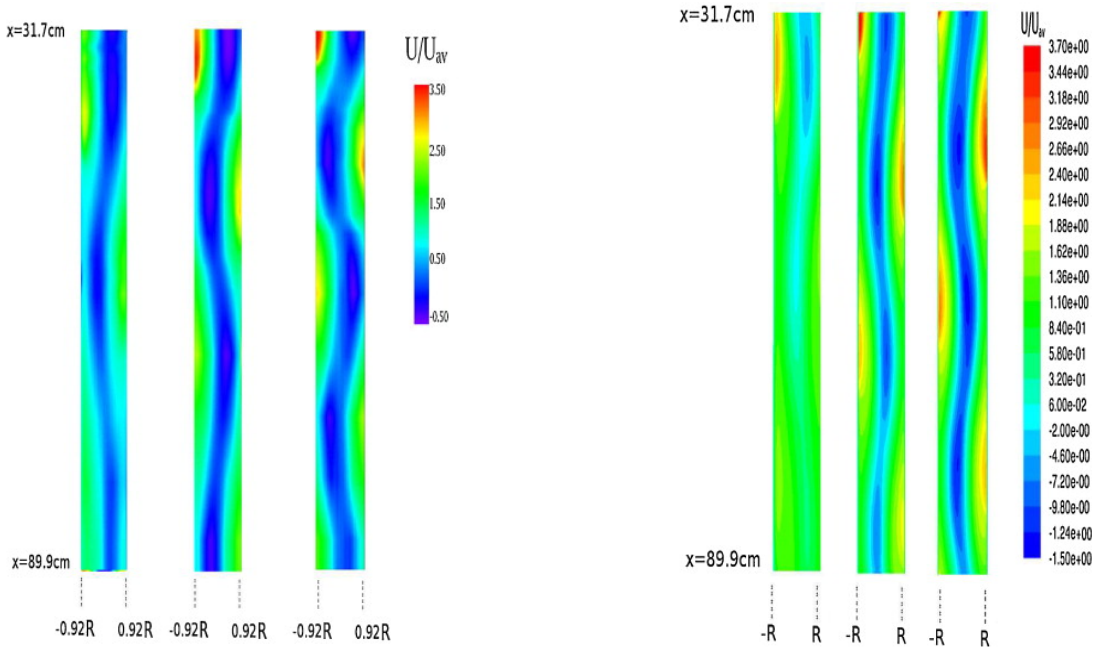

a) Experimental result b) realizable $k-\varepsilon$ model

Figure 3-14 The axial velocity comparison between the experiment and realizable $k-\varepsilon$ model (Hreiz *et al*., 2011)

The high-Reynolds realizable $k-\varepsilon$ model is able to offer the best prediction of the local velocity profiles, and the LES models can give a good prediction when the flow is from one inlet but more realistic results when there are two inlets.

3.7 Summary

This chapter analysed the analytical and numerical simulation studies that have been carried out within the field of separation of gas/liquid flows. The behaviour of vortex flow and swirl flow in pipe and cyclones was explained, and some classic methods used to estimate the cyclone separation efficiency from theoretical considerations have been reviewed, including two main problems normally found in practice: liquid creep and re-entrainment.

The detailed information on the flow profile provided by CFD simulations may in principle yield a more accurate prediction of the performance of gas/liquid separators. In order to predict the separation efficiency of separators with low liquid loading, predicting the liquid droplets behave within the separation area and the gas velocity

profile is requires. The velocity field prediction includes the basic gas flow field and the particle interacting flow field, both of which are simulated in terms of different modelling approaches. Some of the results were validated against experimental measurements, and the advantages and disadvantages of each approach were briefly explained.

4 EXPERIMENTAL AND MODELLING STUDIES OF THE COMPACT GAS/LIQUID SEPARATOR

Prediction of separator performance is critical for the perfecting and optimizing of separators operating in oil and gas processing systems. This chapter describes the development of a predictive model for a compact gas–liquid separator, Pipe-SEP, based on tests of a scaled-down prototype at Cranfield University's Process System Engineering Flow Laboratory. Experiments were carried out in a 150-mm Pipe-SEP prototype operating with a water-air mixture. On the basis of extensive visual observations of flow behaviour and identification of the operational limitations, a simple explicit algorithm was proposed to predict flow regime transitions in the Pipe-SEP. In addition, semi-empirical correlations were used to estimate the separation efficiency to account for the existence of varied flow regimes. Finally, a predictive model was constructed, and the flow regime results and the separation efficiency were validated against corresponding experimental measurements. The model can serve as a design tool to support decision-making in early design stages.

4.1 Introduction

The literature review presented in previous chapters revealed that the difficulties in producing accurate predictions of compact separator performance are mainly due to the complex flow behaviours in separators and uncertainties in upstream and downstream operating conditions. Most of the predictive models depend on empirical or semi-empirical correlations. For instance, the earlier mechanistic models for the GLCC, developed by Tulsa University Separation Technology Projects (TUSTP) include velocity distributions and parameters that define the shape of the gas–liquid interface with satisfactory results. The recently improved models account for bubble trajectory and tangential velocity decay working with some experimental constants (Mantilla *et al*., 1999). The simulation results of these models correctly match the trends that are

observed in experimental data. However, these models are too complex to be used as engineering design and optimization tools.

Usually, the operational range of the compact separator is obtained on the basis of liquid superficial velocities and gas superficial velocities within the separator to limit the occurrence of Liquid Carry Over (LCO) in the gas discharge line and Gas Carry Under (GCU) in the liquid discharge line. Therefore, accurate prediction of the amount of LCO or GCU is essential for estimation of the operational range and for the design of a compact separator(Gomez *et al*., 1999).

In this study, a scaled-down prototype was built to gain a fundamental understanding of the flow hydrodynamic processes and phase separation in the Pipe-SEP to develop a simple model to predict operational constraints and separation efficiency. The model should be easy to use, applicable to a variety of Pipe-SEP applications, and able to simulate the effect of all common geometrical and flow parameters.

4.2 Experimental Set Up

The gas/liquid separation test facility was designed and constructed in the Process System Engineering (PSE) Flow Laboratory at Cranfield University, as shown in Figure 4-1. The test facility is a fully instrumented facility which includes an Inline Separator (I-SEP), a Pipe Separator (Pipe-SEP), a High Separator (Hi-SEP) and a Jet Pump (J-PUMP) test loop. In the present study, the test loop only including the Pipe-SEP and Hi-SEP was used.

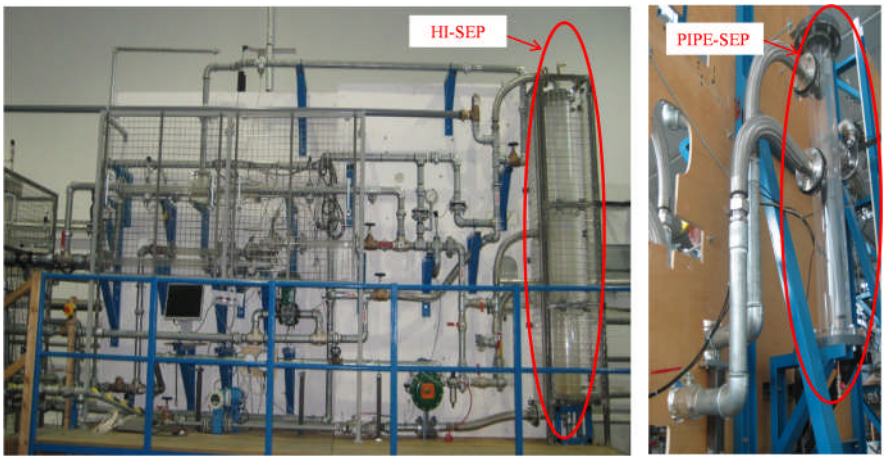

Figure 4-1 Gas-liquid separation facility

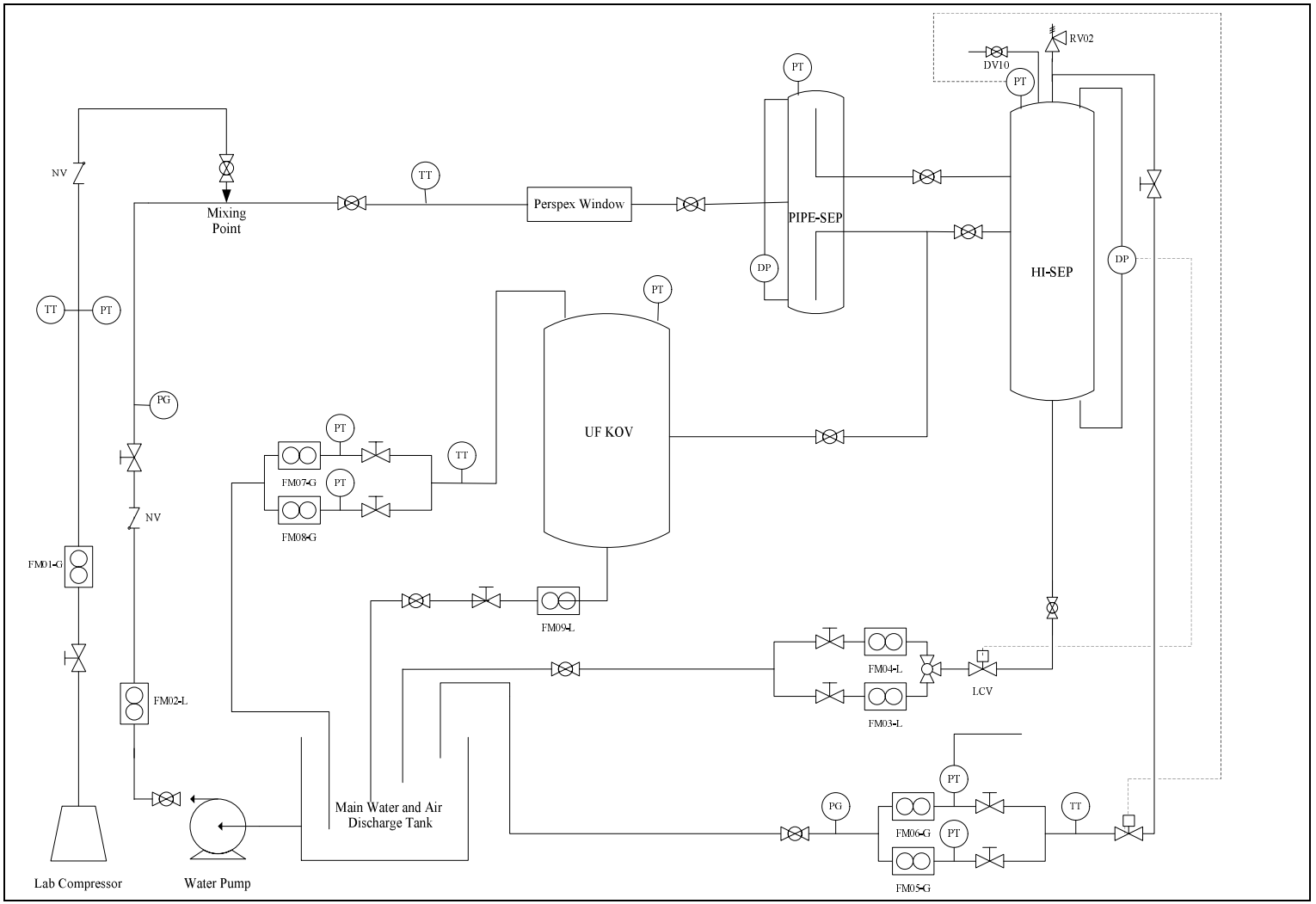

Figure 4-2 Schematic of the Pipe-SEP test facility

Figure 4-2 shows a schematic representation of the apparatus used in the experiment. The apparatus consists of sections for fluid supply, metering, testing, control, and data-acquisition.

4.2.1 Fluid Supply

Water is stored in a tank of 3.5 m^3 capacity, as shown in Figure 4-3. Water is pumped to the test section by a multistage pump, which has a maximum capacity of 36 m^3/hr. Water from the pump is controlled by a by-pass line, where part of the water is recycled back to the tank. After passing through the metering system, the water flow is taken to the mixing point, where it is combined with gas flow and passed to the test section.

Figure 4-3 Water tank

Figure 4-4 Air supply

Air is supplied from a Screw Engineering Compressor (SEC), as shown in Figure 4-4. The compressor has a maximum air flow rate of 280 m^3/hr Free Air Delivery (FAD) @ 7 bara. An air receiver with 2.5m^3 volume is connected after the compressor to reduce the pressure fluctuation from the compressor. From the receiver, air flow goes to the gas meter for metering, and then the gas goes to the mixing point. After mixing, the water and air flow through a 25 m long pipeline (50 mm in diameter) to the testing section. The 25 m long inlet pipeline allows the inlet flow fully developed.

4.2.2 Instrumentation

The flow meters are installed on single-phase flow lines before mixing point and after separation. Water flow is metered by a Promag 50 electromagnetic flowmeter (Endress+Hauser). The electromagnetic flowmeter has a HART output that can be connected to the Data Acquisition System (DAS) via a BNC connection. Gas flows are metered by V-cone flowmeters (McCrometer) and vortex meters. The differential pressure transmitter measures the differential pressure signal. At the gas metering point, temperature and pressure are measured to calculate the actual volumetric flow rate of the gas that enters the test section. All data from the instrumentation of the test facility is recorded by the DAS. Details of the instrumentation for the test loop have been given in Table 4-1.

Table 4-1 Test loop fluids instrumentation

Tag	Description	Details	Range
FM01-G	Inlet gas flowmeter	Vortex meter	0.02 to 0.2 N-m^3/s
FM05-G	Outlet gas flowmeter (high)	V-Cone meter	0.02 to 0.2 N-m^3/s
FM06-G	Outlet gas flowmeter (low)	V-Cone meter	0.005 to 0.05 N-m^3/s
FM02-L	Inlet liquid flowmeter	MagFlow meter	0 to 10 l/s
FM03-L	Outlet liquid flowmeter (low)	MagFlow meter	0 to 4.9 l/s
FM04-L	Outlet liquid flowmeter (high)	MagFlow meter	0 to 12.5 l/s
PT01	Inlet gas pressure sensor	Druck (PMP1400)	0 to 6 bara
PT04	Pipe-SEP inlet pressure sensor	Druck (PMP1400)	0 to 6 bara
PT05	FM05-G pressure sensor	Druck (PMP1400)	0 to 4 bara
PT06	FM06-G pressure sensor	Druck (PMP1400)	0 to 4 bara
PT10	Hi-SEP pressure	Druck (PMP1400)	0 to 6 bara
PT11	Pipe-SEP pressure	Druck (PMP1400)	0 to 6 bara
TT01	Inlet gas temperature sensor	RS thermocouple	-200 to 800°C
TT02	Mixture temperature sensor	RS thermocouple	-200 to 800°C
DP04	Hi-SEP differential pressure	Druck (PMP4110)	-70 to 70 mbara
DP07	Pipe-SEP differential pressure	Druck (PMP4110)	-100 to 100 mbara

4.2.3 Test Section

The test section consists of three separators that are made of Plexiglas, namely the Pipe-SEP, Hi-SEP, and Under Flow Knock-out Vessel (UF KOV). The Pipe-SEP is a vertically installed pipe with 150mm in diameter and 1600 mm in height, The Pipe-SEP is mounted with a 50 mm tangential inlet, as shown in Figure 4-5. The upper part of the Pipe-SEP extends approximately 900 mm. There is an FER and gas ASB near the top. The 'L'-shaped gas out section is fitted inside the separation chamber and is connected through a horizontal pipe to the upper inlet of the Hi-SEP, as shown in Figure 4-2. The lower part of the Pipe-SEP is 700 mm high. The 'L'-shaped liquid out section, which is coupled to a liquid ASB, can discharge the liquid to the lower inlet of the Hi-SEP or to the UF KOV. In the experiments from this PhD work, the liquid was discharged to the UF KOV for further separation and measurement.

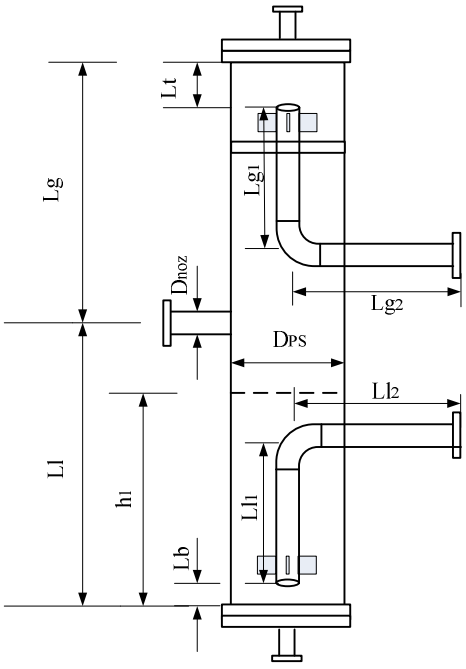

Figure 4-5 Schematic of the Pipe-SEP

The Hi-SEP is geometrical similar to the Pipe-SEP, and is a 2400 mm tall separator with an inner diameter of 204 mm. The Hi-SEP can either be connected with the Pipe-SEP in series through its dual tangential inlet to improve separation performance, or can be used for enhancing measurement. In the experiments from this PhD work, only the

Pipe-SEP was tested, while the Hi-SEP was used to capture and measure the LCO in the gas outflow of the Pipe-SEP.

The UF KOV is a vertical gravity separator, with 500 mm inner diameter and 2400 mm high. The function of UF KOV is to knock out the gas bubble that trapped in the liquid outflow of the Pipe-SEP. This enables the GCU to be measured accurately using the single phase meter.

4.2.4 Control System

The control system is consist of 1) a control valve on the Hi-SEP liquid outlet to maintain the liquid level; 2) a backpressure valve on the Hi-SEP gas outlet to maintain a steady operating pressure; 3) a pressure relief device; 4) a control logic worked under a Labview interface.

The liquid control valve (LCV) is located in the Hi-SEP liquid out section and the gas control valve (GCV) at Hi-SEP gas out section, as shown in Figure 4-6 and Figure 4-7, respectively. The design of the control system is discussed in section 4.3.

Figure 4-6 Liquid control valve

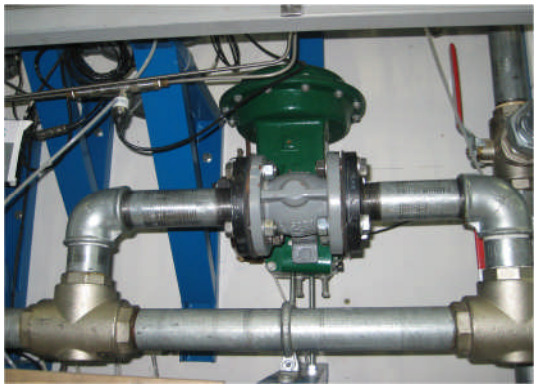

Figure 4-7 Gas control valve

4.2.5 Data-Acquisition System

Data from the compact gas/liquid separator facility is acquired by a dedicated PC-based Data Acquisition System (DAS). This system includes a series of built-in signal conditioning units, which collect and transfer experiment data to computer with the (SCB-68) parallel port multiplexer. The gathering of information and displaying based on a real time principle is achieved by the ‘Virtual Instrument’ Version 7 (Labview) and

DAS hardware under Windows XP-Professional operating system for control and operation purpose.

4.3 Control System

Level control is extremely important for the successful operation of the compact separator system, because it is through the proper control of level that the desired separation performance is achieved. The objective of the control system design in the present experiment is maintaining the liquid level and pressure at or near its target by adjusting the opening of the control valves. In this section, a conventional feedback control strategy, consisting of two PI controllers was designed and tested through simulation in a dynamic Pipe-Hi-SEP program (see Appendix B) before being implemented in the test facility.

4.3.1 Control System Design

As mentioned in previous section, control valves are installed on the gas outlet section and on the liquid outlet section of the Hi-SEP, as shown in Figure 4-8. The following measurements are considered when configuring level control:

- Hi-SEP level. Control of separator level is of utmost importance. Differential pressure transmitter is installed to monitor the level.
- Hi-SEP pressure. The transmitter is installed at the top of the Hi-SEP.
- Gas out-flow and liquid out-flow. In compact separators, this measurement can be challenging. Because compact separator experiences liquid carry over and gas carry under.

Observing the Hi-SEP, with no controls in operation, the following responses are noted:

- Increasing the liquid valve opening decreases the Hi-SEP liquid level and decreases the Hi-SEP pressure.
- Increasing the gas valve opening increases the Hi-SEP liquid level but decreases the Hi-SEP pressure.

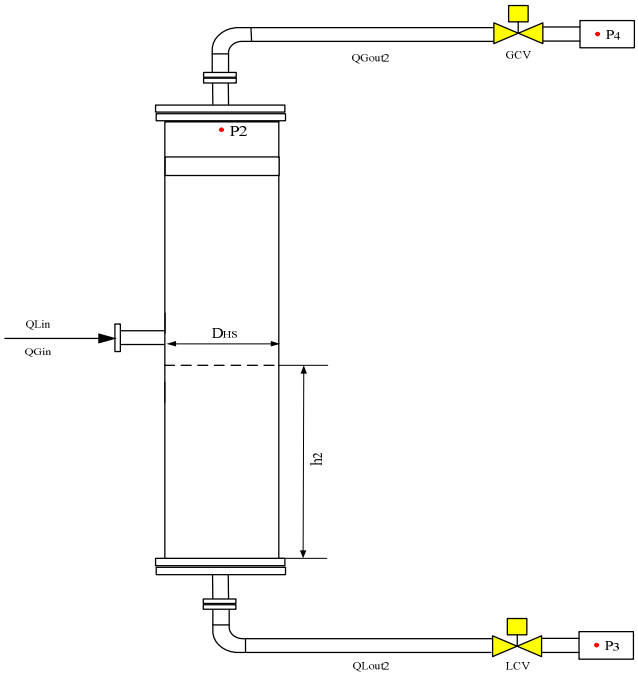

Figure 4-8 Schematic of the Hi-SEP with control valves

Two single-loop controllers are selected to configure the feedback control system. The block diagram for the Hi-SEP with the two single-loop controller is shown in Figure 4-9.

To quantify the degree of loop interaction, quantitative measures of interaction are calculated from the steady-state gains (or sensitivities) for the Hi-SEP. The sensitivities are calculated using the relative gain array (RGA) method.

The RGA is a matrix of elements defined as ratios of open loop to closed loop gains. For example, the sensitivity of Hi-SEP level h_2 to LCV opening at constant GCV opening (open-loop) is expressed by the following partial derivative:

$$K_{11} = \frac{\partial h_2}{\partial LCV}|_{GCV} \cong \frac{\Delta h_2}{\Delta LCV}|_{GCV} \tag{4-1}$$

The sensitivity of h_2 to LCV at constant Hi-SEP pressure P_2 (closed-loop) is expressed as:

$$K'_{11} = \frac{\partial h_2}{\partial LCV}|_{P_2} \cong \frac{\Delta P_2}{\Delta LCV}|_{P_2} \tag{4-2}$$

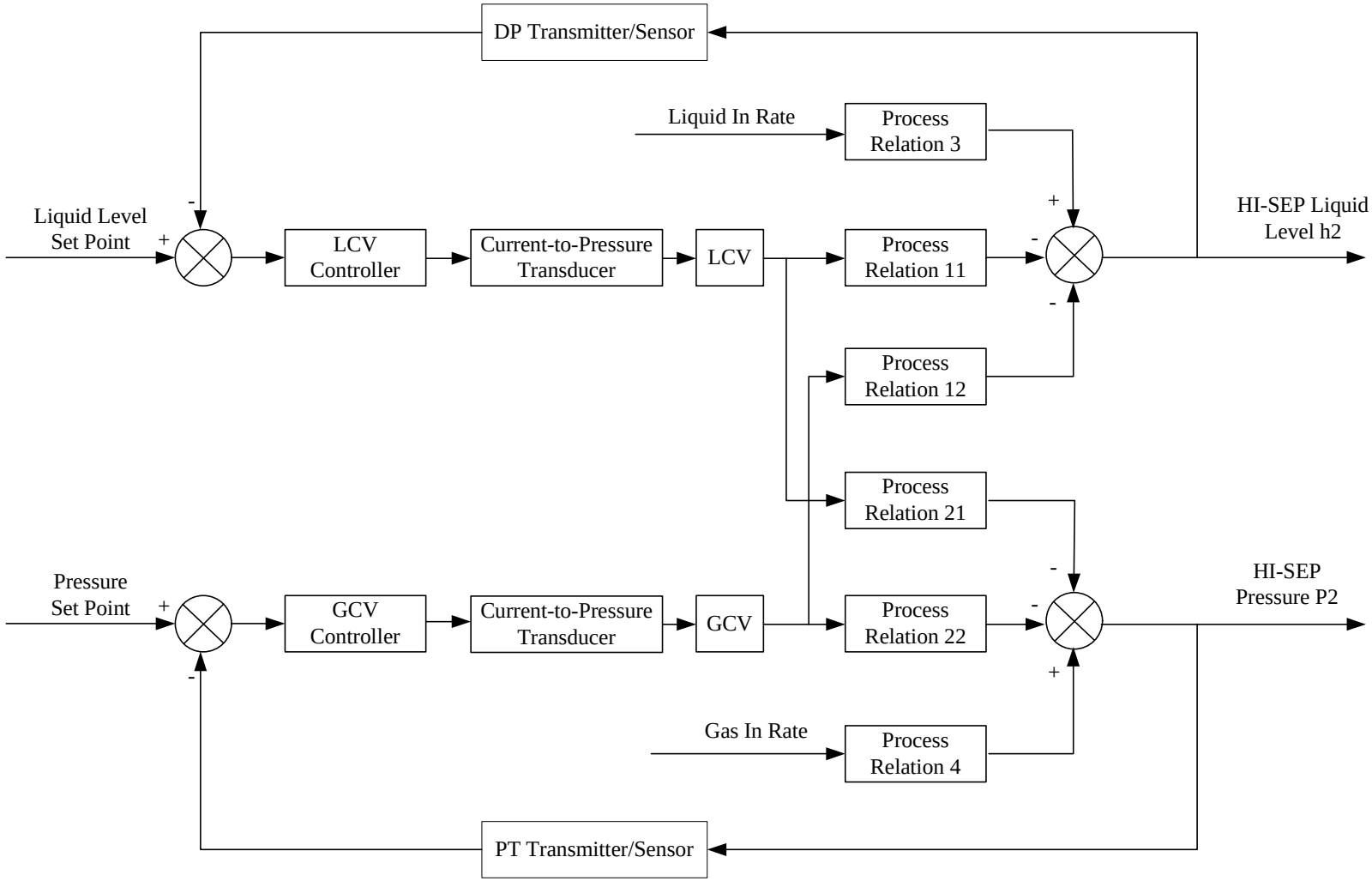

Figure 4-9 Block diagram of an Hi-SEP with two single-loop controllers

The relative gain λ_{11} is the ratio of sensitivities K_{11} to K'_{11}:

$$\lambda_{11} = \frac{K_{11}}{K'_{11}} \tag{4-3}$$

In this study, the value of the relative gain is calculated as: λ_{11}=0.833.

The remaining elements of the relative gain array are calculated from the fact that each row and each column must sum to 1.0. CV is Control Variable and MV represents Manipulate Variable. Here MV_1 is LCV opening, MV_2 is GCV opening. CV_1 is Hi-SEP liquid level and CV_2 is Hi-SEP pressure.

	MV_1	MV_2
CV_1	0.833	0.166
CV_2	0.166	0.833

From the results of the relative gain array, it is clear that the interaction between the pressure and level loop is minor. The pressure is influenced mostly by the GCV and the level is influenced mostly by the LCV, and there is significant dynamic separation between two loops. The pressure responds very rapidly, and the control tuning method will be to tune the pressure loop to respond as rapidly as possible and to slow down the level loop until the degree of oscillations in the two loops is acceptable.

4.3.2 Control System Tuning

The dynamic model of the Pipe-Hi-SEP system has been developed using fundamental principles (see Appendix B). In this section, the empirical model for the Pipe-Hi-SEP system is developed for the needs of process control analysis.

The empirical model is determined by introducing small changes in the input variables on a nominal operating condition. The resulting dynamic response is used to determine the model. The model takes the form of first-order-with-dead-time, which is adequate for process control analysis and design. The form of the model is expressed as follows:

$$\frac{Y(s)}{X(s)} = \frac{K_p e^{-\theta s}}{\tau s+1} \tag{4-4}$$

where $Y(s)$ denoting the output and $X(s)$ denoting the input. The model includes all elements in the process, including instrumentation and transmission.

Experiments are performed on the Hi-SEP to identify the response of the liquid level $Y(s)$ to the liquid control valve opening $X(s)$ and the response of pressure to the gas control valve opening, respectively. The operating liquid flow rate is 7.2 m^3/h and gas flow rate is 200 Sm^3/h. The procedures for identifying the liquid level model are shown below as per example:

Run the system at the base operating conditions to reach steady state.

- Introduce a step change δ in the LCV.
- Record LCV and liquid level response data until the system again reaches steady state.

The experiment data is shown in Figure 4-10. The parameters K_p , τ and θ are determined using the process reaction curve method and summarized as:

δ= -60% open Δ= 0.7899m

$K_p = \frac{\Delta}{\delta}$ = 0.7899m / -60% open = -0.013165m / % open

0.63Δ=0.4976m $t_{63\%}$=94s

0.28Δ=0.221m $t_{28\%}$=32s

τ=1.5($t_{63\%} - t_{28\%}$) =1.5(94-32) s = 93s

$\theta = t_{63\%} - \tau$ = (94-93) s = 1s

where δ is the magnitude of the input change. Δ is the magnitude of the steady-state change in the output. $t_{63\%}$ and $t_{28\%}$ are the times at which the output reaches 63 and 28 percent of its final value.

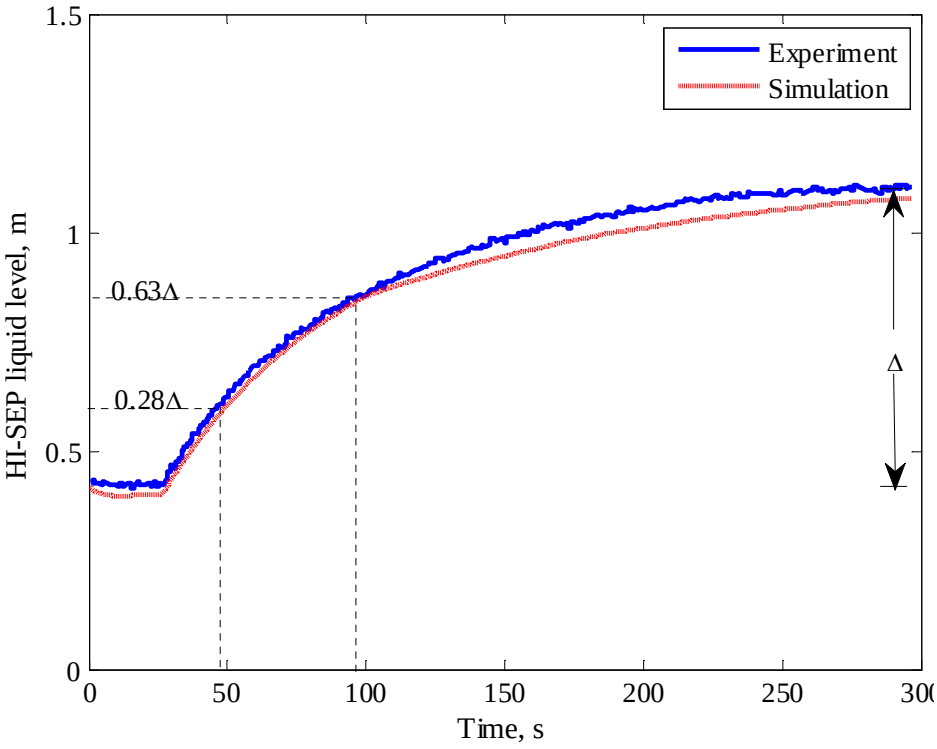

Figure 4-10 Separation process reaction curve

In Figure 4-10, a comparison of measured and simulated data also is presented. Since the data and model do not differ by more than 0.05m throughout the transient. Therefore, the first order with dead time model determined using the reaction curve can adequately approximate the dynamics of processes with to a step input. The model is accepted for tuning the control system later. The empirical model parameters for level loop and pressure loop are summarized in Table 4-2 .

Table 4-2 Empirical model parameters for the Hi-SEP

Model parameters	Level loop	Pressure loop
K_p	0.05369	-0.001225
θ	1	0.033
τ	93	0.177

The PI control algorithm is used to evaluate and determine limiting behaviour for control system. The transfer function for the PI control is as follows

$$G(s) = \frac{MV(s)}{E(s)} = K_c(1 + \frac{1}{T_I s}) \quad (4\text{-}5)$$

The Ciancone tuning correlations (Marlin, 2000) are used to determine the tuning constant values. The tuning constants are summarized in Table 4-3.

Table 4-3 Ciancone tuning constants for the Hi-SEP

Parameters	Level loop	Pressure loop
$\theta/(\theta+\tau)$	0.01	0.21
K_cK_p	1.5	1.065
$T_I/(\theta+\tau)$	0.24	0.5
K_c	0.279	1.964
T_I	0.2256	0.105

4.3.2.1 Hi-SEP dynamic response

The Hi-SEP dynamic response of the feedback system to a step liquid inlet flow rate disturbance of magnitude 20%×7.2 occurring at t=500s is shown in Figure 4-11. It can be seen that the liquid level is well controlled and returns to its set point reasonably quickly without excessive oscillations. The LCV does not experience excessive variation.

The dynamic response of the feedback system to a step gas inlet flow rate disturbance of magnitude 30%×200 occurring at t=500s is shown in Figure 4-12. The pressure dynamic is fast and is well controlled as well. The Ciancomne correlations provide acceptable performance.

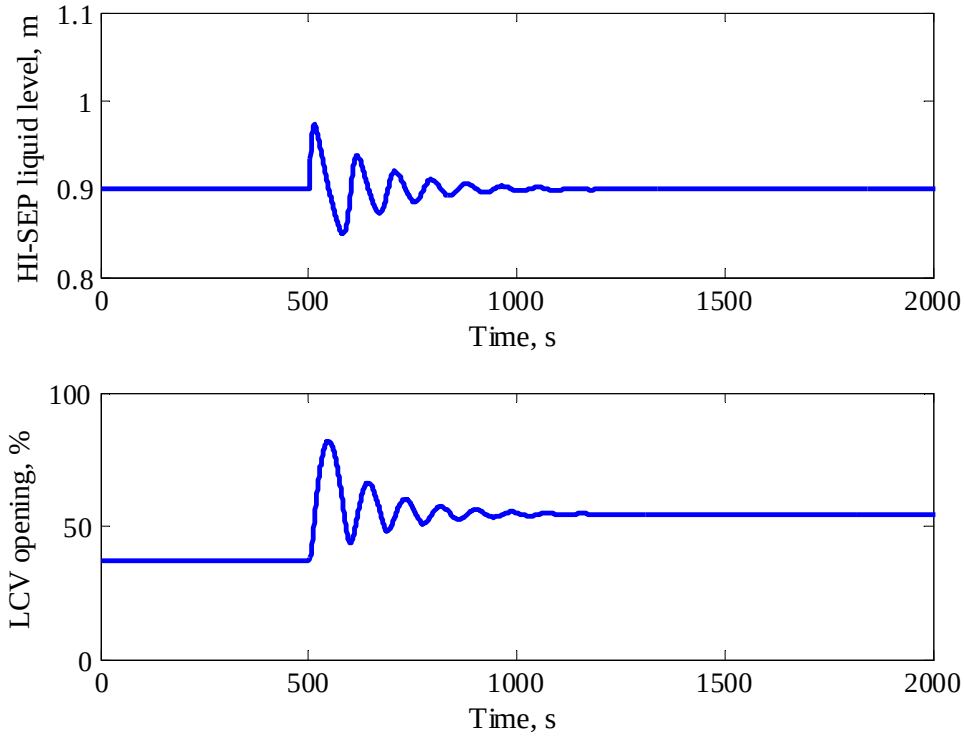

Figure 4-11 Dynamic response of Hi-SEP PI level control loop with Ciancone tuning

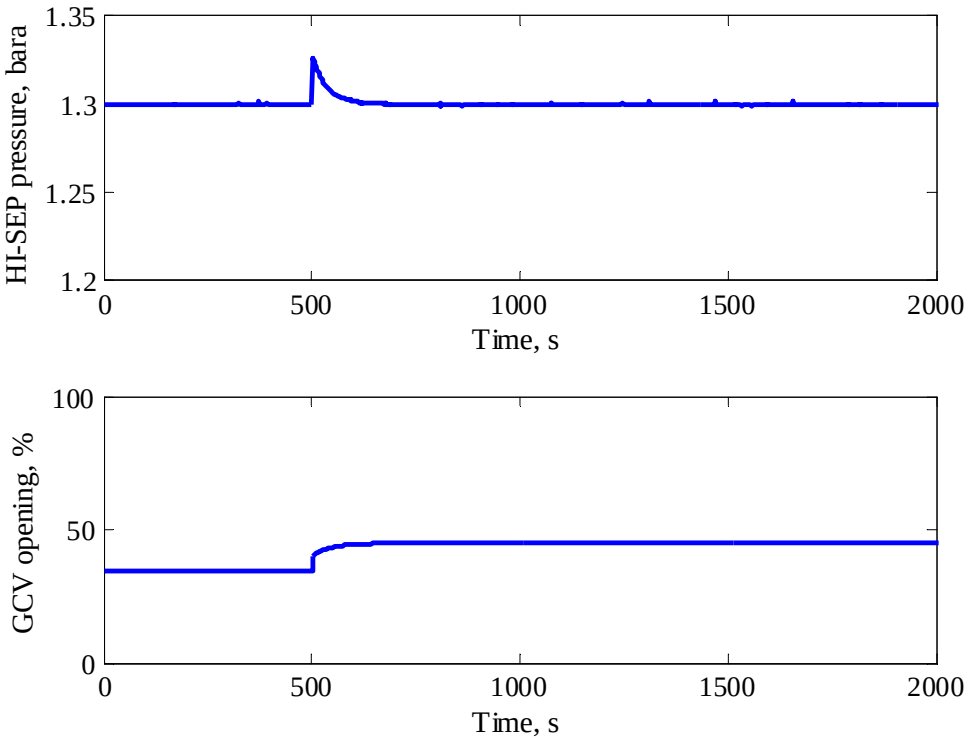

Figure 4-12 Dynamic response of Hi-SEP PI pressure control loop with Ciancone tuning

4.3.2.2 Pipe-SEP effect on Hi-SEP dynamic

To qualify the Pipe-SEP effect on the Hi-SEP dynamic behaviours, a comparative study is performed. Figure 4-13 shows the dynamic response of the Hi-SEP and Pipe-Hi-SEP system to a step liquid inlet flow rate disturbance. It demonstrates that the Pipe-SEP has improved the dynamic behaviour of the separation system. First, the maximum level deviation for a step inlet flow, Δh_{2max} of Pipe-Hi-SEP is smaller, allowing a lower overshoot. Second, the fluctuation of liquid outlet flow rate is smaller.

The dynamic response of the Hi-SEP and Pipe-Hi-SEP system to a step gas inlet flow rate disturbance is shown in Figure 4-14. The pressure and GCV dynamic responses are the same for these two systems. However, in the Pipe-Hi-SEP system, the liquid will be pushed out from Pipe-SEP, resulting in a short-period disturbance to the Hi-SEP liquid level.

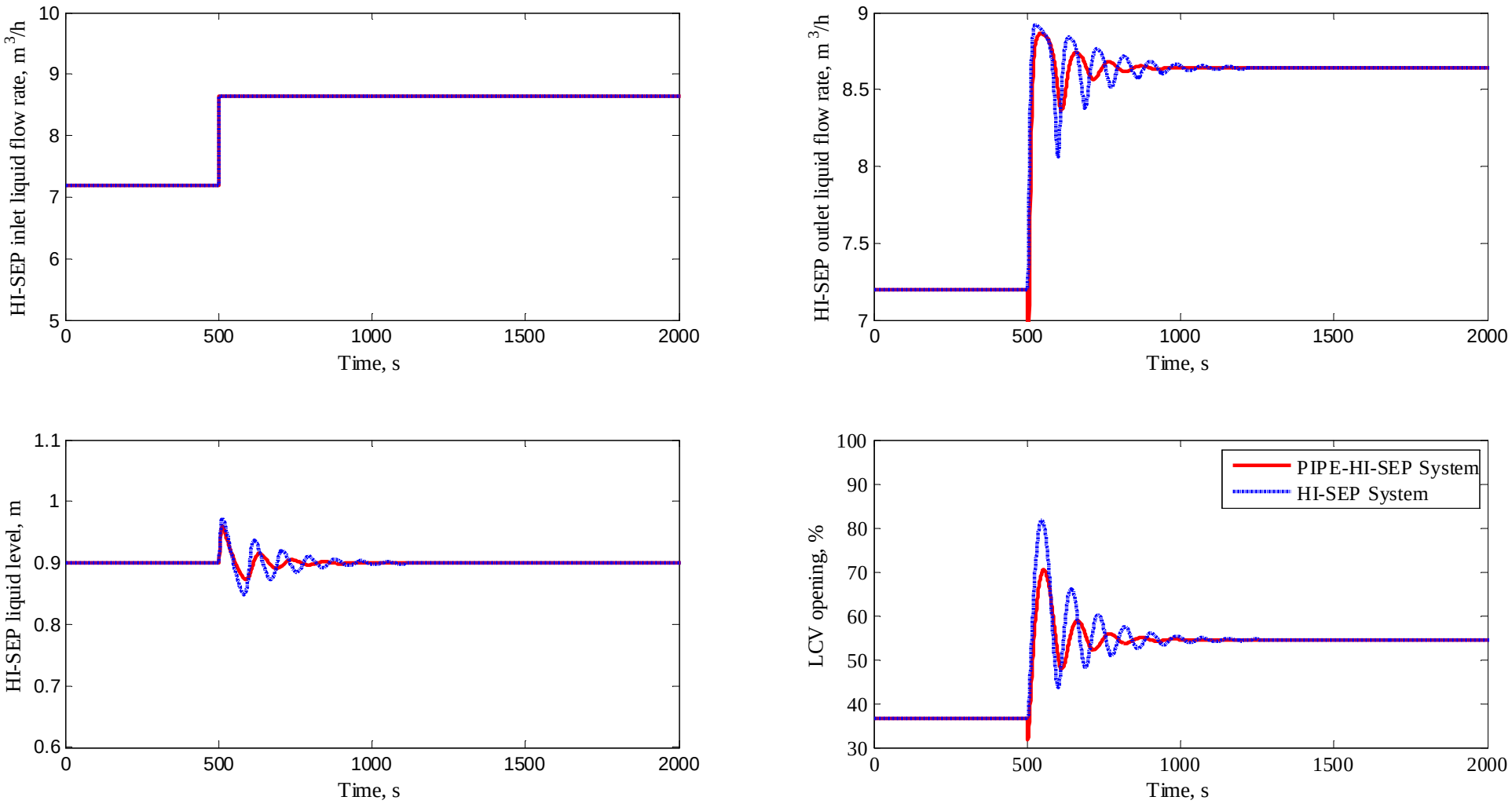

Figure 4-13 Dynamic response of Hi-SEP and Pipe-Hi-SEP level control loop with Ciancone tuning

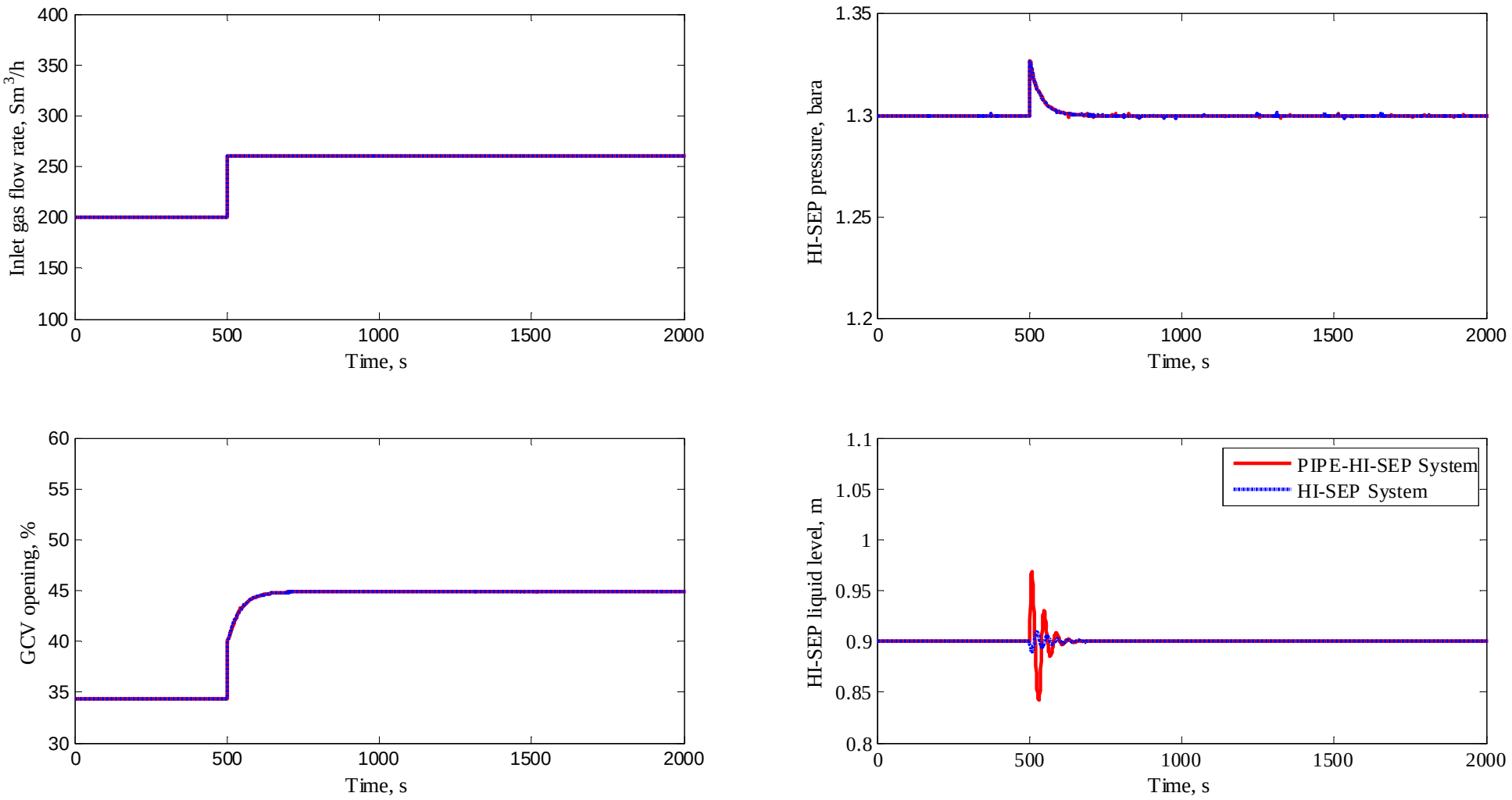

Figure 4-14 Dynamic response of Hi-SEP and Pipe-Hi-SEP pressure control loop with Ciancone tuning

4.4 Physical Phenomena

To help development of mechanistic models of the phase separation processes that take place inside the Pipe-SEP, extensive tests and flow visualizations were performed. Three distinct flow regimes have been identified in the Pipe-SEP, namely swirled, agitated, and gas blow-by. The flow behaviours are quite similar to those in the GLCC and CS separators, as reported by Arpandi *et al.*, (1996) and Rosa *et al.*, (2001), respectively.

1) Swirled flow is likely to occur under regular operating conditions, as illustrated in Figure 4-15 a). Under these conditions, the Equilibrium Liquid Level (ELL) is well below the inlet region. The tangential inlet imparts momentum to the gas/liquid mixture. The mixture starts to rotate along the inner wall of the Pipe-SEP, forming a liquid film with dispersed bubbles. Under the strong centrifugal force, the bubbles tend to move along the radial direction and eventually merge with the inner gas stream. As the film rotates, more gas separates, and eventually the film are eliminated by the FER. When the rate of gas flow exceeds the limitation conditions, the film can pass through the FER and then more liquid droplets are entrained in the gas phase, which leads to LCO.

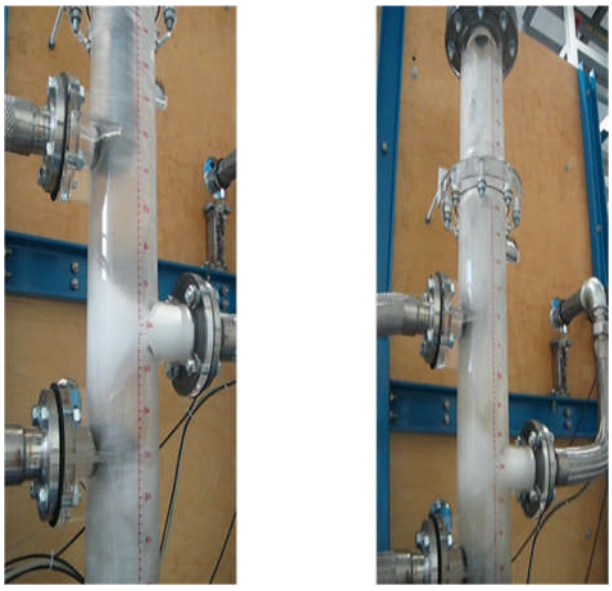

(a) Swirled flow (b) Agitated flow

Figure 4-15 Flow regimes in the upper section of the Pipe-SEP

2) As the liquid flow rate is increased for a certain gas flow rate, the flow regime transitions from swirled flow to agitated flow. During the transition, the liquid and gas become chaotic near the inlet region. The swirled film becomes unstable and excessively thick, and blocks the annular space above the inlet. In the top section of the Pipe-SEP, the liquid phase is dispersed into small discrete droplets in a continuous gas phase, forming an approximately homogenous flow through the annulus cross-sectional area. As the liquid flow rate increases further, agitated flow occurs in the Pipe-SEP.
3) Agitated flow can be observed as huge move upwards liquid waves. A falling liquid film exists between the waves, as shown in Figure 4-15 b). The behaviour in the Pipe-SEP during agitated flow is very similar to that observed with churned flow in a vertical pipe, as reported by Govan *et al.* (1991). Owing to the presence of the channels, a relatively high local void fraction occurs during this regime. Under the agitated flow condition, a large amount of LCO occurs.
4) For a given liquid flow rate, as the gas flow rate increases, the ELL can fall below the liquid discharge outlet. As a consequence, gas blow-by occurs. At the same time, at the inlet region, the liquid can be seen swirls as a film along the inner wall of the Pipe-SEP. LCO is rarely observed in this flow regime.

4.5 Experimental Results and Discussions

Experiments were carried out to investigate the efficiency of the Pipe-SEP under a wide range of flow rates. Experiments were performed at near-atmospheric pressure (1.2 bara). The gas flow rate ranged from 50 to 280 Sm^3/hr. The liquid flow rate is varied from 1.8 to 9 m^3/hr. The input gas-to-liquid volumetric fraction (GVF) ranged from 40 to 98.5. The observed inlet flow patterns are listed in Appendix C and they are basically intermittent flow and annular flow.

4.5.1 Pipe-SEP Flow Regime Map

When a liquid–gas mixture enters into a Pipe-SEP, different flow regimes are possible in the upper part of the Pipe-SEP depending on the magnitude of the flow velocity. Figure 4-16 shows the air-water flow regime map plotted for the Pipe-SEP at 1.2 bara; it is based on experimental observations. At low velocities of both gas and liquid, the

liquid phase swirled as a liquid film with dispersed bubbles. The height of the liquid film was relatively low. As the gas velocity increased, the interfacial force between the liquid film and the gas stream also increased, and the height of the swirled film became higher and higher. When LCO occurred, the film became extremely high. At this point, the separation performance was dominated by the penetration of liquid droplets that were under the cut-size of the Pipe-SEP. As the velocity of the liquid increased, the flow regime transitioned to agitated flow, and the separation performance was dominated by re-entrainment of the liquid. At this point, if there was a high gas velocity to accelerate the centrifugal force, the liquid rotated before forming a film that bridged the inlet region. The flow then transitioned back to swirled flow.

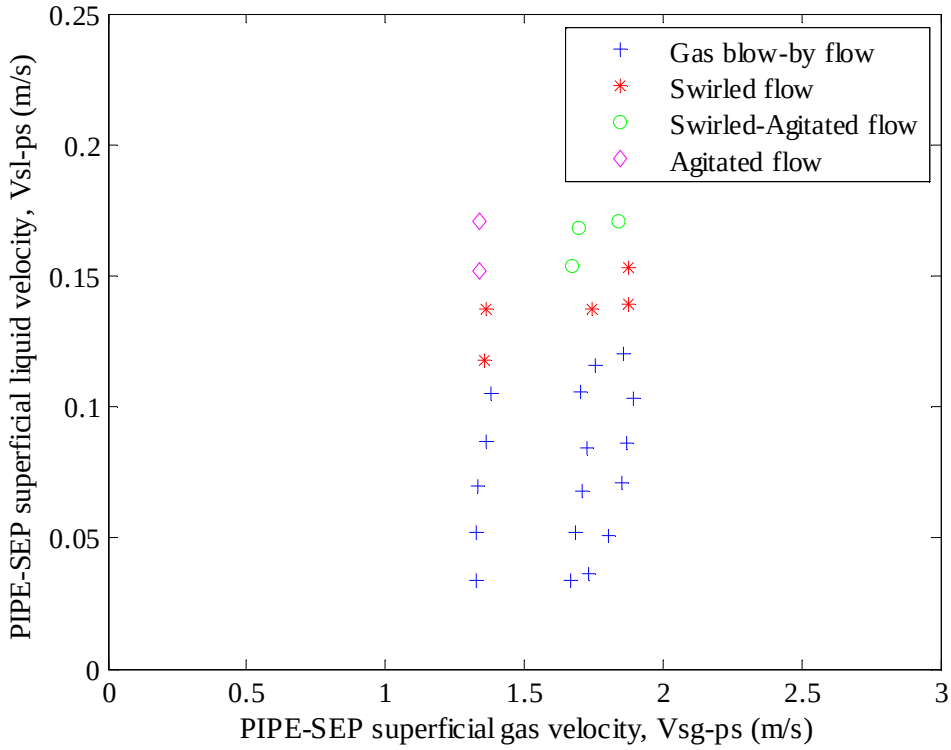

Figure 4-16 Observed flow regimes in the upper section of the Pipe-SEP

4.5.2 Equilibrium Liquid Level

The Equilibrium Liquid Level, ELL is the level of the liquid in the Pipe-SEP. The ELL can be determined by the differential pressure transducer. The ELL data that obtained under 1.2 bara operating conditions is shown in Figure 4-17. Although the ELL is always fluctuating, the average value was taken and plotted versus the Pipe-SEP

superficial liquid velocity, V_{sl-PS}, for three different Pipe-SEP superficial gas velocities, V_{sg-PS}.

It can be seen that the ELL, L_{l1}, increased significantly as the V_{sl-PS} increased, but decreased as the V_{sg-PS} increased. The dashed line represents the boundary for swirled flow to agitated flow as based on visual observations. The boundary line indicates that the ELL was around 600 mm.

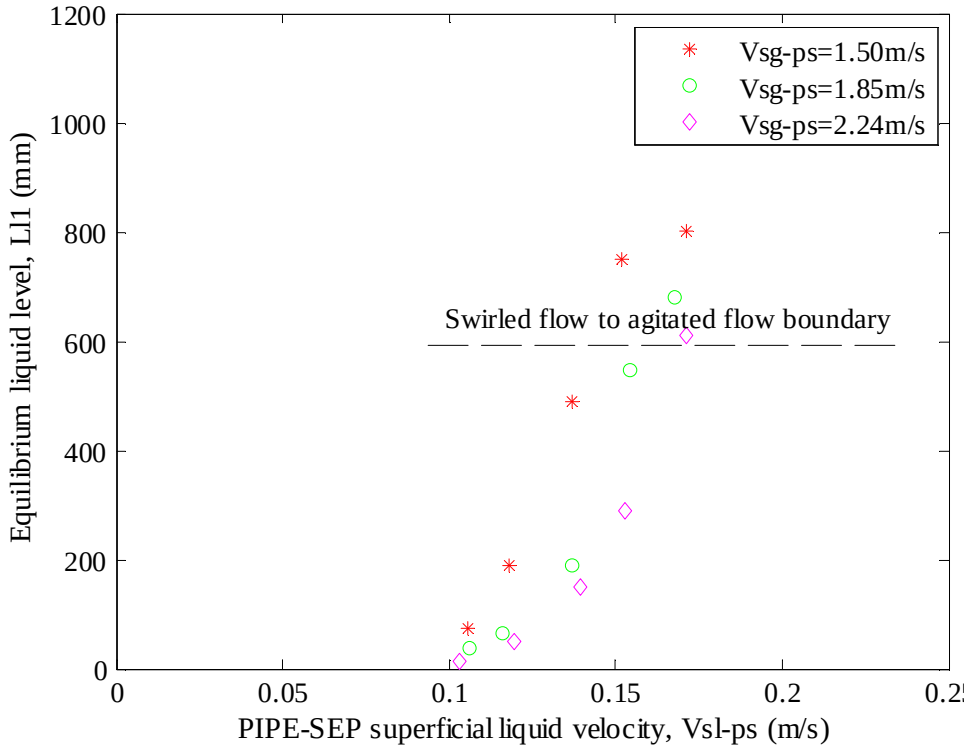

Figure 4-17 Equilibrium liquid level in the Pipe-SEP

4.5.3 Operational Envelope

As mentioned, LCO and GCU are the key parameters determining the separator performance. A procedure was followed to obtain the operational envelope of LCO and GCU for Pipe-SEP. For the LCO, the superficial gas velocity, V_{sg-PS}, is first fixed at a required value. The superficial liquid velocity, V_{sl-PS}, is slowly increased until the liquid carry over point is reached. For the GCU, the superficial gas velocity is fixed at a certain value and then the superficial liquid velocity is increased until the gas carry under disappears. Plotting the locus of the V_{sg-PS} vs. V_{sl-PS} at which LCO is initiated or

GCU is disappeared generates the operational envelope for LCO or GCU, as shown in Figure 4-18.

The LCO curve indicates the onset of liquid entrainment into the gas discharge outlet. The region below the LCO curve is called normal operating region, where there is no LCO in the Pipe-SEP. The region that above the LCO curve is suffered continuous LCO. Even though there are various mechanisms for liquid carry over, only liquid droplet carryover was observed during this experiment. The Pipe-SEP flow regime was swirled flow. In addition, it can be seen that the LCO boundary reveals a limiting liquid velocity, $V_{sl-PS,c}$=0.034m/s, below which no entrainment was possible at any gas flow rate.

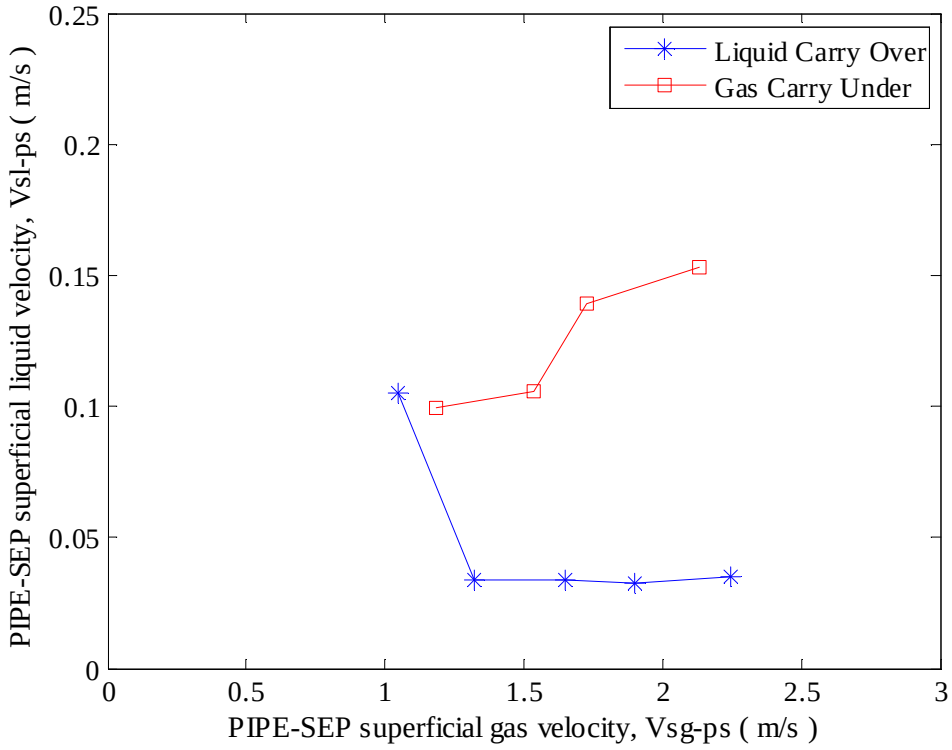

Figure 4-18 Operational envelope for air-water flow in the Pipe-SEP

Due to the limited length of Pipe-SEP in the experiment, the Pipe-SEP can't achieve non-GCU under testing flow rate. The GCU curve in Figure 4-18 is determined by predefining the minimum GCU is 3 Sm^3/h. It can be seen that to prevent the GCU, the liquid loading need to be increased nearly linear with the increasing of the gas loading.

It is also worth noting that the GCU curve is setting above the LCO, which indicates that the Pipe-SEP under the present testing condition can only achieve partial separation.

4.5.4 Effect of Back Pressure on the Operational Envelope

The back pressure on the Pipe-SEP gas outlet was regulated to investigate its effect on the operational envelope of the Pipe-SEP. The data were acquired for three different back pressures of 1.3 bara, 1.4 bara and 1.5 bara for LCO and one different back pressure of 1.3 bara for GCU, as shown in Figure 4-19 and Figure 4-20, respectively.

Figure 4-19 highlights the LCO operational area curve based on the Pipe-SEP superficial velocity. As it can be clearly seen, increasing the back pressure will restrain LCO for the same liquid loading and gas loading. This is due to the fact that increasing the back pressure will decrease the ELL and reduce the gas velocity. Both of them can eliminate the onset of the LCO. For low gas velocity, the effect is significant, while the effect is negligible for high gas velocity (V_{sg-PS}>2.2m/s) or high liquid velocity (V_{sl-PS}>0.17m/s). It also can be concluded that 2.2m/s is the maximum gas superficial velocity in the Pipe-SEP, and above that the flow in the upper section of the Pipe-SEP becomes mist flow. The onset to mist flow represents the theoretical gas capacity limit of the performance of the Pipe-SEP.

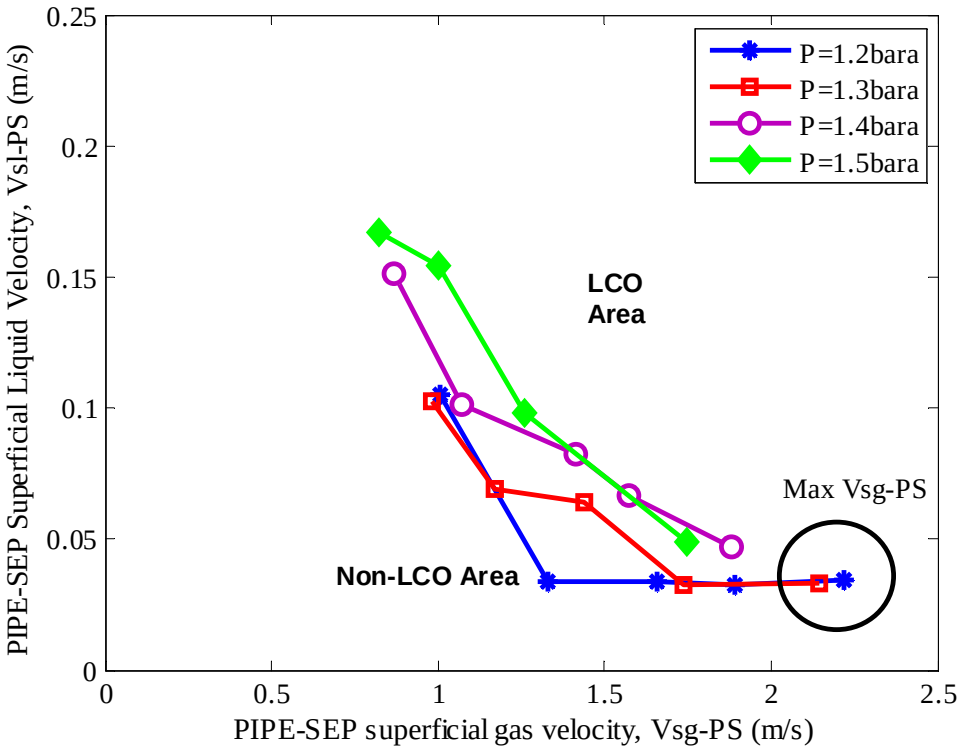

Figure 4-19 LCO operational envelope for Pipe-SEP under different back pressure

Figure 4-20 shows the GCU operational curve based on Pipe-SEP superficial velocity. It can be seen that with a slightly increase in back pressure, the liquid velocity limit for preventing gas blow is increased from 0.1m/s to 0.17m/s.

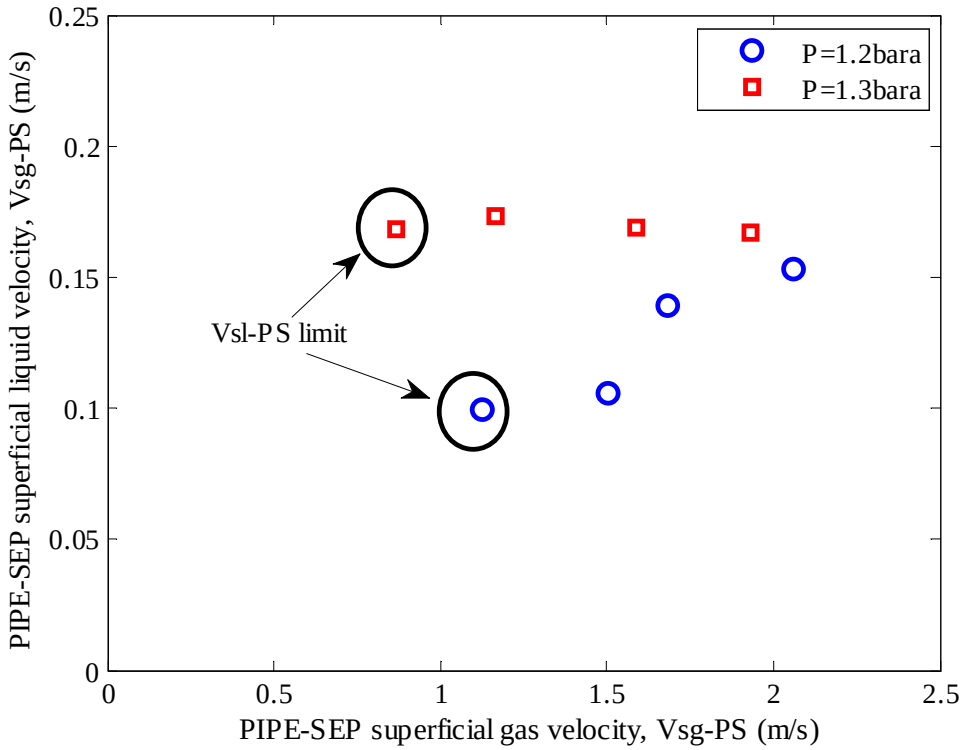

Figure 4-20 GCU operational envelope for Pipe-SEP under different back pressure

4.5.5 LCO and Liquid Separation Efficiency

Experiments have shown that LCO can come from two distinct forms: droplets and re-entrained liquid. In the swirled flow regime, the separated gas contains a large amount of discrete liquid droplets. Birmingham and Davies (1995) analysed the forces that act on a liquid droplet in a gas flow inside a separator and developed relationships that describe the time for a droplet to migrate the radial distance across the separator and the time that a droplet resides inside the separator. The migration and residence times determine whether the droplet strikes the radial wall of the separator or flows out with the gas flow. If the drop strikes the radial wall, it is likely to be separated from the gas flow. In contrast, droplets that reach the gas outlet become LCO.

As liquid loading increases, the separation performance will be dominated by re-entrainment of the liquid rather than the liquid mist. The liquid film becomes excessively thick, and blocks the annular space above the inlet. Gravity is the main driving force, and combines with a moderate centrifugal force and the wall shear stress

to pull the liquid against the flow of the gas. If the liquid loading is high enough, substantial amounts of liquid become LCO.

In the present study, measurement of the LCO flow rate in the swirled flow regime using the liquid extraction method was very difficult. The velocity of the mist in the Hi-SEP is high; most of the mist will travel through the Hi-SEP without be collected. Due to the possibility of incomplete extraction, the experimental data and developed explicit correlation for LCO are limited to the agitated flow regime only.

Figure 4-21 shows the LCO in a percentage of the inlet liquid flow rate for the agitated flow. The data were obtained under 1.2 bara operating conditions for three different liquid velocities. The valve on the Pipe-SEP liquid discharge line was throttled to achieve agitated flow. Unlike in the swirled flow regime, in which the droplet entrained fraction increased with gas velocity, in agitated flow, the LCO decreased with increasing gas velocity. However, a slight increase in the liquid velocity could result in as much as 10% more LCO, as indicated in Figure 4-21.

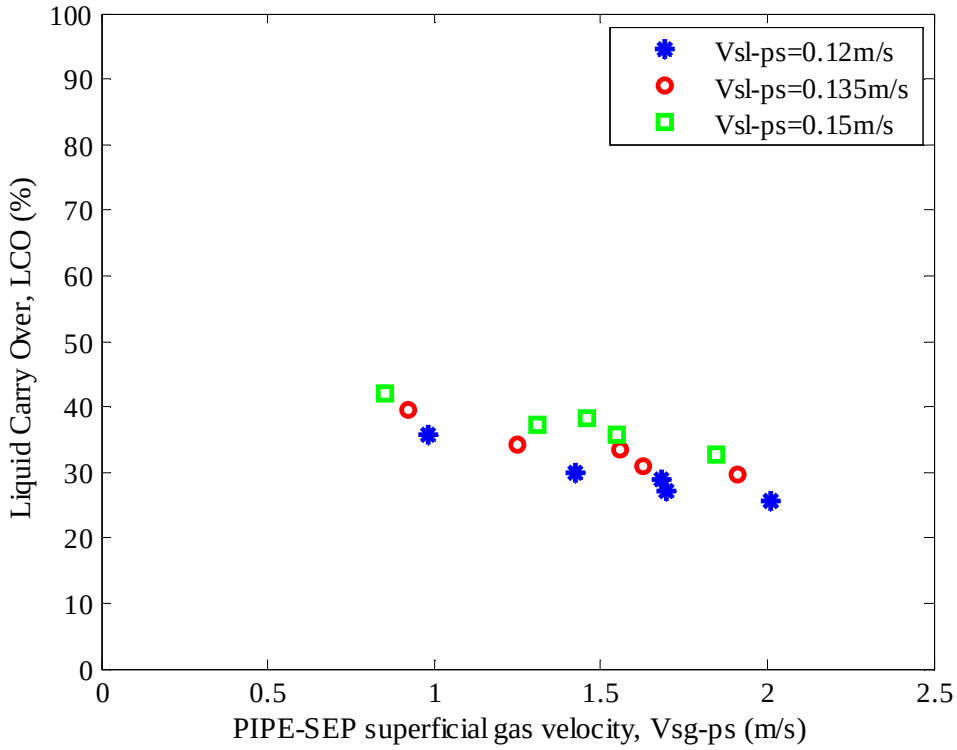

Figure 4-21 LCO of the Pipe-SEP

The liquid separation efficiency, η_L, is based on the mass flow rate of liquids into the Pipe-SEP, W_L, and the rate of LCO, W_{LCO}:

$$\eta_L = 1 - \frac{W_{LCO}}{W_L} \tag{4-6}$$

Figure 4-22 shows the liquid separation performance of the Pipe-SEP under agitated flow conditions. Increasing the gas velocity increased the back pressure, and thus decreased the ELL. As the ELL decreased, the quantity of liquid in the upper part of the Pipe-SEP was not sufficient to be carried to the gas outlet. Consequently, the separation efficiency increased as the gas velocity increased.

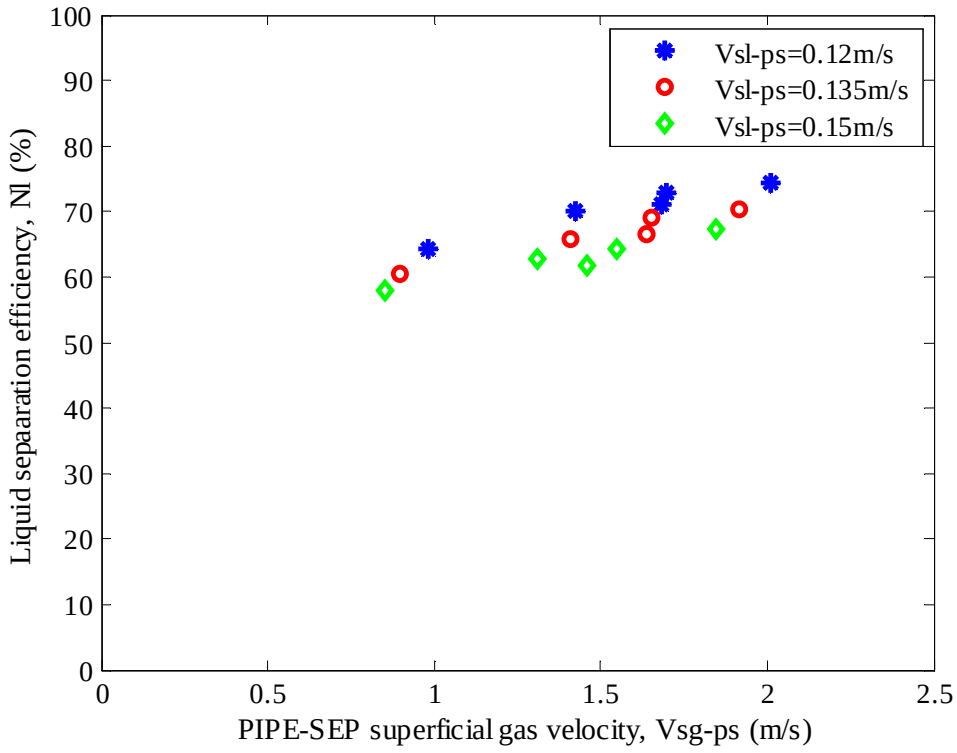

Figure 4-22 Liquid separation efficiency of the Pipe-SEP

4.5.6 GCU and Gas Separation Efficiency

Figure 4-23 shows the GCU in a percentage of the inlet gas flow rate. The data were obtained under 1.2 bara operating conditions for three different gas velocities. When liquid velocities, V_{sl-PS}, greater than 0.1 m/s, the GCU was approximately 3% to 5%. When the liquid velocity reduces below 0.1 m/s, gas blow-by occurred. The experiment

also illustrated that gas velocity had almost no effect on the GCU before any gas blow-by occurred.

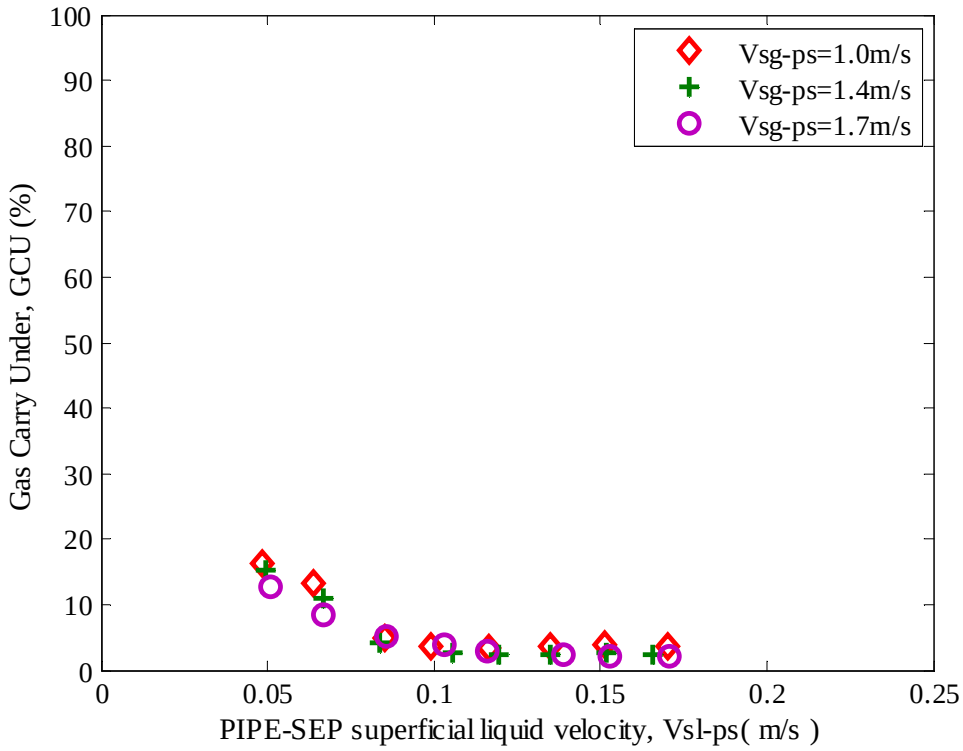

Figure 4-23 GCU of the Pipe-SEP

The gas separation efficiency, η_G, is based on the mass flow rate of gas into the Pipe-SEP, W_G, and the rate of GCU, W_{GCU}:

$$\eta_G = 1 - \frac{W_{GCU}}{W_G} \tag{4-7}$$

In Figure 4-24, the gas separation efficiency is plotted versus Pipe-SEP V_{sl-ps} for three different gas velocities. The gas separation efficiency increased when the liquid velocity increases. The efficiency curve increased sharply at low liquid flow rates, and then increased slightly until the separation efficiency reached approximately 97%. Similarly, gas flow only has an insignificant effect on the gas separation efficiency.

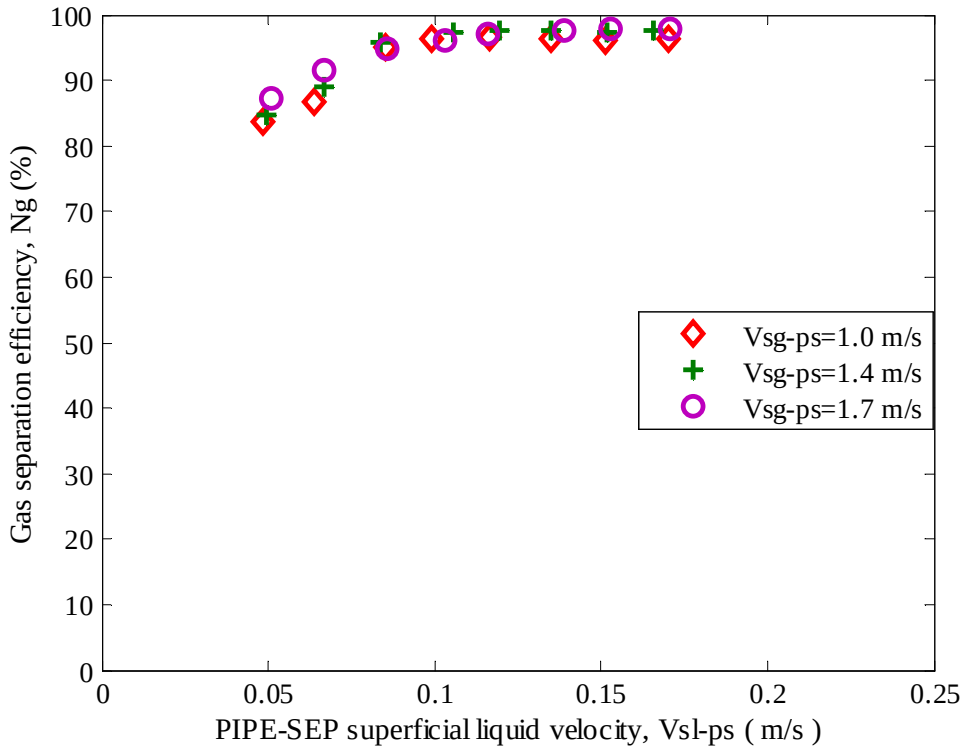

Figure 4-24 Gas separation efficiency of the Pipe-SEP

Since the GCU is strongly related to the ELL, Figure 4-25 plots the ELL vs GCU for all the tests under 1.2 bara. It can be seen that when the ELL is below 85mm, gas blow by occurs and the GCU increase significant. Furthermore, experimental observations indicate that maintaining an appropriate liquid level in Pipe-SEP improves the gas phase separation qualities.

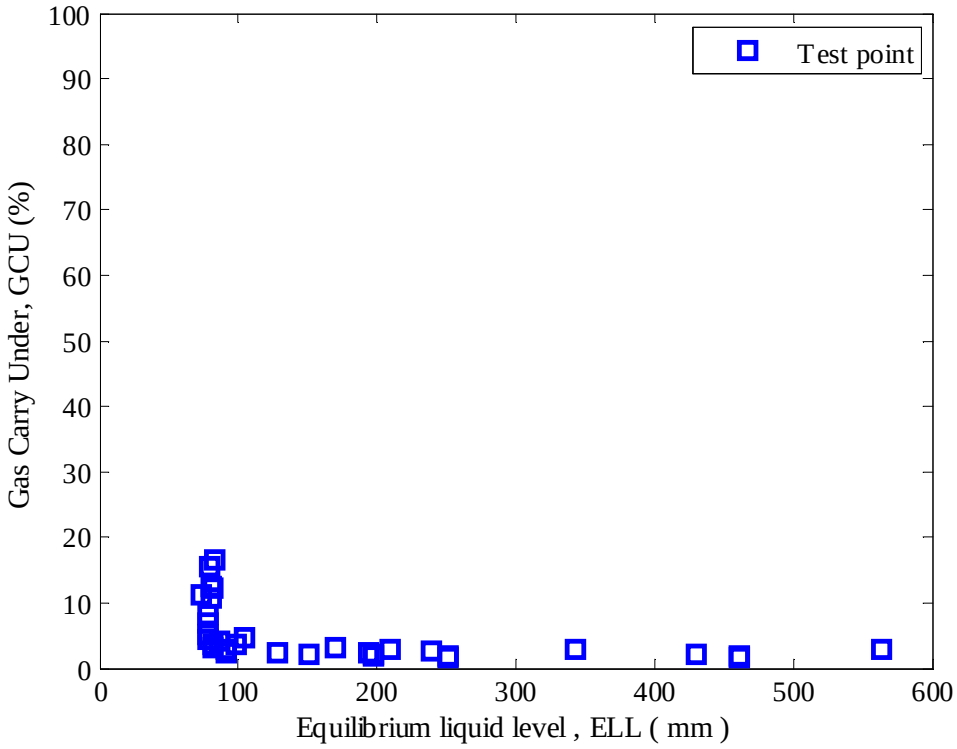

Figure 4-25 The relationship of GCU and ELL

4.5.7 Effect of Back Pressure on the GCU and Gas Separation Efficiency

Figure 4-26 shows the GCU under 1.4bara back pressure for different gas velocity. It shows that gas blow by for each test. Due to the fact that the volumetric flow rate of the gas blew by is similar for each liquid loading, the GCU decrease with increasing gas loading.

Similarly, Figure 4-27 shows the gas separation efficiency of the Pipe-SEP at 1.4bara. The efficiency decreases because of high back pressure. Even with high liquid loading, the separation efficiency is about 92%.

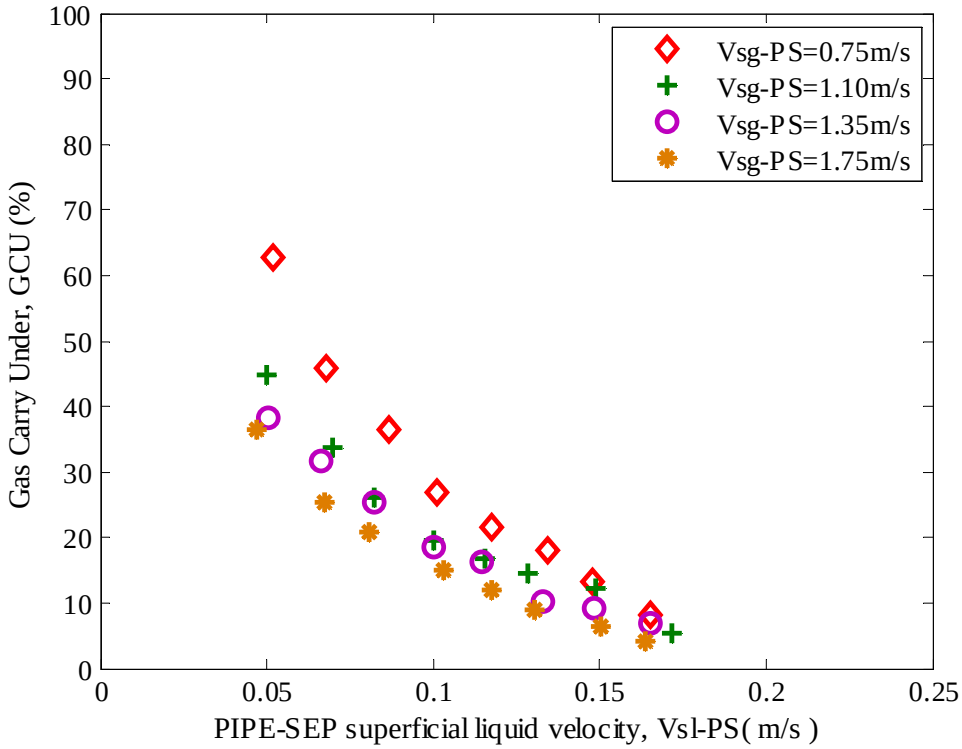

Figure 4-26 GCU of the Pipe-SEP at1.4bara back pressure

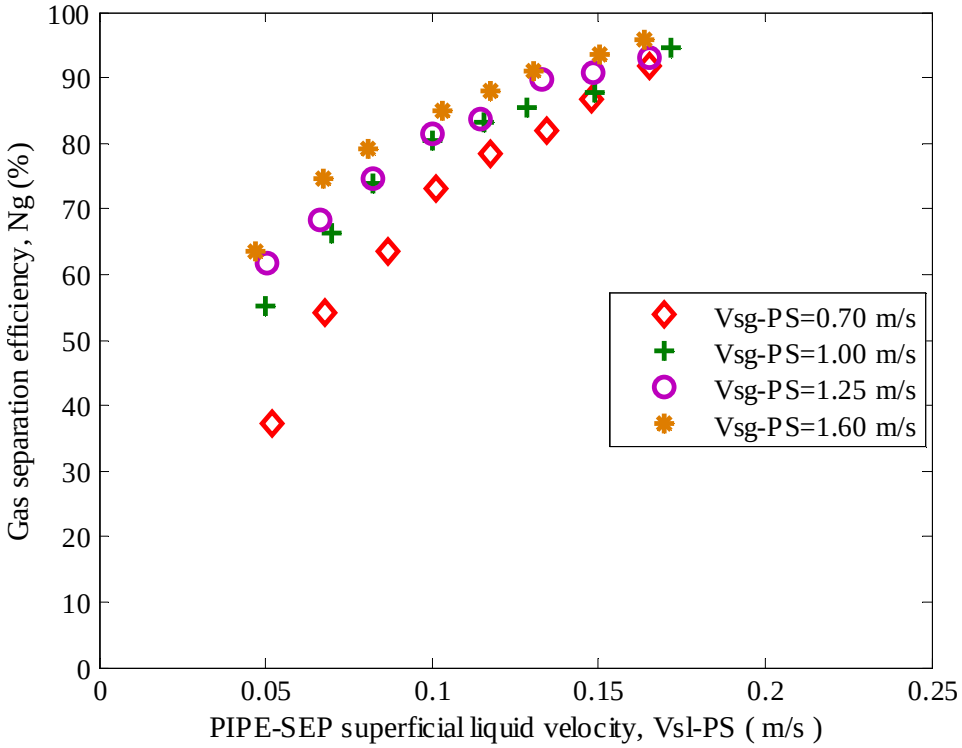

Figure 4-27 Gas separation efficiency of the Pipe-SEP at 1.4bara back pressure

Figure 4-28 shows the effect of the back pressure on the gas carry under for a fixed gas flow rate Q_g=120Sm^3/h. It can be seen that the gas carry under increases with back pressure. The reason is that the gas flow preferentially goes into the lower pressure side, since it does not have enough inertia to overcome the adverse pressure gradient (i.e. back pressure). The result is that a much higher quality gas flow has been carried under.

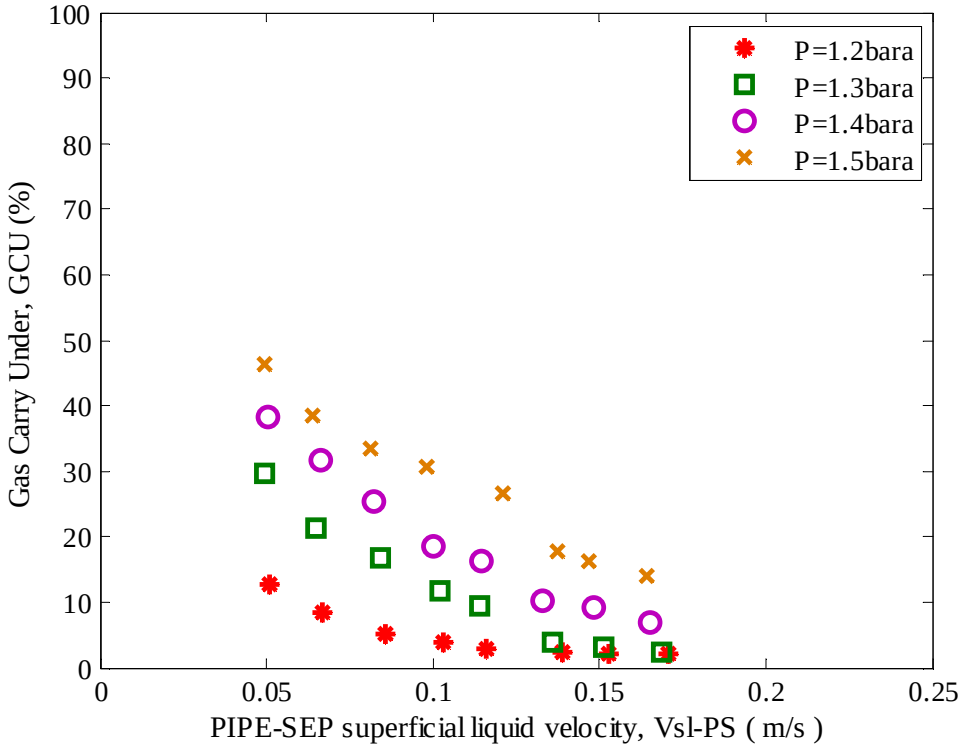

Figure 4-28 GCU for the Pipe-SEP at gas flow rate 120Sm^3/h

4.6 Key Findings of Experiments

Overall, the main findings from the Pipe-SEP experiments are:

- The LCO and GCU is flow region dependent. The ELL is a good indicator for the transition of the flow regime.
- When the ELL is above 600mm, the flow transmits from swirled flow to agitated flow. When the ELL is below 85mm, the flow transmits to gas blow by.
- When the flow regime is swirled flow, the LCO is dominated by droplets. The separation efficiency is determined by the cut size of the Pipe-SEP.
- When the flow regime is agitated flow, the LCO is dominated by liquid entrainment. The separation efficiency ranges from 60 to 80%. Moreover the

separation efficiency increases with the increasing of the liquid loading but decreases with the increasing of the gas loading.

- The GCU ranges from 3% to 5% before the gas blow by. After the onset of the gas blow by, the GCU can reach as high as 50%.
- The maximum gas superficial velocity in the Pipe-SEP is approximately 2.2m/s. After that, significant droplets will be carried out.
- To minimise LCO and GCU, the ELL must be maintained in a certain range. The pressure on the gas outlet and liquid outlet should be accounted to determine the ELL.

4.7 Pipe-SEP Model Development

Based on the experiment results, a simple performance model was developed and was able to predict the flow regime, gas separation efficiency, and liquid separation efficiency in the Pipe-SEP. The model takes account of the transition between three flow regimes: swirled, agitated, and gas blow-by. The process of analysing the flow regimes transitions starts from the ELL. Agitated flow is seen to occur in the entry section of the Pipe-SEP when the ELL is approximately above the inlet. Gas bow by onsets when the ELL approximately below the entrance of the liquid outlet. A generalised relationship for the ELL was developed as follows:

4.7.1 Equilibrium Liquid Level

When considering smooth flow in the test system, it was assumed that the mixture is homogenous for the calculation of fluid properties. The test system is given in Figure 4-29. A balance of the pressure on the Pipe-SEP ($P_{Pipe-SEP}$), the Hi-SEP (P_{Hi-SEP}), and the UF KOV (P_{UF-KOV}) yields

$$P_{Pipe-SEP} = P_{Hi-SEP} + \Delta P_G = P_{UF-KOV} + \Delta P_L \quad (4\text{-}8)$$

where ΔP_G and ΔP_L are the pressure drop in the Pipe-SEP gas and liquid discharge lines, assuming that the hydrodynamic interaction in the gas and liquid phases is negligible.

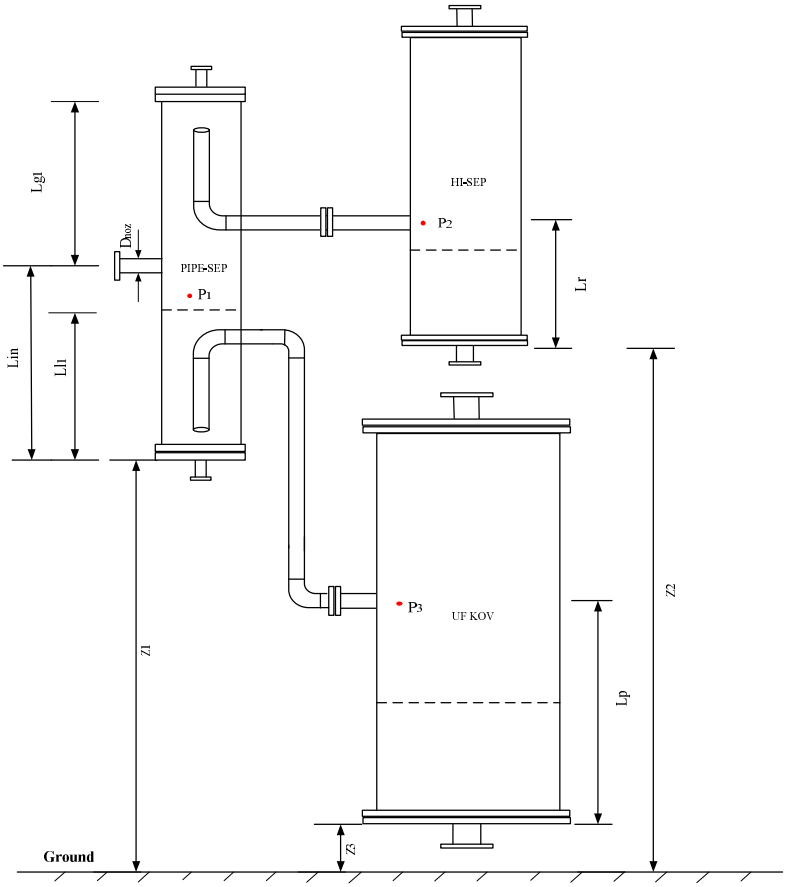

Figure 4-29 Schematic of the Pipe-SEP, Hi-SEP and UF KOV test system

The pressure drop in the liquid discharge line can be determined as

$$\Delta P_L = -\rho_L g\left(Z_1 + L_{L1} - Z_3 - L_p\right) + \sum P_{f,L} + \frac{f_{L1} L_{L1}}{D_{PS}} \frac{\rho_L v_{L1}^2}{2} \tag{4-9}$$

where Z_1 is the elevation difference between Pipe-SEP and UF KOV; L_{L1} is the liquid level in Pipe-SEP; Z_3 is the elevation of UF KOV and L_p is the inlet height of UF KOV. v_{L1} is the liquid velocity in the Pipe-SEP.

$\sum P_{f,L}$ is the total frictional pressure loss in the liquid discharge line, which includes the frictional losses in the pipe segments and pipe fittings.

$$\sum P_{f,L} = \frac{f_{L2}(L_{L\_pipe} + L_{L\_fitting})}{D_{PIPE}} \frac{\rho_L v_{L2}^2}{2} \tag{4-10}$$

f_{L1} is the liquid friction factors for the lower section, and f_{L2} is the liquid discharge line of the Pipe-SEP, respectively. They are evaluated using Blasius (1913) equation:

$$f_{Li} = 0.3164 Re_{Li}^{-0.25} \quad \text{i=1, 2} \tag{4-11}$$

The Reynolds number is calculated from the actual velocity and hydraulic diameter of the liquid phase.

$$Re_{L1} = \frac{\rho_L D_{Pipe-SEP} v_{L1}}{\mu_L} \qquad Re_{L2} = \frac{\rho_L D_{PIPE} v_{L2}}{\mu_L} \tag{4-12}$$

The pressure drop in the gas line can be determined as

$$\Delta P_G = \rho_G g(Z_1 + L_{L1} - Z_2 - L_r) + \sum P_{f,G} + \frac{f_{G1}(L_{g1}+L_{in}-L_{L1})}{D_{PS}} \frac{\rho_G v_{G1}^2}{2} \tag{4-13}$$

where Z_2 is elevation of Hi-SEP and L_r is the inlet height of Hi-SEP.

$\sum P_{f,G}$ is the total frictional pressure loss in the gas line, which includes the frictional losses in the pipe segments and pipe fittings.

$$\sum P_{f,G} = \frac{f_{G2}(L_{g1}+L_{in}-L_{L1})}{D_{PIPE}} \frac{\rho_G v_{G2}^2}{2} \tag{4-14}$$

f_{G1} and f_{G2} are the gas friction factors for the upper section and the gas discharge line of the Pipe-SEP, respectively. They are also evaluated in the conventional manner:

$$f_{Gi} = 0.0056 + 0.5/Re_{Gi}^{0.32} \quad \text{i=1 ,2} \tag{4-15}$$

Thus, the ELL, L_{L1}, can be solved as follows:

$$L_{L1} = \frac{P_{UF-KOV} - P_{Hi-SEP} + \sum P_{f,L} - \sum P_{f,G} - \rho_L g(Z_1 - Z_3 - L_p) - \rho_G g(Z_1 - Z_2 - L_r) - \frac{f_{G2}(L_{g1}+L_{in})\rho_G v_{G1}^2}{D_{PS}\ 2}}{g(\rho_L + \rho_G) - \frac{f_{L1}\rho_L v_{L1}^2}{D_{PS}\ 2} - \frac{f_{G2}\rho_G v_{G1}^2}{D_{PS}\ 2}} \tag{4-16}$$

4.7.2 Transition between Flow Regimes

Previous experimental studies have shown the flow conditions where swirled flow is observed, the liquid level is below the inlet of the Pipe-SEP. As the liquid flow rate increases, the liquid level rises above the inlet and tends to block the inlet flow. At first, the flow becomes irregular and agitated flow appears at the inlet region. When the liquid flow rate is high enough, sufficient liquid is maintained in the Pipe-SEP, and the liquid is lifted up, which leads to Agitated flow. At higher gas flow rates, the back

pressure in the Pipe-SEP increases due to the Bernoulli Effect, which will cause the liquid level to decrease. Thus, the transition between swirled and agitated regimes can be defined as occurring when the ELL rises above the inlet. Fully developed agitated flow can be expected if the liquid level exceeds the Zero Net Liquid Flow level (ZNLFL), which was proposed by Arpandi *et al.*, (1996) to describe the conditions that ELL is located above the inlet, while gas simply passes through the liquid column without any LCO. The definition of the gas blow by flow regime is straight forward. When the ELL is fall below the entrance of the liquid outlet, the gas blow by occurs.

4.7.3 Swirled Flow Model

The swirled flow in Pipe-SEP is very similar to the annular flow as described by Sawant *et al.*, (2008), a portion of the liquid flows adjacent to the wall as a film and the remaining liquid flows as entrained droplets through the gas core. Therefore, some correlations which have been developed for annular flow will be adopted here to estimate the characteristics of the swirled flow in the Pipe-SEP.

4.7.3.1 Swirled film height

It is useful to know the height of the swirled film, because the FER is designed to eliminate the film. The elevation of the swirled film above the inlet is determined mainly by the balance between gravity and the force that is generated by the radial pressure gradient. A correlation was proposed by Rosa *et al.*, (2001) to calculate the height of the film, h, which is expressed as

$$\frac{h}{\sqrt{A_{PIPE}}} = CRe^{n}\sqrt{Fr_n}(1+f)^{-0.25} \tag{4-17}$$

where A_{PIPE} is the area of the inlet pipe, R_e is the Reynolds number that corresponds to the diameter of the inlet pipe, Fr_n is the Froude number, which can be calculated as $Fr_n = \frac{V_{mix}^2}{gD}$, V_{mix} is the inlet mixture velocity, and f is the gas to liquid volumetric ratio, Q_G/Q_L. The constant C and the power n were obtained from experimental data fitting (see Appendix C). In the present study, $C = 2.35$ and $n = 0.022$ were used.

In the swirled flow regime, the liquid film is swept up around the wall of the Pipe-SEP. The gas flow rate has the dominant influence on the thickness of the film. Dobran (1983)

proposed an average representation for the thickness of the continuous liquid layer in annular flow and is adopted in this work to estimate the thickness of swirl film in the Pipe-SEP

$$\frac{\delta_B}{D} = 140 N_L^{0.433} Re_C^{-1.35} \tag{4-18}$$

where

$$N_L = [\frac{gD^3\rho_L(\rho_L-\rho_C)}{\mu_L^2}]^{1/2} \tag{4-19}$$

$$Re_c = u_c\rho_c D/\mu_g \tag{4-20}$$

δ_B is the film thickness; N_L is the two-phase Grashof number; u_c is the superficial gas velocity in the Pipe-SEP and ρ_C is the homogeneous core density.

4.7.3.2 Entrainment fraction

The entrainment fraction in the swirled flow in Pipe-SEP is defined as the fraction of the liquid droplets that flow through the central gas core. Sawant *et al*. (2009) developed the entrainment fraction correlation as follows

$$E = E_{max}\tanh[a(We - We_{cr})^{1.25}] \tag{4-21}$$

$$a = 2.31 \times 10^{-4}\, Re_f^{-0.35} \tag{4-22}$$

$$E_{max} = 1 - \frac{Re_{fflim}}{Re_f} = 1 - \frac{Re_{ffOE}+f(Re_f-Re_{ffOE})}{Re_f} \tag{4-23}$$

$$We = \frac{\rho_g u_{sg}^2 D}{\sigma}[(\rho_L-\rho_g)/\rho_g]^{1/4} \tag{4-24}$$

$$Re_f = \frac{\rho_f u_{sf} D}{\mu_f} = \frac{\rho_f u_{f\delta_B}}{\mu_f} \tag{4-25}$$

where E_{max} is the maximum possible entrainment fraction and We_{cr} is the critical Weber number that refers to the critical gas velocity at the onset of entrainment

$$We_{cr} = \frac{\rho_g u_{sg,cr}^2 D}{\sigma}[(\rho_L-\rho_g)/\rho_g]^{1/4} \tag{4-26}$$

Therefore, the total mass of liquid dispersed in the central gas core is known as

$$W_D = hD_{Pipe-SEP}\delta_B E \quad (4\text{-}27)$$

If the size distribution of the dispersed droplets is known, then the cut size, LCO and separation efficiency of Pipe-SEP can be estimated. This part will be discussed in Chapter 5.

4.7.4 Agitated Flow Model

4.7.4.1 Liquid entrained fraction

It is suggested that when the ELL in the Pipe-SEP is above the inlet, agitated flow will develop. Agitated flow is characterised by the presence of large and irregular waves. The amplitude of the waves decrease as the increasing of the gas flow rate. If the liquid flow rates are small, the waves are small, and virtually no liquid is carried in the gas flow. If the liquid flow rate adds up or a critical gas velocity is reached, the waves reach the top of the Pipe-SEP, which results in flooding. Adequate analytical solutions have not been developed to describe the complex agitated flow in the separator. However, many reports have been published in relation to churned flow during vertical upward flow in pipes. The fraction of liquid which entrains in the gas phase can be estimated. The available data show that during churned flow, as the superficial gas velocity increases the entrained fraction decreases. In the present study of agitated flow in the Pipe-SEP, the lower part of the Pipe-SEP could be treated as single phase liquid flow, and the GCU was less than 2%. The upper part of the Pipe-SEP was evaluated using a simple dimensional equation that has been developed by Azzopardi and Wren (2004) to describe the entrained fraction, E_f. They found that the diameter of the pipe has no effect on the entrained fraction; for velocities greater than 5m/s, there was a small correlation between the entrained fraction and the gas superficial velocity, and also with the liquid superficial velocity.

$$E_f = 0.47 v_{sg}^{0.16} v_{sl}^{0.35} \quad \text{for } v_{sg} < 5m/s \quad (4\text{-}28)$$

$$E_f = 0.6 v_{sl}^{0.35} \quad \text{for } v_{sg} > 5m/s \quad (4\text{-}29)$$

4.7.4.2 Zero Net Liquid Flow Level

In the present study, ZNLF is used as the criterion to describe the transition between agitated and fully developed agitated flow. Visual observations show that there is a minimal liquid level at which the flow progresses to fully developed agitated flow. If the liquid level is below the minimal value, the liquid flow will be churned up but the liquid will not reach the top of the Pipe-SEP. Experiments were performed under steady-state conditions (see Appendix C) and the correlation for the ZNLFL was developed to quantify the minimal liquid loading for each gas loading as follows:

$$ZNLFL = L_{inlet} + 345.7 - 123.9 \times V_{sg-ps} \quad (4\text{-}30)$$

4.7.4.3 Gas blow-by model

Normally, the operational flow rates of the Pipe-SEP should be selected carefully and account for the downstream operating conditions. The GCU used in Eq. (4-31) is an empirical correlation, which was derived from the experimental data fitting shown in Figure 4-23.

$$GCU = -500 * \Delta P^2 + 1445\Delta P - 976 \quad (4\text{-}31)$$

where ΔP is the pressure difference between the gas and liquid discharge outlets.

As for the LCO in the gas blow-by model, it can be estimated using the same method in the swirled flow region.

4.7.5 Calculation Procedure

The separation of fluids in the Pipe-SEP depends not only on the geometry of the Pipe-SEP itself but also on the pressures in the downstream discharge lines and the status of the fluid flowing in the inlet pipe. Owing to all these controlling factors, predicting the performance of the separator is not easy. A predictive algorithm that is depicted in Figure 4-30 is proposed for the simulation of the Pipe-SEP. The algorithm consists of three sections: the input, Flow Regime (FR)-loop, and output section. The input to the algorithm is divided into four groups. The geometrical parameters consist of the diameter and length of the Pipe-SEP, and of the associated inlet and outlet pipes. The fluid properties and operating conditions consist of case-specific data such as flow rates,

pressure, and density. A complete separation (LCO=0 and GCU=0) is assumed initially to estimate the ELL and ZNLFL. Subsequently, the flow regime is determined on the basis of the ELL criteria.

The FR-loop consists of three segments, which correspond to the three flow regimes. The first segment is agitated flow, which is expected to occur when the ELL exceeds the ZNLFL. In this segment, the GCU flow rate is assumed to be 2 Sm^3/h, which is the value that was determined under agitated flow experiment. The LCO can be determined by applying Eq. (4-28) and Eq. (4-29). Then, the pressure loss in the Pipe-SEP, liquid discharge line, and gas discharge line can be obtained on the basis of the properties of the mixture. If the new ELL meets the criteria for agitated flow, and $\frac{|Ll_{1_{new}} - Ll_1|}{Ll_1} < 0.1$, then the calculated result will be the output. If the new ELL does not meet the criteria, then the procedure will iterate in the FR-loop by suggesting a new ELL for the variable until convergence is reached. The swirled flow model is defined as occurring when the ELL is below inlet. In this segment, the GCU flow rate is assumed to be 2.7 Sm^3/h and the LCO can be obtained from Eq. (4-17) to Eq. (4-27). The Gas Blow-by model is defined as occurring when the ELL is below the liquid discharge line inlet. The LCO is estimated with the same Eq. (4-17) to Eq. (4-27) of swirled flow model and the GCU is iteratively determined by Eq. (4-31).

The model procedure can be summarised as follows:

1. Assume complete separation of gas and liquid. Initial LCO and GCU are set to zero.
2. Determine ELL, Ll_1.
3. Determine the flow regime.
4. Calculate LCO and GCU.
5. Recalculate ELL, $Ll_{1_{new}}$.
6. Check that the flow regime is correct and $\frac{|Ll_{1_{new}} - Ll_1|}{Ll_1} < 0.1$ to determine convergence.
7. Repeat steps 3 to 6 with $Ll_{1_{new}}$ until convergence is reached.

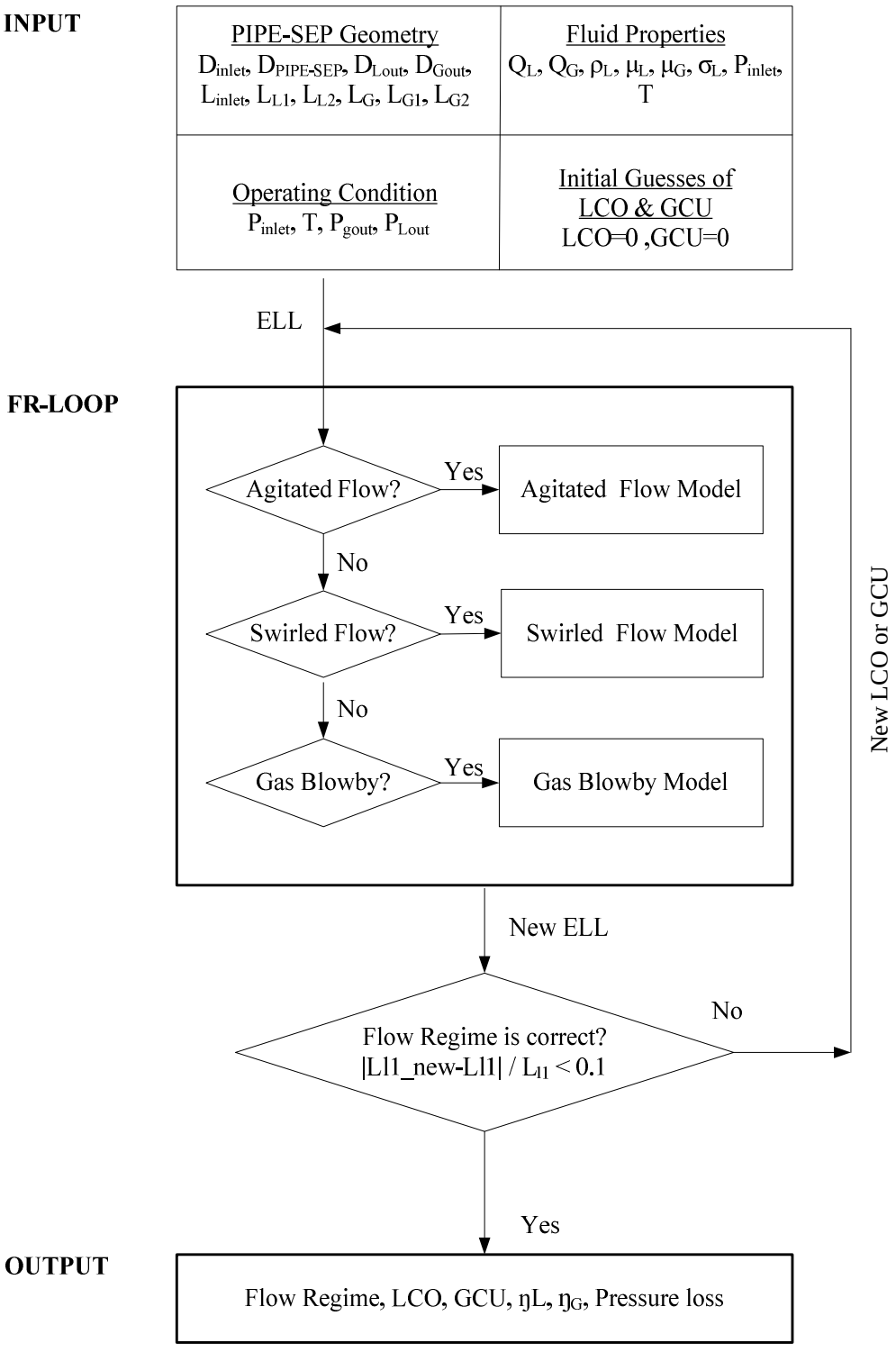

Figure 4-30 Pipe-SEP predictive algorithm

4.8 Predictive Model Validation

4.8.1 Pipe-SEP Flow Regime Map

The predictive model has been validated with available experiment data. Figure 4-31 shows the predicted flow regimes in the Pipe-SEP. The predicted flow regimes can be compared with the experimental observations (Figure 4-15). For low liquid flow rates, the model predicted the boundary of gas blow-by–swirled flow well and agreed with the visual observations. As the liquid flow rate increased, swirled flow began to transition to agitated flow. Although fully developed agitated flow is not predicted in Figure 4-31, the predictions of the transition of agitated flow back to swirled flow were in excellent agreement with the experimental observations.

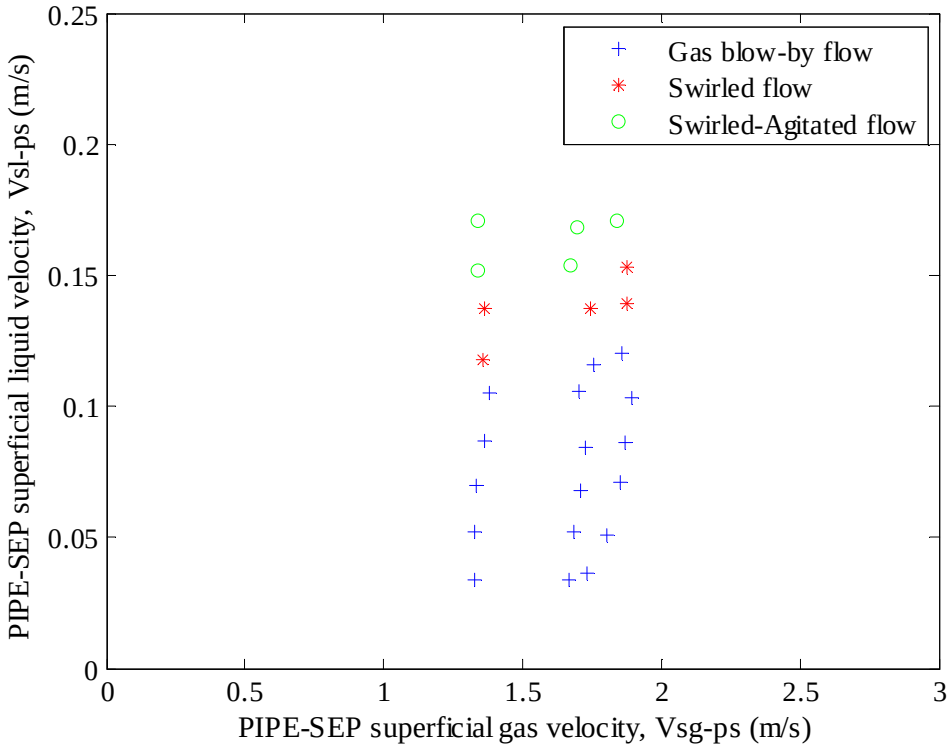

Figure 4-31 Predicted Pipe-SEP flow regimes

4.8.2 Comparison of the ELL

The comparison of the model prediction with the experiment data of ELL for 1.2 bara operating condition is shown in Figure 4-32. For the swirled flow and agitated flow region, ELL is above 85mm, the model prediction agrees well with the experiment data.

As the ELL fall below 85mm, the model over-predicts the level. This over-prediction indicates that the assumption of homogenous flow may not be valid when significant amount of gas has been carried out in the gas discharge line.

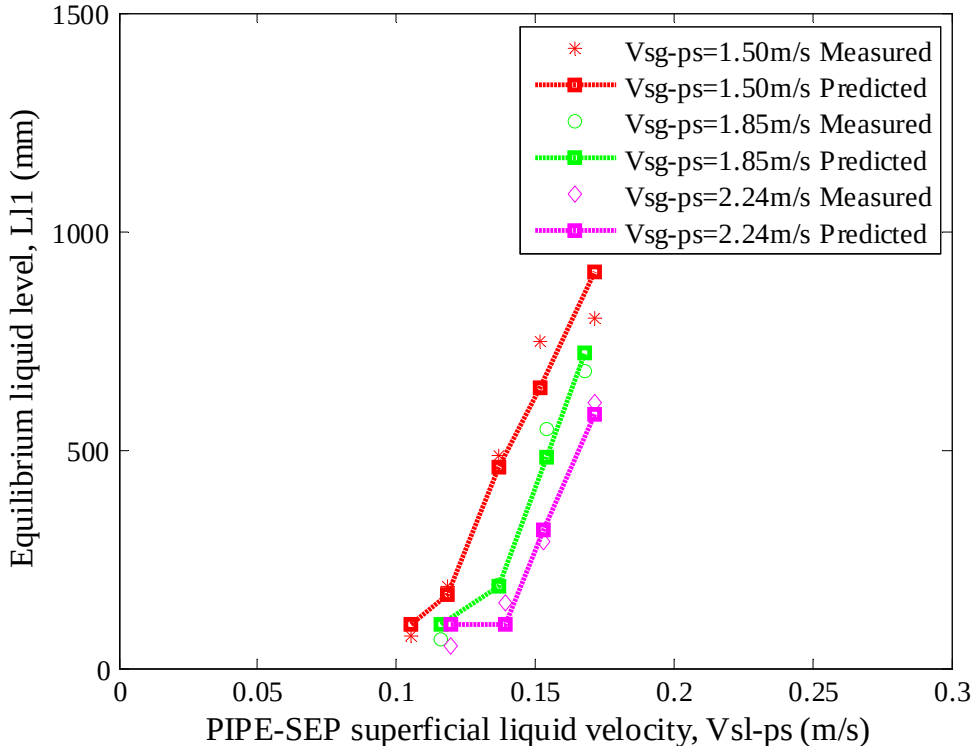

Figure 4-32 Comparison of the equilibrium liquid level

4.8.3 Operational Envelope

The operational envelope represents the flow conditions for the onset of LCO and GCU. Any point on the LCO operational envelope has zero LCO. Any point on the GCU operational envelope has 3Sm^3/h GCU (was predefined in this particular experiment condition). The predicting model has been used to determine the operational envelope. The trial and error procedure is similar to the experimental procedure and is described as follows:

1. The superficial gas velocity, V_{sg-PS}, is selected at a required value.
2. Assume a low superficial liquid velocity, V_{sl-PS}.
3. Follow the procedure of the Pipe-SEP model described in section 4.7.5, calculate the LCO and GCU.

4. Check the LCO, whether is just above zero or not. Check the GCU, whether is just below 3Sm^3/h.
5. Repeat steps 2 to 4 with a new V_{sl-PS} until the LCO above zero or the GCU below 3Sm^3/h.
6. Repeat the whole procedure for different V_{sg-PS} to obtain the operational envelope for LCO or GCU

The comparison of the predicted operational envelope for the LCO and GCU and the experiment observation is shown in Figure 4-33. The prediction is represented by the dashed line. It can be seen that in the higher V_{sg-PS} region, the model predicted accurately the liquid velocity limit for the LCO. However in the lower V_{sg-PS} region, the model over-predicted the liquid velocity limit. For the GCU, the model results are all slightly above the experiment results. Overall, the model can capture the trend of the operational envelope well and can provide the information for early engineering design.

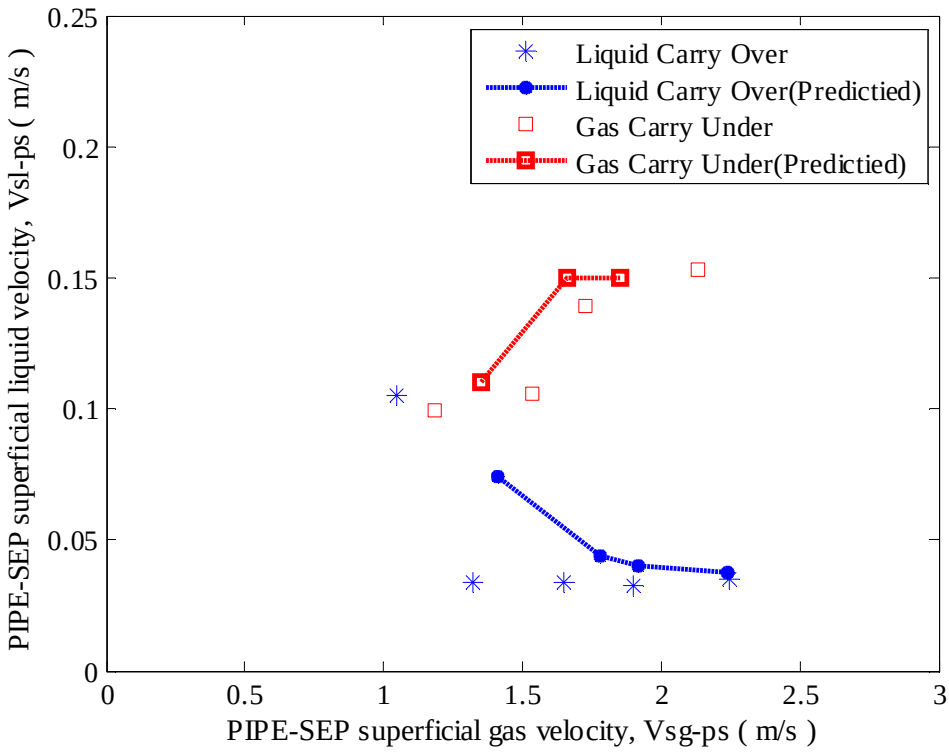

Figure 4-33 Comparison of the operational area

4.8.4 Separation Efficiency

For the liquid separation efficiency under swirled flow and gas blow by condition where no experiment data are available, only the predictions are presented. In Figure 4-34, the liquid separation efficiency is calculated for V_{sg-ps} =1.35m/s. Due to the volumetric flow rate of the LCO increases slightly with liquid loading, the liquid separation efficiency increases.

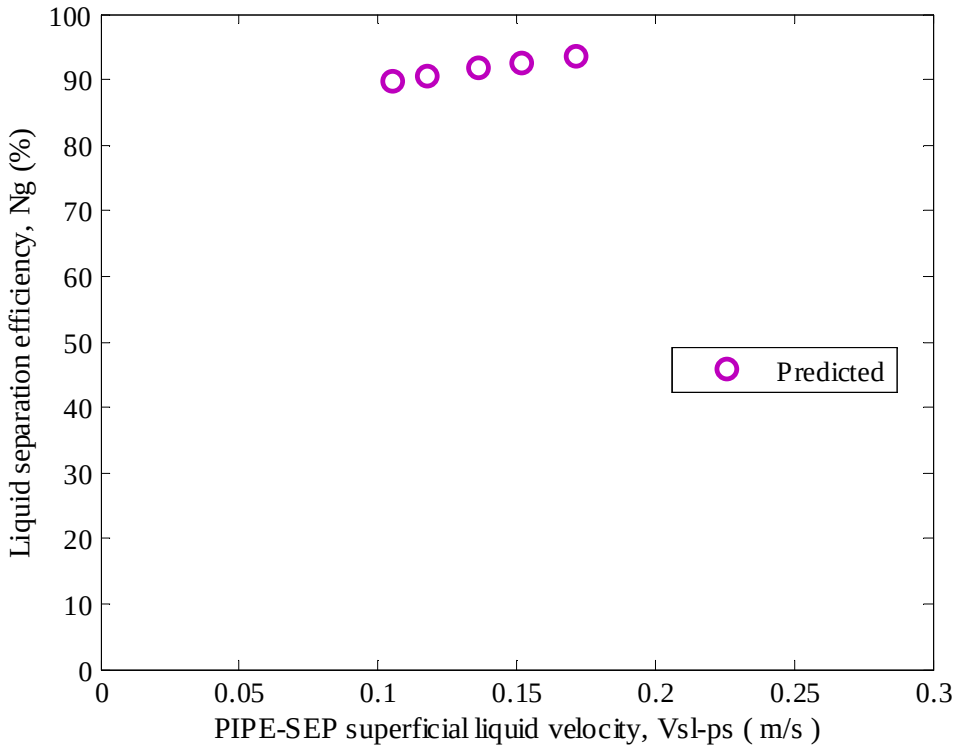

Figure 4-34 Liquid separation efficiency prediction

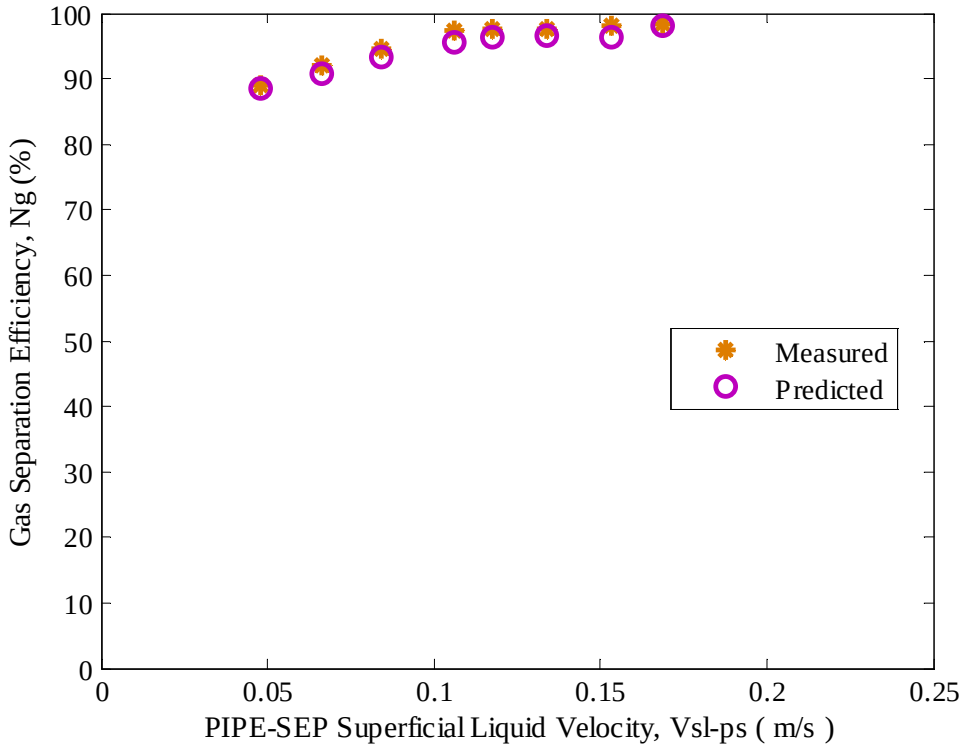

Figure 4-35 Comparison of gas separation efficiency between the Pipe-SEP model and data obtained at $V_{sg\text{-}PS}$=2.0m/s

Comparison of the predicted and measured gas separation at $V_{sg-ps} = 2.0$m/s is shown in Figure 4-35. The predictions agree well with the experimental data.

4.9 Summary

Prediction of the flow regime and separation efficiency in a Pipe-SEP is challenging because the behaviour of the gas–liquid mixture inside the separator is affected by many factors, such as flow characteristics, mixture properties, geometry of the separator, and downstream conditions. Consequently, fundamental understandings of the physical phenomena that occur and appropriate interpretation of experimental results are required to model the Pipe-SEP successfully. A semi-empirical model has been proposed by defining the flow regime in the Pipe-SEP, and applying a conservation equation to the pressure loss. Despite the approximations to homogenous flow, the computed result agrees well with the experimental data. In addition, the following conclusions can be drawn from the present study.

1. The separation efficiency depends on the flow regime, which is affected by the flow parameters and Pipe-SEP geometry. Under normal operating conditions, flow is generally swirled flow and the LCO increases with gas flow rate; however, as the liquid flow rate being added up to a certain level, the flow starts to change to agitated flow. The most interesting results were obtained for agitated flow, during which the LCO decreases as the gas flow rate increases. In practice, the agitated flow and gas blow by flow are undesirable and should be avoided with the help of an appropriate design. In the next chapter, only the swirled flow will be studied.
2. Prediction of the loss of pressure is very important and plays an important role in the present model. Homogenous flow was assumed for the calculation and this might cause the computed results to deviate somewhat from the experimental data.
3. The geometry of the discharge line affects pressure losses, and consequently the flow regime and separation efficiency. A long liquid discharge line or one with a small diameter is not preferable from the point of view of pressure losses, whereas a discharge line with a large diameter is difficult to fit inside the Pipe-SEP, or affect the separator performance. Further studies by means of numerical simulation are required in this area and will be presented in chapter 5.

5 NUMERICAL SIMULATION OF THE COMPACT GAS/LIQUID SEPARATOR

In this chapter results are presented on the modelling and simulation of the gas and droplet flow in the Pipe-SEP. Firstly, the numerical techniques which were used to determine the simulation strategy are discussed. Afterwards the simulation results of the gas flow field of the laboratory prototype Pipe-SEP are presented. The effect of the 'L' outlet section, gas inlet velocity and separator diameter on the flow field is studied. Finally, the Discrete Phase Model (DPM) simulations are performed for the assessment of the best modelling approach for Pipe-SEP. Both the classic cyclone separator models and scaling rules are compared with the simulation results. The best model is selected and combined with an optimization procedure to form a Pipe-SEP design model.

5.1 Introduction

The cyclonic separators have been subject to extensive experimental and numerical study because of their importance for the processing industries. The swirling flow in separators can either induced by proper designed inlets or swirl generators. The swirling flow exhibits high level of turbulence and strong anisotropy features. Although several empirical and semi-empirical correlations have been proposed in the literature (see Sec. 3.5) for predicting the pressure drop, cut size and separation efficiency, most models are focused on cylinder-on-cone cyclones, which are installed with a tangential inlet. Due to the reason that there is inadequate knowledge of the flow behaviour inside the Pipe-SEP, the objective of the present chapter is to perform CFD simulation studies to evaluate the influences on the Pipe-SEP's performance, by altering the operational parameters and the device dimensions .

5.2 CFD Approach

The literature review on CFD modelling of cyclonic separators (Sec. 3.5) revealed that the modelling approach for separators operating at low particles loading is generally

based on an Euler-Lagrange approach, and it will be used in the present study. Also as proposed by Newton (2007), if one phase dominates the volumetric flow rate in the vessel, then it should be possible to model the section of the vessel in which the highest volume fraction for the primary phase can be found. For such cases, the upper section of the Pipe-SEP will be modelled. Two assumptions are made in the present simulation study. The liquid droplets are simulated with one-way coupling method within the flow field of the model, and moreover the droplets do not interact with each other, and do not coalesce or break up. Due to the fact that the major objective of current study regards conditions with high efficiency Pipe-Hi-SEP systems operating with high GVF (>90 Vol%) incoming flow, the assumptions can be deemed to be valid. More to the point, the second stage separator Hi-SEP is usually subject to more than 95 Vol% gas flow. Another thing need to mention is that the Hi-SEP has similar geometry with the Pipe-SEP. To get realisable results with limited computer effort, only the Pipe-SEP will be simulated in detail. The Hi-SEP simulation will be used to validate the scale rule. The detailed components within the CFD simulations and the reason for selecting them are explained in the following sub-sections.

5.2.1 Computational Domain and Grid

The computation domains for the Pipe-SEP were developed based on the prototype used in previous experimental work (see Sec. 4.2). The Pipe-SEP section above the liquid level is simulated. The liquid level should always be kept below the inlet (200mm in this case). To explore the effects of the outlet section on flow profile, two cases without the presence of the “L” outlet in Pipe-SEP called Pipe-SEP I, and one with the “L” outlet called Pipe-SEP II were developed, as shown in Figure 5-1 and Figure 5-2. The diameter of the Pipe-SEPs was 150mm. The diameter and the length of the “L” outlet in Pipe-SEP II were 50mm and 500mm, respectively. The dimensions of the computation domain and observation planes employed in this study are also given in Figure 5-1 and Figure 5-2. Four plotting sections are used to reveal the flow filed inside Pipe-SEP as given by Table 5-1.

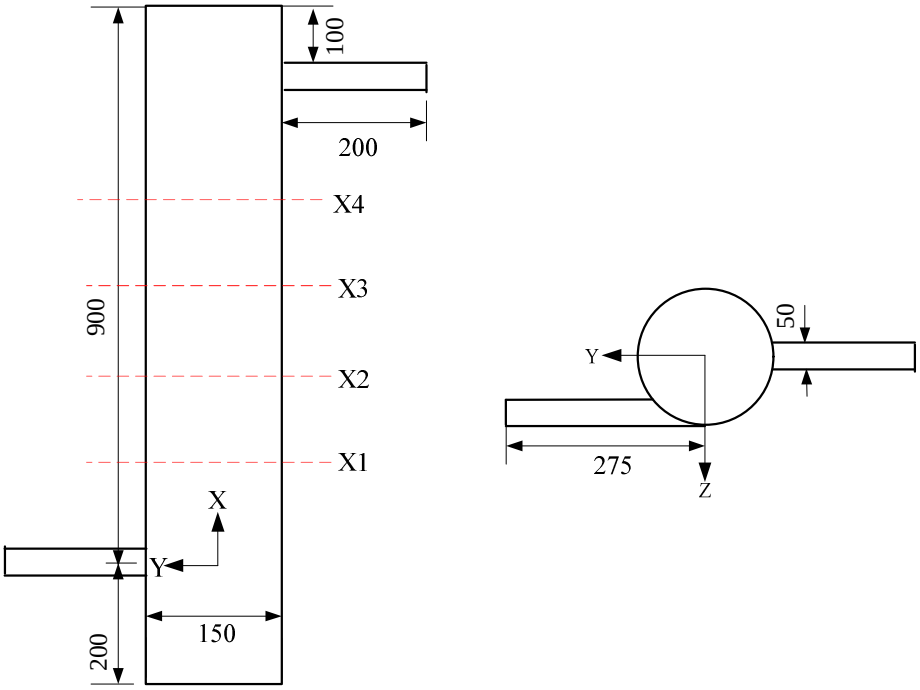

Figure 5-1 Schematic of the Pipe-SEP I geometry and coordinate definition

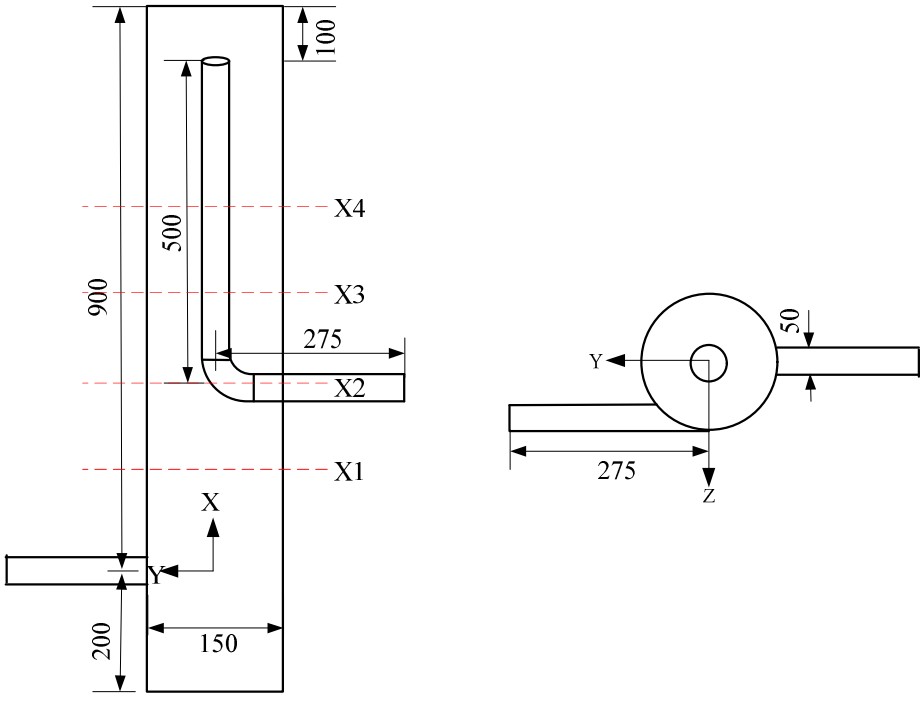

Figure 5-2 Schematic of the Pipe-SEP II geometry and coordinate definition

Table 5-1 The locations of each section within the plots

Section	X_1	X_2	X_3	X_4
X(mm)	150	300	450	600
X/D	1	2	3	4

5.2.2 Selection of Turbulence Model

The numerical simulation quality depends largely on the type of turbulence modelling applied for approximation of turbulence. There are various turbulence models available in ANSYS FLUENT to simulate the rotational turbulent flow within the Pipe-SEP. The literature review on CFD modelling of cyclonic separators (Sec. 3.5) revealed that the k-ϵ models are not appropriate for strongly swirling flows. Both of the RSM model and LES model have been widely applied and provide accurate predictions of the swirl flow pattern and velocity profile. Since the RSM model can yield reasonable results with limited computer resources, the RSM will be used in the present study to reveal the flow field.

5.2.3 Selection of the Discretization Schemes

Kaya and Karagoz (2008) and ANSYS FLUENT recommended the QUICK scheme for the momentum discretization. Kaya and Karagoz (2008) also recommended the Presto scheme for pressure and SIMPLE algorithm for pressure-velocity coupling. In terms of the discretising the Reynolds' stress equation, the first order upwind method is suggested, but Shukla *et al*., (2011a) suggested the second order one in terms of the kinetic energy equation including the study of the dissipation rate. Table 5-2 lists the numerical schemes used in the present simulations.

Table 5-2 The numerical settings for the present simulation

Pressure discretization	PRESTO
Pressure velocity coupling	SIMPLE
Momentum discretization	QUICK
Turbulent kinetic energy	Second order upwind
Turbulent dissipation rate	Second order upwind
Reynolds stress	First order upwind

5.2.4 Boundary Conditions

A velocity inlet is applied at the inlet boundary, with an air inlet velocity of $V_{gas-inlet}$ having an initially value of 10 m/s, corresponding to an air inlet volumetric flow rate Q_g=145 Sm^3/h. The air properties used were: air density 2.5 kg/m^3, viscosity 1.73E-5 Pa·s, with a resulting Reynolds number 72254 based on the inlet diameter and the velocity of inlet nozzle. The turbulence intensity was determined as recommended by FLUENT 12 guidelines, using the following equation:

$$I = 0.16Re^{-0.125} \quad (5\text{-}1)$$

The turbulence intensity $I$is 3.95% and the hydraulic diameter equals the diameter of the inlet nozzle. The near-wall treatment and the effect of the wall roughness were modelled using non-Equilibrium wall functions. The out flow is gas outlet and its operational pressure is set as 0 Pa.

5.2.5 Grid Independency Study

The grid was generated in ANSYS Workbench. The Pipe-SEP I consists of purely trihedral grids. The Pipe-SEP II consists of trihedral grids at the separator body and tetrahedral grids at the gas outlet section. Figure 5-3 shows the grid configuration that was used for the simulation study. The Pipe-SEP I grid domain contains 169955 elements. The Pipe-SEP II grid domain contains 414369 elements.

The grid independence investigation was carried out within the Pipe-SEP I and Pipe-SEP II simulations. In order to make sure the final simulation results are insensitive to the grid condition, three levels of grids were applied as shown in Figure 5-4 and Figure 5-5.

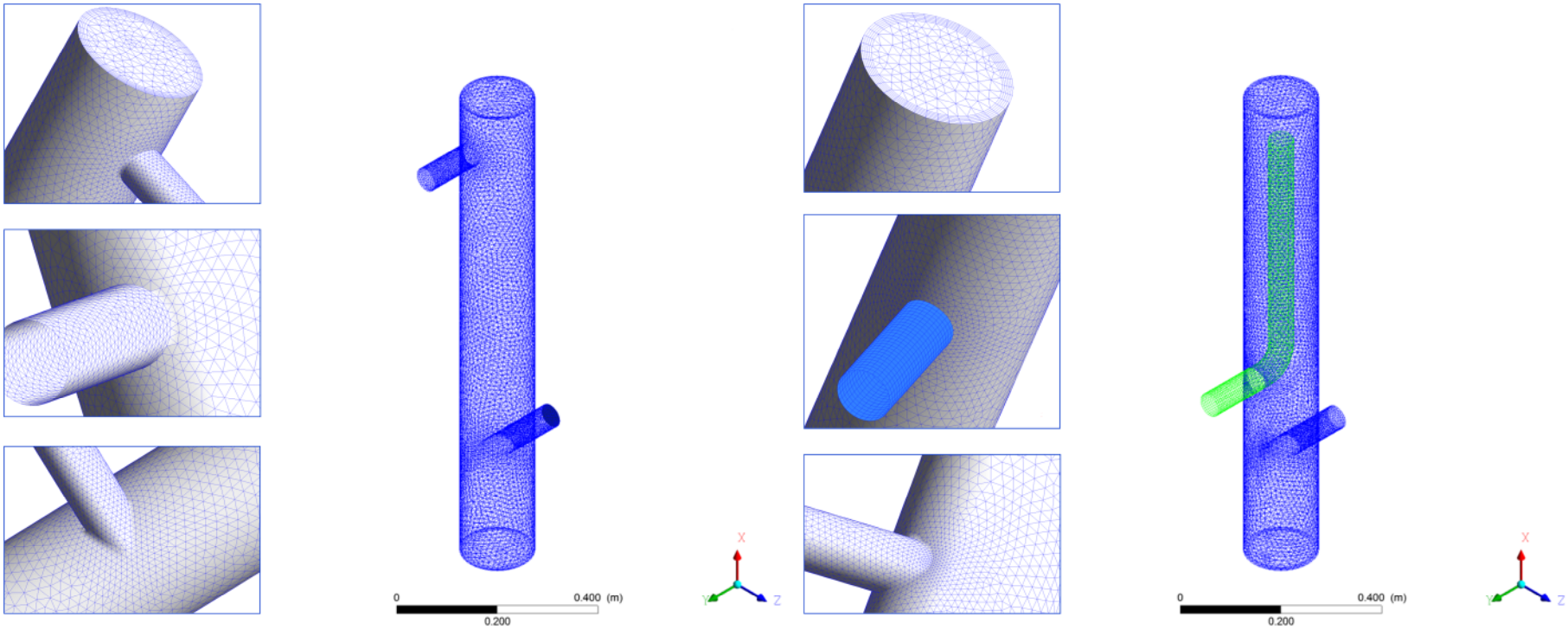

(a) Pipe-SEP I

(b) Pipe-SEP II

Figure 5-3 Grid of Pipe-SEP I and Pipe-SEP II

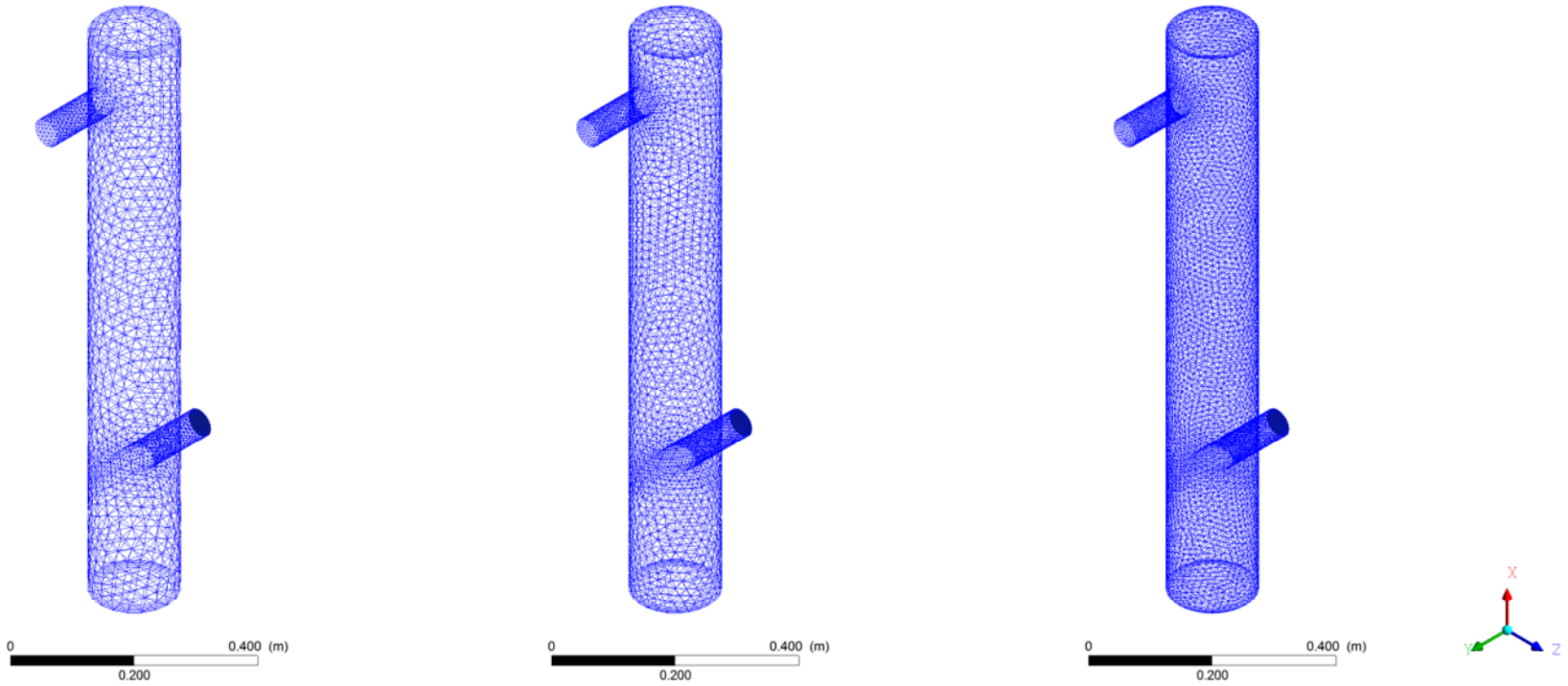

(a) Coarse grid (b) Medium grid (c) Fine grid

Figure 5-4 Three different levels of Pipe-SEP I grid domains

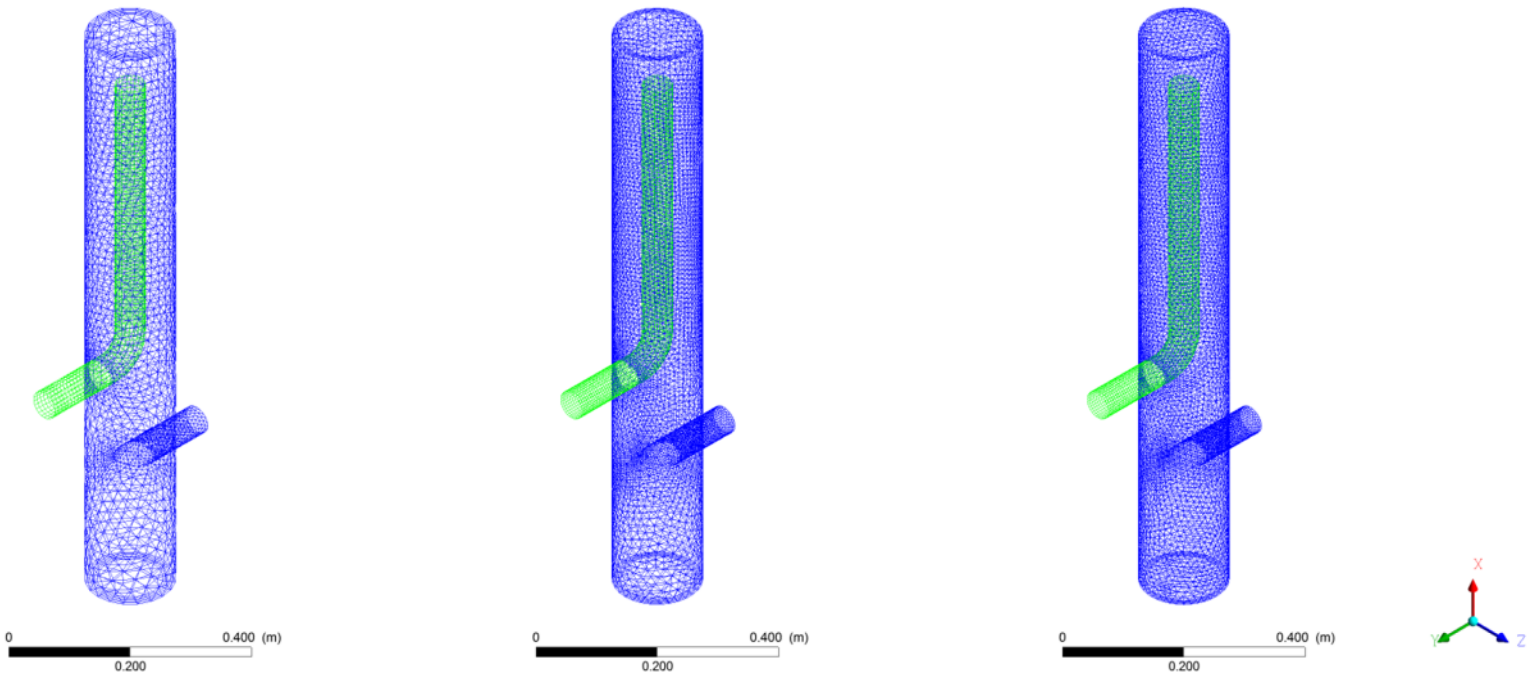

(a) Coarse grid (b) Medium grid (c) Fine grid

Figure 5-5 Three different levels of Pipe-SEP II grid domains

The simulated results of tangential velocity profile at X2 for Pipe-SEP I and Pipe-SEP II are shown in Figure 5-6 and Figure 5-7, respectively. It can be seen that the results for the three grids are very similar to each other in the centre region. In the near wall region, as the grid density increase, the result of medium grid and fine grid are very close.

Furthermore, Table 5-3 lists the grid details, which indicate that the outcomes for the fine and medium grids have very close values, particularly for the Eu values and cut size D_{50}. Due to the better performance, even though the medium grid is able to offer a good prediction, to obtain the best results and avoid unnecessary uncertainties, the fine grid was adopted for all the simulations.

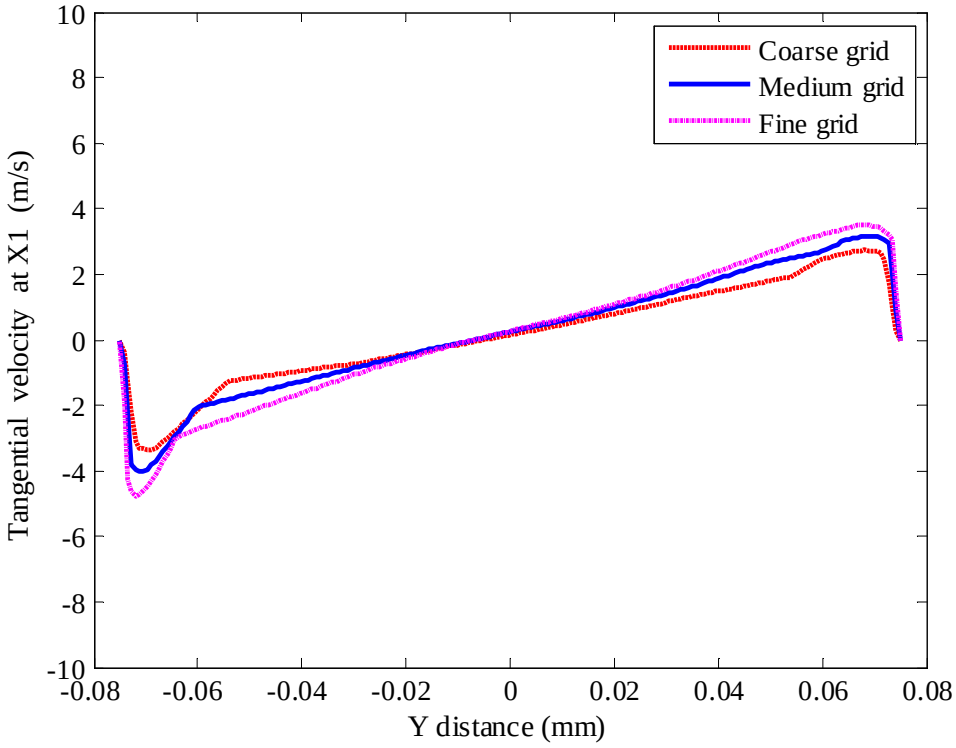

Figure 5-6 The tangential velocity profile at X2 for Pipe-SEP I with different grids

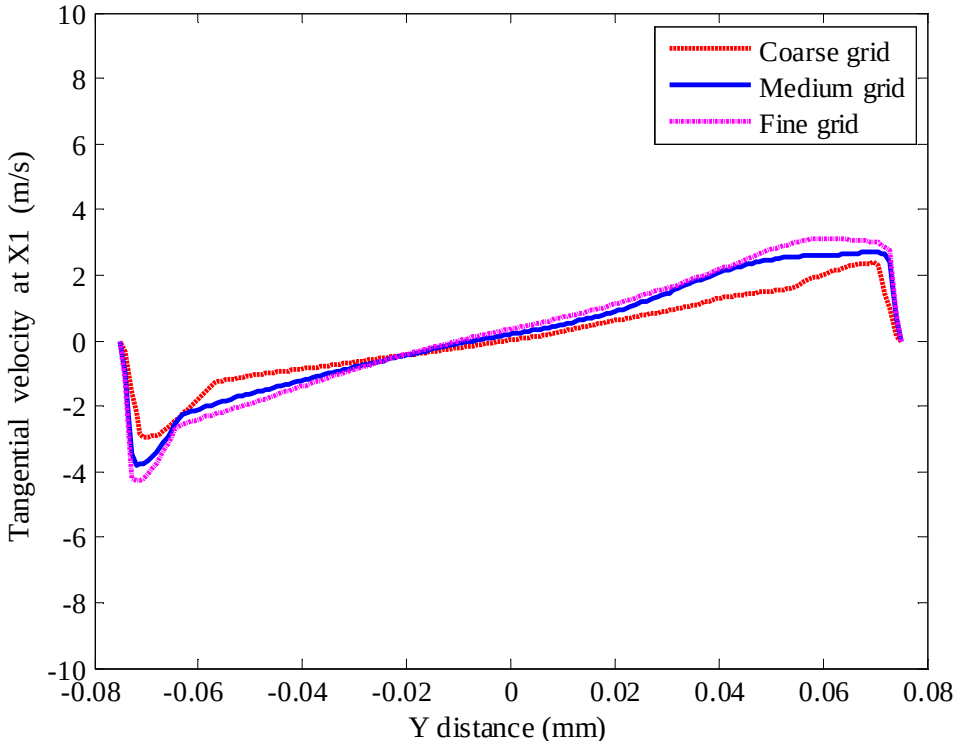

Figure 5-7 The tangential velocity profile at X2 for Pipe-SEP II with different grids

Table 5-3 Grid details of the Pipe-SEP in the simulation

	Pipe-SEP I			Pipe-SEP II		
	Elements	Eu	D_{50}	Elements	Eu	D_{50}
Coarse mesh	33903	0.8616	8.7	96354	0.9188	6.2
Medium mesh	93658	0.8536	9.2	298357	0.9113	6.9
Fine mesh	169955	0.8584	8.9	414369	0.9146	6.3

5.2.6 Convergence Criteria

As for the convergence criteria, two aspects are adopted. Firstly, the solution is assumed to be converged with pre-set scaled residuals of 1E-07. Secondly, the gas velocity at gas outlet should become constant and stable.

5.3 Gas Flow in the Pipe-SEP

In this section, results are presented on the simulation of the pressure field and gas flow filed in Pipe-SEP I and Pipe-SEP II. The effect of the gas outlet section, gas inlet velocity and separator diameter on the flow profile is discussed.

5.3.1 Pressure Field

The static pressure results based on time averaging are shown in Figure 5-8, and the position is chosen to be at section Z equal to 0, for the gas inlet velocity $V_{gas-inlet}$ =10m/s. The Pipe-SEP I (Figure 5-8 left) show that the static pressure increases as the radius increase from the centre of the separator to the wall. Because of the high rotational speed of the vortex, a low-pressure region would form at the centre part. For the Pipe-SEP II (Figure 5-8 right), the static pressure also increases with increasing radius. It can be seen that the presence of the "L" outlet section yields a larger pressure loss across the Pipe-SEP II.

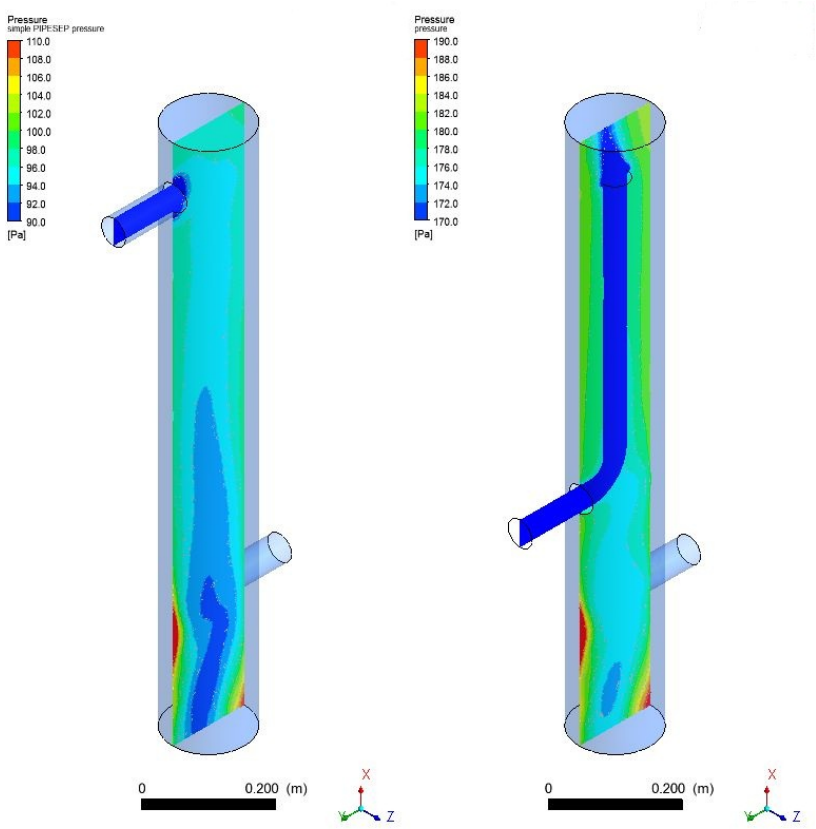

Pipe-SEP I Pipe-SEP II

Figure 5-8 Contours plots for the static pressure at the X-Y plane (Z=0)

Corresponding to the contours plots, the time averaged static pressure results at section X1, X2, X3 and X4 (see Table 5-1) for Pipe-SEP I and II are shown in Figure 5-9 and Figure 5-10, respectively. It is clear that the static pressure is strongly dependent upon the radial position, and has its maximum value at the wall. As the swirling component

decays in the axial direction as a result of wall friction, the radial pressure gradient $\frac{\partial P}{\partial r}$ which is directed to the separator centre also decreases. That means the pressure curve tends to flatten. However, the gradient in the axial direction is insignificant in the Pipe-SEP I.

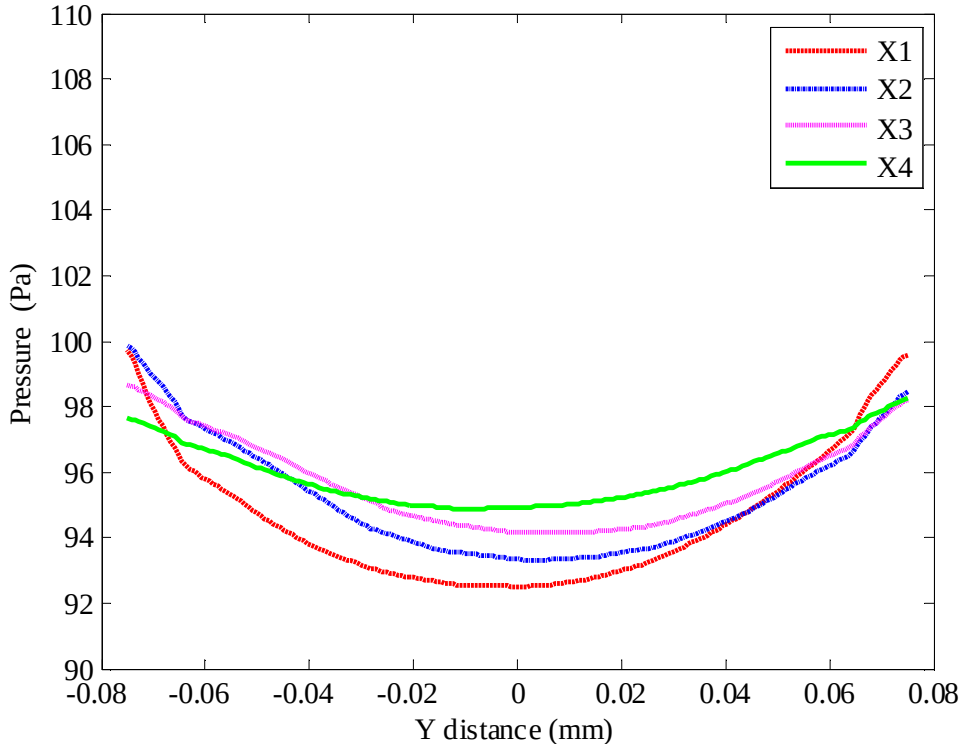

Figure 5-9 Radial contribution of the static pressure of various parts on the X-Y plane (Z=0) of Pipe-SEP I

As discussed in Sec.4.3, the pressure losses in the cyclonic separator with low particle loading are often negligible compared to the losses in the outlet section. In the present case, the pressure loss through Pipe-SEP I gas outlet is nearly 97.7 Pa, which is 25 times larger than the losses in Pipe-SEP I body. In Pipe-SEP II, the "L" outlet section contributes an extra 80 Pa to the total pressure loss, which results in a total pressure loss of 177.7 Pa for the Pipe-SEP II. The Euler number which used to characterise Pipe-SEP can be calculated as 0.86 and 0.91 for Pipe-SEP I and Pipe-SEP II, respectively.

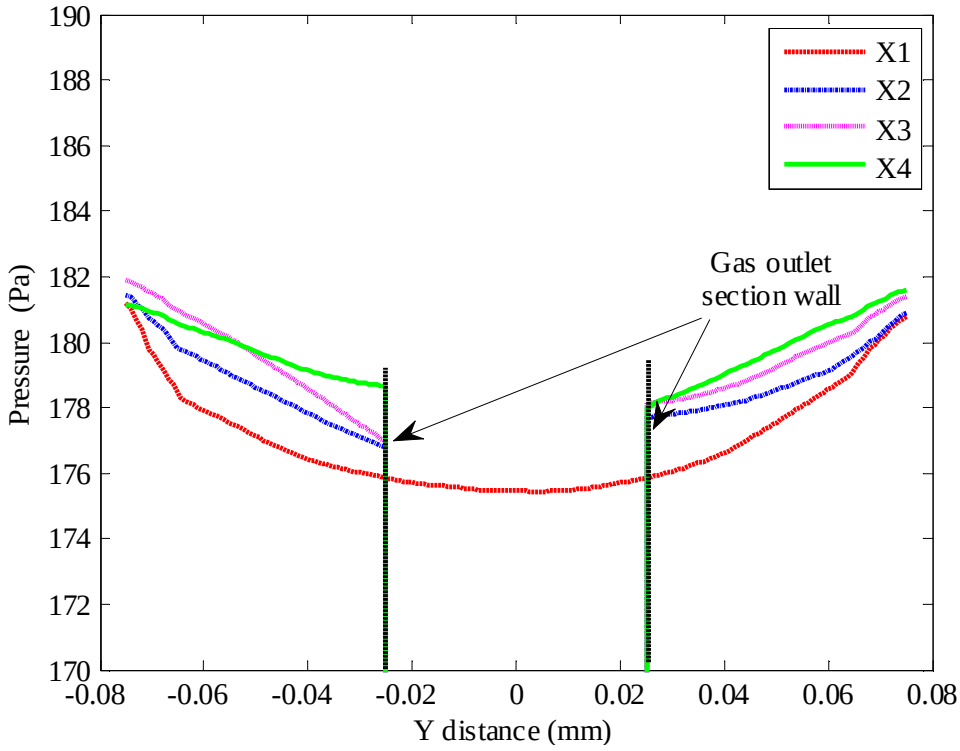

Figure 5-10 Radial contribution of the static pressure of various parts on the X-Y plane (Z=0) of Pipe-SEP II

5.3.2 Tangential Velocity

The mean tangential velocity fields of Pipe-SEP I and II are depicted through contours in Figure 5-11, at the gas inlet velocity $V_{gas-inlet}$ equal to 10m/s. As the flow rotates with the same angular velocity, the flow radial tangential profile in the Pipe-SEP can be generally described by a solid body vortex. In the Pipe-SEP I, a region with a low tangential velocity was discovered, marked in blue at the centre of the separation space and it appears to be asymmetrical. At the near-wall the tangential velocity takes a higher value. The tangential velocity values do not stay constant within the axial direction. In the Pipe-SEP II, this region with low tangential velocity is occupied by the gas outlet section. Strongly swirl flow can be seen at the entrance of the gas out section.

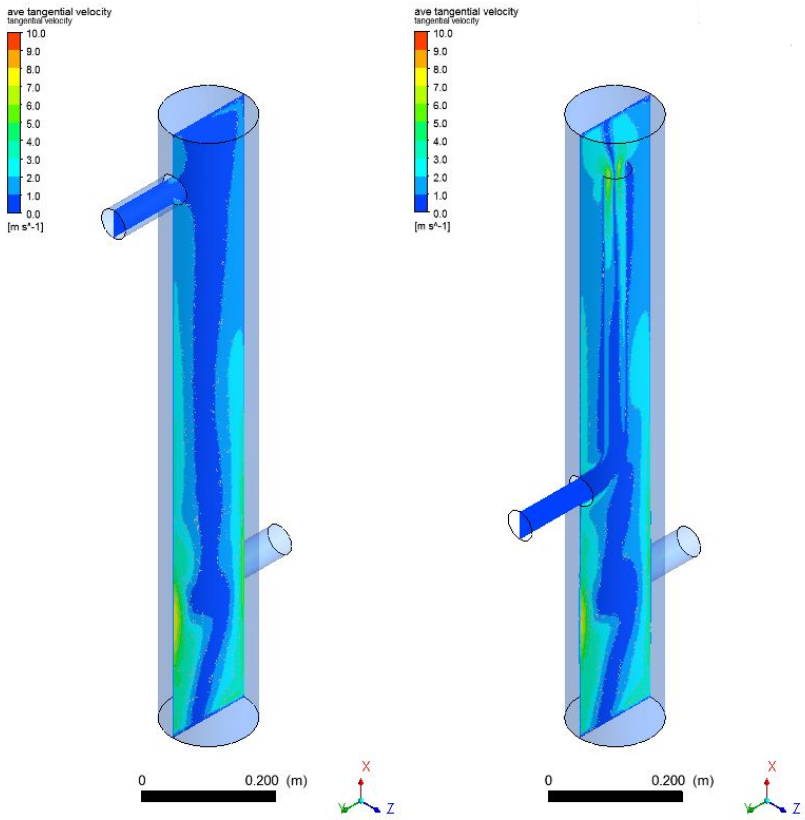

Pipe-SEP I Pipe-SEP II

Figure 5-11 Contours plots for the tangential velocity at X-Y plane (Z=0)

Figure 5-12 and Figure 5-13 show the plot of time averaged tangential velocity at sections X1, X2, X3 and X4 (see Table 5-1) for Pipe-SEP I and II, respectively. In Figure 5-12, the tangential flow profile of Pipe-SEP I exhibits a strong similarity along the axial direction. The forced vortex region dominates the separation space, which implies that the tangential velocity increases with increasing radius with the n value equal to -1. The values of the tangential velocity decline rapidly at the near wall region after the peak, which is the behaviour of the solid body type vortex as mentioned in Sec. 3.2. These data also show that the tangential velocities at the upper sections (X2, X3, X4) show a better symmetrical distribution.

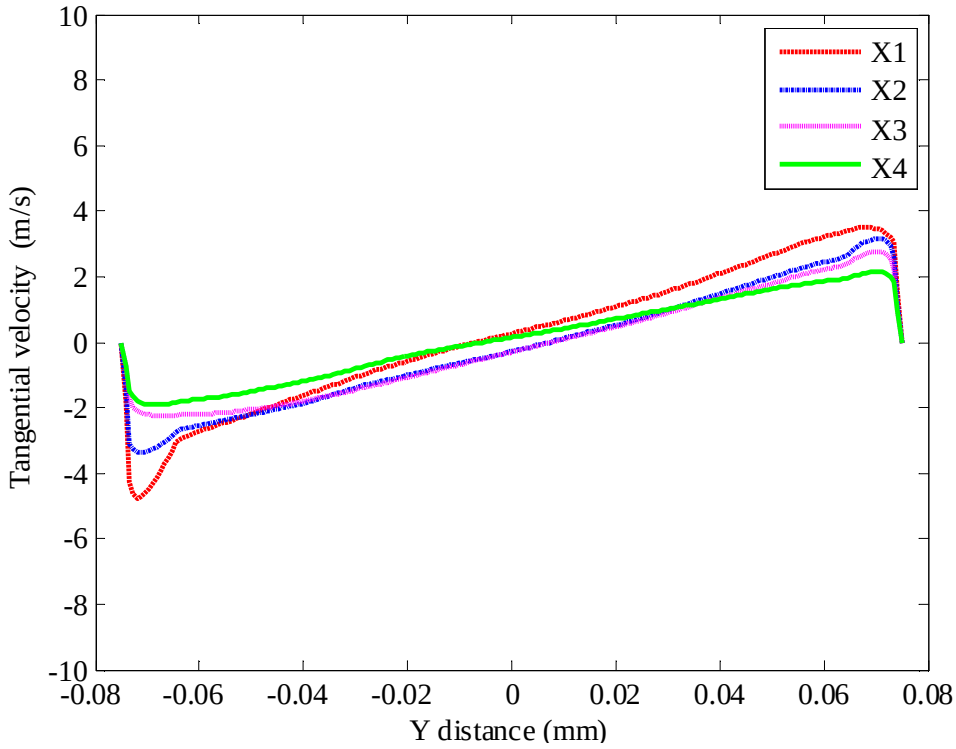

Figure 5-12 Plot of the radial contribution of the tangential velocity of various parts on the X-Y plane (Z=0) of Pipe-SEP I

The tangential velocity profiles of the Pipe-SEP II in Figure 5-13 indicate that the tangential velocity within the annulus separator space is almost the same as in the Pipe-SEP I, while the swirl flow nears the wall of gas outlet section vanished. Therefore, as expected, the gas outlet will not reduce the effective separation area. It can also be observed that the swirl is present in the gas outlet section, which is indicated by the dotted black line. The swirl flow in the outlet has other effects, which are important for next stage separator.

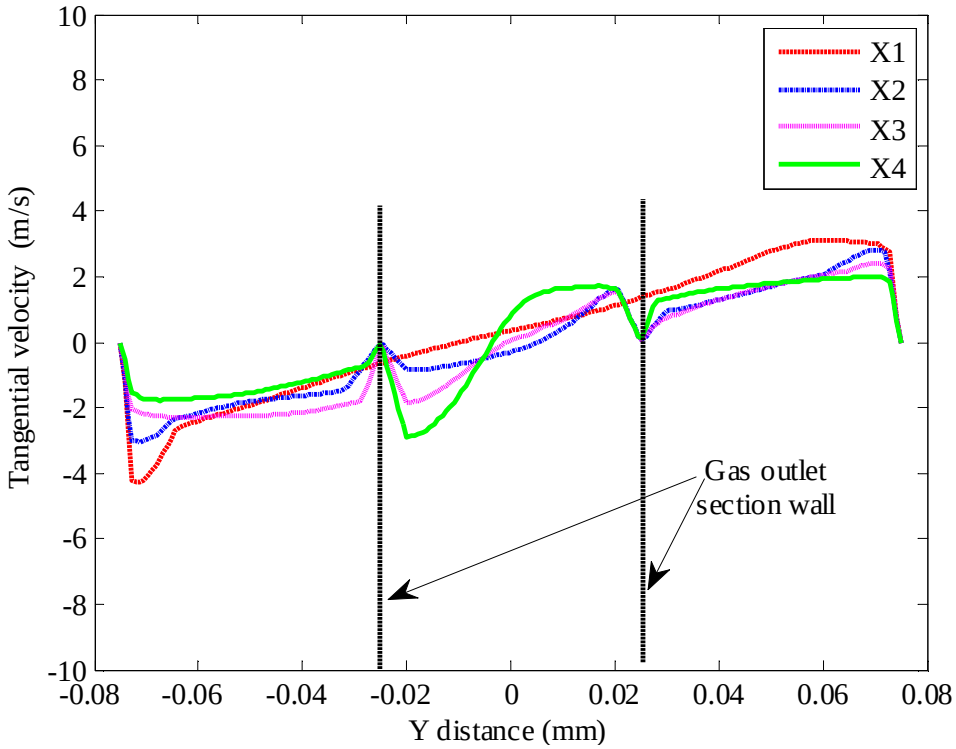

Figure 5-13 Plot of the radial contribution of the tangential velocity of various parts on the X-Y plane (Z=0) of Pipe-SEP II

The maximum tangential velocities predicted by CFD are compared with the Barth model, and are listed in Table 5-4. The maximum tangential velocity equals approx. 3.50m/s and appears in the near wall region of X1. This maximum tangential velocity deviates from the value (8.69m/s) on the cyclone wall predicted by the Barth model.

Table 5-4 Comparison of the maximum tangential velocity predicted by CFD and the Barth model

	Tangential velocity (m/s)	
	CFD model	Barth model
Pipe-SEP I	3.50	8.69
Pipe-SEP II	3.09	8.69

Since the flow in the Pipe-SEP is the forced vortex, Eq. (3-1) with the n value equal to -1 can be used to describe the tangential flow distribution. The maximum tangential

velocity, $V_{tang,max}$ and constant C for different section is summarized in Table 5-5 below.

Table 5-5 The maximum tangential velocity and constant C for different sections

	Pipe-SEP I		Pipe-SEP II	
	$V_{tang,max}$, m/s	C	$V_{tang,max}$, m/s	C
X1	3.50	46.7	3.09	41.2
X2	3.15	42.0	2.80	37.3
X3	2.76	36.8	2.39	31.9
X4	2.14	28.5	2.00	26.7

The maximum tangential velocity decays with the increasing of the axial distance, and so does the constant C. To get a simple correlation of the constant C, the constant C is plotted vs axial distance, as shown in Figure 5-14. The constant C is linear with X. The correlations are obtained by the curve fitting, and expressed as follows:

$$\text{Pipe-SEP I} \quad C_I = -0.03986\,X + 53.45 \tag{5-2}$$

$$\text{Pipe-SEP II} \quad C_{II} = -0.00326\,X + 46.5 \tag{5-3}$$

It is worth noting that $C \rightarrow 0$ as $V_{tang,max} \rightarrow 0$ for the 'no swirl' case. Extending the trend in the Figure 5-14, a maximum X distance is obtained. The maximum X distance represents the end of the vortex. In this case, the natural vortex length for the Pipe-SEP is approximately equal to 1400mm.

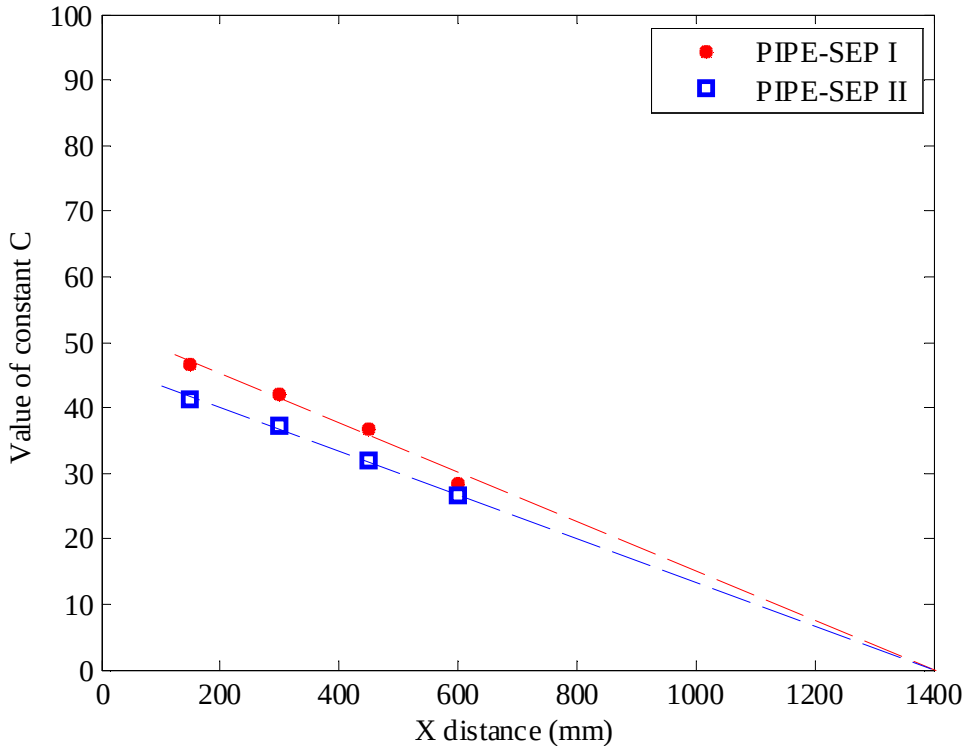

Figure 5-14 Plot of the value of the constant C along the X direction of Pipe-SEP

5.3.3 Axial Velocity

The mean axial velocity fields of Pipe-SEP I and II are depicted through contours in Figure 5-15, at the gas inlet velocity$V_{gas-inlet}$ equal to 10m/s. The axial velocity can be decomposed in three characteristic regions, i.e a downward directed flow in the centre; an upward directed flow and a 'wall jet' near the wall. The upward flow and wall jet at the outer part of the Pipe-SEP are critically important as the upward flow is the dominant mechanism for carrying droplets out of the gas outlet, while the wall jet is responsible for the liquid re-entrainment.

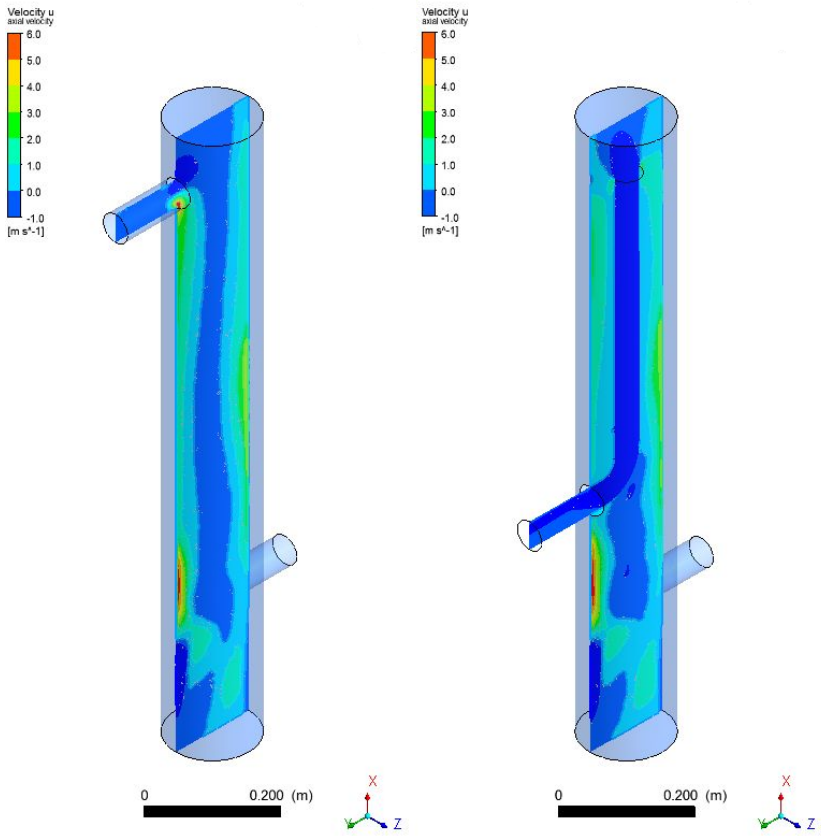

Pipe-SEP I Pipe-SEP II

Figure 5-15 Contours plots for the axial velocity at X-Y plane (Z=0)

The radial profiles presented in Figure 5-16 and Figure 5-17 represent time averaged axial velocities at sections X1, X2, X3 and X4 for Pipe-SEP I and II, respectively. The axial velocities for the two Pipe-SEP are identical in the outer part, which means the axial velocity does not increase when there is a reduction in flow area. It can be seen that on the wall boundary the axial velocity is zero and the peak axial velocity equals nearly 4 times the mean axial velocity. This position is near the region experienced the peak tangential velocity. However, the maximum axial velocity near wall poses a few problems relative to liquid re-entrainment and gas maldistribution. As observed in Sec. 4.2, the majority of the incoming liquid tends to be pushed to the walls of the separator in the form of a swirl wall film. Re-entrainment from the wall may take place if the gas velocity here is sufficient high. This re-entrainment can be partially avoided through the use of appropriate designed “anti-creep” internals, which have been discussed in Sec. 3.5.1.

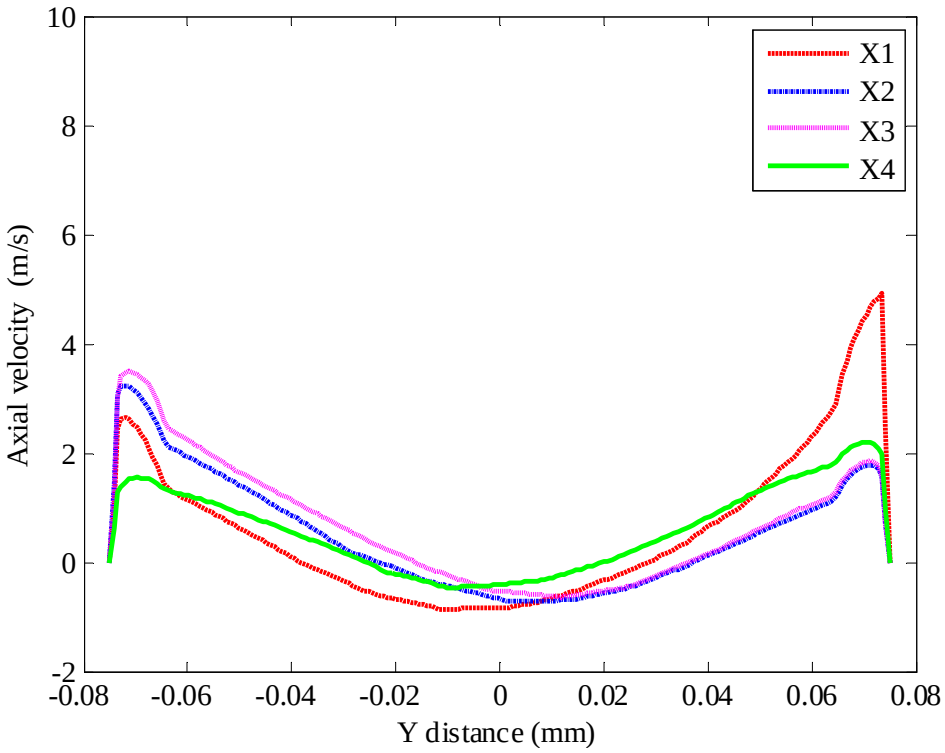

Figure 5-16 Plot of the radial contribution of the axial velocity of various parts on the X-Y plane (Z=0) of Pipe-SEP I

In the Pipe-SEP II, the “L” gas outlet design results in a stationary zone near the gas outlet wall. The gas outlet is inserted in the separation space, and if liquid creep takes place from the Pipe-SEP wall, the liquid film will be dragged up to the outer wall of the gas outlet due to the low pressure in the centre. The liquid cannot be held in this position and it will drop down from the Pipe-SEP centre. The amplitude of the wall jet is reduced along the axial direction. At section X4, the velocity profile exhibits a more flattened curve.

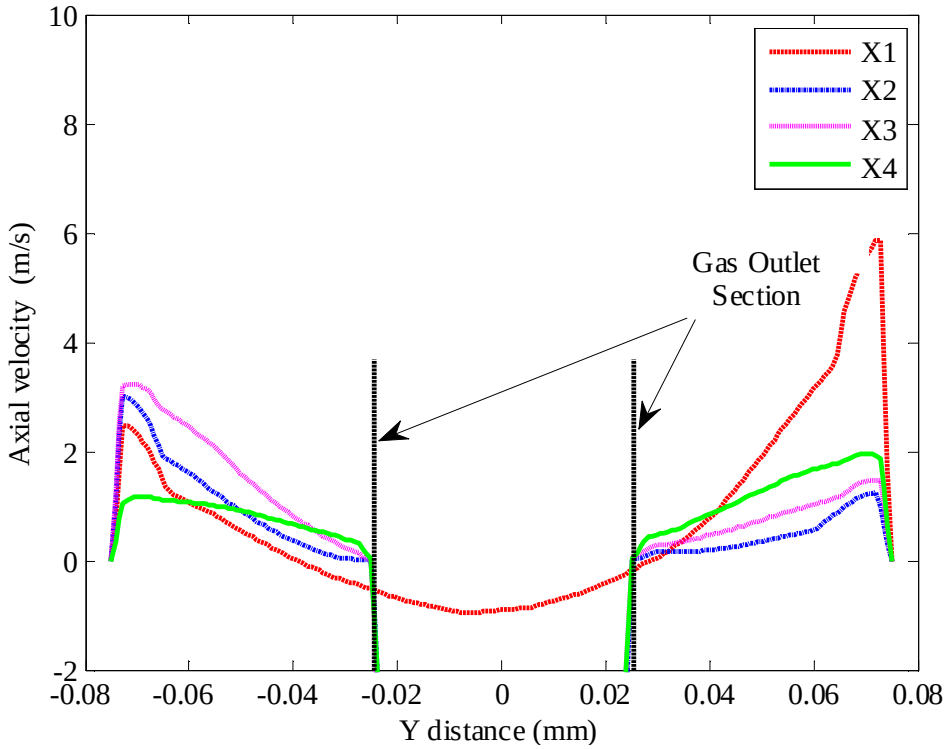

Figure 5-17 Radial profile of the axial velocity at different sections on the X-Y plane (Z=0) of Pipe-SEP II

In the Barth model, the axial velocity is assumed to be uniform over the cross section for both inner upward region and outer downward region. Actually in the Pipe-SEP I and II, the radius of the inner region of downward flow is about 0.025mm, which is the same radius of the gas outlet section. The axial velocity in the outer region of upward flow increases linearly with the radius. Therefore, the axial velocity can take a form similar as the tangential velocity. The maximum axial velocity, $V_{axial,max}$ and the constant D for different sections are summarized in Table 5-6 below.

Table 5-6 The maximum axial velocity and constant D for different sections

	Pipe-SEP I		Pipe-SEP II	
	$V_{axial,max}$, m/s	D	$V_{axial,max}$, m/s	D
X1	4.91	98.2	5.86	117.2
X2	3.23	64.6	3.02	60.4
X3	3.48	69.6	3.24	64.8
X4	2.20	44.0	1.96	39.2

It is interesting to note that the maximum axial velocity at X2 is slightly smaller than the velocity at X3, due to the fact that the X2 is just at the position where the gas outlet is installed. This effect obviously complicates the procedure if a universal expression is needed to construct to describe the constant D. Besides, a higher wall jet is seen at X1 of the Pipe-SEP II than in the Pipe-SEP I due to the constriction of the gas out section, while at section X2, X3 and X4, the Pipe-SEP II has a lower maximum axial velocity than the Pipe-SEP I, resulting in a more flatten distribution of the axial velocity. A lower axial velocity near the wall also means less chance to re-entrainment.

A simple correlation of the constant D is obtained by plotting the constant D vs axial distance, as shown in Figure 5-18. The maximum axial velocity at X2 is excluded. The constant D is linear to the X. The correlations are obtained by curve fitting, and are expressed as follows:

$$\text{Pipe-SEP I} \quad D_I = -0.11686\,X + 117.34 \tag{5-4}$$

$$\text{Pipe-SEP II} \quad D_{II} = -0.17352\,X + 143.14 \tag{5-5}$$

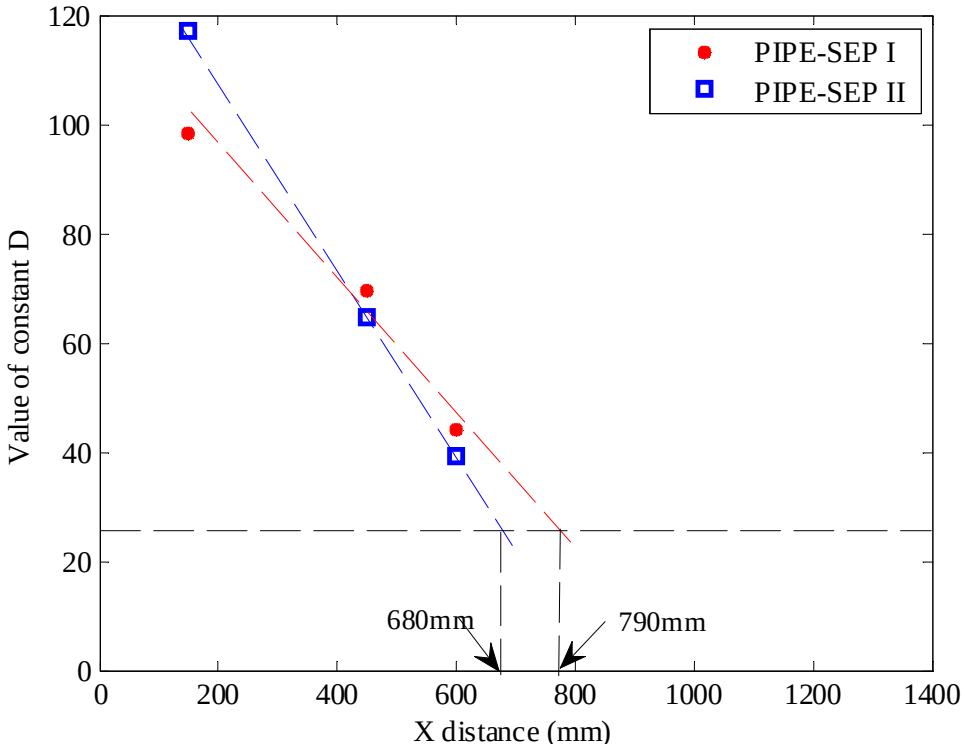

Figure 5-18 Plot of the value of the constant D along the X direction of Pipe-SEP

It can be seen that D→ 25 as $V_{axial,max}$ → mean axial velocity. Extending the trend in the above figure, maximum X distances are obtained for Pipe-SEP I and Pipe-SEP II. The maximum X distance represents a re-uniformed axial velocity. In this case, the distance for the axial velocity in the Pipe-SEP I to re-uniform is approximately 790mm, while for the Pipe-SEP II, the distance is shorted to 680mm.

5.3.4 Effect of the Inlet Gas Velocity on the Gas Flow Profile

To evaluate the effect of changing the gas inlet velocity on the gas flow profile inside Pipe-SEP II, the tangential and axial velocity profile for three different gas inlet velocities (5m/s, 10m/s and 15m/s) are compared in this section. Figure 5-19 shows the flow streamline within the Pipe-SEP II. The flow is spread immediately at the entrance, while the swirl turns increases slightly with the increasing of the inlet velocity.

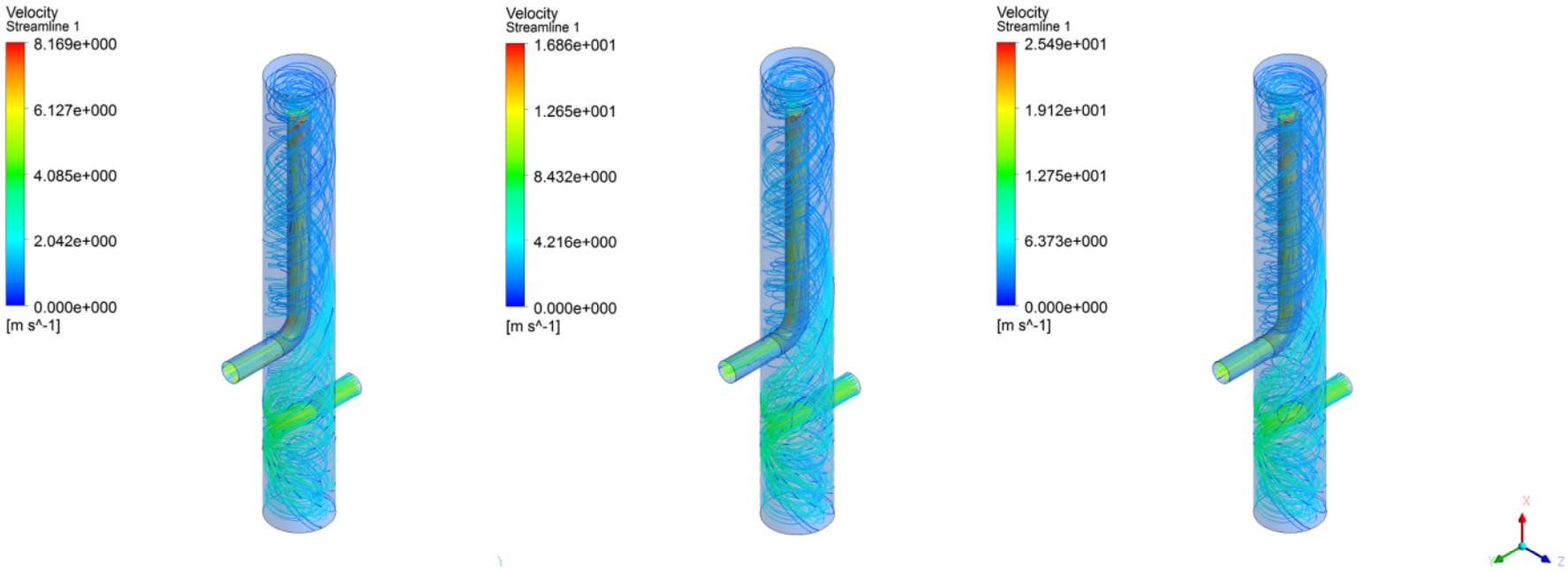

Figure 5-19 Velocity streamline within the Pipe-SEP II

5.3.4.1 Effect on the tangential velocity profile

The tangential velocity profiles under three different gas inlet velocities at section X1 and X3 are shown in Figure 5-20 and Figure 5-21, respectively. As shown in Figure 5-20, the angular momentum of the vortex increases with increasing inlet velocity. At a high inlet velocity 15m/s, where the maximum tangential velocity near the wall is around 6.2 m/s at -Y coordinate, however it appears that the tangential velocity is weakened by the gas outlet at +Y coordinate. Especially at the near wall region, the wall jet is not obvious.

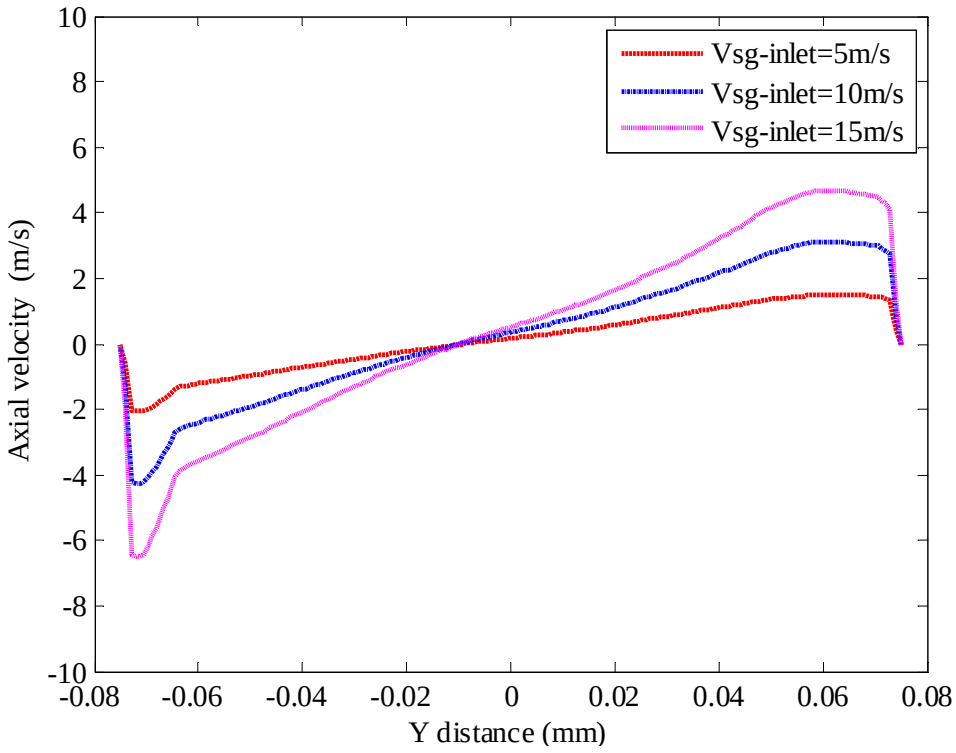

Figure 5-20 Radial profile of the tangential velocity at different inlet gas velocity on the X-Y plane (Z=0, X1 section) of Pipe-SEP II

Figure 5-21 shows the plot of the tangential velocity profile at section X3. In general, the profiles are much flatter than those at X1. The maximum tangential velocity also decreased along the axial distance.

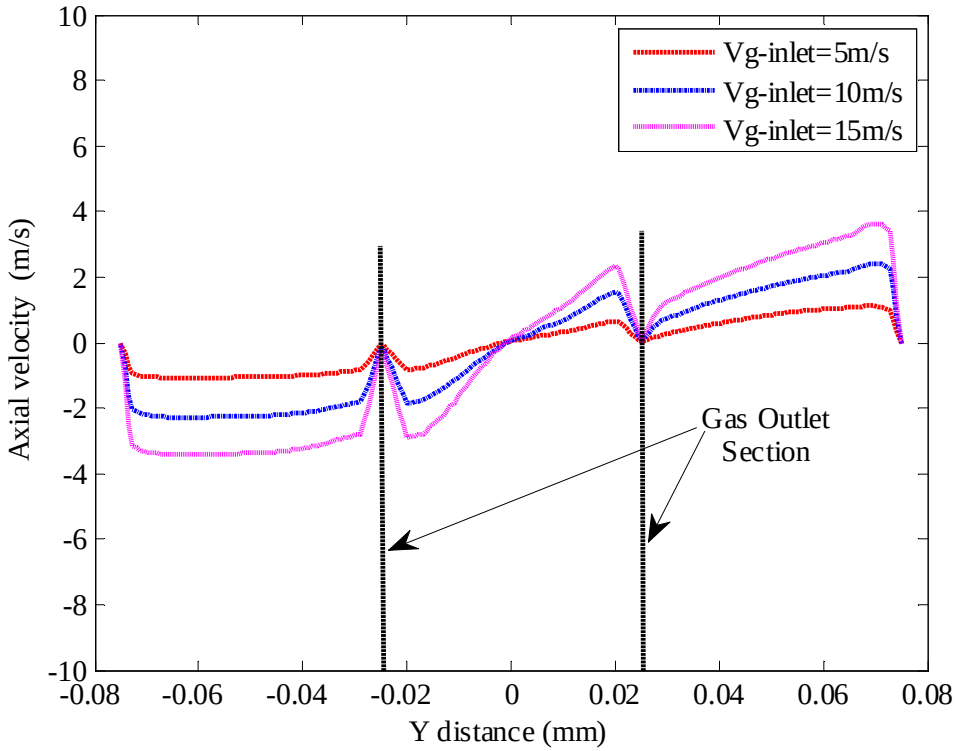

Figure 5-21 Radial profile of the tangential velocity at different inlet gas velocity on the X-Y plane (Z=0, X3 section) of Pipe-SEP II

The maximum tangential velocity and the constant C for different sections are summarized in Table 5-7 below. The value of C is strongly related to the inlet velocity and the X distance.

Table 5-7 The maximum tangential velocity and constant C at different sections for inlet gas velocity 5m/s, 10m/s and 15 m/s

	$V_{sg-inlet}$=5m/s		$V_{sg-inlet}$=10m/s		$V_{sg-inlet}$=15m/s	
	$V_{tang,max}$, m/s	C	$V_{tang,max}$, m/s	C	$V_{tang,max}$, m/s	C
X1	1.48	19.73	3.09	41.2	4.66	62.13
X2	1.36	18.13	2.80	37.3	4.22	56.27
X3	1.12	14.93	2.39	31.9	3.62	48.27
X4	0.92	12.27	2.00	26.7	3.06	40.80

To construct a correlation to predict the effect of gas inlet velocity on the constant C in Table 5-7, the constant C is plotted vs. inlet velocity, as shown in Figure 5-22. The correlation is expressed as follows:

$$C_{II} = (-0.0031X+4.72) \times V_{sg-inlet} - 1.38 \quad (5\text{-}6)$$

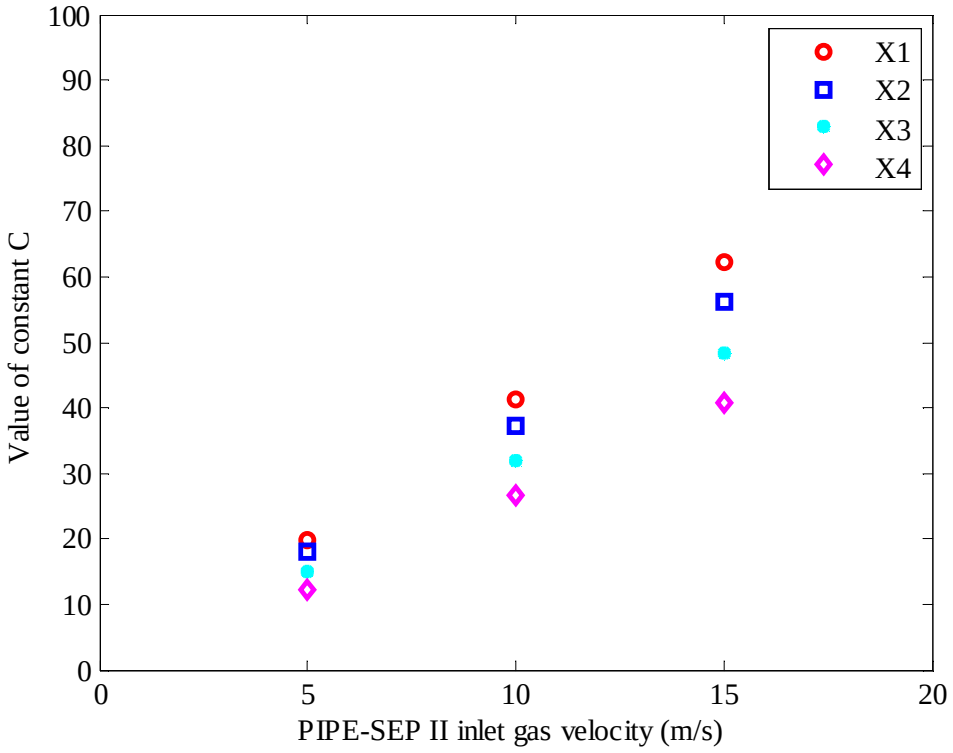

Figure 5-22 Plot of the value of the constant C for different gas inlet velocities in Pipe-SEP II

5.3.4.2 Effect on the axial velocity profile

The axial velocity profiles under three different gas inlet velocities at sections X1 and X3 are shown in Figure 5-23 and Figure 5-24, respectively. As shown in Figure 5-23, the higher inlet velocity imposes a higher wall jet immediately after it enters the Pipe-SEP II. The highest value of the axial velocity is 9.03m/s. In the inner core flow region, the downward axial velocity also increases with increasing inlet velocity. The boundary of the inner and outer region is the same for all three inlet velocities.

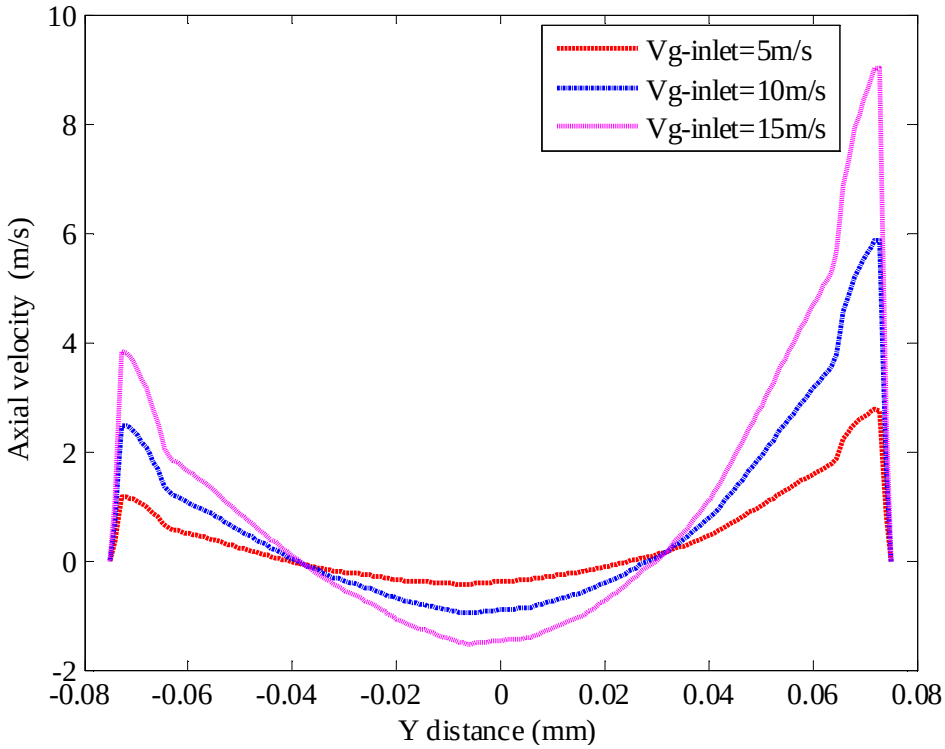

Figure 5-23 Radial profile of the axial velocity at different inlet gas velocity on the X-Y plane (Z=0, X1 section) of Pipe-SEP II

Figure 5-24 shows the plot of the axial velocity profile at section X3. The axial velocity pattern is very similar for all inlet velocities. The velocity gradient is not as sharp as those on the X1.

The maximum axial velocity and the constant D for different sections are summarized in Table 5-8 below. Similarly, a correlation that predicts the effect of gas inlet velocity on the constant D is obtained by plotting the constant D vs inlet velocity, as shown in Figure 5-25. The correlation is expressed as follows:

$$D_{II} = (-0.019X+15.38) \times V_{sg-inlet} + 0.0174X - 9.98 \quad (5\text{-}7)$$

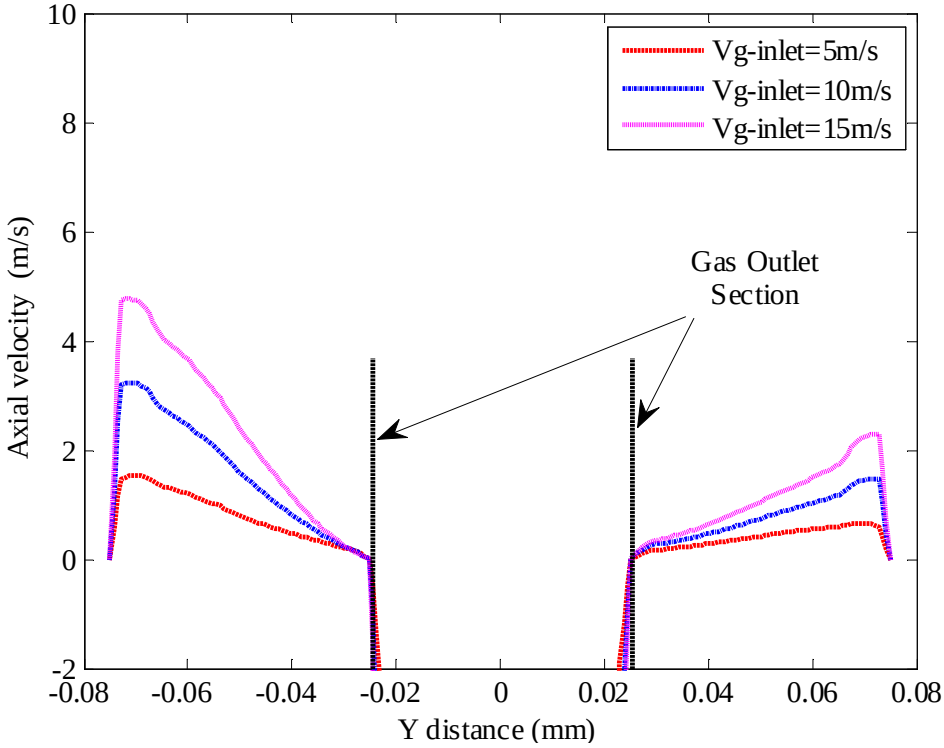

Figure 5-24 Radial profile of the axial velocity at different inlet gas velocity on the X-Y plane (Z=0, X3 section) of Pipe-SEP II

Table 5-8 The value of constant D at different section for inlet gas velocity 5m/s, 10m/s and 15 m/s

	$V_{sg-inlet}$=5m/s		$V_{sg-inlet}$=10m/s		$V_{sg-inlet}$=15m/s	
	$V_{axial,max}$, m/s	D	$V_{axial,max}$, m/s	D	$V_{axial,max}$, m/s	D
X1	2.76	55.2	5.86	117.2	9.03	180.6
X2	1.38	27.6	3.02	60.4	4.72	94.4
X3	1.54	30.8	3.24	64.8	4.78	95.6
X4	0.95	19.0	1.96	39.2	2.90	58.0

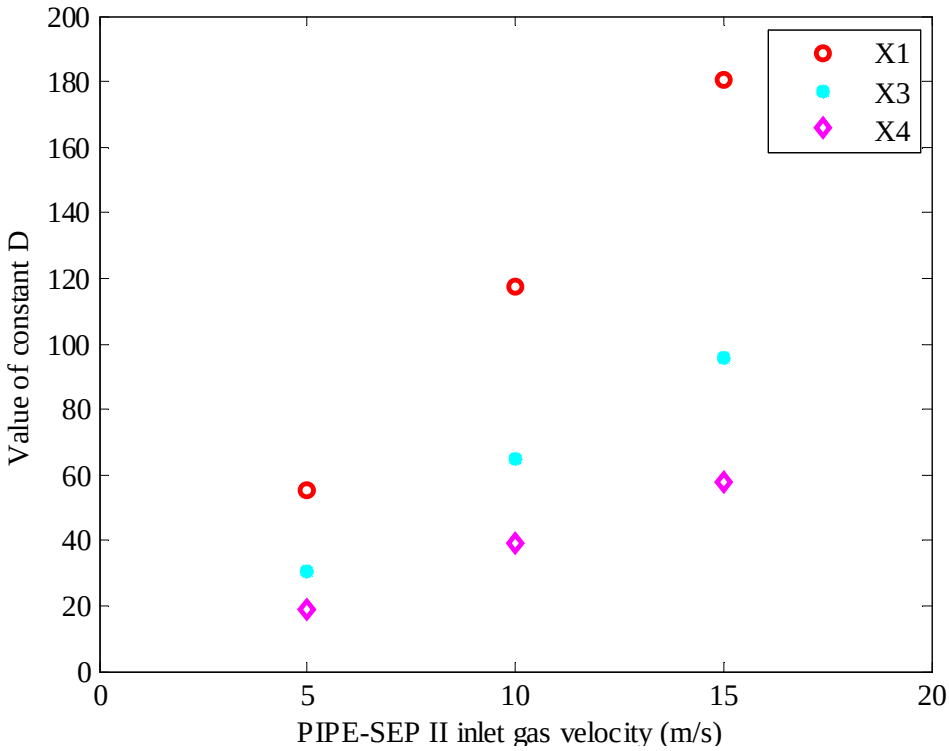

Figure 5-25 Plot of the value of the constant D for different gas inlet velocities in Pipe-SEP II

5.3.5 Effect of the Separator Diameter on the Gas Flow Profile

To evaluate the effect of the separator diameter on the gas flow profile inside Pipe-SEP II, the tangential and axial velocity profile for Pipe-SEP II and Hi-SEP are compared in this section. The Hi-SEP has the following dimensions: 0.204 mm in diameter and 900 mm in separation height. It is equipped with the same inlet and outlet as the Pipe-SEP II.

5.3.5.1 Effect on the tangential velocity profile

The tangential velocity profiles inside Pipe-SEP II and Hi-SEP at section X1 and X3 are shown in Figure 5-26 and Figure 5-27, respectively. As shown in Figure 5-26, the maximum tangential velocity near wall in the Pipe-SEP II is slightly smaller than the velocity in the Hi-SEP. To determine the effect that an increase in separator diameter would have on tangential velocity, the Barth model (Eq. (3-5) and Eq. (3-6) in chapter 3) is applied here. For a given inlet nozzle, the ratio of moment-of momenta of the gas flowing along the wall and the gas in the inlet, $1/\alpha$ decreases with the increasing of the separator diameter. Conversely, the value of R_{in}/R will increase. However, the R_{in}/R ratio will increase more rapidly, and as a consequence, the tangential velocity near wall

will increase with the separator diameter, if the wall friction loss is ignored. If the wall friction loss is accounted for, as it will reduce the vortex intensity, the net effect of the separator diameter is more complicate to predict.

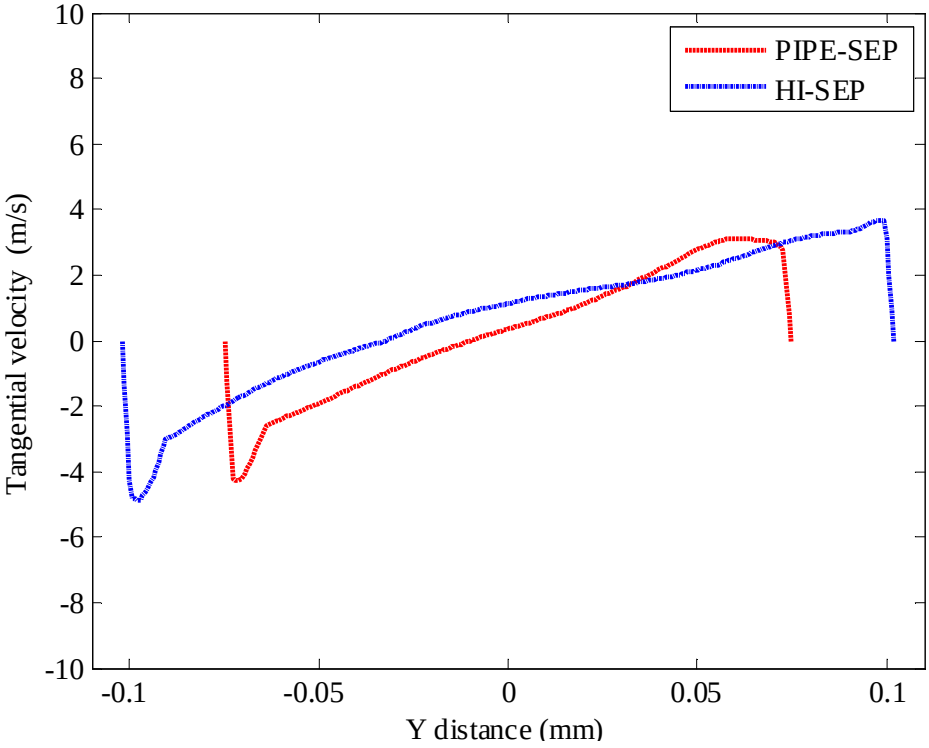

Figure 5-26 Radial profile of the tangential velocity on the X-Y plane (Z=0, X1 section) of Pipe-SEP II and Hi-SEP

Figure 5-27 shows the plot of the tangential velocity profile at section X3. The profiles are similar for the two separators. Even though the maximum tangential velocity in the Hi-SEP is slightly higher than in the Pipe-SEP II, the mean tangential velocity is smaller than in the Pipe-SEP II.

The maximum tangential velocity and the constant C for different sections are summarized in Table 5-9 below. It seems the value of C is not strongly affected by the separator diameter. A simple correlation was developed to account for the effect of the separator diameter on the tangential velocity, and is expressed as follows:

$$C_{HI} = C_{II}\left(\frac{D_{PIPE-SEP}}{D_{HI-SEP}}\right)^{m} \tag{5-8}$$

where m=0.3 for the present case.

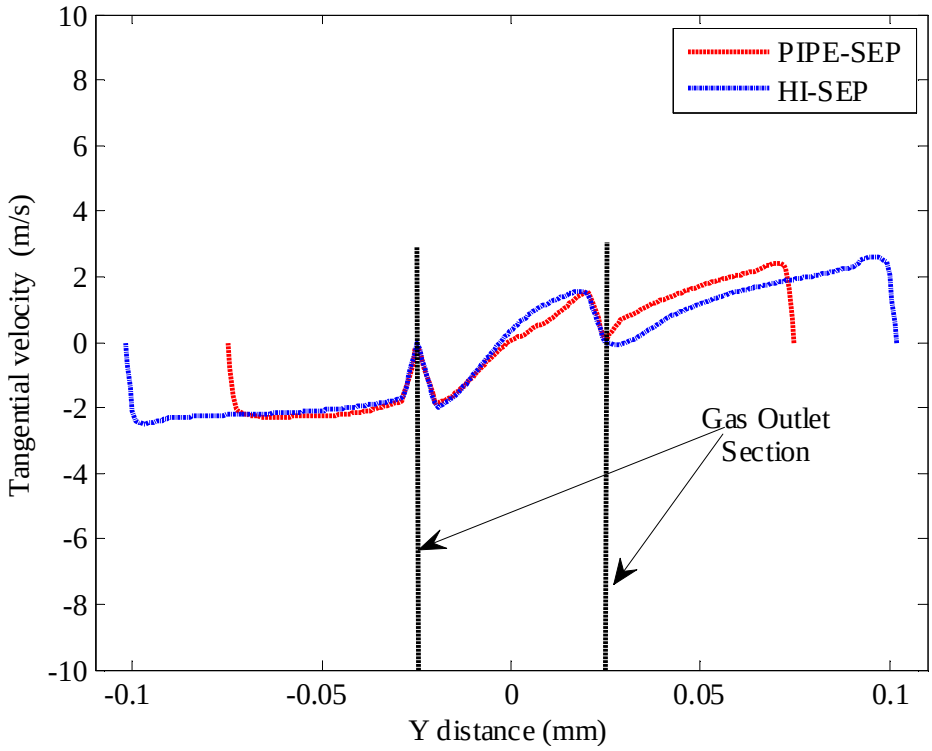

Figure 5-27 Radial profile of the tangential velocity on the X-Y plane (Z=0, X3 section) of Pipe-SEP II and Hi-SEP

Table 5-9 The maximum tangential velocity and constant C at different sections for Pipe-SEP II and Hi-SEP

	Pipe-SEP II		Hi-SEP	
	$V_{tang,max}$, m/s	C	$V_{tang,max}$, m/s	C
X1	3.09	41.2	3.67	47.66
X2	2.80	37.3	3.01	39.10
X3	2.39	31.9	2.61	33.90
X4	2.00	26.7	2.23	28.96

5.3.5.2 Effect on the axial velocity profile

The axial velocity profiles of Pipe-SEP II and Hi-SEP at section X1 and X3 are shown in Figure 5-28 and Figure 5-29, respectively. As shown in Figure 5-28, the higher inlet velocity imposes a wall jet immediately after it enters the two separators. The highest value of the axial velocity is around 5.85m/s in Pipe-SEP II, which is slightly higher

than the velocity in Hi-SEP. In addition, a wider inner downward flow region is clear in the Hi-SEP. The gradient of axial velocity along the radius reduces with the increasing of separator diameter.

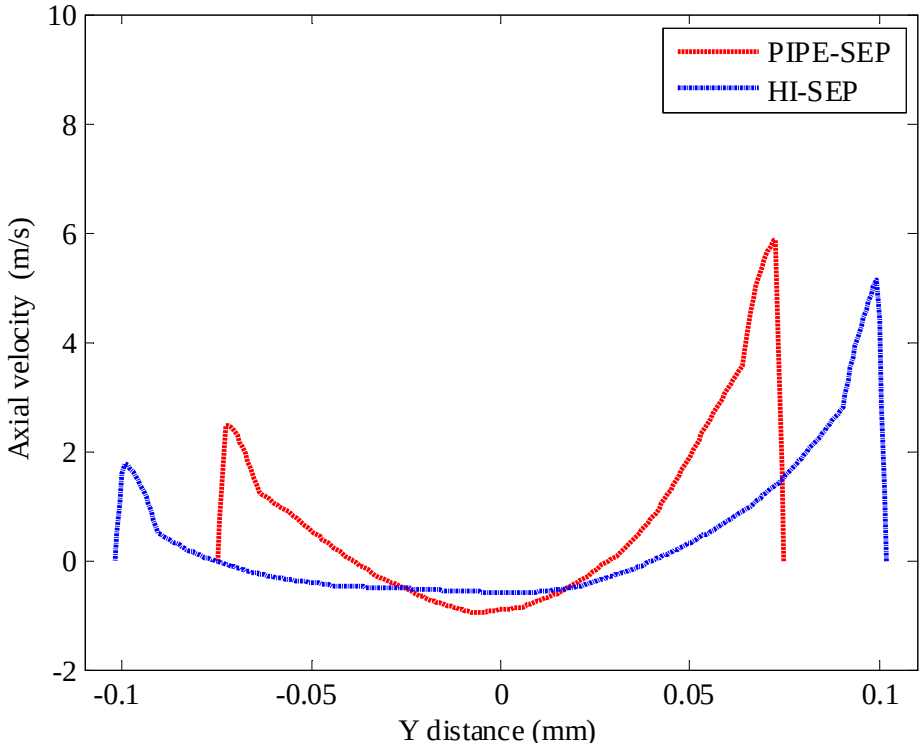

Figure 5-28 Radial profile of the axial velocity on the X-Y plane (Z=0, X1 section) of Pipe-SEP II and Hi-SEP

Figure 5-29 shows the plot of the axial velocity profile at section X3. The axial velocity pattern is rather similar for the two separators. Even though the maximum axial velocity near wall in the Pipe-SEP II is only slightly higher than the velocity in the Hi-SEP, the mean axial velocity in Pipe-SEP II is 1.85 times of the velocity in the Hi-SEP.

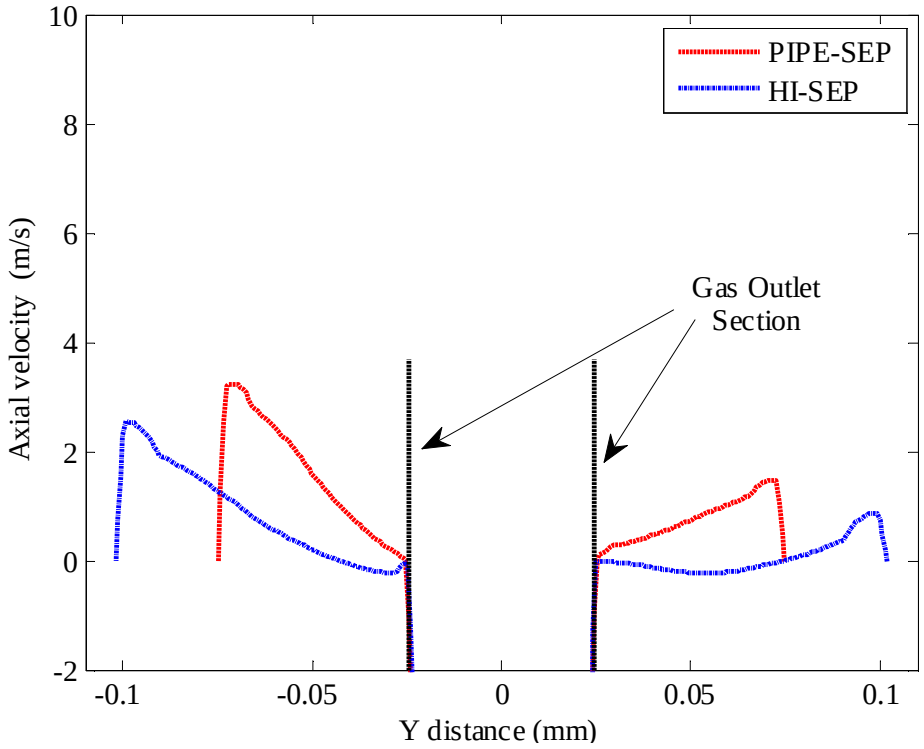

Figure 5-29 Radial profile of the axial velocity on the X-Y plane (Z=0, X3 section) of Pipe-SEP II and Hi-SEP

The maximum axial velocity and the constant D for different sections are summarized in Table 5-8 below. Similarly, a correlation that predicts the effect of separator diameter on the constant D is obtained and is expressed as follows:

$$D_{HI} = D_{II}\left(\frac{D_{PIPE-SEP}}{D_{HI-SEP}}\right)^{m} \tag{5-9}$$

where m=2 in the present case.

Table 5-10 The value of constant D at different sections for Pipe-SEP II and Hi-SEP

	Pipe-SEP II		Hi-SEP	
	$V_{axial,max}$, m/s	D	$V_{axial,max}$, m/s (m/s)	D
X1	5.86	117.2	5.13	66.62
X2	3.02	60.4	2.23	28.96
X3	3.24	64.8	2.54	32.98
X4	1.96	39.2	1.54	20.00

5.4 DPM Modelling of Pipe-SEP

The DPM model is supported within the package of FLUENT 12.1, and it is applied in this section in order to study the droplet trajectories and to estimate the separation efficiency of the Pipe-SEP. The gas flow is calculated with the Navier-Stokes equation using time averaging. The dispersed phase is calculated by monitoring a certain number of droplets passing through the chosen flow region. In this present case, firstly, the droplet diameters vary between 1 and 20 μm, and they are injected and tracked. Each time, 140 droplets with the same diameter and velocity equal to 10 m/s enter the separator from the inlet surface. The amount of the droplets is based on the cells number placed on the inlet boundary face, since each cell occupies one droplet. The density of the droplet injected is 998.2kg/m^3. Particles touching the walls of the Pipe-SEP and outer wall of the gas outlet section were assumed to be trapped. The grade efficiency curve of Pipe-SEP I and Pipe-SEP II can be obtained. Secondly, the effect of the inlet velocity on grade efficiency is investigated in the Pipe-SEP II. The results of three different inlet gas velocities, 5m/s, 10m/s and 15m/s are presented. Finally, the simulation results are compared with the Barth model and the Rosin model to assess which model can better represent the performance of Pipe-SEP and to validate the scale rules.

5.4.1 Grade Efficiency

Figure 5-30 shows the grade efficiency of Pipe-SEP I and II vs. the droplet diameters for the gas velocity equal to 10 m/s. Based on the efficiency results, the cut sizes were estimated, where for the Pipe-SEP I the cut size is 8.9 μm and for the Pipe-SEP II it is 6.3 μm, which implies that the Pipe-SEP II has slightly higher separation efficiency. This is due to the fact that not only the droplets being flung to the wall of the separator will be separated, but also those that came in contact with the outer wall of the gas outlet will be separated. Especially the smaller diameter droplets will flow closer to the centre of the separator, and therefore they will have a higher chance of reaching the outer wall of the gas outlet.

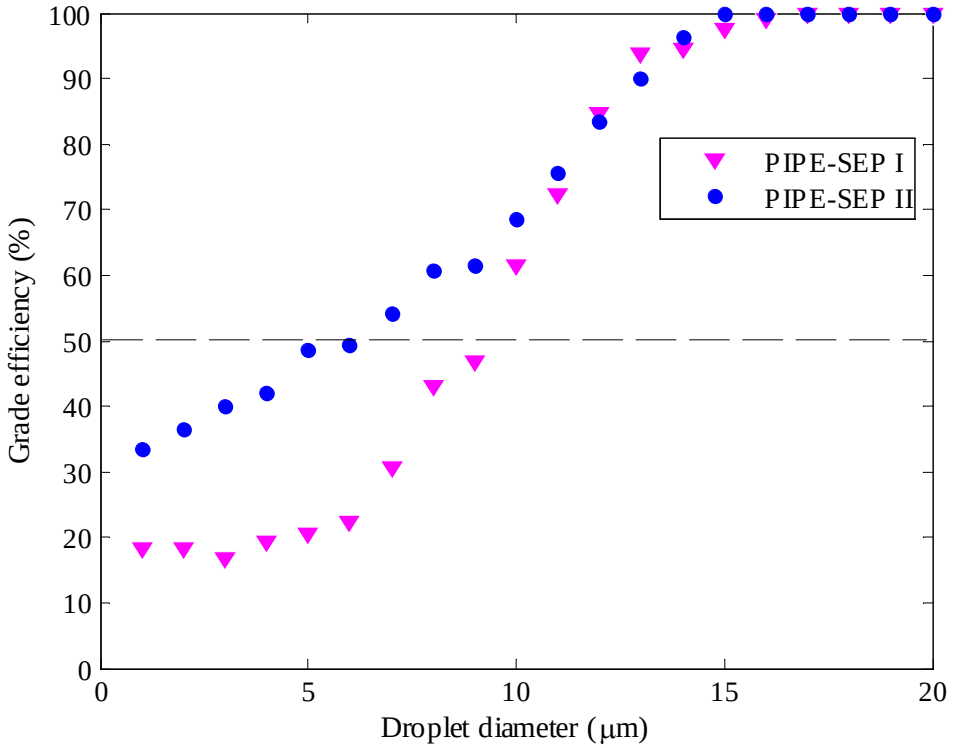

Figure 5-30 Grade efficiency for a Pipe-SEP operating at gas inlet velocity 10m/s

The GEC of Pipe-SEP I exhibit a shape similar to that of the 'universal curve', as shown in Figure 3-5 in chapter 3. The structure of Eq. (3-10) in chapter 3 can roughly describe the Pipe-SEP I's GEC with the exponent equal to 6. On the other hand, the GEC of the Pipe-SEP II is almost overlapped with the one of Pipe-SEP I when the droplet diameter is larger than 11 μm. In the smaller diameter, as shown above, the curve begins to deviate from the 'universal curve' and it tends to be linear. Therefore the GEC of Pipe-SEP II can be expressed as

$$\eta(D) = 0.65(\frac{D}{D_{50}})^{0.48} \tag{5-10}$$

5.4.2 Separation Efficiency

Usually the droplet size and size distribution in the flow to a separator is very difficult to predict, because it depends on the flow conditions in the upstream piping and its fluid properties. To have an impression of the separation efficiency of the Pipe-SEP in the present work, a case with typical experimental flow conditions (Q_g =145 Sm^3/hr, GVF=90%) has been used to illustrate the relationship between the grade efficiency and

separation efficiency. The Sauter mean droplet size is estimated according to the equation from (Steinmayer, 1995)

$$d_{32} = 0.79(\frac{\sigma}{\rho_g})^{0.6}(\frac{1}{v_g})^{1.2}D_{nozzel}^{0.4} \quad (5\text{-}11)$$

where d_{32} is the Sauter mean droplet diameter, and in this case it equals to 1794μm.

The common size distribution function of Rosin-Rammler (Vesilind, 1980) is adopted, as follows:

$$Y_d = \exp[-(\frac{d}{d_{32}})^n] \quad (5\text{-}12)$$

where Y_d is the mass percentage of the inlet droplets having a diameter greater than d, n is the spread parameter, which indicates the width of the distribution, and it is normally obtained from a mathematical fitting of the actual particle size to a Rosin-Rammler exponential relationship. Here n is taken as 0.8. The following Table 5-11 shows the mass fraction of different droplet diameters.

Table 5-11 Mass fraction of different droplet diameters

Diameter, d (μm)	Mass fraction with diameter greater than d, Y_d
2	0.9957
4	0.9925
6	0.9896
8	0.9869
10	0.9844
15	0.9785
20	0.9730
50	0.9446
100	0.9055
500	0.6978
1000	0.5345

It can be seen that only 5.6% of the droplets is less than 50 μm. According to 3-14 in chapter 3, the separation efficiency of Pipe-SEP I and Pipe-SEP II can be estimated to be 98.35% and 98.68%, respectively.

5.4.3 Effect of the Inlet Gas Velocity on the Grade Efficiency

The GEC of Pipe-SEP II operating at 5m/s, 10m/s and 15m/s are presented in Figure 5-31. The cut size reduces slightly with increasing inlet gas velocity. When the droplets are smaller than the cut size, the grade efficiency for 10m/s and 15m/s is identical and higher than the one for a 5m/s velocity. The correlation in Eq. (5-2) can still be applied here. Figure 5-31 also shows that when the droplet is bigger than the cut size, it is easier to be separated at a higher inlet gas flow velocity. As mentioned before, increasing inlet gas velocity causes an increase in the vortex swirl velocity and in the centrifugal force. Such centrifugal force drags the droplet to the wall and increases separation performance.

A higher inlet gas velocity can be achieved either by reducing the nozzle size or increasing the flow rate, which is the case mentioned above. Although the performance is enhanced by increasing the inlet velocity, however if not appropriate designed, liquid re-entrainment may occur. Thus, there should be an optimum size of inlet-to-separator diameter.

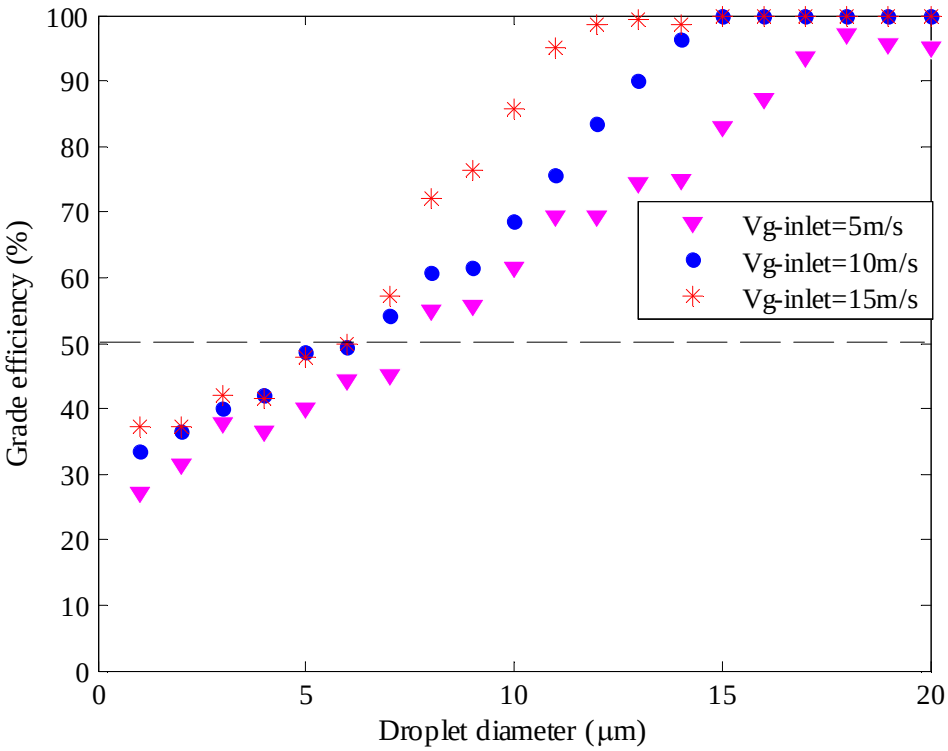

Figure 5-31 Effect of inlet gas velocity on the grade efficiency of Pipe-SEP II

5.4.4 Effect of the Separator Diameter on Grade Efficiency

The effect of the separator diameter on grade efficiency has also been studied on a Hi-SEP with the help of CFD simulations. The GEC of Hi-SEP and Pipe-SEP II at inlet gas velocity 10 m/s are shown in Figure 5-32. The cut size is seen to increase slightly with increasing separator diameter as expected. This is because, as the diameter increases, the spin in the vortex will decrease. According to the Barth model, a less intensive vortex means less centrifugal force on the droplet. In this case, the cut size will become bigger.

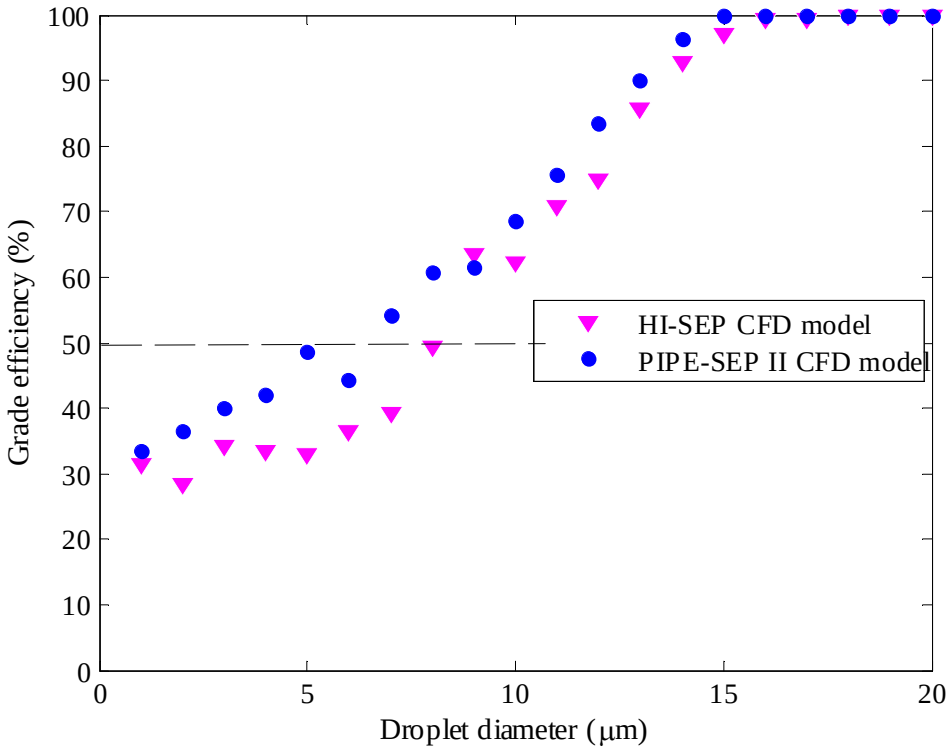

Figure 5-32 Effect of separator diameter on the grade efficiency

5.4.5 Comparison with Mathematical Models

The cut size of Pipe-SEP I and II calculated by CFD simulations and the one predicted by Barth model and Rosin model are given in Table 5-12. It is clear that the Barth model under-predicts the cut size of both Pipe-SEP I and Pipe-SEP II. The Rosin model over-predicts the cut size of Pipe-SEP II but predicts the cut size of Pipe-SEP I quite well. Thus these results show that the Rosin model is better suited to the Pipe-SEP, and that the assumptions of the Barth model are not appropriate for the Pipe-SEP. As

mentioned in Sec. 5.4.2, the tangential velocity in CS is over-predicted in the Barth model.

Table 5-12 Cut size of Pipe-SEP

Model/method	Cut size (μm)
Pipe-SEP I CFD simulation	8.9
Pipe-SEP II CFD simulation	6.3
Barth model	4.98
Rosin model	9.15

In the Barth model, the value of the tangential velocity within the flow was assumed to be the only factor responsible for the swirling element, and it is kept constant even if the separator length is changed. The simplification within the Barth model is valid for cyclones with a ratio of length over diameter less than 5. However, as mentioned in Sec. 3.4, the increase in separator length results in lower vortex and radial velocities. It is not obvious whether the longer separator performs better. In the experiment conducted by Hoffman (2001), the results showed an improvement in cyclone performance with cyclone length increasing up to 5.5 times of cyclone diameter. The length of separation space in Pipe-SEP is 800 mm, which is 5.3 times the diameter. Therefore the Barth model would have predicted a smaller cut size in Pipe-SEP, which would indicate a better performance.

The Rosin model considers the migration time of a droplet to the wall. It is assumed that the tangential gas velocity profile does not change with axial position, which is true in the Pipe-SEP (see Figure 5-12 and Figure 5-13). For a given fluid, the cut size estimated by Rosin model only depends on the inlet nozzle diameter and inlet gas flow rate.

The GEC is calculated based on the cut size in Table 5-12 and the Eq. (3-10) in chapter 3, as shown in Figure 5-33. The Rosin model exhibits a similar trend with Pipe-SEP I and Pipe-SEP II when the droplet diameter is larger than the cut size. On the other hand in the smaller droplet diameter region, Eq. (3-10) cannot represent the GEC well; instead, a modified Eq. (5-10) should be used for the GEC prediction.

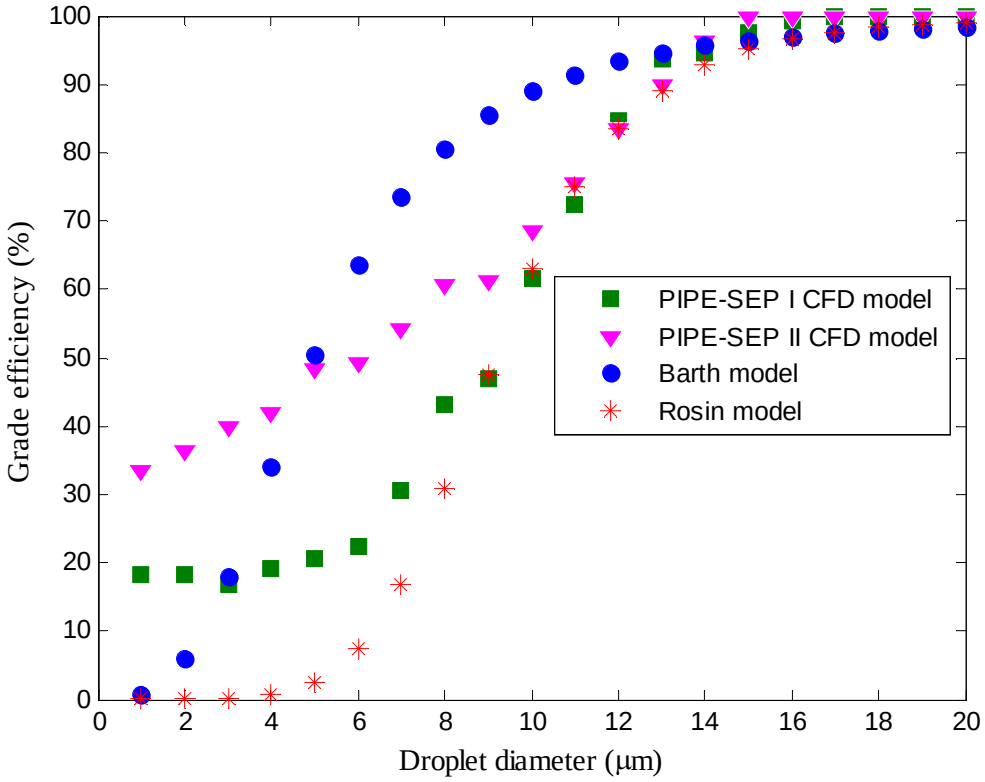

Figure 5-33 Comparison of grade efficiencies calculated by CFD and predicted by models

Therefore, the GEC of Pipe-SEP II can be estimated as follow

$$\begin{cases} \eta(D) = \frac{1}{1+(\frac{D_{50}}{D})^6} & \mathrm{D} \geq D_{50} \\ \eta(D) = 0.65(\frac{D}{D_{50}})^{0.48} & \mathrm{D} < D_{50} \end{cases} \tag{5-13}$$

5.4.6 Scaling Rules

Scaling rules have been used to study the performance of 'commercial cyclones' from the model tested. For geometrically similar cyclones, the Euler number is assumed to be constant, and so is the Stokes number. In Sec. 2.2.2, the Stk_{50} was given as

$$Stk_{50} = \frac{\Delta\rho D_{50}^2 v_{ch}}{18\mu_g D} \tag{5-14}$$

where v_{ch} is the averaged axial velocity within the separator. The cut sizes of Hi-SEP can be estimated using Stokesian scaling from the Pipe-SEP

$$Stk_{50-Hi-SEP} = Stk_{50-Pipe-SEP} \tag{5-15}$$

The results of applying Stokesian scaling, the Barth model, the Rosin model and CFD simulations to estimate the cut size for Hi-SEP are given in Table 5-13.

Table 5-13 Cut size of Hi-SEP calculated in various models

Model/method	Cut size (μm)
Hi-SEP CFD simulation	8.20
Barth model	6.20
Rosin model	9.15
Stokesian scaling	9.99

It is clear the Rosin model did not account for the diameter effect on the model. The cut size of Hi-SEP is the same as with Pipe-SEP. The Barth model and Stokesian scaling can capture the trend of the effect. The Stokesian scaling predicts a slightly bigger cut size, which gives the desired design margin and is therefore more preferable in real applications.

5.5 Summary

The numerical simulations of the Pipe-SEP upper section with gas and droplets has been carried out to obtain an insightful study into the flow field. The flow field of the Pipe-SEP was computed for two cases with and without the presence of the “L” outlet section. The numerical solutions confirmed, in agreement with the experimental observations, that:

1. A forced swirl flow is generated at the upper section of the Pipe-SEP. The tangential velocity profile confirmed the swirl type characteristics to be that of solid body swirls.
2. The tangential inlet creates turbulence which imparts a higher velocity to the flow.
3. Axial velocities were minimum at the Pipe-SEP centre and maximum at near wall. The same behaviour was shown by the tangential velocity.
4. The induced swirl decays slightly with increasing axial distance.
5. The gas inlet velocity can significant effect the gas flow profile, while the effect of the separator diameter is insignificant.

Also, it was found that the effect of the “L” outlet on the flow field is insignificant, and other effects caused by the “L” outlet, namely film creep could be positive for the separator.

The Lagrangian models show the comprehensive behaviour of a droplet within the Pipe-SEP, particularly for the upper area. The cut size and grade efficiency of the two Pipe-SEPs were also computed. The comparison between the model and the theoretical outcomes indicates a good agreement for the Rosin model. The Barth model was found, in this case, to under predict the Pipe-SEP separation performance. Moreover the Stokesian scaling results also showed a reasonable cut size prediction for the Hi-SEP.

Overall, the CFD models were successfully employed to enhance the understanding of the flow behaviour inside Pipe-SEP. The Rosin model is selected to be used in the following optimization procedure, as it is comparatively simple. It appears to yield accurate results and can be integrated into optimization procedures to reflect the real situations of droplets and gas phase movement with the Pipe-SEP.

6 PARAMETRIC APPROACH FOR THE OPTIMAL DESIGN OF Pipe-Hi-SEP SYSTEM

In this chapter a parametric optimisation procedure is proposed to determine an optimal Pipe-Hi-SEP system that will yield the lowest weight at required separation efficiency and operating conditions. The optimisation procedure combined the existing conventional separator design procedure and the unique fluid dynamic and mechanical constraints of a cyclonic separator. The design procedure can be improved significantly by formulating it and solving it as a mathematical program. Moreover, the application of this approach to the practical design of Pipe-Hi-SEP system is demonstrated by an example.

6.1 Introduction

Many literature sources and vast amounts of guidelines are available for conventional separator design. For example, the most comprehensive approach was presented by Svrcek and Monnery (1993) as included in Appendix A. These design procedures involve significant manual iterations with extensive table look-ups and require the application of many rules of thumb. Grodal and Realff (1999) and Hernandez *et al*., (2007) developed a parametric optimisation procedure to determine the optimal horizontal separator design and a knockout drums design, respectively. Because of nonlinearity in the separator design problem, the sequential quadratic programming (SQP) and a heuristic algorithm have been use to search for the optimal solutions. The mathematical optimisation techniques have shown very efficient in integrating and solving system design. In this chapter, the algorithmic mathematical optimisation techniques will be applied for the design of a Pipe-Hi-SEP system under various scenarios.

6.2 Mathematical Programming

The compact separator optimal design problem can be cast into a mathematical program as follows

$$\text{Max (or min)} \qquad z = f(x_1, x_2, \dots \dots x_n) \tag{6-1}$$

$$\text{Subject to} \qquad \mathrm{h}(x_1, x_2, \dots \dots x_n) = 0$$

$$\mathrm{g}(x_1, x_2, \dots \dots x_n) \leq 0$$

where z is the objective function, which is a function of the design variables (x_{i}). $\mathrm{h}(x_1, x_2, \dots \dots x_n) = 0$ are model equations that describe the variable relationship of the system, and $\mathrm{g}(x_1, x_2, \dots \dots x_n) \leq 0$ is the inequality constraints, which can define system specifications or constraints for feasible designs. The compact separator design is a nonlinear programming problem. A number of algorithms have been created to solve mathematical programs very efficiently and have been implemented in software, such as MATLAB. This chapter focuses on the model representing the behaviour of separation and constraints in the Pipe-Hi-SEP system. The built-in sequential quadratic programming (SQP) in MATLAB will be used to find the optimal design.

6.3 Foundations in Pipe-Hi-SEP Design

Pipe-Hi-SEP is preferred for separating liquid from mixtures with a high GLR. A typical Pipe-Hi-SEP system includes the following essential components and features:

- A Pipe-SEP that includes (a) tangential inlet; (b) inlet region; (c) gas settling section; (d) gas outlet; (e) liquid settling section; (f) liquid outlet.
- A Hi-SEP that includes (a) tangential gas and liquid inlet; (b) inlet region; (c) gas settling section; (d) gas outlet; (e) liquid settling section; (f) liquid outlet.
- Adequate volumetric liquid capacity to handle liquid surges.
- Adequate separator diameter and height to ensure the separation requirement.
- A mist eliminator in Hi-SEP (optional).
- A means of controlling liquid level in the separator, which usually includes a liquid level controller and a control valve on the Hi-SEP liquid outlet.

- A backpressure valve on the Hi-SEP gas outlet to maintain a steady pressure in the system.
- Pressure relief devices.

The Pipe-Hi-SEP design is constrained by a set of fluid dynamic and mechanical relationships formulated from gravity settling theory, re-entrainment models, unique characteristics of cyclonic separators and controllability issues.

In the following sections, the physical design relationships of Pipe-Hi-SEP are expressed as mathematical formulations. The optimisation objective is to find the solution which yields the minimum total system weight. Figure 6-1 shows the sketches of a Pipe-Hi-SEP system and related geometrical notation.

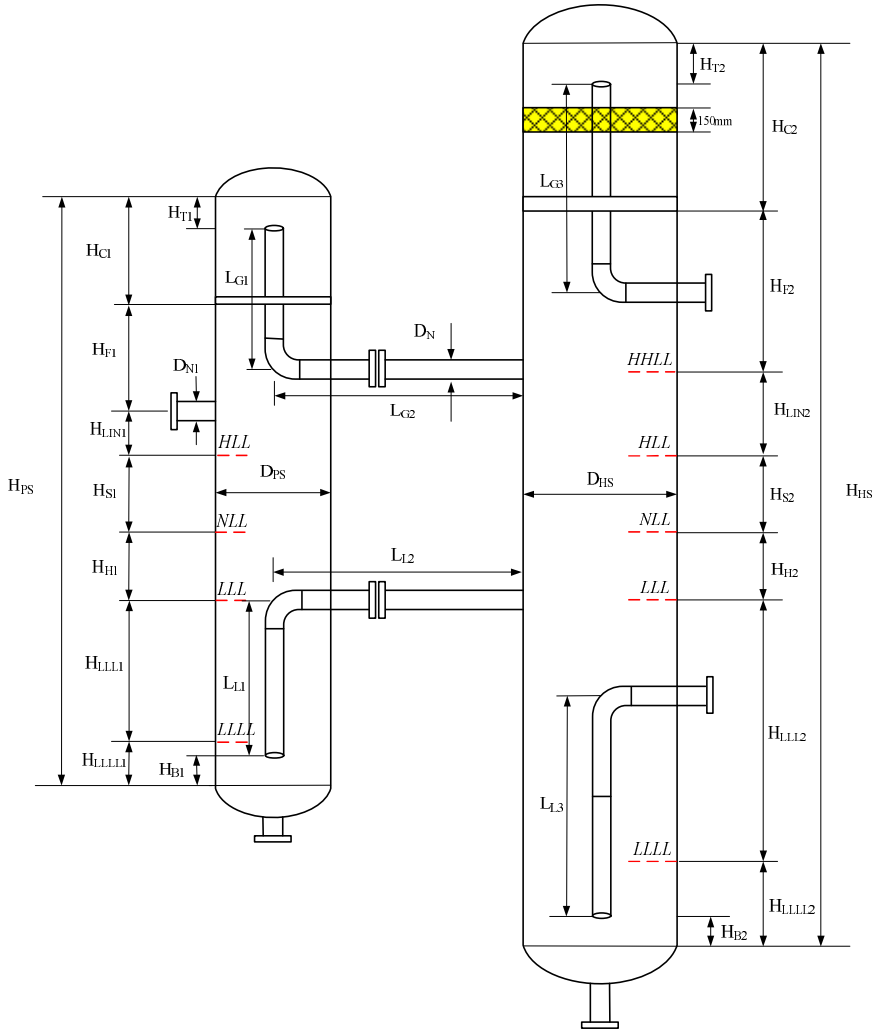

Geometrical Notation

D_{N1}	Inlet pipe diameter
D_{PS}	PIPE-SEP diameter
H_{PS}	PIPE-SEP total height
H_{C1}	PIPE-SEP centrifugal length
H_{F1}	PIPE-SEP swirl film length
H_{LIN1}	PIPE-SEP inlet section length
H_{S1}	PIPE-SEP liquid surge level
H_{H1}	PIPE-SEP liquid holdup level
H_{LLL1}	PIPE-SEP low liquid level
H_{LLLL1}	PIPE-SEP low-low liquid level
H_{T1}	PIPE-SEP top length
H_{B1}	PIPE-SEP bottom length
L_{G1}	PIPE-SEP interconnection gas pipe length 1
L_{G2}	PIPE-SEP interconnection gas pipe length 2
L_{L1}	PIPE-SEP interconnection liquid pipe length I
L_{L2}	PIPE-SEP interconnection liquid pipe length 2
D_N	PIPE-SEP interconnection pipe diameter
D_{HS}	HI-SEP diameter
H_{HS}	HI -SEP total height
H_{C2}	HI-SEP centrifugal length
H_{F2}	HI-SEP swirl film length
H_{LIN2}	HI-SEP inlet section length
H_{S2}	HI-SEP liquid surge level
H_{H2}	HI-SEP liquid holdup level
H_{LLL2}	HI-SEP low liquid level
H_{LLLL2}	HI-SEP low-low liquid level
H_{T2}	HI-SEP top length
H_{B2}	HI-SEP bottom length
L_{G3}	HI-SEP liquid pipe length 3
L_{L3}	HI-SEP gas pipe length 3

Figure 6-1 Sketches of a Pipe-SEP system and geometrical notation

6.4 Mathematical Formulation of Pipe-Hi-SEP models

The Pipe-Hi-SEP model comprises four main sections and models the complete separation system including inlet pipe-work, inlet nozzle, separator body and internals. For each section, the physical design relationships are expressed as inequalities or equalities and highlighted below.

6.4.1 Inlet Piping

As suggested by Hoffmann and Stein (2008), the inlet piping to a cyclonic separator should have a straight section of pipe, with the length at least 10 times the pipe diameter. The upstream bends also need to ensure that the mixture is turned in the same rotational direction as that within the separator. Generally, the inlet pipe feeding a Pipe-Hi-SEP should not be too small to avoiding a large pressure loss. Nor should it be too large to reduce the tangential impact it causes. Wherever possible, the inlet piping should be kept in line with the upstream pipeline.

In some applications, an intermit flow may exist due to the operation condition or terrain. In these cases, the instantaneous high rates normally can be handled if the Pipe-Hi-SEP system has sufficient volume. But the intermit flow tends to encourage the fluctuation of liquid level. If possible, the inlet piping should be designed to stratify the flow by inclining slightly downward or using special flow conditioner so that the Pipe-Hi-SEP system can be subject to a wide variety of inlet flow regimes including annular flow, stratified flow, slugging flow etc.

According to Svrcek and monnery (1993), the diameter of inlet piping can be estimated from

$$D_{N1} \geq \left(\frac{4Q_{m,N1}}{\pi 60}\right)^{\frac{1}{2}} \times \frac{0.0604}{\sqrt{\rho_{m,N1}}} \tag{6-2}$$

$$Q_{m,N1} = Q_l + Q_g \tag{6-3}$$

$$\rho_{m,N1} = \rho_l \lambda_{N1} + \rho_g (1 - \lambda_{N1}) \tag{6-4}$$

$$\lambda_{N1} = \frac{Q_l}{Q_l + Q_g} \tag{6-5}$$

where Q_l is the liquid flow rate; Q_g is the gas flow rate; $Q_{m,N1}$ is the gas and liquid mixture flow rate; $\rho_{m,N1}$ is the mixture density at the inlet; λ_{N1} is the liquid volumetric fraction at the inlet.

According to Gomez *et al*., (1999), an optimized 'G' force should be maintained between 50 and 200, since the centrifugal force is the main drive to accelerate the separation process, and a reduced area nozzle is often needed to aid in creating swirl flow

$$50 \leq G_{PS} \leq 200 \tag{6-6}$$

where G_{PS} is the centrifugal force in the Pipe-SEP, and it is defined as

$$G_{PS} = \frac{v_{m,N1}^2}{D_{PS}g} = \frac{16Q_{m,N1}^2}{\pi^2 D_{N1}^2 D_{PS}g} \tag{6-7}$$

where $v_{m.N1}$ is the mixture velocity at inlet; D_{PS} is the Pipe-SEP diameter.

6.4.2 Pipe-SEP Gas Capacity Constraint

Conventionally, the design of gas capacity in a separator follows the same theory as the gravity settling, however, the Pipe-SEP is functionally designed as a high output separator. It is expected that the Pipe-SEP can remove 95% of incoming liquid, which leave only 5% of liquid to be carried to the Hi-SEP.

The incoming liquid to the Pipe-SEP is separated in two stages. A portion of the liquid is separated immediately upon its entrance into the Pipe-SEP and a portion of the liquid forms the wall film, which will drop down to the liquid collect section because of gravity. On the other hand the droplets dispersed in the gas core will be separated via centrifugal forces. In extreme conditions, it is assumed that all the dispersed droplets become the LCO. Therefore, the total mass of liquid dispersed in the central gas core should less than the 5% LCO requirement.

In order to estimate the LCO, the characteristics of the wall film are required. As mentioned in chapter 4, the thickness of the wall film, δ_{PS} and the entrainment fraction, E in the central gas core can be estimated from Eq. (4-17) to Eq. (4-27). The limit for the LCO can be expressed as

$$\pi h_{PS} D_{PS} \delta_{PS} E \leq 0.05 \tag{6-8}$$

where h_{PS} is the swirl film height, it can be estimated from Eq.(4-17).

As the liquid mass effect may occur in the Pipe-SEP, the wall film may reduce the swirl intensity and decrease the separator performance. In a conservative design, it is required to design the Pipe-SEP for removal of a droplet of size of at least 500μm based on liquid droplet gravity settling. The minimum Pipe-SEP diameter will be the largest of the diameter calculated from Eq. (6-8) or terminal velocity, and is shown as

$$V_{t1} \leq 0.75 \times \sqrt{\frac{4g}{3}\frac{d_{d1}}{C_{D1}}} \times \sqrt{\frac{\rho_l - \rho_g}{\rho_g}} \tag{6-9}$$

Expressing the gas velocity in terms of average volumetric flow rate and the cross-sectional area for gas flow, the following expression is obtained:

$$\frac{4Q_g}{\pi(D_{PS}^2 - D_{N2}^2)} \leq 0.75 \times \sqrt{\frac{4g}{3}\frac{d_{d1}}{C_{D1}}} \times \sqrt{\frac{\rho_l - \rho_g}{\rho_g}} \tag{6-10}$$

where the drag coefficient C_{D1} can be calculated from Table 2-2. D_{N2} is the diameter of the inter-middle pipe, which connects Pipe-SEP and Hi-SEP.

6.4.3 Pipe-SEP Liquid Capacity Constraint

Like the conventional vertical separator, the liquid section of the Pipe-Hi-SEP system must be designed to handle the instantaneous high liquid rates attempting to flood the gas part of the separator. Additionally, the system must be designed so that the trapped gas in the liquid section can escape from liquid phase. Sufficient liquid disengagement space is just as important with Pipe-Hi-SEP as it is for conventional vertical separator.

Adopting the Svrcek's method, the total height of the Pipe-SEP can be divided into seven sections, as shown in Figure 6-1. The height H_{PS} is the sum of the height of each section.

$$H_{PS} = H_{C1} + H_{F1} + H_{LIN1} + H_{H1} + H_{S1} + H_{LLL1} + H_{LLLL1} \tag{6-11}$$

a) H_{C1} is the height from the FER to the top tangent line of the Pipe-SEP. There is no other internal component installed in this part, expect the gas outlet which is mounted with a vortex breaker. The vortex breaker takes the same height as the gas

outlet diameter. The gap between the gas outlet and the top tangent line of the Pipe-SEP is suggested to be half of the Pipe-SEP diameter. The minimum height H_{C1} is required as

$$H_{C1} \geq (H_{T1} + 3 \times D_{N2}) \tag{6-12}$$

$$H_{T1} = \frac{D_{PS}}{2} \tag{6-13}$$

b) H_{F1} is the Pipe-SEP liquid film height. The wall film within a Pipe-SEP does not normally spread out as a uniformly thick film. Instead, the liquid tends to segregate somewhat even though most of the wall areas may be wetted. In this case, the wall film is simply assumed to be uniform, and the height of the liquid film can be estimated as

$$H_{F1} \geq 2.35\sqrt{A_{N1}} Re_{N1}^{0.022} \sqrt{Fr_{N1}} (1 + f_{N1})^{-0.25} \tag{6-14}$$

$$Fr_{N1} = \frac{V_{m,N1}^2}{gD_{PS}} \tag{6-15}$$

$$A_{N1} = \frac{\pi}{4} D_{N1}^2 \tag{6-16}$$

$$f_{N1} = Q_g / Q_l \tag{6-17}$$

where A_{N1} is the cross area of inlet nozzle; $f_{N1}$is the gas to liquid volumetric ratio.

c) The Pipe-SEP inlet is the 'slotted' inlet. This slot-type inlet is inexpensive, easy to construct, and generally gives good performance. If foamy oil is present, it is preferred to use special a designed inlet internal to avoid any liquid fall rapidly. Such as a helical internal component has been tested by Roberto (2011), and they observed the separator with the helix can have a more stable liquid interface than those without the helix. In the present study, it is assumed that the potential problems due to waxing, foaming and emulsions are solved through chemical injections. Therefore, the height of inlet section H_{LIN1} is determined by

$$H_{LIN1} = 0.3 + \frac{1}{2} D_{N1} \tag{6-18}$$

d) The liquid level in Pipe-SEP generally is maintained as the same as the Hi-SEP. Since the Pipe-SEP is smaller than the Hi-SEP in diameter, when the intermittent flow enters into the separation system, the liquid level in the Pipe-SEP is higher than in the Hi-SEP (as illustrated in Figure B-6 in Appendix B) and, as a consequence, agitated flow occurs in the Pipe-SEP. However, this phenomenon normally can be damped very quickly and has an insignificant effect on the overall efficiency. If it becomes the bottleneck of the separator operation, it is often preferred to estimate the peak level of the Pipe-SEP. From a simplified design point of view, the liquid hold up level H_{H1} and the liquid surge level H_{S1} of Pipe-SEP are equal to the Hi-SEP's level.

$$H_{H1} = H_{H2} \tag{6-19}$$

$$H_{S1} = H_{S2} \tag{6-20}$$

e) The low liquid level of Pipe-SEP, H_{LLL1} prevents a large amount of gas from entering the Hi-SEP. The liquid inter-middle pipe connected to the Hi-SEP is often submerged in the liquid phase under normal operation. This type of inlet is to reduce the splashing of separated liquid. Although the height of the H_{LLL1} is not so critical to the system performance, the practice design should consider the limit of gas blow out. Therefore, the minimum value of H_{LLL1} should be determined by the largest value from Table A-3 in Appendix A, which is expressed as follows:

$$\begin{cases} H_{LLL1} \geq 0.15 & \text{if } P \geq 20\ bar \\ H_{LLL1} \geq 0.38 & \text{if } P < 20\ bar \end{cases} \tag{6-21}$$

In extreme cases, the liquid level in Hi-SEP falls below the liquid inter-middle pipe, the Pipe-SEP becomes non-self-regulated. For the limit of gas blow out, it is required that the liquid level in Pipe-SEP is always above the entrance of the liquid inter-middle pipe. Since the equilibrium liquid level is determined by the pressure loss across the inter-middle gas pipe and liquid pipe, Eq. (6-22) and Eq. (6-23) give the limit condition

$$(\rho_l g(H_{LLL1} + H_{LLLL1} - H_{B1}) + \sum hfl_1) \geq \sum hfg_1 \tag{6-22}$$

$$(\rho_l g(H_{LLL1} + H_{LLLL1} - H_{B1}) + f_{l1}\rho_l(\frac{Q_l}{A_{N1}})^2 \geq f_{g2}\rho_g(\frac{Q_g}{P_2 A_{N1}})^2 \tag{6-23}$$

where f_{l1} f_{g2} are the pressure loss coefficients for inter-middle liquid pipe and gas pipe, respectively. They were defined in Eq. (4-11) and Eq. (4-15).

f) The low-low liquid level of Pipe-SEP, H_{LLLL1} is determined by

$$H_{LLLL1} \geq \max(2 \times DN_2, H_{B1} + D_{PS}/2) \tag{6-24}$$

$$H_{B1} = D_{PS}/2 \tag{6-25}$$

6.4.4 Inter-Middle Pipe

Similar to the inlet pipe, the diameter of the gas inter-middle nozzle, $D_{N\mathrm{g}}$ can be calculated from

$$D_{N\mathrm{g}} \geq \left(\frac{4Q_{m,N\mathrm{g}}}{\pi 60/\sqrt{\rho_{m,N\mathrm{g}}}}\right)^{1/2} \times 0.0604 \tag{6-26}$$

$$Q_{m,N\mathrm{g}} = Q_g + Q_{l,N\mathrm{g}} \tag{6-27}$$

$$Q_{l,N\mathrm{g}} = Q_l \times LCO_{PS} \tag{6-28}$$

$$\rho_{m,N\mathrm{g}} = \rho_l \lambda_{N\mathrm{g}} + \rho_g(1 - \lambda_{N\mathrm{g}}) \tag{6-29}$$

$$\lambda_{N\mathrm{g}} = \frac{Q_{l,Ng}}{Q_{l,Ng} + Q_g} \tag{6-30}$$

where $Q_{m,N\mathrm{g}}$ is the flow rate of mixture in the gas inter-middle pipe; $\rho_{m,N\mathrm{g}}$ is the mixture density; $\lambda_{N\mathrm{g}}$ is the liquid volumetric fraction.

The liquid inter-middle pipe can be calculated from

$$D_{N\mathrm{l}} \geq \left(\frac{4Q_{m,N\mathrm{l}}}{\pi 60/\sqrt{\rho_l}}\right)^{1/2} \times 0.0604 \tag{6-31}$$

$$Q_{m,N\mathrm{l}} = Q_l \times (1 - LCO_{PS}) \tag{6-32}$$

where $Q_{m,N\mathrm{l}}$ is the flow rate of mixture in the liquid inter-middle pipe.

The diameter of the inter-middle pipe will be the largest of the $D_{N\mathrm{g}}$ and $D_{N\mathrm{l}}$.

$$D_{N2} = \max\left[D_{N\mathrm{g}}, D_{N\mathrm{l}}\right] \tag{6-33}$$

The length is at least 10 diameter lengths

$$L_{N2} \geq 10 \times D_{N2} \tag{6-34}$$

A suitable 'g' force should be maintained between 50 and 200 at the Hi-SEP gas inlet as well, which is expressed as

$$50 \leq G_{HS} \leq 200 \tag{6-35}$$

$$G_{HS} = \frac{V_{m,Ng}^2}{D_{HS}g} = \frac{16Q_{m,Ng}^2}{\pi^2 D_{N2}^2 D_{HS}g} \tag{6-36}$$

where D_{HS} is the Hi-SEP diameter.

6.4.5 Hi-SEP Gas Capacity Constraint

Hi-SEP has a vane type mist eliminator on the top. The purpose of the vane type mist eliminator is to capture the entrained droplets and condition the gas outlet flow. The superficial gas velocity should be maintained at appropriate levels in the mist eliminator. According to Stewart and Arnold (2008), if a set of parallel vanes installed on the top, the maximum gas velocity defined by

$$V_{t2} \leq 0.75 \times 2.38 \times (\frac{\sigma g}{\rho_l})^{0.25} (\frac{\rho_l - \rho_g}{\rho_g})^{0.5} \tag{6-37}$$

Expressing the gas velocity in terms of average volumetric flow rate and the cross-sectional area for gas flow

$$\frac{4Q_g}{\pi(D_{HS}^2 - D_N^2)} \leq 0.75 \times 2.38 \times (\frac{\sigma g}{\rho_l})^{0.25} (\frac{\rho_l - \rho_g}{\rho_g})^{0.5} \tag{6-38}$$

6.4.6 Hi-SEP Liquid Capacity Constraint

The total height of the Hi-SEP is divided into seven sections as well, as shown in Figure 6-1. The Hi-SEP height H_{HS} is the sum of the heights of each section.

$$H_{HS} = H_{C2} + H_{F2} + H_{LIN2} + H_{H2} + H_{S2} + H_{LLL2} + H_{LLLL2} \tag{6-39}$$

a) H_{C2} is the height from the FER to the top tangent line of the Hi-SEP, and the minimum height is required as

$$H_{C2} \geq (H_{T2} + 3 \times D_{N2} + H_E) \tag{6-40}$$

$$H_{T2} = \frac{D_{HS}}{2} \tag{6-41}$$

where H_E is the height of mist eliminator, which is usually taken as 0.2m.

b) H_{F2} is the Hi-SEP liquid film height, which is can be estimated as

$$H_{F2} \geq 2.35\sqrt{A_{N2}}Re_{N2}^{0.022}\sqrt{Fr_{N2}}(1+f_{N2})^{-0.25} \tag{6-42}$$

$$Fr_{N2} = \frac{V_{m,N2}^2}{gD_{HS}} \tag{6-43}$$

$$A_{N2} = \frac{\pi}{4}D_{N2}^2 \tag{6-44}$$

$$f_{N2} = Q_g/(Q_l \times LCO_{Ps}) \tag{6-45}$$

where A_{N2} is the cross area of inter-middle nozzle; $f_{N2}$is the gas to liquid volumetric ratio.

The H_{F2} section is also required when providing the droplet disengagement space. As known from previous chapters, the Hi-SEP is subject to a very high GVF (>95 Vol%) incoming flow. The majority portion of the incoming liquid is in the form of dispersed droplet. The Hi-SEP's GEC has the exponent 6, which indicates that the Hi-SEP woks like the 'sieve' type of separator. Therefore, it is assumed that the Hi-SEP can capture all droplets greater than its cut size and will lose those that are smaller.

The Sauter mean droplet size in Hi-SEP, d_{32} can be estimated according to Eq. (5-12). Y_d is defined as the mass fraction of the droplets with diameter greater than d. It is required that the Hi-SEP can capture 99% of incoming droplets, so the limit of the cut size can be set by the following equation

$$Y_d = \exp[-(\frac{d_{50-HS}}{d_{32}})^n] \geq 0.99 \tag{6-46}$$

where d_{50-HS} is the cut size for Hi-SEP. Consequently, an extra constraint on the H_{F2} is set as

$$d_{50-HS} \leq \sqrt{\frac{9D_{N2}\mu_g}{\pi N_s v_{m,N2}(\rho_l-\rho_g)}} \tag{6-47}$$

$$H_{F2} \geq \pi D N_s \tag{6-48}$$

H_{F2} will be the largest of the height calculate by Eq.(6-42) and Eq.(6-48).

c) The upper gas inlet of the Hi-SEP should be above the inlet of the Pipe-SEP to avoid the incoming liquid impact on the inter-middle gas pipe and to reduce the swirl intensity in the Pipe-SEP. As concluded from the CFD simulation, the gas between these two pipes should be kept at least equal to 0.2m. The height of Hi-SEP inlet section is determined by

$$H_{LIN2} \geq \max[\left(0.3 + \frac{1}{2} D_{N2}\right), (H_{LIN1} + 0.2)] \tag{6-49}$$

d) The Hi-SEP should be designed to handle a certain slug and surge flow without causing operational instability. The desired slug and surge capacity can be determined based on the simulation of the flow in the flow lines. The slug and surge capacity constraints related to the normal liquid level are formulated as:

$$V_{slug} \leq \frac{\pi}{4}(D_{HS}^2 + D_{PS}^2) H_{S2} \tag{6-50}$$

$$V_{surge} \leq \frac{\pi}{4}(D_{HS}^2 + D_{PS}^2) H_{H2} \tag{6-51}$$

If there is lack of slug and surge information, the liquid hold up level H_{H2} and the liquid surge level H_{S2} of Hi-SEP are determined by the liquid hold up time T_{H2} and the liquid surge time T_{S2}, which can obtained from Table A-2 in Appendix A. The holdup liquid level and surge liquid level are calculated as

$$H_{H2} \geq \frac{T_{H2} Q_l}{\left(\frac{\pi}{4}\right)(D_{HS}^2 + D_{PS}^2)} \tag{6-52}$$

$$H_{s2} \geq \frac{T_{S2} Q_l}{\left(\frac{\pi}{4}\right)(D_{HS}^2 + D_{PS}^2)} \tag{6-53}$$

e) The low liquid level of Hi-SEP, H_{LLL2} is based on the required retention time. Residence time is an empirical factor selected for reasons other than just degassing, such as proper instrumentation operation and process control. The retention time in Hi-SEP is usually 30s, which is insufficient to achieve a gas free liquid, but is enough to achieve the desired 20% gas carry under in the separation and boosting application. Otherwise, a liquid hold-up drum should be equipped with the Pipe-Hi-SEP system to provide an extra volume.

$$H_{LLL2} = \frac{4T_{LLL2}Q_l}{\pi(D_{HS}^2 - D_{N2}^2)} \tag{6-54}$$

Or the low liquid level of Hi-SEP is obtained from Table A-3 in Appendix A.

$$\begin{cases} H_{LLL2} \geq 0.15 & \text{if } P \geq 20\ bar \\ H_{LLL2} \geq 0.38 & \text{if } P < 20\ bar \end{cases} \tag{6-55}$$

Ideally, the liquid level in Hi-SEP should always be above the low liquid level. If the low liquid level is reached, the system will automatically recirculate part of the flow until the liquid level goes back to normal.

f) The low-low liquid level constraint is based on operational considerations. If the low-low level is reached, an alarm will notify the operator, and the system will automatically recirculate all the flow until the liquid level goes back to normal. The Hi-SEP low-low liquid level height is required as

$$H_{LLLL1} \geq \max(2 \times DN_2, H_{B2} + D_{HS}/2) \tag{6-56}$$

$$H_{B2} = D_{HS}/2 \tag{6-57}$$

6.4.7 Hi-SEP Liquid Re-Entrainment Constraints

As mentioned earlier droplet entrainment can occur in a swirled liquid film. Entrainment refers to liquid droplets breaking away from a gas liquid interface to become suspended in the gas phase. Liquid re-entrainment is often caused by high gas velocities. The term re-entrainment is used in Hi-SEP design because it generally is assumed that droplets have settled to the liquid film phase and then are returned to the gas phase. Re-entrainment must be avoided in Hi-SEP. This necessity imposes an upper limit on the gas velocity allowed across the liquid film surface in the upper section of the Hi-SEP.

Ishii and Grolmes (1975) proposed correlations for predicting the minimum velocity required for re-entrainment of liquid into gas for concurrent flow. $V_{t2,max}$ is defined through the film Reynolds number and an interfacial viscosity number that characterise the two phase flow. These are defined as:

$$Re_f = \rho_l u_f \delta / \mu_l \tag{6-58}$$

$$N_\mu = \mu_l / [\rho_l \sigma (\frac{\sigma}{(v_{\theta,l}^2 / D_{HS})(\rho_l - \rho_g)})^{0.5}]^{0.5} \tag{6-59}$$

$$V_{\theta,l} = V_{\theta}/2 \tag{6-60}$$

where $V_{\theta,l}$ is the tangential film velocity. In case of missing information regarding the film, $V_{\theta,l}$ is assumed as half of the gas tangential velocity, V_{θ} near the separator wall.

V_{θ} can be estimated from the CFD results in chapter 5 and is expressed as follows

$$V_{\theta} = \frac{((-3.1X+4.72)\times V_{sg-inlet}-1.38)(\frac{0.15}{D_{HS}})\text{^}0.3}{D_{HS}/2} \tag{6-61}$$

Table 6-1 presents the re-entrainment criteria.

Table 6-1 Re-entrainment criteria

Re_f	N_{μ}	V_{t2},max
<160	-	$0.4572(\sigma/\mu_l)(\rho_l/\rho_g)^{0.5}Re_f^{-0.5}$
$160 \leq Re_f \leq 1635$	$\leq 1/15$	$3.5905(\sigma/\mu_l)(\rho_l/\rho_g)^{0.5}N_{\mu}^{0.8}Re_f^{-1/3}$
$160 \leq Re_f \leq 1635$	$> 1/15$	$0.4115(\sigma/\mu_l)(\rho_l/\rho_g)^{0.5}Re_f^{-1/3}$
>1635	$\leq 1/15$	$0.3048(\sigma/\mu_l)(\rho_l/\rho_g)^{0.5}Re_f^{0.8}$
>1635	$> 1/15$	$0.03493(\sigma/\mu_l)(\rho_l/\rho_g)^{0.5}$

$V_{t2,max}$ is the maximum allowed gas velocity through the film surface. The CFD simulation in chapter 5 also showed that at the near wall area, the gas axial velocity is about 2-4 times the mean axial velocity. Therefore, the V_{t2},max imposed constraint on the gas capacity can be expressed as

$$V_{t2,max} \leq \frac{(-19X+15.38)\times V_{sg-inlet}+17.4X-9.98)(0.15/D_{HS})\text{^}2}{D_{HS}/2} \tag{6-62}$$

X is assumed as 0.2m for a conventional design.

6.4.8 Geometrical Constraints

The gas and liquid outlets are mounted with vortex breakers. These are designed according to the suggestions by Hernandez *et al*., (2007) of being twice the size of the inner diameter of the nozzles. From the installation point of view, the following relationships should be met

$$D_{HS} \geq 2 \times D_{N2} \tag{6-63}$$

$$D_{PS} \geq 2 \times D_{N2} \tag{6-64}$$

$$L_{N2} \geq D_{HS} + D_{PS} \tag{6-65}$$

6.4.9 Slenderness Ratio

The slenderness ratio is defined as

$$SR = H/D \tag{6-66}$$

In a conventional vertical separator whose sizing is liquid dominated, it is common to choose slenderness ratio not greater than 3 to keep the height of the liquid collection section to a reasonable level. Choices in the range of 3 to 4 are most common. In the present system, the slenderness ratio is not critical; the height of the Pipe-Hi-SEP system is restricted by the installation space available and other environment factors. For safety considerations, the SR is normally less than 15.

6.4.10 Mechanical Design Equations

According to Grodal and Realff (1999), the wall thickness in the cylindrical section is determined as

$$t_{cs} \geq \frac{P_D D_i}{2\sigma E - 1.2P_D} + t_c \tag{6-67}$$

where the design pressure is the operating pressure with either 2 bar added to it or increased by 10%, whichever is greater:

$$P_D \geq \max[P + 200000, 1.1P] \tag{6-68}$$

The allowable stress is a safety factor towards the material tensile strength. ASME suggests a safety factor of 4. The tensile strength for the carbon steel commonly used for separators is 3800 bar, i.e. $\sigma = 950\ bar$. The joint efficiency ranges from 0.6 to 1.0 for 100% X-rayed joints. The corrosion allowance typically ranges from 1.5 mm to 3.2 mm.

6.4.11 Vessel Weight

The vessel weight is estimated to be

$$W = \pi(D_{HS}H_{HS} + t_{cs,PS}D_{PS}H_{PS}) \tag{6-69}$$

The designs of heads and the weight of the inlet pipe and inter-middle pipe are not included.

6.5 The Mathematic Program

For the optimised design of Pipe-Hi-SEP, a mathematic program is developed in MATLAB as shown in Appendix E. The program consists of three sub-programs: PIPEHIOptimal, PIPEHIconstraint and PIPEHIcost. The PIPEHIOptimal consists of initial guess and optimization function. The PIPEHIconstraint includes all the equalities and inequalities, which presents the Pipe-Hi-SEP relationship. The PIPEHIcost consists of the objective function.

A total of 21 design variables are selected. Even though the number of variables can be reduced by grouping some of the variables, the program is trying to keep the design straightforward. The design variables are listed in Table 6-2 below.

Table 6-2 Design variables

Pipeline	Pipe-SEP	Hi-SEP
D_{N1}	D_{PS}	D_{HS}
D_{N2}	H_{C1}	H_{C2}
D_{N3}	H_{F1}	H_{F2}
	H_{LIN1}	H_{LIN2}
	H_{S1}	H_{S2}
	H_{H1}	H_{H2}
	H_{LLL1}	H_{LLL2}
	H_{LLLL1}	H_{LLLL2}
	$t_{cs,PS}$	$t_{cs,HS}$

The inputs to the program consist of two groups of parameters: the design parameter and constraints, and initial guesses of design variable. The design parameter and constants are listed in Table 6-3. The initial guesses of the design variable can use any reasonable guess.

Table 6-3 The design parameters and constants

Design parameters and constants		
Q_l	ρ_l	T_{LLL2}
Q_g	ρ_g	T_{H2}
P	$\sigma_{l,g}$	T_{S2}
T	μ_l	D_{m1}
LCO	μ_l	D_{m2}

6.6 Case Study

The typical design case reported in the literature has been selected as the reference case for the optimisation. The selected reference case is associated to an operating pressure of 68.94 bar (1000 psia) and operating temperature 15.55°C (60°F). The gas flow is 11800 Sm^3/hr (10MMscfd) at 0.6 specific gravity. The liquid flow is 13.24 m^3/hr (2000bpd) at 40 °API. Furthermore, a retention time of 3 minutes is assumed. There was no specific slug or surge volume requirement; however 24" were designed between the normal liquid level and the inlet to provide the slug volume. The separator shall be designed to separate 140mμ liquid droplets. The reference case has been calculated using the conventional design method, a 0.9144m (36in) ×3.04m (10ft) vertical separator were selected. According to the Eq. (6-67) and Eq. (6-68), the wall thickness of the separator is estimated as 51.4mm, which yields a total weight of 3524Kg.

In the present Pipe-Hi-SEP design, a total hold up and surge time of 1 min are defined in order to corresponding the same slug volume in the reference case. The design parameters are summarized in Table 6-4. The constants and known variables are listed in Table 6-5.

Table 6-4 Design parameters to Pipe-Hi-SEP case study

Operating pressure	68.94 bar
Operating temperature	15.55°C
Gas flow rate	11800 Sm^3/hr
Gas density	59.42 kg/ m^3
Gas viscosity	1.03e-05 pa.s
Liquid flow rate	13.24 m^3/hr
Liquid density	824.9 kg/ m^3
Liquid viscosity	3.0e-03 pa.s
Liquid surface tension	0.07 N/m

Table 6-5 Constants and known variables for Pipe-Hi-SEP case study

Retention time	3 minutes
Holdup time	30 s
Surge time	30 s
Pipe-SEP separation requirement	500 mμ (or LCO<0.05)
Hi-SEP separation requirement	50 mμ

The initial guess is listed in Table 6-6. The program ran 5 SQP-iterations to find the optimal solution. The outcome of the optimal solution is summarized in Table 6-7. The weight of the Pipe-Hi-SEP is 3263 Kg, which is 261 Kg less compared to the reference design.

Table 6-6 Initial value of Pipe-Hi-SEP case study

D_{HS}	0.5	D_{PS}	0.2
H_{F2}	0.6	H_{F1}	0.1
H_{C2}	1.0	H_{C1}	0.1
H_{LLLL2}	0.2	H_{LLLL1}	0.1
H_{LLL2}	1.7	H_{LLL1}	0.1
H_{H2}	0.3	H_{H1}	0.3
H_{S2}	0.3	H_{S1}	0.3
H_{LIN2}	0.4	H_{LIN1}	0.2
$t_{cs,HS}$	32	$t_{cs,PS}$	20
D_{N1}	0.11	D_{N2}	0.09
D_{N3}	0.02		

Table 6-7 The optimised solution of Pipe-Hi-SEP design study

D_{HS}	0.727	D_{PS}	0.256
H_{F2}	0.86	H_{F1}	0.57
H_{C2}	0.55	H_{C1}	0.48
H_{LLLL2}	0.15	H_{LLLL1}	0.17
H_{LLL2}	1.61	H_{LLL1}	0.15
H_{H2}	0.26	H_{H1}	0.26
H_{S2}	0.26	H_{S1}	0.26
H_{LIN2}	0.55	H_{LIN1}	0.35
$t_{cs,HS}$	41.58	$t_{cs,PS}$	16.74
D_{N1}	0.102	D_{N2}	0.087
D_{N3}	0.042	Weight	3263.50

For this specific design case, a Multi-Pipe-Hi-SEP made of parallel Pipe-Hi-SEP units has also been investigated. The inlet flow rate is assumed to be distributed evenly into each unit. The outcome of the optimal solution is also summarised in Table 6-8. It is clear that as the flow rate is reduced, the separator diameter will be reduced, and as a consequence, the wall thickness and the weight of the Pipe-Hi-SEP units will be reduced. As for the height of swirl film, it decreases with decreasing flow rate. Therefore, a slight decrease of the height of the upper part of the separator can be seen

as expected. Since the lower part is mainly determined by the retention time and slug time, the height of the lower part is the same for all cases.

Figure 6-2 shows the plot of total weight vs. number of units. The gradient of the total weight is seen to reduce greatly when the unit increases from 1 to 3 while it reduces slightly when the number of units is more than 4. It can be concluded that the 4 parallel Pipe-Hi-SEP units with Pipe-SEP D×H = 0.128×1.73 and Hi-SEP D×H = 0.363×3.21 is the desired design.

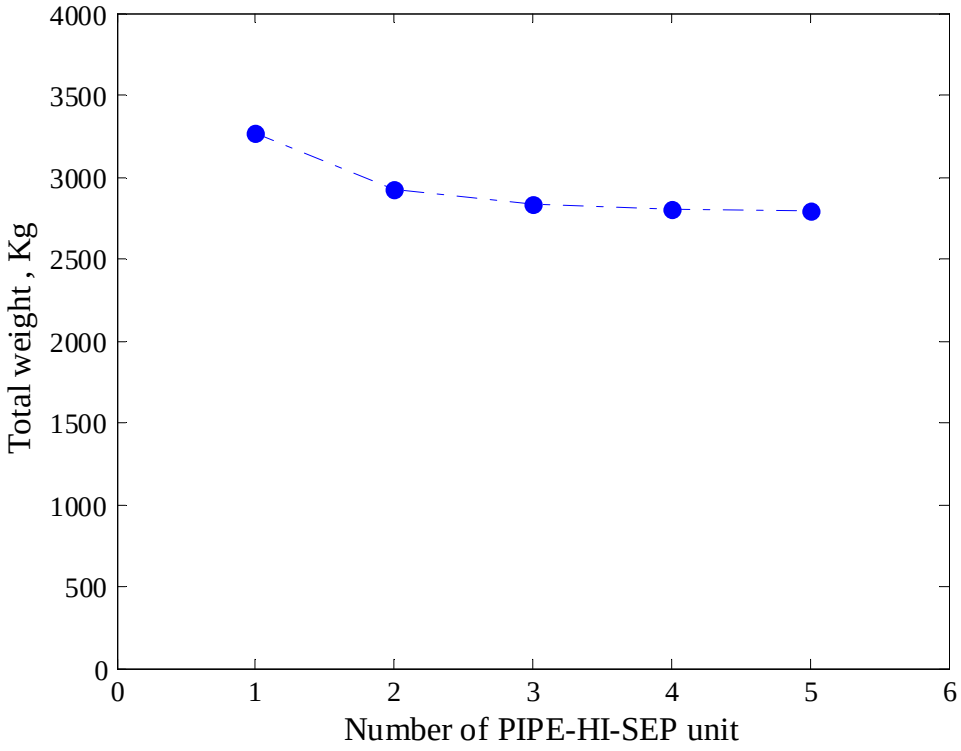

Figure 6-2 Plot of the relationship of the Pipe-Hi-SEP unit number and the total weight

Table 6-8 The result of Multi-Pipe-Hi-SEP case study

Number of Pipe-Hi-SEP unit	1	2	3	4	5
Gas flow, m^3/h	11800	5900	3933	2950	2360
Liquid flow, m^3/h	13.24	6.62	4.41	3.31	2.65
Operating pressure, bar	68.94	68.94	68.94	68.94	68.94
Operating temperature, °C	15.55	15.55	15.55	15.55	15.55
Inlet GVF, %	92.80	92.80	92.80	92.80	92.80
Mixture inlet nozzle diameter, m	0.102	0.072	0.059	0.051	0.046
Hi-SEP G force	8.85	12.51	15.32	17.70	19.79
Gas inter-middle nozzle diameter, m	0.087	0.061	0.050	0.043	0.039
Liquid inter-middle nozzle diameter, m	0.042	0.030	0.025	0.021	0.02
Hi-SEP diameter, m	0.727	0.514	0.420	0.363	0.325
Hi-SEP terminal velocity, m/s	0.11	0.11	0.11	0.11	0.11
Hi-SEP gas part length, m/s	1.41	0.88	0.69	0.59	0.53
HF2	0.86	0.43	0.29	0.21	0.17
HC2	0.55	0.45	0.40	0.38	0.36
HT2	0.17	0.12	0.10	0.08	0.08
Hi-SEP liquid part length, m	2.64	2.63	2.62	2.62	2.62
HLLLL2	0.15	0.15	0.15	0.15	0.15
HB2	0.17	0.12	0.10	0.09	0.08
HLLL2	1.61	1.61	1.61	1.61	1.61
HH2	0.26	0.26	0.26	0.26	0.26
HS2	0.26	0.26	0.26	0.26	0.26
HLIN2	0.54	0.53	0.52	0.52	0.52

Hi-SEP Height, m	4.25	3.70	3.51	3.41	3.34
Hi-SEP L/D ratio	5.57	6.82	7.89	8.83	9.67
Pipe-SEP diameter, m	0.256	0.181	0.148	0.128	0.114
Pipe-SEP G force	15.49	21.91	26.8	30.98	34.64
Pipe-SEP terminal velocity, m/s	1.04	1.04	1.04	1.04	1.04
Pipe-SEP gas part length, m/s	1.05	0.82	0.71	0.64	0.59
HF1	0.57	0.48	0.43	0.40	0.38
HC1	0.48	0.39	0.28	0.24	0.21
HT1	0.17	0.12	0.10	0.09	0.08
Pipe-SEP liquid part length, m	1.20	1.14	1.11	1.09	1.08
HLLLL1	0.17	0.12	0.10	0.08	0.07
HLLL1	0.15	0.15	0.15	0.15	0.15
HH1	0.26	0.26	0.26	0.26	0.26
HS1	0.26	0.26	0.26	0.26	0.26
HLIN1	0.35	0.33	0.33	0.32	0.32
Pipe-SEP Height, m	2.26	1.96	1.82	1.73	1.67
Pipe-SEP L/D ratio	8.81	10.80	12.29	13.53	14.60
Hi-SEP wall thickness, mm	41.58	30.34	25.36	22.39	20.36
Pipe-SEP wall thickness, mm	16.74	12.77	11.01	9.97	9.25
Pipe-Hi-SEP unit weight, Kg	3263.50	1462.21	943.64	699.72	558.15
Total weight, Kg	3263.50	2924.42	2830.93	2798.90	2790.77

6.7 Summary

A systematic optimisation procedure for the design of PIPE-HI separator has been developed. The model is a combination of conventional design procedures and the unique cyclonic hydrodynamic relationship developed from the experimental results and the CFD simulation. A case study was performed and successfully illustrated the efficiency and effectiveness of the proposed systematic optimised design method.

7 CONCLUSIONS AND RECOMMENDATIONS

7.1 Main Conclusions

Pipe-SEP experiment

1. Based on the observation of the flow behaviour in the scaled-down Pipe-SEP, three distinct flow regimes were identified, namely swirled, agitated, and gas blow-by. The transition of the flow regimes are affected by flow characteristics, mixture properties, geometry of the separator, and downstream conditions. Under normal operating conditions, the Equilibrium Liquid Level (ELL) is below the inlet. The flow regime is generally swirled flow and the liquid carry over increases with gas flow rate; however, when the liquid flow rate is increased to a certain level, the ELL exceeds the inlet level, and the flow starts to transition to agitated flow. The most interesting result obtained for agitated flow is that the liquid carry over decreases as the gas flow rate increases. As the ELL falls below the liquid discharge outlet, gas blow-by occurs and results in significant amount of gas carry under.
2. A predictive algorithm which is capable of predicting the transition of flow regimes was developed. Moreover, semi-empirical correlations were used to estimate the separation efficiency to account for the existence of varied flow regimes. The flow regimes were well predicted by the model. The comparison of the ELL and separation efficiency agrees well with the experiment data. The model can serve as a design tool to support decision-making in early design stages.

Numerical simulation

1. Fluid Computational Dynamic (CFD) simulation of the Pipe-SEP flow field shows that the swirl velocity profile is characterised by a forced vortex, where a uniform angular velocity is present at all radii, like a rotating solid body. The maximum tangential velocity exists near the separator wall and the gradient along axial direction is negligible. The tangential velocity profile exhibits better symmetry as the axial distance increases. The presence of the ‘L’ gas outlet section has a slightly positive effect on the velocity profile, but also an increase of the Pipe-SEP pressure drop.

2. The axial velocity in the Pipe-SEP I is characterised by a slightly reverse flow pattern, where near the wall the flow is directed upward, while in the centre region the flow is directed downward. The maximum axial velocity equals nearly 3-4 times the mean axial velocity and the amplitude of the maximum axial velocity is reduced along the axial direction. The high axial velocity near the wall is the main force to drag the wall film up, and consequently, liquid creep and re-entrainment could occur.
3. The axial velocity in the Pipe-SEP II is identical to the Pipe-SEP I in the outer region, while in the centre region the axial velocity is suppressed due to the presence of the gas outlet section.
4. The effect of the gas inlet velocity and separator diameter on the flow profile was studied for the Pipe-SEP II. The swirl velocity profile is confirmed to be forced vortex at all conditions. Both the maximum tangential velocity and the maximum axial velocity near the separator wall increase with the increasing of the gas inlet velocity. The boundary of the inner and outer region is seen to be the same at all inlet velocities. The velocity profile relies less on the changing of the separator diameter, but a wider inner downward flow region is clearly observable as the separator diameter increases. Universal expressions are developed to describe the velocity distribution.
5. The “L” shape gas outlet section has a strong influence on the distribution of the velocity near the separator wall. The axial and tangential velocity reduces sharply when the flow impacts the horizontal part of the gas outlet section, resulting in a less intensive vortex in the separator. Therefore, a minimum 0.2 m gap between the inlets with the horizontal part of the gas out section is recommended.
6. By means of DPM modelling the cut size and the grade efficiency curve can be obtained by tracking particles with different diameters. The cut size of the Pipe-SEP II is slightly smaller than the Pipe-SEP I’s due to the extra surface provided by the gas out section. The overall separation efficiency is estimated by integration of the grade efficiency curve and the R-R particle size distribution. The smaller cut size in Pipe-SEP II results in a slightly higher separation efficiency.
7. Based on a comparison of different inlet gas velocity effects on the grade efficiency, it can be concluded that the gas velocity will not affect the grade efficiency, when the droplet is smaller than the cut size diameter. But normally the higher the inlet

gas velocity the more intense the swirl, and consequently, an increase of the separator efficiency will occur.

8. The effect of the separator diameter on the grade efficiency was studied by simulating a Hi-SEP, which is geometrically similar to the Pipe-SEP, but with a bigger diameter. When the droplets size is bigger than the cut size, the Hi-SEP performed as well as the Pipe-SEP, but due to less intensity in the swirl, the overall efficiency of Hi-SEP was likely below the one of the Pipe-SEP.
9. The cut sizes calculated by CFD simulation are compared with those predicted by the Barth model and the Rosin model. The Barth model over-predicted the maximum bangtail velocity, and consequently, under-predicted the cut size. Moreover, a significant deviation from the grade efficiency curve confirmed that the assumption of Barth model is not suitable for Pipe-SEP. The Rosin model predicted a reasonable close cut size and yielded a better agreement with the CFD predicted grade efficiency curve. However, the Rosin model doesn't account for the effect of separator diameter, which may under-predict the cut size as the separator diameter increases.
10. A Stokesian scaling rule is capable of estimating the performance of 'commercial Pipe-SEP' from the laboratory scale prototype. The effect of the inlet velocity and separator diameter in the separator performance can be captured. The agreement between the Scaling rule and CFD simulation on the cut size of Hi-SEP was reasonable.

Optimising design

1. The Pipe-Hi-SEP system was formulated into a mathematical program, which combined the existing conventional separator design procedure and the unique fluid dynamic and mechanical constrains of a cyclonic separator. By means of a non-linear optimisation procedure, an optimal Pipe-Hi-SEP system can be obtained that had the lowest weight at the required flow rate and separation efficiency.
2. The application of this optimisation procedure for practical engineering design is illustrated by a case study. It is seen that the efficiency and effectiveness of the Pipe-Hi-SEP design procedure are improved significantly. Using the formulated mathematical program, the optimum design is obtained through a simultaneous search over all the design variables. Moreover, the solution provides the designer with insight into what constrains the design.

7.2 Suggestions for Further Work

1. Although the classic cyclone model and droplet distribution model is capable of predicting the LCO at low liquid loading incoming flow, the model could still be improved, especially with respect to the mass loading effect. It was shown that the liquid film on the separator wall affects the separation efficiency significantly. In the present study, the prediction of the liquid film is based on the annular flow, whereas the characteristic may different with the swirl flow.
2. For the laboratory-scale Pipe-SEP, the LCO is less than 1% and the GCU is less than 5% under the normal operation conditions. The accuracy of the measurement could be improved by implementing LDA.
3. Although the RSM model is capable of capturing the main flow features of the Pipe-SEP, more accurate prediction could be gained by using the Large Eddy Simulations and more insight could be gained by simulating the wall film. The DPM modelling of Pipe-SEP also benefits from the two-way coupling of droplet and gas flow, whereas omitting this coupling lead to reasonable predictions at relative low computational cost.
4. More research is needed to investigate the influence that the tangential inlet and the "L" shape gas outlet section may bring to the Pipe-SEP, such as erosive wear and vibration of separator body.
5. The optimal design model described in this thesis has illustrated that the method could well be applied to practical Pipe-Hi-SEP engineering. The geometrical parameter of Pipe-Hi-SEP can be characterised by several sections, and the optimisation procedure is straightforward. The model accuracy, however, could be improved by more accurate relationships.
6. The optimal design model is declarative and thus its components can be modified with little effort. For example, the objective could be to minimize cost, length or footprint area and this would require minimal change to the model.

8 REFERENCES

ANSYS(2012). Fluent 12.1 Documentation. ANSYS Inc.

ALEX, C. P. R. 2010. Global overview of offshore oil & gas operations for 2005-2009. offshore magazine.

ALEXANDER, R. M. 1949. Fundamentals of cyclone design and operation Proceedings of the Australian Institute of Ming and Metellurgy, 152-153, 25.

ARATO, E. G., DAVIES, O. M. & SAUNDERS, D. H. 2002. Cyclone separator.

ARPANDI, I. A., JOSHI, A. R., SHOHAM, O., SHIRAZI, S. A. & KOUBA, G. E. 1996. Hydrodynamics of two-phase flow in Gas-Liquid Cylindrical Cyclone separators. SPE Journal, 1, 427-436.

AUSTRHEIM, T. 2006. Experimental Characterization of High Pressure Natural Gas Scrubbers. University of Bergen.

AUSTRHEIM, T., GJERTSEN, L. H. & HOFFMANN, A. C. 2007. Re-entrainment correlations for demisting cyclones acting at elevated pressures on a range of fluids. Energy and Fuels, 21, 2969-2976.

AUSTRHEIM, T., GJERTSEN, L. H. & HOFFMANN, A. C. 2008. An experimental investigation of scrubber internals at conditions of low pressure. Chemical Engineering Journal, 138, 95-102.

AZZOPARDI, B. J. & WREN, E. 2004. What is entrainment in vertical two-phase churn flow? International Journal of Multiphase Flow, 30, 89-103.

BARTH, W. 1956. Design and Layout of the Cyclone Separator on the Basis of New Investigations. Brennstoff-Wärme-Kraft, 8(4), 9.

BIRKELAND, E., JERNSLETTEN, J., OLSEN, G., WAALMANN, J. G. & NYBORG, K. 2004. An Efficient Wellstream Booster Solution for Deep and Ultra Deep Water Oil Fields. Offshore Technology Conference Houston, Texas.

BIRMINGHAM, D. P. & DAVIES, S. R. 1995. Evaluation of Compact Steam/Water Separation Equipment for Gas/Oil Systems. Offshore Europe, . Aberdeen, United Kingdom.

BON, L. 2009. Pazflor: A World Technology First in Subsea Separation. Offshore Europe, . Aberdeen, UK: Society of Petroleum Engineers

BRADLEY, H. B. (ed.) 1992. Petroleum Engineering Handbook: Society of Petroleum Engineers.

BRUNAZZI, E., PAGLIANTI, A. 1998. Design of Wire Mesh Mist Eliminators

AIChE, 44, 505-512.

CALVERT, S., JASHNANI, I.L., YUNG, S. 1974. Entrainment Separators for Scrubbers. The Air Pollution Control Association 971-975.

DERKSEN, J. J. 2003. Separation performance predictions of a stairmand high-efficiency cyclone. AIChE Journal, 49, 1359-1371.

DERKSEN, J. J., SUNDARESAN, S. & VAN DEN AKKER, H. E. A. 2006. Simulation of mass-loading effects in gas-solid cyclone separators. Powder Technology, 163, 59-68.

DEUEL, C., CHIN, Y. D., HARRIS, J., GERMANESE, J. & SEUNSOM, N. 2011. Field Validation and Learning of the Parque das Conchas (BC-10) Subsea Processing System and Flow Assurance Design. Offshore Technology Conference Houston, Texas, USA.

DI SILVESTRO ROBERTO, ABRAND STEPHANIE, SHAIEK SADIA, BUTIN NICOLAS, RIOU XAVIER & DECRIN MARIE KATHLEEN 2011. A Novel Gas/liquid Separator to Enhance Production of Deepwater Marginal. Offshore Technology Conference. Houston, Texas, USA.

DIRGO, J. & LEITH, D. 1985. Cyclone collection efficiency: Comparison of experimental results with theoretical predictions. Aerosol Science and Technology, 4, 401-415.

DOBRAN, F. 1983. HYDRODYNAMIC AND HEAT TRANSFER ANALYSIS OF TWO-PHASE ANNULAR FLOW WITH A NEW LIQUID FILM MODEL OF TURBULENCE. International Journal of Heat and Mass Transfer, 26, 1159-1171.

ELSAYED, K. & LACOR, C. 2011a. The effect of cyclone inlet dimensions on the flow pattern and performance. Applied Mathematical Modelling, 35, 1952-1968.

ELSAYED, K. & LACOR, C. 2011b. Numerical modeling of the flow field and performance in cyclones of different cone-tip diameters. Computers and Fluids, 51, 48-59.

ERDAL, F. M. & SHIRAZI, S. A. Year. Local velocity measurements and computational fluid dynamics (CFD) simulations of swirling flow in a cylindrical cyclone separator. In, 2001. 823-833.

FANTOFT, R., AKDIM, R., MIKKELSEN, R., ABDALLA, T., WESTRA, R. & HAAS, E. D. 2010. Revolutionizing Offshore Production by InLine Separation Technology. SPE Annual Technical Conference and Exhibition. Florence, Italy: Society of Petroleum Engineers

FRANCA, F. A., ROSA, E. S., BANNWART, A. C., MOURA, L. F. & ALHANATI, F. J. Year. Hydrodynamic studies on a cyclonic separator. In, 1996. 281-289.

GERUNDA, A. 1981. How to size liquid vapor separators. chemical engineering 88, 3.

GOMEZ, L. E., MOHAN, R. S., SHOHAM, O., MARRELLI, J. D. & KOUBA, G. E. 1999. Aspect ratio modeling and design procedure for GLCC compact separators. Journal of Energy Resources Technology, Transactions of the ASME, 121, 15-23.

GPSA 1998. GPSA Engineering Data Book, Tulsa, Gas Processors Suppliers Association.

GRODAL, E. O. & REALFF, M. J. Year. Optimal design of two- and three-phase separators: a mathematical programming formulation. In, 1999. PI/.

GRONALD, G. & DERKSEN, J. J. 2011. Simulating turbulent swirling flow in a gas cyclone: A comparison of various modeling approaches. Powder Technology, 205, 160-171.

GRUEHAGEN, H. & LIM, D. 2009. Subsea Separation and Boosting—An Overview of Ongoing Projects. Asia Pacific Oil and Gas Conference & Exhibition. Jakarta, Indonesia: Society of Petroleum Engineers

GUPTA, A. & KUMAR, R. 2007. Three-dimensional turbulent swirling flow in a cylinder: Experiments and computations. International Journal of Heat and Fluid Flow, 28, 249-261.

GUPTA, A. K., LILLEY, D. G. & SYRED, N. 1984. Swirl Flows.

HÅHEIM, S. & GAILLARD, X. 2009. A Simplified Subsea Separation and Pumping System. SPE Annual Technical Conference and Exhibition. New Orleans, Louisiana: Society of Petroleum Engineers

HANNISDAL, A., WESTRA, R., AKDIM, M. R., BYMASTER, A., GRAVE, E. & TENG, D. 2012. Compact Separation Technologies and Their Applicability for Subsea Field Development in Deep Water. Offshore Technology Conference Houston, Texas, USA.

HERNÁNDEZ-SUÁREZ, R., PUEBLA, H. & AGUILAR-LÓPEZ, R. 2007. Parametric approach for the optimal design of knockout drums. Industrial and Engineering Chemistry Research, 46, 7008-7017.

HOFFMANN, A. C., DE GROOT, M., PENG, W., DRIES, H. W. A. & KATER, J. 2001. Advantages and risks in increasing cyclone separator length. AIChE Journal, 47, 2452-2460.

HOFFMANN, A. C. & STEIN, L. E. (eds.) 2008. Gas Cyclones and Swirl Tubes: Principles, Design and Operation: Springer.

HREIZ, R., GENTRIC, C. & MIDOUX, N. 2011. Numerical investigation of swirling flow in cylindrical cyclones. Chemical Engineering Research and Design, 89, 2521-2539.

ISHII, M. & GROLMES, M. A. 1975. INCEPTION CRITERIA FOR DROPLET ENTRAINMENT IN TWO-PHASE CONCURRENT FILM FLOW. AIChE Journal, 21, 308-318.

JIAO, J., LIU, Z. & ZHENG, Y. 2007. Evaluations and modifications on Reynolds stress model in cyclone simulations. Chemical Engineering and Technology, 30, 15-20.

JU, G. T., LITTELL, H. S., COOK, T. B., DUPRE, M., CLAUSING, K. M., SHUMILAK, E. & SCHOPPA, W. W. 2010. Perdido Development: Subsea and Flowline Systems. Offshore Technology Conference. Houston, Texas, USA.

KAYA, F. & KARAGOZ, I. 2008. Performance analysis of numerical schemes in highly swirling turbulent flows in cyclones. Current Science, 94, 1273-1278.

KITOH, O. 1991. Experimental study of turbulent swirling flow in a straight pipe. Journal of Fluid Mechanics, 225, 445-479.

L.G. GIBILARO, R. DI FELICE & WALDRAM, S. P. 1985. Generalized friction factor and drag coefficient correlations for fluid-particle interactions. Chemical Engineering Science, 40, 8.

MANNING, FRANCIS S., E, R. & THOMPSON 1991. oilfiled processing of petroleum, Tulsa, penn well books.

MANTILLA, I., SHIRAZI, S. A. & SHOHAM, O. Year. Flow field prediction and bubble trajectory model in gas-liquid cylindrical cyclone (GLCC) separators. In, 1999.

MARLIN, T. E. 2000. Process control : designing processes and control systems for dynamic performance Boston, McGraw-Hill.

MUSCHELKNAUTZ 1972. Chemie-Ing.-Techn.

MUSCHELKNAUTZ 1980. VDI-Berichte.

MUSCHELKNAUTZ, E. & DAHL, H. D. 1994. Cyclone as Droplet Separators. Chem Ing Techn, 66, 223-229.

PENG, W., HOFFMANN, A. C., BOOT, P. J. A. J., UDDING, A., DRIES, H. W. A., EKKER, A. & KATER, J. 2002. Flow pattern in reverse-flow centrifugal separators. Powder Technology, 127, 212-222.

RAOUFI, A., SHAMS, M., FARZANEH, M. & EBRAHIMI, R. 2008. Numerical simulation and optimization of fluid flow in cyclone vortex finder. Chemical Engineering and Processing: Process Intensification, 47, 128-137.

RHODES, M. (ed.) 2008. Introduction to Particle Technology: John Wiley & Sons.

ROSA, E. S., FRANÇA, F. A. & RIBEIRO, G. S. 2001. The cyclone gas-liquid separator: Operation and mechanistic modeling. Journal of Petroleum Science and Engineering, 32, 87-101.

ROSA, E. S., MORANDIN, M. L., DIAS, S. G. & FRANCA, F. A. 1996. Liquid film motion under the action of gravitational and centrifugal fields. VI Encontro Nacional Ciencias Termicas-ENCIT, 27-31.

ROSIN, P., RAMMLER, E. & INTELMANN, W. 1932. Zeit.Ver.Deutscher Ing. 76.

SAWANT, P., ISHII, M., HAZUKU, T., TAKAMASA, T. & MORI, M. 2008. Properties of disturbance waves in vertical annular two-phase flow. Nuclear Engineering and Design, 238, 3528-3541.

SCHOOK, R. & ASPEREN, V. V. 2005. Compact separation by means of inline technology. SPE Middle East Oil and Gas Show and Conference, . Kingdom of Bahrain.

SHEPHERD, C. B. & LAPPLE, C. E. 1939. Air Pollution Control: A Design Approach, 127-139.

SHERWOOD, T. K., SHIPLEY, G. H. & HOLLOWAY, F. A. L. 1938. Flooding Velocities in Packed Columns. Ind. Eng. Chem, 30 765–769.

SHOHAM, O. & KOUBA, G. E. 1998. State of the art of gas/liquid cylindrical-cyclone compact-separator technology. JPT, Journal of Petroleum Technology, 50, 58-65.

SHUKLA, S. K., SHUKLA, P. & GHOSH, P. 2011a. Evaluation of numerical schemes for dispersed phase modeling of cyclone separators. Engineering Applications of Computational Fluid Mechanics, 5, 235-246.

SHUKLA, S. K., SHUKLA, P. & GHOSH, P. 2011b. Evaluation of numerical schemes using different simulation methods for the continuous phase modeling of cyclone separators. Advanced Powder Technology, 22, 209-219.

SIRI JACOBSSON , T. A., AND ALEX C. HOFFMANN 2006. experimental and computational fluid dynamic investigation of the flow in and around once through swirl tubes. Ind.Eng.Chem.Res, 45, 5.

SMITH, H. V. 1987. Oil and Gas Separators,Petroleum Engineering Handbook

Society of Petroleum Engineers.

STEENBERGEN, W. & VOSKAMP, J. 1998. The rate of decay of swirl in turbulent pipe flow. Flow Measurement and Instrumentation, 9, 67-78.

STEINMAYER, D. 1995. Use power/mass to estimate drop size in gas/liquid contactors. Chem. Eng. Prog., 91, 72-80.

STEWART, M. & ARNOLD, K. E. (eds.) 2008. Surface Production Operations Gulf Professional Publishing.

SVRCEK, W. Y. & MONNERY, W. D. 1993. Design two-phase separators within the right limits. Chemical Engineering Progress, 89, 53-60.

SWANBORN, R. A. 1988. A new approach to the design of gas-liquid separators for the oil industry.

VESILIND, P. A. 1980. The Rosin-Rammler particle size distribution. Resource Recovery and Conservation, 5, 275-277.

VU, V. K., FANTOFT, R., SHAW, C. & GRUEHAGEN, H. 2008. Comparison Of Subsea Separation Systems. Offshore Technology Conference. Houston, Texas,USA.

WALAS, S. M. 1990. Chemical Process Equipment Selection and Design Houston, Butterworth-Heinemann.

APPENDIXES

Appendix A: Gas-Liquid Separators Design Procedures

The most comprehensive approach of designing gas-liquid separator was presented by Svrcek and Monnery (1993). The following section provides the procedure. The unit is field unit.

Inlet Nozzel

d_N is calculated as

$$d_N \geq \left(\frac{4Q_m}{\pi 60}\right)^{\frac{1}{2}} \quad \text{ft} \qquad \text{(A-1)}$$

$$Q_m = Q_g + Q_l \qquad \text{(A-2)}$$

$$\rho_m = \rho_l \lambda + \rho_g (1 - \lambda) \qquad \text{(A-3)}$$

$$\lambda = \frac{Q_l}{Q_g + Q_l} \qquad \text{(A-4)}$$

Separator Diameter

The terminal velocity is calculated as following

$$v_t = \sqrt{\frac{4g}{3}\left(\frac{\rho_l - \rho_g}{\rho_l}\right)\frac{d_p}{C_D}} \qquad \text{(A-5)}$$

Typically the maximum allowable vertical velocity is set as

$$v_v = 0.75 v_t \qquad \text{(A-6)}$$

Or the maximum allowable velocity at operating conditions is calculated as following

$$V_t = K\sqrt{\frac{\rho_l - \rho_g}{\rho_g}} \qquad \text{(A-7)}$$

The *K* value can be obtained from the Gas Processor's Supplier Association (GPSA) "Engineering Data Book" or from the correlations provided by York Mist Eliminator supplier.

Table A-1 Separator K values

Separator K values		
Mist Eliminator Supplier		
1≤ P ≤15	K=0.1821+0.0029P+0.0460ln(P)	
15 ≤ P ≤ 40	K=0.35	P, psia
40 ≤ P ≤ 5500	K=0.43-0.023ln(P)	
GPSA		
0 ≤ P ≤ 1500	K=0.35-0.01((P-100)/100)	P, psia
NOTE: K has the dimension ft/sec		

The separator diameter can be calculated as

$$D_{VD} = \sqrt{\frac{4Q_g}{\pi v_v}} \tag{A-8}$$

Separator Height

The total height equals to the sum of each sections, as shown in Figure A-1.

$$H_T = H_{LLL} + H_H + H_s + H_{LIN} + H_D \tag{A-9}$$

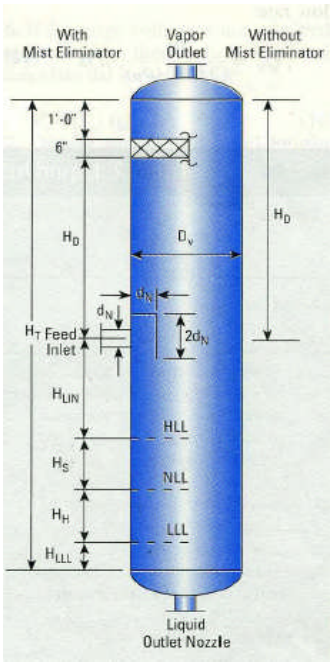

Figure A-1 Vertical two-phase separator (Svrcek and Monnery, 1993)

The holdup timeT_H and surge time T_S can obtain from the Table A-2.

Table A-2 Liquid holdup and surge times

Services	Holdup Times	Surge Times
Feed to column	5	3
Feed to other drum or tank		
With pump or through	5	2
Without pump	2	1
Feed to fired heater	10	3

The holdup liquid level H_s and surge liquid level are calculated as

$$H_H = \frac{T_H Q_l}{(\frac{\pi}{4})D_V^2} \quad \text{(A-10)}$$

$$H_s = \frac{T_S Q_l}{(\frac{\pi}{4})D_V^2} \quad \text{(A-11)}$$

The low liquid level height, H_{LLL} is determined from Table A-3 below

Table A-3 Low liquid level height

Vessel diameter	LLL	
	<300psia	>300psia
≤4ft	15in.	6in.
6ft	15in.	6in.
8ft	15in.	6in.
10ft	6in.	6in.
12ft	6in.	6in.
16ft	6in.	6in.

The height from high liquid level to the centerline of the inlet nozzle is expressed as

$$H_{LIN} = 12 + d_N, \text{ in. (with inlet diverter)} \quad \text{(A-12)}$$

$$H_{LIN} = 12 + \frac{1}{2} d_N, \text{ in. (without inlet diverter)} \quad \text{(A-13)}$$

The disengagement height, from the centerline of the inlet nozzle to 1) The vessel top tangent line if there is no mist eliminator or 2) The bottom of the demister pad

$$H_D = 0.5 D_p \text{ or a minimum of} \quad \text{(A-14)}$$

$$H_D = 36 + 1/2 d_N \text{ (without mist eliminator)} \quad \text{(A-15)}$$

$$H_D = 24 + 1/2 d_N \text{ (with mist eliminator)} \quad \text{(A-16)}$$

If there is a mist eliminator, take 6 in, for the mist eliminator and take 1 ft from the top of the mist eliminator to the top tangent line of the vessel.

Appendix B: Pipe-Hi-SEP Dynamical Model

The model is developed from fundamental principles, and provided valuable insight in the relationships between parameters in the physical system and the transient behaviour of the system.

Assumption

- The liquid density is constant.
- The gas is ideal gas.
- The cross-section area of the separators does not change with height.
- No heat is transferred from the flow or the pipe.

Liquid level rate of change

For the Pipe-Hi-SEP system, shown in Figure B-1, the rate of change in liquid mass flow is the difference between the inlet mass flow and mass outlet flow. The balance for the height of the liquid in Pipe-SEP and Hi-SEP follows the mass balance, shown by Eq.(B-1) and Eq.(B-2) for constant liquid density.

Pipe-SEP $$\rho_l \frac{dV_{L1}}{dt} = \rho_l A_{PIPE-SEP} \frac{dh_1}{dt} = \rho_l (Q_{Lin} - Q_{Lout1}) \quad \text{(B-1)}$$

Hi-SEP $$\rho_l \frac{dV_{L2}}{dt} = \rho_l A_{HI-SEP} \frac{dh_2}{dt} = \rho_l (Q_{Lout1} - Q_{Lout2}) \quad \text{(B-2)}$$

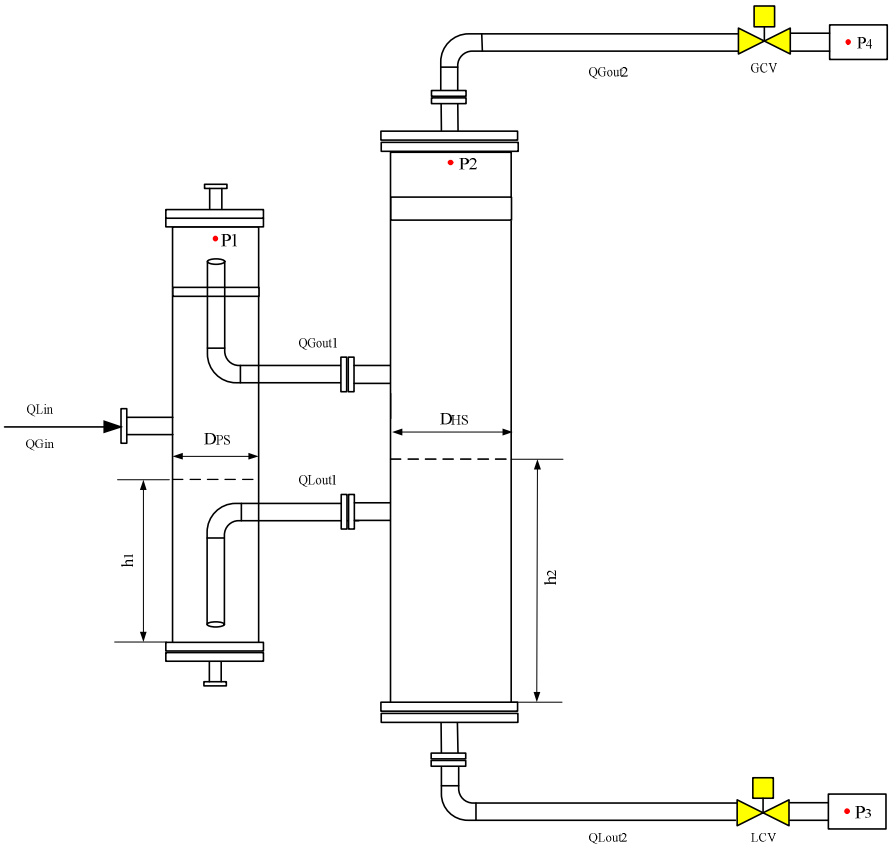

Figure B-1 Pipe-Hi-SEP system

Therefore, the liquid level balances on both separators are:

Pipe-SEP $$\frac{dh_1}{dt} = \frac{1}{A_{PIPE-SEP}}(Q_{Lin} - Q_{Lout1}) \quad \text{(B-3)}$$

Hi-SEP $$\frac{dh_2}{dt} = \frac{1}{A_{HI-SEP}}(Q_{Lout1} - Q_{Lout2}) \quad \text{(B-4)}$$

For the purpose of the analysing the Pipe-Hi-SEP system in Cranfield University PSE lab, the following Pipe-Hi-SEP system geometrical parameters and nomenclature are used as shown in Figure B-2.

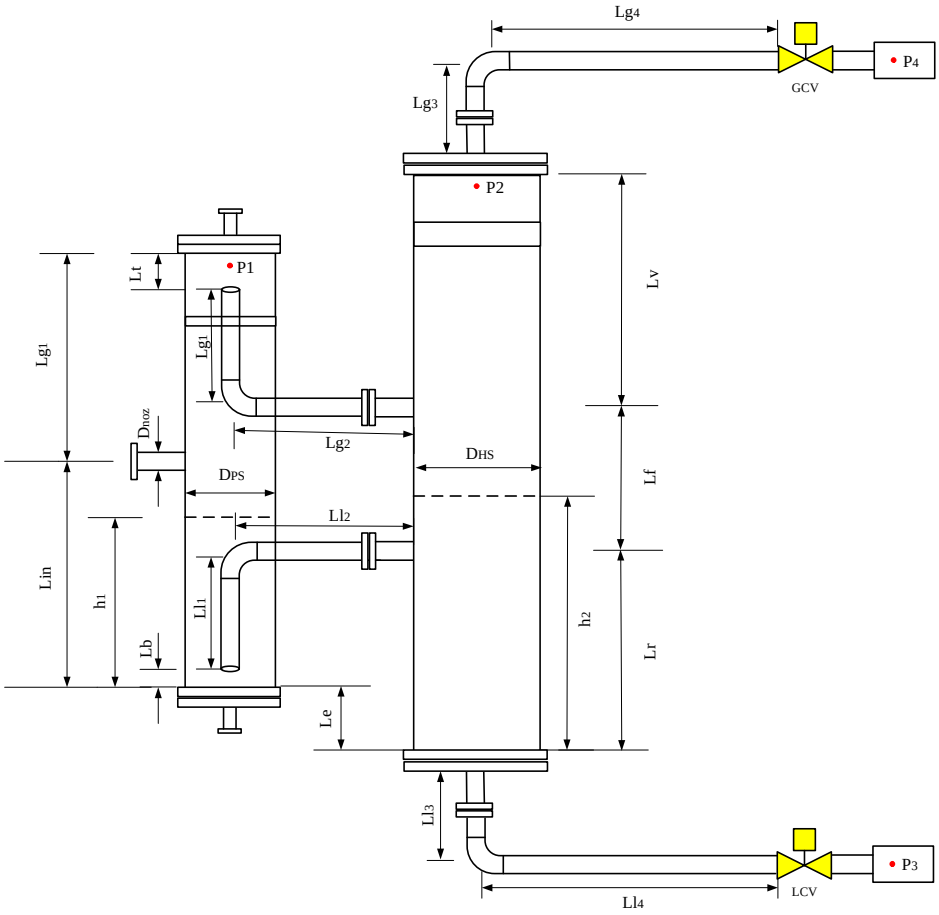

Figure B-2 Pipe-Hi-SEP system geometrical parameters and nomenclature

Liquid discharge flow rates

For the Pipe-SEP liquid outlet flow Q_{Lout1} , it can be written as follow:

$$Q_{Lout1} = A_{pipe} \times U_{L1} \tag{B-5}$$

A_{pipe} is the area of the interconnection liquid pipe, and U_{L1} is the liquid velocity in the interconnection liquid pipe.

It can further assumed that the liquid velocity in Pipe-SEP and Hi-SEP $U_{L1-1"} \approx U_{L2-2"}$. According to Bernoulli,

Pipe-SEP

$$\begin{cases} gZ_1 = gZ_2 + \frac{P_2 - P_1}{\rho_L} + \frac{\sum hfL_1}{\rho_L} \\ Z_1 = h_1 + L_e \\ Z_2 = h_2 \end{cases} \tag{B-6}$$

$\sum hfL_1$ is the pressure drop across the interconnection liquid pipe. The relationship between pressure drop $\sum hfL_1$ and liquid velocity U_{L1} can be written as:

$$\sum hfL_1 = K_1 u_{L1}^2 \tag{B-7}$$

K_1 is a coefficient which was determined experimentally. It depends on the flow situation and pipe geometry. In the present experiment, K_1 is validated as 0.0426.

For $h_2 \geq l_r$, the Pipe-SEP liquid outlet flow is:

$$Q_{Lout1} = 3600 A_{pipe} \left(\frac{\rho_L g(h_1 + L_e - h_2) - P_2 + P_1}{K_1}\right)^{1/2} \tag{B-8}$$

For $h_2 < l_r$, the Pipe-SEP liquid outlet flow is:

$$Q_{Lout1} = 3600 A_{pipe} \left(\frac{\rho_L g(h_1 + L_e - l_r) - P_2 + P_1}{K_1}\right)^{1/2} \tag{B-9}$$

For the Hi-SEP liquid discharge line, it consists of a control valve and a segment of line. The pressure loss across the valve and line is included by use of the loss coefficients. The relationship between the liquid flow rate Q_{Lout2} and pressure loss across the liquid control valve and pipe is written as:

$$Q_{Lout2} = A_{pipe} \times U_{L2} \tag{B-10}$$

$$\sum hfL_2 = K_3 u_{L2}^2 \tag{B-11}$$

Resulting in:

$$Q_{Lout2} = A_{pipe} \left(\frac{\sum hfL_2}{K_3}\right)^{1/2} \tag{B-12}$$

K_3 is the coefficient which depending on the LCV opening and downstream pipe geometry. In the present experiment, K_3 is validated as:

$$K_3 = 0.0031 \times \frac{1}{LCV^4} - 0.0083 \times \frac{1}{LCV^2} + 0.226 \tag{B-13}$$

According to Bernoulli, the pressure loss $\sum hfL_2$ is written as:

$$\sum hfL_2 = P_2 + \rho_L g(h_2 + L_{l3}) - P_3 \tag{B-14}$$

After substitution the Hi-SEP liquid outlet flow is:

$$Q_{Lout2} = 3600 \times A_{pipe}\left(\frac{P_2+\rho_L g(h_2+L_{l3})-P_3}{K_3}\right)^{1/2} \quad \text{(B-15)}$$

Pressure rate of change

The equation of state for the gas in the Pipe-SEP is

$$P_1 V_{G1} = Z n_{G1} RT \quad \text{(B-16)}$$

Differentiating Eq. (B-16) with respect to time yields

$$V_{G1}\frac{dP_1}{dt} = ZRT\frac{dn_{G1}}{dt} - P_1\frac{dV_{G1}}{dt} \quad \text{(B-17)}$$

As the volume of the Pipe-SEP is constant

$$\frac{dV_{G1}}{dt} = -\frac{dV_{L1}}{dt} = -(Q_{Lin} - Q_{Lout1}) \quad \text{(B-18)}$$

The mass balance in the Pipe-SEP is

$$\frac{dn_{G1}}{dt} = (Q_{Gin} - Q_{Gout1})\frac{\rho_{G1}}{M_G} \quad \text{(B-19)}$$

Substituting Eq. (B-18) and Eq. (B-19) in Eq. (B-17) yields

$$V_{G1}\frac{dP_1}{dt} = ZRT\frac{\rho_{G1}}{M_G}(Q_{Gin} - Q_{Gout1}) + P_1(Q_{Lin} - Q_{Lout1}) \quad \text{(B-20)}$$

$$\begin{cases} V_{G1} = (h_{PIPE-SEP} - h_1)A_{PIPE-SEP} \\ \rho_{G1} = \frac{P_1 M_G}{RT} \\ Z = 1 \end{cases} \quad \text{(B-21)}$$

$$\frac{dP_1}{dt} = \frac{1}{(H_{PIPE-SEP}-h_1)A_1}\left[P_1(Q_{Gin} - Q_{Gout1}) + P_1 A_1\frac{dh_1}{dt}\right] \quad \text{(B-22)}$$

The equation of state for the gas in the Hi-SEP is

$$P_2 V_{G2} = Z n_{G2} RT \quad \text{(B-23)}$$

Differentiating Eq. (B-23) with respect to time yields

$$V_{G2}\frac{dP_2}{dt} = ZRT\frac{dn_{G2}}{dt} - P_2\frac{dV_{G2}}{dt} \quad \text{(B-24)}$$

As the volume of the Hi-SEP is constant

$$\frac{dV_{G2}}{dt} = -\frac{dV_{L2}}{dt} = -(Q_{Lout1} - Q_{Lout2}) \quad \text{(B-25)}$$

The mass balance in the Hi-SEP is

$$\frac{dn_{G2}}{dt} = (Q_{Gout1} - Q_{Gout2})\frac{\rho_{G2}}{M_G} \tag{B-26}$$

Substituting Eq. (B-25) and Eq. (B-26) in Eq. (B-24) yields

$$V_{G2}\frac{dP_2}{dt} = ZRT\frac{\rho_{G2}}{M_G}(Q_{Gout1} - Q_{Gout2}) + P_2(Q_{Lout1} - Q_{Lout2}) \tag{B-27}$$

$$\begin{cases} V_{G2} = (h_{HI-SEP} - h)A_{HI-SEP} \\ \rho_{G2} = \frac{P_2 M_G}{RT} \\ Z = 1 \end{cases} \tag{B-28}$$

$$\frac{dP_2}{dt} = \frac{1}{(H_{HI-SEP} - h_2)A_2}\left[P_2(Q_{Gout1} - Q_{Gout2}) + P_2 A_2 \frac{dh_2}{dt}\right] \tag{B-29}$$

Gas discharge flow rates

The gas discharge flow rate from Pipe-SEP is:

$$Q_{Gout1} = U_g \times P_2 \times A_{pipe} \tag{B-30}$$

Q_{Gout1} is in standard condition with Sm^3/h unit.

According to Bernoulli,

$$\sum hfG_1 = K_2 U_g^2 = \frac{P_1 - P_2}{\rho_{G1}} \tag{B-31}$$

Substituting Eq. (B-30) in Eq. (B-31) yields

$$P_1 = P_2 + \rho_{G1} K_2 \left(\frac{Q_{Gout1}}{3600 P_2 A_{pipe}}\right)^2 \tag{B-32}$$

K_2 is the gas coefficient which was determined experimentally. It depends on the flow situation and pipe geometry. In the present experiment, K_2 is validated as $K_2 = 5.6 \times 10^{-5}$.

For the Hi-SEP gas discharge line, the relationship between the gas flow rate and pressure loss across the gas control valve is given as:

$$Q_{Gout2} = 3600 A_{pipe}\left(\frac{\Delta P_2}{K_4}\right)^{1/2} \tag{B-33}$$

$$\Delta P_2 = P_2 - P_4 \tag{B-34}$$

P_4 is the gas discharge pressure. K_4 is the coefficient which depending on the GCV opening and downstream pipe geometry. In the present experiment, K_4 is validated as

$$K_4 = 0.00001\frac{1}{GCV^4} - 0.00003\frac{1}{GCV^2} + 0.00043 \quad \text{(B-35)}$$

Substituting Eq. (B-35) in Eq. (B-33) yields

$$Q_{Gout2} = 3600A_{pipe}\left(\frac{P_2 - P_4}{0.00001\frac{1}{GCV^4} - 0.00003\frac{1}{GCV^2} + 0.00043}\right)^{1/2} \quad \text{(B-36)}$$

Simulation Model Development

The simulation model is developed in MATLAB & SIMULINK. The system geometrical parameters are used in the model is summarised in Table B-4.

Table B-4 Pipe-SEP and Hi-SEP system geometrical parameters

Items	**Unit**	**Parameter**
The physical properties of fluids:		
Liquid density, rho_L	Kg/m^3	1000
Liquid viscosity , mu_L	pa.s	1.23e-03
Liquid surface tension, sur_ten	N/m	0.0728
Gas viscosity	pa.s	1.73e-05
Constant:		
Gravitational acceleration**,** g	m/s^2	9.8
Gas molecular weight, M_G	/	29
Gas compression factor, Z	/	1
Gas constant, R	L-atm/K-mol	0.082
The geometry of the Pipe:		
PIPE diameter, D_PIPE	m	0.05
Full cross-sectional area of the PIPE, A_PIPE	m^2	0.0020
The geometry of the Pipe-SEP :		
Pipe-SEP diameter, D_PIPE_SEP	m	0.15
Cross-sectional area of the Pipe-SEP , A_PIPE_SEP	m^2	0.0177
Pipe-SEP total height, H_PIPE_SEP	m	1.6

Pipe-SEP inlet position, L_in	m	0.7
Items	**Unit**	**Parameter**
Pipe-SEP interconnection liquid pipe length I, L_l1	m	0.49
Pipe-SEP interconnection liquid pipe length II, L_l2	m	2.3
Pipe-SEP interconnection equivalent liquid pipe length, L_le	m	3.5
Pipe-SEP upper part length, L_g	m	0.9
Pipe-SEP interconnection gas pipe length 1, L_g1	m	0.55
Pipe-SEP interconnection gas pipe length 2, L_g2	m	2.6
Pipe-SEP interconnection equivalent gas pipe length, L_ge	m	18
Pipe-SEP / distance between interconnection liquid pipe inlet to Pipe-SEP bottom, L_b	m	0.05
Pipe-SEP installation elevation respect to Hi-SEP , L_e	m	0.31
The geometry of the Hi-SEP :		
Hi-SEP diameter, D_HI_SEP	m	0.204
Cross-sectional area of the Hi-SEP , A_HI_SEP	m^2	0.0327
Hi-SEP total height, H_HI_SEP	m	2.4
Hi-SEP inlet section length, L_f	m	0.4
Hi-SEP upper part length, L_v	m	1.15
Hi-SEP lower part length, L_r	m	0.85
Hi-SEP liquid outlet line elevation, L_l3	m	0.126
Inlet flow condition:		
Inlet pipe pressure, P_inlet	bara	Varied
Inlet pipe temperature, T_inlet	K	288.15
Outlet flow condition:		
Liquid outlet pressure, P3	bara	1.05
Gas outlet pressure, P4	bara	1.05
interconnection pipe loss coefficient:		
interconnection liquid pipe, K1	$bar.s^2/m^2$	0.0426
interconnection gas pipe, K2	$bar.s^2/m^2$	5.6e-5

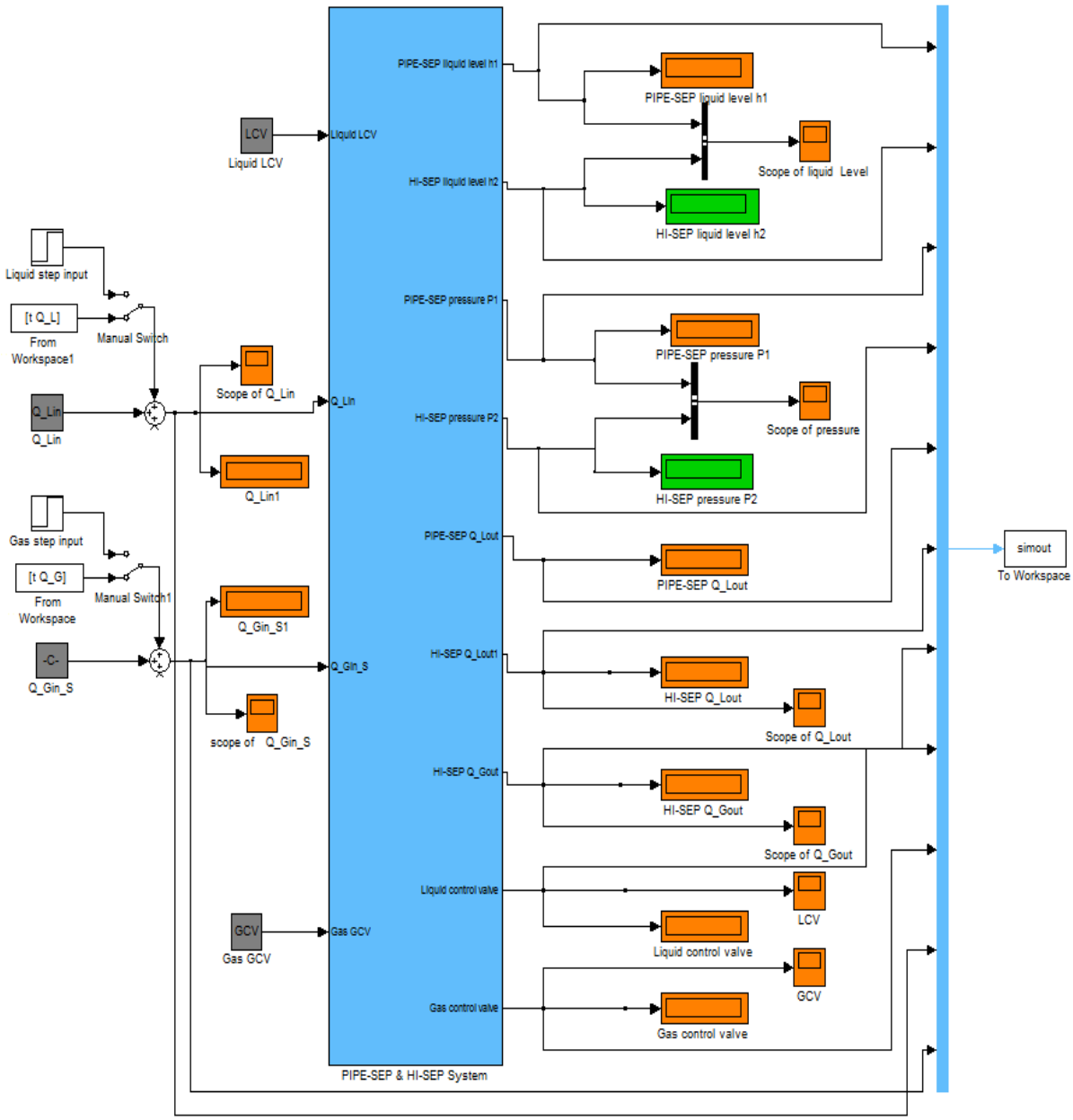

Figure B-3 Pipe-Hi-SEP dynamic simulation model

Interconnection liquid pipe pressure loss coefficient calibration (K1)

No.	Inlet liquid flow rate Q_{Lin} (m^3/h)	Interconnection liquid pipe				Error%
		Liquid superficial velocity (m/s)	Liquid superficial velocity^2 (m^2/s^2)	Measured Pressure loss (bar)	Calculated Pressure loss (bar)	
1#	2.68	0.378	0.143	0.00475	0.00611	-28.5%
2#	3.59	0.507	0.257	0.01208	0.01096	9.2%
3#	4.44	0.627	0.394	0.01804	0.01678	7.0%
4#	5.49	0.776	0.603	0.02476	0.02568	3.7%

Interconnection gas pipe pressure loss coefficient calibration (K2)

No.	Inlet gas flow rate Q_{Gin} (Sm^3/h)	Interconnection gas pipe				Error%
		Gas superficial velocity (m/s)	Gas superficial velocity^2 (m^2/s^2)	Measured Pressure loss (bar)	Calculated Pressure loss (bar)	
1#	73.10	9.34	87.18	0.00481	0.00488	-1.5%
2#	84.49	10.67	113.91	0.00618	0.00638	-3.3%
3#	92.06	11.54	133.13	0.00712	0.00746	-4.7%
4#	103.51	12.81	164.09	0.00874	0.00919	-5.2%
5#	112.89	13.81	190.80	0.01017	0.01069	-5.1%
6#	130.09	15.57	242.46	0.01299	0.01358	-4.5%
7#	142.91	16.80	282.31	0.01549	0.01581	-2.0%
8#	162.32	18.53	343.23	0.01939	0.01922	0.9%
9#	179.21	19.91	396.26	0.02323	0.02219	4.5%
10#	198.67	21.34	455.32	0.02808	0.02550	9.2%
11#	258.85	25.03	626.55	0.04421	0.03509	20.6%

$K_1 = 0.0426$

$\Delta P_1 = 0.0426 U_{l1}^2$

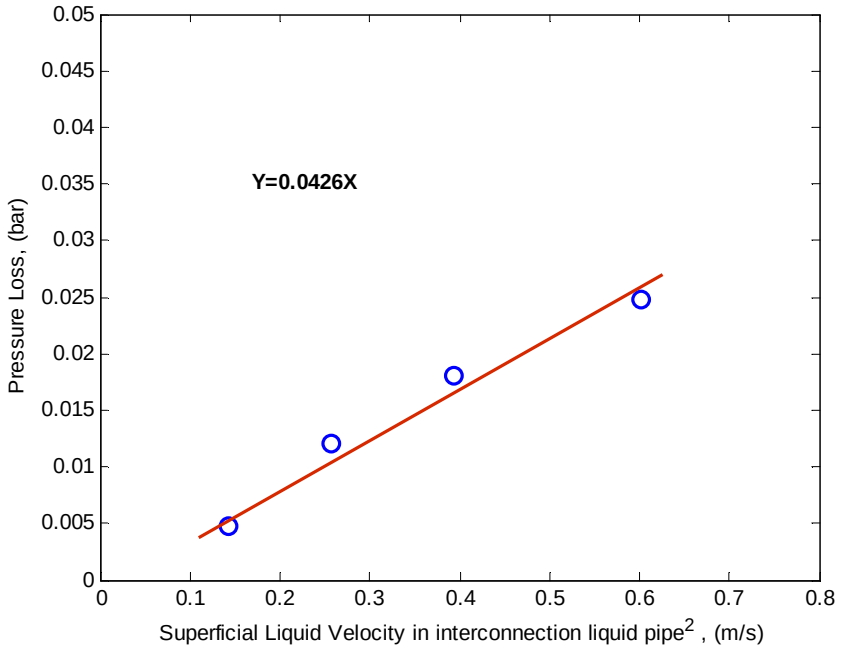

Figure B-4 Pressure loss along interconnection liquid pipe

$K_2 = 0.000056$

$\Delta P_2 = 0.000056 \times U_{g1}^2$

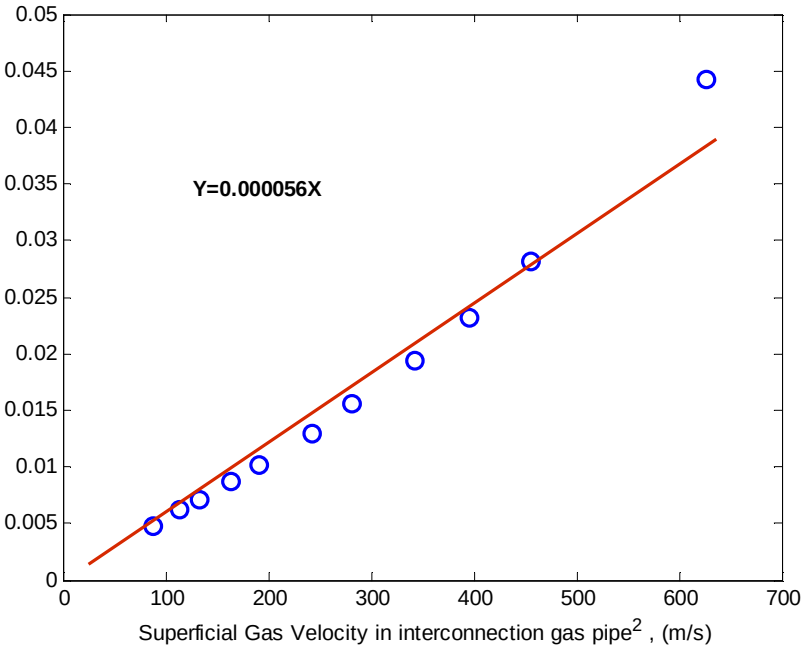

Figure B-5 Pressure loss along interconnection gas pipe

Liquid discharge line coefficient (K3)

No.	Inlet liquid flow rate Q_{Lin} (m^3/h)	LCV opening	Liquid discharge pipe line				Error%
			Liquid superficial velocity (m/s)	Liquid superficial velocity^2 (m^2/s^2)	Measured Pressure loss (bar)	Calculated Pressure loss (bar)	
1#	1.50	0.9	0.213	0.045	0.0104	0.00999	0.04%
2#	2.75	0.9	0.389	0.151	0.0321	0.0333	0.11%
3#	3.63	0.9	0.514	0.264	0.0566	0.0581	0.15%
4#	4.48	0.9	0.634	0.402	0.0870	0.0886	0.16%
5#	5.37	0.9	0.760	0.577	0.1251	0.1273	0.22%
6#	3.58	0.9	0.507	0.258	0.0554	0.0569	-2.69%
7#	3.47	0.8	0.492	0.242	0.0540	0.0533	1.05%
8#	3.62	0.7	0.512	0.262	0.0526	0.0583	10.72%
9#	3.59	0.6	0.508	0.258	0.0586	0.0586	0.10%
10#	3.58	0.5	0.507	0.257	0.0610	0.0624	2.34%
11#	3.50	0.4	0.495	0.245	0.0737	0.0723	1.77%
12#	3.50	0.3	0.495	0.245	0.1271	0.1266	0.36%

$$K_3^{"} = 0.0031\frac{1}{LCV^4} - 0.0083\frac{1}{LCV^2} + 0.0097$$

$$K_3 = K_3^{"} + 0.226$$

$$\Delta P_3 = \left(0.0031\frac{1}{LCV^4} - 0.0083\frac{1}{LCV^2} + 0.226\right) \times U_{l2}^2$$

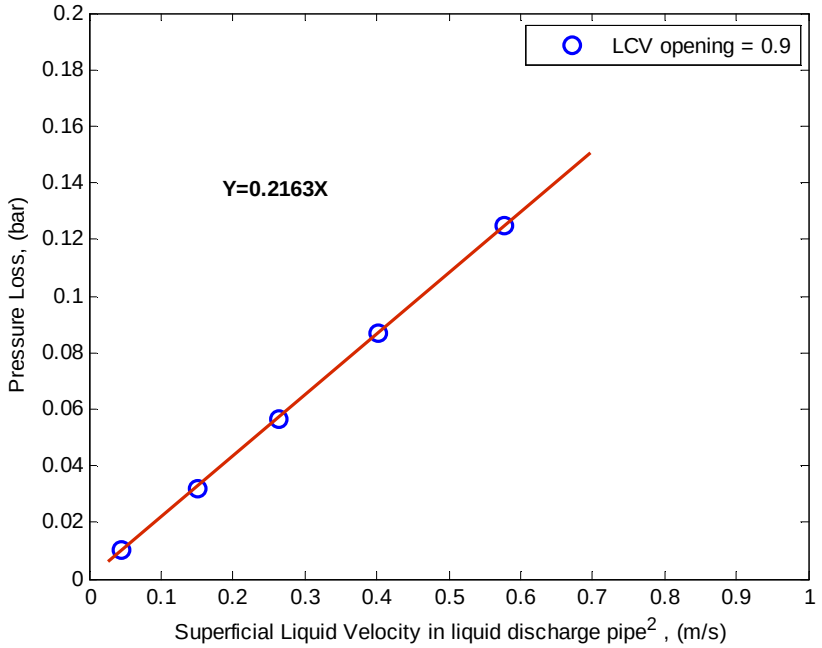

Figure B-6 Pressure loss along liquid discharge pipe

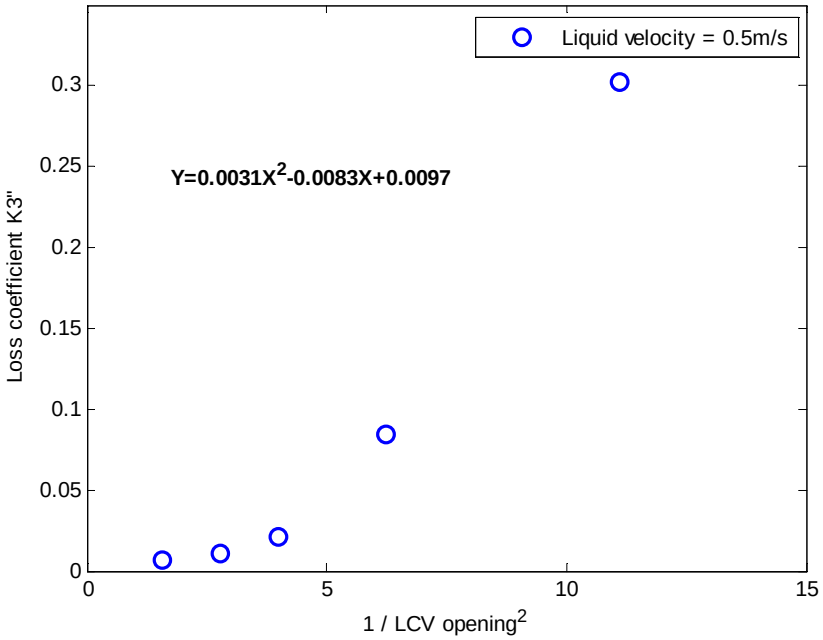

Figure B-7 LCV loss coefficient

Gas discharge line coefficient (k4)

No.	Inlet Gas flow rate Q_{Gin} (m^3/h)	GCV opening	Gas discharge pipe line				Error%
			Gas superficial velocity (m/s)	Gas superficial velocity^2 (m^2/s^2)	Measured Pressure loss (bar)	Calculated Pressure loss (bar)	
1#	112.8	0.9	13.76	189.35	0.0994	0.0887	14.6%
2#	130.1	0.9	15.52	240.85	0.1194	0.1079	9.6%
3#	142.9	0.9	16.76	280.86	0.1357	0.1258	7.2%
4#	162.3	0.9	18.50	342.25	0.1634	0.1533	6.1%
5#	179.2	0.9	19.89	395.85	0.1896	0.1774	6.4%
6#	198.6	0.9	21.35	455.82	0.2226	0.2043	8.2%
7#	214.9	0.9	22.48	505.49	0.2498	0.2265	9.3%
8#	258.8	0.9	25.13	631.57	0.3320	0.2830	14.7%
9#	166.16	0.9	19.24	370.43	0.1485	0.166032	11.8%
10#	170.15	0.8	19.57	383.23	0.1537	0.171512	11.5%
11#	168.59	0.7	19.43	377.79	0.1507	0.170167	12.9%

12#	163.32	0.6	18.94	359.03	0.1447	0.166531	15.0%
13#	171.60	0.5	19.43	377.69	0.1718	0.192623	12.0%
14#	165.28	0.4	18.34	336.38	0.2004	0.226429	12.9%

$$K_4^{"} = 0.00001\frac{1}{GCV^4} - 0.00003\frac{1}{GCV^2} - 0.00007$$

$$K_4 = K_4^{"} + 0.00043$$

$$\Delta P_4 = \left(0.00001\frac{1}{GCV^4} - 0.00003\frac{1}{GCV^2} + 0.00043\right) \times U_{g2}^2$$

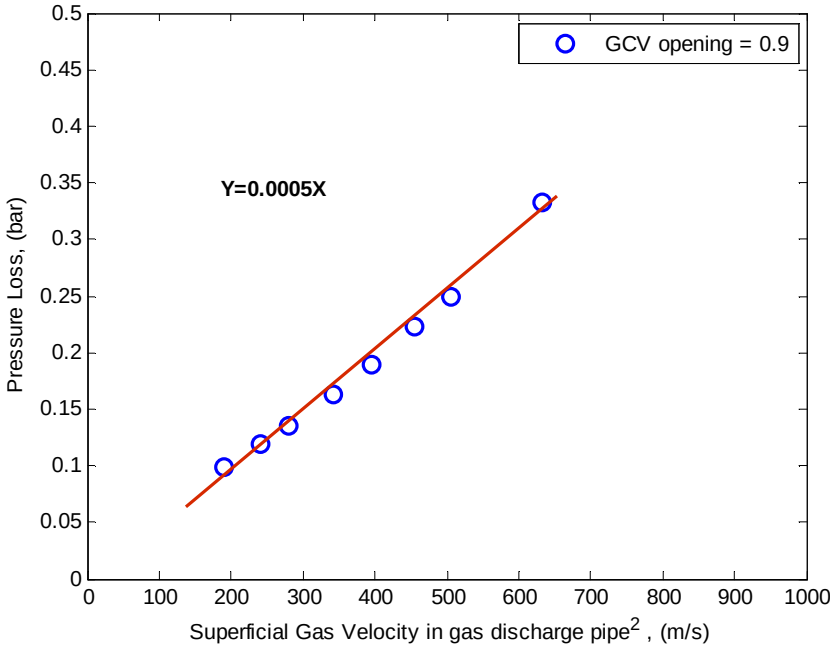

Figure B-8 Pressure loss along gas discharge pipe

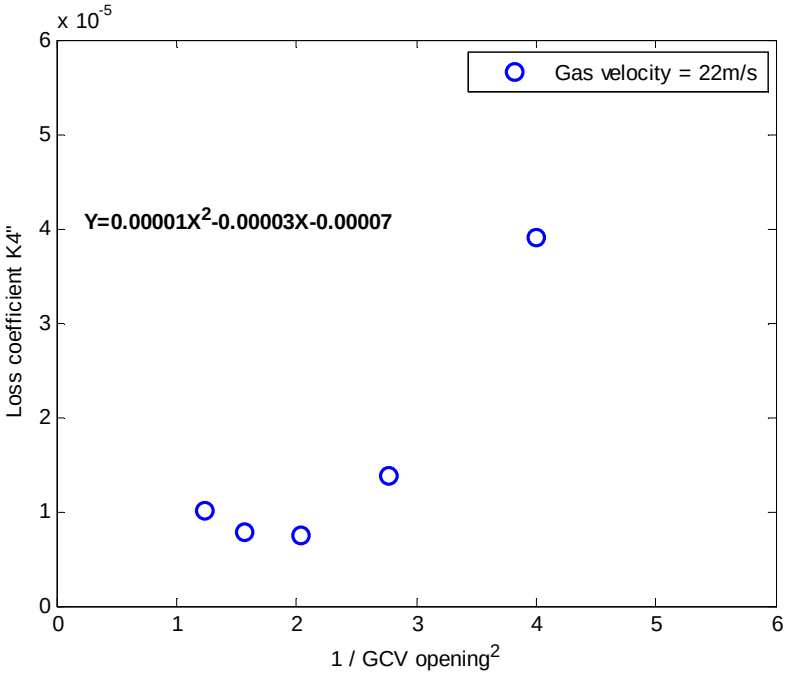

Figure B-9 GCV loss coefficient

Appendix C: Experiment Data

Table C-1 Observation of inlet flow pattern

Vsg (m/s)	Vsl(m/s)	Flow Pattern	Vsg (m/s)	Vsl(m/s)	Flow Pattern
4.98	0.25	Slug	6.57	0.27	Slug
4.15	0.37	Slug	6.91	0.37	Slug
4.10	0.51	Slug	6.66	0.50	Slug
3.87	0.62	Slug	6.30	0.65	Slug
3.97	0.77	Slug	5.75	0.79	Slug
3.72	0.90	Slug	5.54	0.91	Slug
3.53	1.05	Slug	5.31	1.04	Slug
3.35	1.13	Slug	5.10	1.18	Slug
3.24	1.28	Slug	4.82	1.30	Slug
9.14	0.25	Annular	11.18	0.25	Annular
8.24	0.36	Slug	10.42	0.37	Annular
7.80	0.48	Slug	9.65	0.50	Slug
7.48	0.64	Slug	8.97	0.63	Slug
7.10	0.74	Slug	8.47	0.79	Slug
6.86	0.88	Slug	8.04	0.90	Slug
6.44	1.02	Slug	7.83	1.01	Slug
6.10	1.14	Slug	7.51	1.14	Slug
5.80	1.28	Slug	6.91	1.25	Slug
12.52	0.24	Annular	13.94	0.26	Annular
11.34	0.38	Annular	13.66	0.36	Annular
10.80	0.50	Annular	12.74	0.50	Annular
9.98	0.64	Slug	11.68	0.63	Slug
9.36	0.77	Slug	10.44	0.80	Slug
8.98	0.87	Slug	9.94	0.90	Slug
8.21	1.05	Slug	9.64	1.01	Slug
7.91	1.15	Slug	8.78	1.15	Slug
7.43	1.29	Slug	8.37	1.27	Slug

Figure C-1 shows the inlet conditions together with the flow pattern boundaries suggested by Taitel and Dukler (1976). They are basically, intermittent flow and annular flow. Visual observation of the inlet flows agreed with the predicted flow patterns.

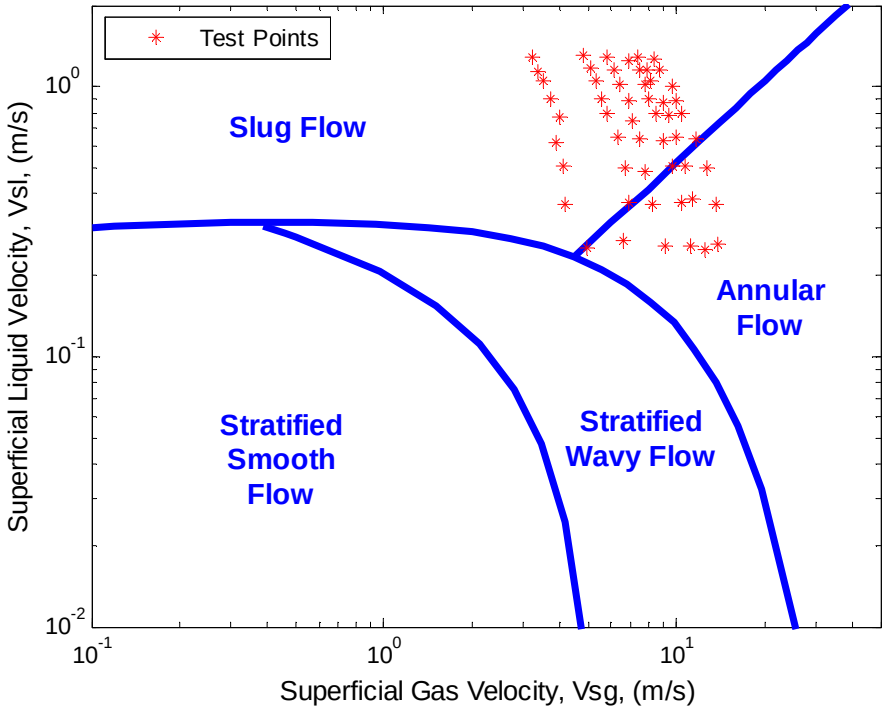

Figure C-1 Flow patterns map as suggested by Taitel and Dukler (1976)

Table B-2 Observation of Pipe-SEP upper flow pattern and equilibrium liquid level

No.	Vsg-PS (m/s)	Vsl-PS (m/s)	Flow Pattern	Equilibrium Liquid Level L_{l1} ( )	Swirled Film Height (mm)
1#	1.324	0.034	S*	65.2	750
2#	1.330	0.052	S	35.1	900
3#	1.334	0.070	S	50.8	1050
4#	1.361	0.087	S	97.4	1300
5#	1.381	0.105	S	74.6	1300
6#	1.356	0.118	S	188.1	1350
7#	1.360	0.137	S	488.3	1450
8#	1.341	0.152	C*	749.9	1500
9#	1.336	0.171	C	802.8	1500
10#	1.669	0.034	S	-43.5	850
11#	1.684	0.052	S	-32.4	870
12#	1.706	0.068	S	-38.2	1050
13#	1.727	0.084	S	-47.8	1300
14#	1.702	0.106	S	39.0	1350
15#	1.756	0.116	S	66.4	1350
16#	1.744	0.137	S	190.5	1500
17#	1.674	0.154	S-C*	545.6	1500
18#	1.698	0.168	S-C	679.0	1500
19#	1.730	0.036	S	-53.7	850
20#	1.803	0.051	S	-58.8	900
21#	1.852	0.071	S	49.7	1150
22#	1.872	0.086	S	28.1	1300
23#	1.893	0.103	S	13.9	1300
24#	1.859	0.120	S	50.9	1450
25#	1.873	0.139	S	149.5	1500
26#	1.873	0.153	S	288.8	1500
27#	1.840	0.171	S-C	609.4	1500

Notes: S ------ Swirled Flow S-C ------- Swirled to Churned Flow C ------ Churned Fl

Table C-3 Pipe-SEP swirled film height

No.	Mix Velocity (m/s)	Gas-to-Liquid Volumetric Ratio	Swirled Film Height (mm)		Error (%)
			Observation	Calculated	
1#	10.64	45.21	750	746	0.47
2#	10.92	30.01	900	855	5.03
3#	11.01	21.97	1050	937	10.80
4#	11.30	18.15	1300	1012	22.14
5#	11.57	15.04	1300	1089	16.22
6#	11.50	13.20	1350	1119	17.10
7#	11.67	11.45	1450	1179	18.67
8#	11.76	10.27	1500	1223	18.49
9#	12.03	9.18	1500	1287	14.17
10#	13.56	50.76	850	926	-8.93
11#	13.61	33.57	870	1038	-19.28
12#	13.80	25.43	1050	1134	-7.98
13#	14.07	20.85	1300	1220	6.15
14#	14.05	16.30	1350	1300	3.72
15#	14.59	15.47	1350	1370	-1.51
16#	14.63	12.98	1500	1438	4.15
17#	14.32	11.13	1500	1464	2.42
18#	14.64	10.30	1500	1527	-1.81
19#	14.22	51.18	850	970	-14.16
20#	14.72	36.98	900	1097	-21.85
21#	15.08	26.92	1150	1224	-6.43
22#	15.24	22.09	1300	1305	-0.36
23#	15.58	18.78	1300	1394	-7.21
24#	15.44	15.88	1450	1443	0.48
25#	15.67	13.71	1500	1522	-1.47
26#	15.78	12.46	1500	1572	-4.77
27#	15.75	10.92	1500	1623	-8.21

The swirled film came out from the data fitting shown in Figure C-2. The experiment data were collected with three different gas flow rate with nine different liquid flow rates, operating with 1.2bara pressure. Although the liquid film is always fluctuation, the max value is taken as listed in Table C-2.

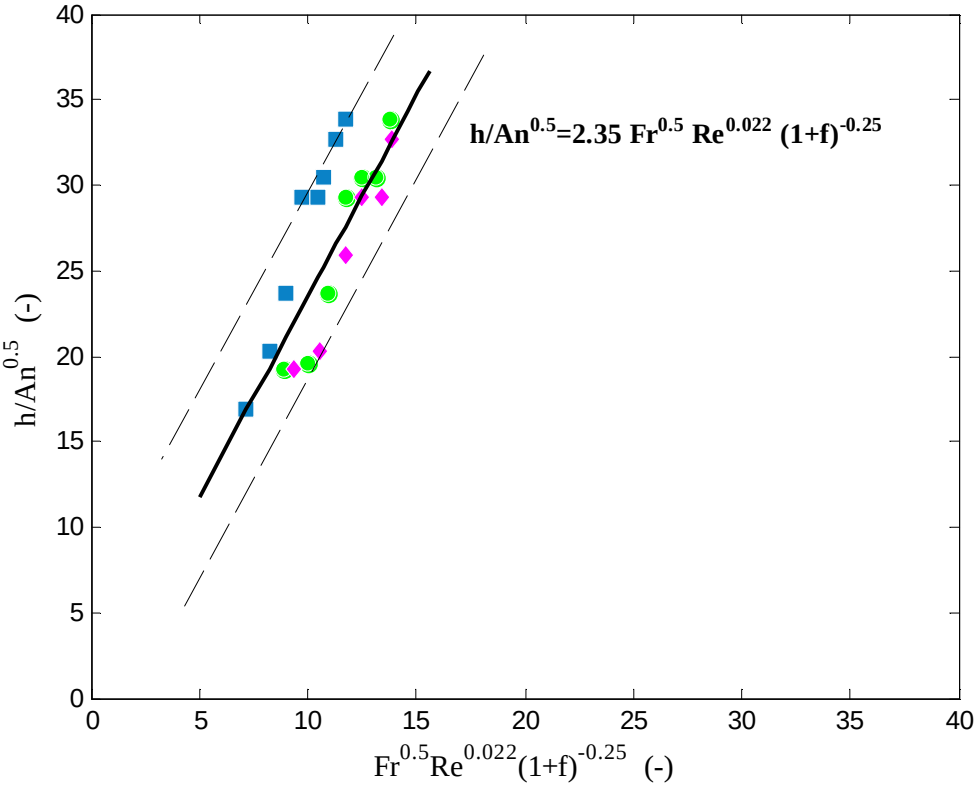

Figure C-2 Scatter plot of the dimensionless film height

Appendix D: Pipe-SEP Performance Model

```
% PIPE-SEP Performance Predicting Model
% developed by Yinghui--------Jan 2012
%%==========================================
clear all;
clc;
close;

% The physical properties of fluids:

rho_L = 1000;                                   % Liquid density, (Kg/m^3);
mu_L = 1.23e-03;                                % Liquid viscosity, (pa.s);
sur_tension = 0.0728;                           % Liquid surface tension, (N/m);
mu_G = 1.73e-05;                                % Gas viscosity, (pa.s);

% The geometry of the PIPE:

D_PIPE = 0.05;                                  % PIPE diameter, (m);
A_PIPE = ( pi * D_PIPE ^ 2 ) / 4;               % Full cross-sectional area of the PIPE, (m^2);

% The geometry of the PIPE-SEP:

D_PIPE_SEP = 0.15;                              % PIPE-SEP diameter, (m);
A_PIPE_SEP = ( pi * D_PIPE_SEP ^ 2 ) / 4;       % Cross-sectional area of the PIPE-SEP, (m^2);
OD_G_PIPE = 0.06;                               % Out diameter of the PIPE-SEP gas out line, (m);
A_G_PIPE = ( pi * OD_G_PIPE ^ 2 ) / 4;          % Cross-sectional area of the PIPE-SEP gas outline, (m^2);
A_PIPE_SEP_R = A_PIPE_SEP - A_G_PIPE;           % Restricted cross-sectional area of the PIPE-SEP, (m^2);
D_PIPE_SEP_e = (4*A_PIPE_SEP_R/pi)^0.5;         % PIPE-SEP equivalent diameter, (m);
L_inlet = 0.7;                                  % Position of the PIPE-SEP inlet nozzle, (m);
L_g1 = 0.9;                                     % Length of the PIPE-SEP upper part, (m);
L_t = 0.1;                                      % Length of gas outlet part I, (m);
L_g2 = 0.55;                                    % Distance between PIPE-SEP top and gas outlet, (m);
```

```
L_g3 = 0.2;                                   % Length of gas outlet part II, (m);
L_g4 = 0.95;                                  % Length of gas outlet part III, (m);
L_g5 = 0.4;                                   % Length of gas outlet part IIII, (m);
L_g6 = 1.05;                                  % Length of flexible gas outlet part, (m);
L_b = 0.06;                                   % Distance between PIPE-SEP bottom and liquid outlet,(m);
L_l2 = 0.49;                                  % Length of liquid outlet part I, (m);
L_l3 = 0.5;                                   % Length of liquid outlet part II, (m);
L_l4 = 0.7;                                   % Length of liquid outlet part III, (m);
L_l5 = 0.4;                                   % Length of liquid outlet part IIII, (m);
L_l6 = 0.7;                                   % Length of flexible liquid outlet part, (m);
L_e = 0.40;                                   % Distance between PIPE-SEP bottom and HI-SEP bottom,(m);
L_a = 0.44;                                   % Distance between HI-SEP top and PIPE-SEP top, (m);
Z_1 = 1.9;                                    % Elevation of PIPE-SEP, (m);

% The geometry of the HI-SEP:

D_HI_SEP = 0.204;                             % HI-SEP diameter, (m);
A_HI_SEP = ( pi * D_HI_SEP ^ 2 ) / 4;         % Cross-sectional area of the HI-SEP, (m^2);
L_v = 1.15;                                   % Length of HI-SEP upper part, (m);
L_f = 0.4;                                    % Length of HI-SEP inlet section, (m);
L_r = 0.85;                                   % length of HI-SEP lower part, (m);
L_m = 0.75;                                   % HI-SEP liquid level, (m);
Z_2 = 1.25;                                   % Elevation of HI-SEP, (m);

% The geometry of the UF KOV:

Z_3 = 0.75;                                   % Elevation of UF KOV, (m);
L_p = 0.8;                                    % Distance between UF KOV bottom and UF KOV inlet, (m);


% Constant:

g = 9.8;                                      % The gravitational acceleration constant, (m/s^2);

%%==========================================
```

```
%Inlet and operation condition:

P_inlet = 2.0315;                                   % Inlet pipe pressure, (bara);
T_inlet = 15.6628;                                  % Inlet pipe temperature, (degree);
P_HI_SEP = 1.2;                                     % HI-SEP operation pressure, (bara);
P_UF_KOV = 1.08;                                    % UF KOV operation pressure, (bara);
Q_L = 0.75;                                         % Inlet liquid flow rate, (l/s);
Q_G_S = 160;                                        % Standard Inlet gas flow rate, (Sm^3/hr);

% Calculate inlet flow properties:

Vsl = Q_L*1e-3 / A_PIPE;                            % Superficial inlet liquid velocity, (m/s);
 Q_G_A = Q_G_S/P_inlet;                             % Actual inlet gas flow rate, (Am^3/hr);
Vsg = ( Q_G_A/3600 )/A_PIPE;                        % Superficial inlet gas velocity, (m/s);
Vmix = Vsl + Vsg;                                   % Mixture inlet velocity, (m/s);
GVF_inlet = Q_G_A /(Q_G_A + Q_L*1e-3*3600); f_inlet = Q_G_A /   % Inlet gas void fraction, GVF;
(Q_L*1e-3*3600);                                    % Inlet gas to liquid volumetric ratio ;

% Calculate Inlet mixture properties:

rho_G_inlet = ( P_inlet *101330*28.96 )/ (8314 * (273 + T_inlet ));   % Gas density at inlet pipe, (kg/m^3);
rho_mix = rho_L*(1-GVF_inlet)+ rho_G_inlet * GVF_inlet;               % Mixture density, (Kg/m^3);
mu_mix = mu_L*(1-GVF_inlet)+ mu_G * GVF_inlet;                        % Mixture viscosity, (pa.s);
Reno_inlet = rho_mix * D_PIPE * Vmix /mu_mix;                         % Reynolds number at inlet;


%%==========================================

% Flow pattern in inlet pipe:

Vsg_crit_PIPE = 3.1 *(sur_tension*g*(rho_L-                           % Annular flow transition criterion in horizontal pipe, (m/s);
rho_G_inlet)/rho_G_inlet^2)^(1/4);

if Vsg >= Vsg_crit_PIPE
  disp ('Inlet Flow Pattern: Annular flow');
```

```
else
  disp('Inlet Flow Pattern: Non Annular flow');
end


% Estimate Equilibrium Liquid Level

% Calculate Gas Density at HI-SEP and UF KOV :

rho_G_HI_SEP = (P_HI_SEP*101330*28.96 )/ (8314 * (273 +
T_inlet ));                                          % Gas density in HI-SEP, (kg/m^3);
rho_G_UF_KOV = (P_UF_KOV*101330*28.96 )/ (8314 * (273 +
T_inlet ));                                          % Gas density in UF KOV, (kg/m^3);

% Set the PIPE-SEP LCO and GCU :

LCO_PIPE_SEP = 0.0;
GCU_PIPE_SEP = 0.0;


% Calculate Equilibrum Liquid Level:

GVF_LCO = Q_G_S*(1-GCU_PIPE_SEP)/P_HI_SEP /(Q_G_S*(1-
GCU_PIPE_SEP)/P_HI_SEP +Q_L*LCO_PIPE_SEP *1e-3*3600);
                                                     % Estimating GVF in PIPE-SEP gas out line, GVF

Vsg_est = ( Q_G_S*(1-GCU_PIPE_SEP)/P_HI_SEP/3600 ) / A_PIPE;
rho_mix_1 = rho_L*(1-GVF_LCO)+ rho_G_HI_SEP * GVF_LCO;
                                                     % Estimating gas velocity in PIPE-SEP gas leg, (m/s);

mu_mix_1 = mu_L*(1-GVF_LCO)+ mu_G *GVF_LCO;
                                                     % Estimating Mixture density of PIPE-SEP gas out line, (Kg/m^3);

Reno_PIPE_SEP_O = rho_mix_1 * D_PIPE * Vsg_est /mu_mix_1;
                                                     % Estimating Mixture viscosity of PIPE-SEP gas out line, (Pa.s);
f_G = 0.0056+0.5*Reno_PIPE_SEP_O^(-0.32);            % Estimating Reynolds number of PIPE-SEP gas out line;
L_Gas = L_g2+L_g3+L_g4+L_g5+L_g6;
L_fitting_G = 12.35;                                 % Gas friction factor in PIPE-SEP gas out line;
DP_G = (((f_G*(L_Gas+L_fitting_G)/0.05+1.5)*Vsg_est^2/2-
g*0.65)*rho_mix_1/100000);                           % Total length of gas out line, (m);
```

```
P_PIPE_SEP = P_HI_SEP+DP_G;                                   % Gas out line fittings equivalent length, (m);


% Calculated Gas Density at PIPE-SEP :

rho_G_PIPE_SEP = (P_PIPE_SEP*101330*28.96 )/ (8314 * (273 +   % Gas density in PIPE-SEP, (kg/m^3);
T_inlet ));

% Calculate superficial velocity in PIPE-SEP:

Q_G_A_PIPE_SEP = Q_G_S/P_PIPE_SEP;                            % Actual gas flow rate in PIPE-SEP, (Am^3/hr);
Vsg_PIPE_SEP = ( Q_G_A_PIPE_SEP/3600 ) /A_PIPE_SEP_R ;        % Superficial gas velocity in PIPE-SEP, (m/s);
Vsg_PIPE_SEP_O = ( Q_G_A_PIPE_SEP/3600 )/A_PIPE;              % Superficial gas velocity in PIPE-SEP gas out line, (m/s);
Vsl_PIPE_SEP = Q_L*1e-3 /A_PIPE_SEP_R;                        % Superficial liquid velocity in PIPE-SEP, (m/s);
Vsl_PIPE_SEP_O = Q_L*1e-3 /A_PIPE;                            % Superficial liquid velocity in PIPE-SEP liquid out line, (m/s);

% Calculate superficial velocity in HI-SEP:

Q_G_A_HI_SEP =  Q_G_S/P_HI_SEP;                               % Actual gas flow rate in HI-SEP, (Am^3/hr);
Vsg_HI_SEP = ( Q_G_A_HI_SEP/3600 ) /A_HI_SEP ;                % Superficial gas velocity in HI-SEP, (m/s);
Vsl_HI_SEP = Q_L*1e-3 /A_HI_SEP;                              % Superficial liquid velocity in HI-SEP, (m/s);

% Calculate PIPE-SEP liquid leg pressure loss:

L_liquid = L_l2 + L_l3 + L_l4 + L_l5 + L_l6;                  % Total liquid out line length, (m);
L_fitting_L = 45.71;                                          % Liquid out line fittings equivalent length, (m);
                                                              (2 valves, 4 bends, and 1 tee)

% Calculate the mixture properties in PIPE-SEP liquid out line

GVF_GCU =GCU_PIPE_SEP*Q_G_S/P_PIPE_SEP                        % Estimating GVF in PIPE-SEP liquid out line, GVF
/(GCU_PIPE_SEP*Q_G_S/P_PIPE_SEP +Q_L*(1-
LCO_PIPE_SEP)*1e-3*3600);
```

```
rho_mix_2 = rho_L*(1-GVF_GCU)+ rho_G_PIPE_SEP * GVF_GCU;   % Calculate mixture density of PIPE-SEP liquid out line, (Kg/m^3);

mu_mix_2 = mu_L*(1-GVF_GCU)+ mu_G *GVF_GCU;                % Calculate mixture viscosity of PIPE-SEP liquid out line, (Pa.s);

Vsl_mix_2 = (Q_L*(1-LCO_PIPE_SEP)*1e-3)/A_PIPE*(1-
GVF_GCU)+( GCU_PIPE_SEP*Q_G_S/3600 )/A_PIPE*GVF_GCU;       % Mixture velocity in PIPE-SEP liquid out line, (m/s);
Vsl_mix_3 = (Q_L*(1-LCO_PIPE_SEP)*1e-3)/A_PIPE_SEP_R*(1-
GVF_GCU)+( GCU_PIPE_SEP*Q_G_S/3600 )/A_PIPE_SEP_R*GVF
_GCU;                                                      % Mixture velocity in PIPE-SEP, (m/s);
Reno_L = rho_mix_2 * D_PIPE_SEP  * Vsl_mix_3 / mu_mix_2;   % Liquid Reynolds number in PIPE-SEP;
Reno_L_L = rho_mix_2 *  D_PIPE * Vsl_mix_2 / mu_mix_2;     % Liquid Reynolds number in PIPE-SEP liquid out line;

% Calculate liquid friction factor at PIPE-SEP by Drew method

f_L = 0.0056+0.5* Reno_L^(-0.32);                          % Liquid friction factor in PIPE-SEP;
f_L_L = 0.0056+0.5* Reno_L_L^(-0.32);                      % Liquid friction factor in PIPE-SEP liquid out line;

% Calculate pressure loss along PIPE-SEP liquid out line

DP_L = (f_L_L *(L_fitting_L+L_liquid)/D_PIPE+1.5)*(rho_mix_2*
Vsl_mix_2^2/2)/100000;                                     %  Pressure loss in PIPE-SEP liquid out line, (Pa);

L_l1 = ((P_UF_KOV-P_HI_SEP)*100000+DP_L*100000 -
DP_G*100000- rho_mix_2*g*(Z_1-Z_3-L_p)- rho_mix_1 *g *(Z_1-
Z_2-L_r))/(g*(rho_L+rho_G_PIPE_SEP)-
f_L*rho_mix_2*Vsl_PIPE_SEP^2/2/D_PIPE_SEP);                % PIPE-SEP Equilibrium Liquid Level


%==============================================

% Agitated flow model

CM=L_inlet+(345.7-123.9*Vsg_PIPE_SEP)/1000;
disp( num2str(CM) );
```

```
if L_l1>=CM & CM >=0.7

Q_GCU = 2.06;                                                    % Gas carry under (Sm^3/h)
GCU_PIPE_SEP=Q_GCU/Q_G_S;

% Calculate agitated flow entrained fraction

E_C=0.47*Vsg_PIPE_SEP^0.16*(Vsl_PIPE_SEP)^2;                     % liquid carry over (l/s)
LCO_PIPE_SEP=Q_LCO/Q_L;

K = 1;

while 1

GVF_LCO = Q_G_S*(1-GCU_PIPE_SEP)/P_HI_SEP /(Q_G_S*(1-            % Estimating GVF in PIPE-SEP gas out line, GVF
GCU_PIPE_SEP)/P_HI_SEP +Q_L*LCO_PIPE_SEP *1e-3*3600);
Vsg_est = (( Q_G_S*(1-                                           % Estimating gas velocity in PIPE-SEP gas leg, (m/s);
GCU_PIPE_SEP)+Q_L*LCO_PIPE_SEP)/P_HI_SEP/3600 ) / A_PIPE;
Vsg_est_PIPE_SEP= (( Q_G_S*(1-                                   % Estimating gas velocity in PIPE-SEP, (m/s);
GCU_PIPE_SEP)+Q_L*LCO_PIPE_SEP)/P_HI_SEP/3600 ) /
A_PIPE_SEP;
rho_mix_1 = rho_L*(1-GVF_LCO)+ rho_G_PIPE_SEP * GVF_LCO;         % Estimating Mixture density of PIPE-SEP gas out line, (Kg/m^3);
mu_mix_1 = mu_L*(1-GVF_LCO)+ mu_G *GVF_LCO;                      % Estimating Mixture viscosity of PIPE-SEP gas out line, (Pa.s);

Reno_PIPE_SEP_O = rho_mix_1 * D_PIPE * Vsg_est /mu_mix_1;        % Estimating Reynolds number of PIPE-SEP gas out line;
Reno_PIPE_SEP = rho_mix_1 * D_PIPE_SEP * Vsg_est_PIPE_SEP
/mu_mix_1;
f_G = 0.0056+0.5*Reno_PIPE_SEP_O^(-0.32);                        % Estimating Reynolds number of PIPE-SEP ;
f_G_G=0.0056+0.5*Reno_PIPE_SEP^(-0.32);                  L_Gas   % Gas friction factor in PIPE-SEP gas out line;
=L_g2+L_g3+L_g4+L_g5+L_g6;                                       % Gas friction factor in PIPE-SEP ;
L_fitting_G = 12.35;                                             % Total length of gas out line, (m);
DP_G =( ((f_G*(L_Gas+L_fitting_G)/0.05+1.5)*Vsg_est^2/2-         % Gas out line fittings equivalent length, (m);
g*0.65)*rho_mix_1/100000);                                       % Estimating pressure loss along PIPE-SEP gas out line, (bar)

P_PIPE_SEP = P_HI_SEP+DP_G;
```

```
% Calculated Gas Density at PIPE-SEP :

rho_G_PIPE_SEP = (P_PIPE_SEP*101330*28.96 )/ (8314 * (273 +
T_inlet ));                                              % Gas density in PIPE-SEP, (kg/m^3);

% Calculate superficial velocity in PIPE-SEP:

Q_G_A_PIPE_SEP = Q_G_S/P_PIPE_SEP;                       % Actual gas flow rate in PIPE-SEP, (Am^3/hr);
Vsg_PIPE_SEP = ( Q_G_A_PIPE_SEP/3600 ) /A_PIPE_SEP_R ;   % Superficial gas velocity in PIPE-SEP, (m/s);
Vsg_PIPE_SEP_O = ( Q_G_A_PIPE_SEP/3600 )/A_PIPE;

                                                         % Superficial gas velocity in PIPE-SEP gas out line, (m/s);
Vsl_PIPE_SEP = Q_L*1e-3 /A_PIPE_SEP_R;                   % Superficial liquid velocity in PIPE-SEP, (m/s);
Vsl_PIPE_SEP_O = Q_L*1e-3 /A_PIPE;                       % Superficial liquid velocity in PIPE-SEP liquid out line, (m/s);

% Calculate superficial velocity in HI-SEP:

                                                         % Actual gas flow rate in HI-SEP, (Am^3/hr);
Q_G_A_HI_SEP =  Q_G_S/P_HI_SEP;                          % Superficial gas velocity in HI-SEP, (m/s);
Vsg_HI_SEP = ( Q_G_A_HI_SEP/3600 ) /A_HI_SEP ;           % Superficial liquid velocity in HI-SEP, (m/s);
Vsl_HI_SEP = Q_L*1e-3 /A_HI_SEP;

% Calculate PIPE-SEP liquid leg pressure loss:

L_liquid = L_l2 + L_l3 + L_l4 + L_l5 + L_l6;             % Total liquid out line length, (m);
 L_fitting_L = 45.71;                                    % Liquid out line fittings equivalent length, (m); (2 valves, 4 bends, and 1 tee)

% Calculate the mixture in PIPE-SEP liquid out line

GVF_GCU =GCU_PIPE_SEP*Q_G_S/P_PIPE_SEP                   % Estimating GVF in PIPE-SEP liquid out line, GVF
/(GCU_PIPE_SEP*Q_G_S/P_PIPE_SEP +Q_L*(1-
LCO_PIPE_SEP)*1e-3*3600);

rho_mix_2 = rho_L*(1-GVF_GCU)+ rho_G_PIPE_SEP * GVF_GCU; % Calculate mixture density of PIPE-SEP liquid out line, (Kg/m^3);
mu_mix_2 = mu_L*(1-GVF_GCU)+ mu_G *GVF_GCU;              % Calculate mixture viscosity of PIPE-SEP liquid out line, (Pa.s);
                                                         % Mixture velocity in PIPE-SEP liquid out line, (m/s);
```

```
Vsl_mix_2 = (Q_L*(1-LCO_PIPE_SEP)*1e-
3)/A_PIPE+( GCU_PIPE_SEP*Q_G_S/3600 )/A_PIPE;                % Mixture velocity in PIPE-SEP, (m/s);
Vsl_mix_3 = (Q_L*(1-LCO_PIPE_SEP)*1e-
3)/A_PIPE_SEP+( GCU_PIPE_SEP*Q_G_S/3600 )/A_PIPE_SEP;

Reno_L = rho_mix_2 * D_PIPE_SEP  * Vsl_mix_3 / mu_mix_2;    % Liquid Reynolds number in PIPE-SEP;
Reno_L_L = rho_mix_2 *  D_PIPE * Vsl_mix_2 / mu_mix_2;      % Liquid Reynolds number in PIPE-SEP liquid out line;

% Calculate liquid friction factor at PIPE-SEP by Drew method

f_L = 0.0056+0.5* Reno_L^(-0.32);                           % Liquid friction factor in PIPE-SEP;
f_L_L = 0.0056+0.5* Reno_L_L^(-0.32);                       % Liquid friction factor in PIPE-SEP liquid out line;

% Calculate pressure loss along PIPE-SEP liquid out line

DP_L = (f_L_L *(L_fitting_L+L_liquid)/D_PIPE+1.5)*(rho_mix_2*   %  Pressure loss in PIPE-SEP liquid out line, (bar);
Vsl_mix_2^2/2)/100000;

% PIPE-SEP Equilibrium Liquid Level

L_l1_new= ((P_UF_KOV-P_HI_SEP)*100000+DP_L*100000 -
DP_G*100000- rho_mix_2*g*(Z_1-Z_3-L_p)- rho_mix_1 *g *(Z_1-
Z_2-L_r)-
f_G_G*(L_g1+L_inlet)*rho_mix_1*Vsg_est_PIPE_SEP^2/D_PIPE_SE
P/2)/(g*(rho_L+rho_G_PIPE_SEP)-
f_L*rho_mix_2*Vsl_PIPE_SEP^2/2/D_PIPE_SEP-
f_G_G*rho_mix_1*Vsg_est_PIPE_SEP^2/D_PIPE_SEP/2);

delta= (L_l1_new-L_l1);

if delta>0.1
   LCO_PIPE_SEP=LCO_PIPE_SEP+0.0001;
K=K+1;
end
```

```
if delta<-0.1
   LCO_PIPE_SEP=LCO_PIPE_SEP-0.0001;
K=K+1;
end

if delta<=0.1 & delta>=-0.1
break;
end

end

if L_l1_new>=CM
disp(' Agitated Flow')
end

if L_l1_new<=CM
 L_l1=L_l1_new;
end

end

%%=============================================

% Swirled flow model

if L_l1 >=0.085 & L_l1 <= CM

Q_GCU = 2.7;                                                    % Gas carry under, (Sm^3/h);
GCU_PIPE_SEP=Q_GCU/Q_G_S;

% Calculate film thickness:
Reno_G_C=
(Vsg_PIPE_SEP*rho_G_PIPE_SEP*D_PIPE_SEP_e)/mu_G;                % Reno number of gas phase in PIPE-SEP;
N_L = (g*D_PIPE_SEP_e^3*rho_L*(rho_L-
rho_G_PIPE_SEP)/mu_L^2)^0.5;                                    % Two phase Grashoff number;
```

```
Theta_B = 140*N_L^0.433*Reno_G_C^(-1.35)*D_PIPE_SEP;          % Swirled film thickness, (m);

% Calculate film height

Frn = Vmix^2/(g* D_PIPE_SEP);
                                                              % The Froude number;
C = 2.35;
n = 0.022;
                                                              % Constant C and the power n
H_film = C *(Frn) ^0.5*(Reno_inlet)^n *(1+f_inlet)^(-0.25) *
A_PIPE^0.5;                                                   % Swirled film height, (m);

% Liquid split ratio

S_R = pi*D_PIPE_SEP*H_film*Theta_B*1000/Q_L
Vsl_film = S_R *Q_L/1000/(pi/4*(D_PIPE_SEP^2-(D_PIPE_SEP-
Theta_B)^2));                                                 % Swirled film velocity, (m/s);

% Entrainment fraction

N_uf = mu_L/(rho_L*sur_tension*(sur_tension/g/(rho_L-
rho_G_PIPE_SEP))^0.5);
Reno_film = rho_L*Vsl_film*Theta_B/mu_L;
Reno_f_film = 250*log(Reno_film)-1265;
a = 2.31e-04 * Reno_film^(-0.35);
E_max = 1-Reno_f_film/Reno_film;

V=0.1;

% Liquid carry over

LCO_PIPE_SEP =S_R*E_max*V;
```

```
K = 1;

while 1

GVF_LCO = Q_G_S*(1-GCU_PIPE_SEP)/P_HI_SEP /(Q_G_S*(1-GCU_PIPE_SEP)/P_HI_SEP +Q_L*LCO_PIPE_SEP *1e-3*3600);   % Estimating GVF in PIPE-SEP gas out line, GVF
Vsg_est = (( Q_G_S*(1-GCU_PIPE_SEP)+Q_L*LCO_PIPE_SEP)/P_HI_SEP/3600 ) / A_PIPE;   % Estimating gas velocity in PIPE-SEP gas leg, (m/s);
Vsg_est_PIPE_SEP= (( Q_G_S*(1-GCU_PIPE_SEP)+Q_L*LCO_PIPE_SEP)/P_HI_SEP/3600 ) / A_PIPE_SEP;   % Estimating gas velocity in PIPE-SEP, (m/s);
rho_mix_1 = rho_L*(1-GVF_LCO)+ rho_G_PIPE_SEP * GVF_LCO;   % Estimating Mixture density of PIPE-SEP gas out line, (Kg/m^3);
mu_mix_1 = mu_L*(1-GVF_LCO)+ mu_G *GVF_LCO;   % Estimating Mixture viscosity of PIPE-SEP gas out line, (Pa.s);

Reno_PIPE_SEP_O = rho_mix_1 * D_PIPE * Vsg_est /mu_mix_1;   % Estimating Reynolds number of PIPE-SEP gas out line;
Reno_PIPE_SEP = rho_mix_1 * D_PIPE_SEP * Vsg_est_PIPE_SEP /mu_mix_1;   % Estimating Reynolds number of PIPE-SEP ;
f_G = 0.0056+0.5*Reno_PIPE_SEP_O^(-0.32);   % Gas friction factor in PIPE-SEP gas out line;
f_G_G=0.0056+0.5*Reno_PIPE_SEP^(-0.32);   % Gas friction factor in PIPE-SEP ;
  L_Gas =L_g2+L_g3+L_g4+L_g5+L_g6;   % Total length of gas out line, (m);
L_fitting_G = 12.35;   % Gas out line fittings equivalent length, (m);
DP_G =( ((f_G*(L_Gas+L_fitting_G)/0.05+1.5)*Vsg_est^2/2-g*0.65)*rho_mix_1/100000);   % Estimating pressure loss along PIPE-SEP gas out line, (bar)

P_PIPE_SEP = P_HI_SEP+DP_G;

% Calculated Gas Density at PIPE-SEP :

rho_G_PIPE_SEP = (P_PIPE_SEP*101330*28.96 )/ (8314 * (273 + T_inlet ));   % Gas density in PIPE-SEP, (kg/m^3);

% Calculate superficial velocity in PIPE-SEP:

Q_G_A_PIPE_SEP = Q_G_S/P_PIPE_SEP;   % Actual gas flow rate in PIPE-SEP, (Am^3/hr);
Vsg_PIPE_SEP = ( Q_G_A_PIPE_SEP/3600 ) /A_PIPE_SEP_R ;   % Superficial gas velocity in PIPE-SEP, (m/s);
```

```
Vsg_PIPE_SEP_O = ( Q_G_A_PIPE_SEP/3600 )/A_PIPE;

Vsl_PIPE_SEP = Q_L*1e-3 /A_PIPE_SEP_R;
Vsl_PIPE_SEP_O = Q_L*1e-3 /A_PIPE;

% Calculate superficial velocity in HI-SEP:

Q_G_A_HI_SEP =  Q_G_S/P_HI_SEP;
Vsg_HI_SEP = ( Q_G_A_HI_SEP/3600 ) /A_HI_SEP ;
Vsl_HI_SEP = Q_L*1e-3 /A_HI_SEP;

% Calculate PIPE-SEP liquid leg pressure loss:

L_liquid = L_l2 + L_l3 + L_l4 + L_l5 + L_l6;
L_fitting_L = 45.71;

% Calculate the mixture in PIPE-SEP liquid out line

GVF_GCU =GCU_PIPE_SEP*Q_G_S/P_PIPE_SEP
/(GCU_PIPE_SEP*Q_G_S/P_PIPE_SEP +Q_L*(1-
LCO_PIPE_SEP)*1e-3*3600);

rho_mix_2 = rho_L*(1-GVF_GCU)+ rho_G_PIPE_SEP * GVF_GCU;
mu_mix_2 = mu_L*(1-GVF_GCU)+ mu_G *GVF_GCU;


Vsl_mix_2 = (Q_L*(1-LCO_PIPE_SEP)*1e-
3)/A_PIPE+( GCU_PIPE_SEP*Q_G_S/3600 )/A_PIPE;
Vsl_mix_3 = (Q_L*(1-LCO_PIPE_SEP)*1e-
3)/A_PIPE_SEP+( GCU_PIPE_SEP*Q_G_S/3600 )/A_PIPE_SEP;

Reno_L = rho_mix_2 * D_PIPE_SEP  * Vsl_mix_3 / mu_mix_2;
Reno_L_L = rho_mix_2 *  D_PIPE * Vsl_mix_2 / mu_mix_2;

% Calculate liquid friction factor at PIPE-SEP by Drew method
```

```
% Superficial gas velocity in PIPE-SEP gas out line, (m/s);
% Superficial liquid velocity in PIPE-SEP, (m/s);
% Superficial liquid velocity in PIPE-SEP liquid out line, (m/s);

% Actual gas flow rate in HI-SEP, (Am^3/hr);
% Superficial gas velocity in HI-SEP, (m/s);
% Superficial liquid velocity in HI-SEP, (m/s);

% Total liquid out line length, (m);
% Liquid out line fittings equivalent length, (m); (2 valves, 4 bends, and 1 tee)

% Estimating GVF in PIPE-SEP liquid out line, GVF

% Calculate mixture density of PIPE-SEP liquid out line, (Kg/m^3);
% Calculate mixture viscosity of PIPE-SEP liquid out line, (Pa.s);
% Mixture velocity in PIPE-SEP liquid out line, (m/s);

% Mixture velocity in PIPE-SEP, (m/s);

% Liquid Reynolds number in PIPE-SEP;

% Liquid Reynolds number in PIPE-SEP liquid out line;
```

```
f_L = 0.0056+0.5* Reno_L^(-0.32);
f_L_L = 0.0056+0.5* Reno_L_L^(-0.32);

% Calculate pressure loss along PIPE-SEP liquid out line

DP_L = (f_L_L *(L_fitting_L+L_liquid)/D_PIPE+1.5)*(rho_mix_2*
Vsl_mix_2^2/2)/100000;

% PIPE-SEP Equilibrium Liquid Level

L_l1_new= ((P_UF_KOV-P_HI_SEP)*100000+DP_L*100000 -
DP_G*100000- rho_mix_2*g*(Z_1-Z_3-L_p)- rho_mix_1 *g *(Z_1-
Z_2-L_r)-
f_G_G*(L_g1+L_inlet)*rho_mix_1*Vsg_est_PIPE_SEP^2/D_PIPE_SE
P/2)/(g*(rho_L+rho_G_PIPE_SEP)-
f_L*rho_mix_2*Vsl_PIPE_SEP^2/2/D_PIPE_SEP-
f_G_G*rho_mix_1*Vsg_est_PIPE_SEP^2/D_PIPE_SEP/2);

delta= (L_l1_new-L_l1);

if delta>0.1
   LCO_PIPE_SEP=LCO_PIPE_SEP+0.0001;
 K=K+1;
end
 if delta<-0.1
   LCO_PIPE_SEP=LCO_PIPE_SEP-0.0001;
 K=K+1;
end
 if delta<=0.1 & delta>=-0.1
break;
end

end
```

```
% Liquid friction factor in PIPE-SEP;
% Liquid friction factor in PIPE-SEP liquid out line;

%  Pressure loss in PIPE-SEP liquid out line, (bar);
```

```
if L_l1_new>0.7 & L_l1_new<=CM
 disp('Swirled Flow to Agitated Flow')
end

if L_l1_new>0.085 & L_l1_new<=0.7
 disp('Swirled Flow')
end
end

%%=============================================

% Gas blow by model

if L_l1 <=0.085

% Liquid carry over
LCO_PIPE_SEP =0.001;
Q_GCU=-500*P_PIPE_SEP^2+1445*P_PIPE_SEP-976;
GCU_PIPE_SEP=Q_GCU/Q_G_S;

K = 1;

while 1

GVF_LCO = Q_G_S*(1-GCU_PIPE_SEP)/P_HI_SEP /(Q_G_S*(1-
GCU_PIPE_SEP)/P_HI_SEP +Q_L*LCO_PIPE_SEP *1e-3*3600);
Vsg_est = (( Q_G_S*(1-
GCU_PIPE_SEP)+Q_L*LCO_PIPE_SEP)/P_HI_SEP/3600 ) / A_PIPE;
Vsg_est_PIPE_SEP= (( Q_G_S*(1-
GCU_PIPE_SEP)+Q_L*LCO_PIPE_SEP)/P_HI_SEP/3600 ) /
A_PIPE_SEP;
rho_mix_1 = rho_L*(1-GVF_LCO)+ rho_G_PIPE_SEP * GVF_LCO;
mu_mix_1 = mu_L*(1-GVF_LCO)+ mu_G *GVF_LCO;

Reno_PIPE_SEP_O = rho_mix_1 * D_PIPE * Vsg_est /mu_mix_1;
```

```
Reno_PIPE_SEP = rho_mix_1 * D_PIPE_SEP * Vsg_est_PIPE_SEP
/mu_mix_1;
f_G = 0.0056+0.5*Reno_PIPE_SEP_O^(-0.32);
f_G_G=0.0056+0.5*Reno_PIPE_SEP^(-0.32);
L_Gas =L_g2+L_g3+L_g4+L_g5+L_g6;
L_fitting_G = 12.35;
DP_G =( ((f_G*(L_Gas+L_fitting_G)/0.05+1.5)*Vsg_est^2/2-
g*0.65)*rho_mix_1/100000);

P_PIPE_SEP = P_HI_SEP+DP_G;

% Calculated Gas Density at PIPE-SEP :

rho_G_PIPE_SEP = (P_PIPE_SEP*101330*28.96 )/ (8314 * (273 +
T_inlet ));

% Calculate superficial velocity in PIPE-SEP:

Q_G_A_PIPE_SEP = Q_G_S/P_PIPE_SEP;
Vsg_PIPE_SEP = ( Q_G_A_PIPE_SEP/3600 ) /A_PIPE_SEP_R ;
Vsg_PIPE_SEP_O = ( Q_G_A_PIPE_SEP/3600 )/A_PIPE;

Vsl_PIPE_SEP = Q_L*1e-3 /A_PIPE_SEP_R;
Vsl_PIPE_SEP_O = Q_L*1e-3 /A_PIPE;

% Calculate superficial velocity in HI-SEP:

Q_G_A_HI_SEP =  Q_G_S/P_HI_SEP;
Vsg_HI_SEP = ( Q_G_A_HI_SEP/3600 ) /A_HI_SEP ;
Vsl_HI_SEP = Q_L*1e-3 /A_HI_SEP;

% Calculate PIPE-SEP liquid leg pressure loss:

L_liquid = L_l2 + L_l3 + L_l4 + L_l5 + L_l6;
L_fitting_L = 45.71;
```

```
% Actual gas flow rate in PIPE-SEP, (Am^3/hr);
% Superficial gas velocity in PIPE-SEP, (m/s);

% Superficial gas velocity in PIPE-SEP gas out line, (m/s);
% Superficial liquid velocity in PIPE-SEP, (m/s);
% Superficial liquid velocity in PIPE-SEP liquid out line, (m/s);


% Actual gas flow rate in HI-SEP, (Am^3/hr);
% Superficial gas velocity in HI-SEP, (m/s);
% Superficial liquid velocity in HI-SEP, (m/s);


% Total liquid out line length, (m);
% Liquid out line fittings equivalent length, (m); (2 valves, 4 bends, and 1 tee)


% Estimating GVF in PIPE-SEP liquid out line, GVF


% Calculate mixture density of PIPE-SEP liquid out line, (Kg/m^3);
% Calculate mixture viscosity of PIPE-SEP liquid out line, (Pa.s);
% Mixture velocity in PIPE-SEP liquid out line, (m/s);

% Mixture velocity in PIPE-SEP, (m/s);
```

```
% Calculate the mixture in PIPE-SEP liquid out line

GVF_GCU =GCU_PIPE_SEP*Q_G_S/P_PIPE_SEP
/(GCU_PIPE_SEP*Q_G_S/P_PIPE_SEP +Q_L*(1-
LCO_PIPE_SEP)*1e-3*3600);

rho_mix_2 = rho_L*(1-GVF_GCU)+ rho_G_PIPE_SEP * GVF_GCU;
mu_mix_2 = mu_L*(1-GVF_GCU)+ mu_G *GVF_GCU;


Vsl_mix_2 = (Q_L*(1-LCO_PIPE_SEP)*1e-
3)/A_PIPE+( GCU_PIPE_SEP*Q_G_S/3600 )/A_PIPE;
Vsl_mix_3 = (Q_L*(1-LCO_PIPE_SEP)*1e-
3)/A_PIPE_SEP+( GCU_PIPE_SEP*Q_G_S/3600 )/A_PIPE_SEP;

Reno_L = rho_mix_2 * D_PIPE_SEP  * Vsl_mix_3 / mu_mix_2;
Reno_L_L = rho_mix_2 *  D_PIPE * Vsl_mix_2 / mu_mix_2;

% Calculate liquid friction factor at PIPE-SEP by Drew method

f_L = 0.0056+0.5* Reno_L^(-0.32);
f_L_L = 0.0056+0.5* Reno_L_L^(-0.32);

% Calculate pressure loss along PIPE-SEP liquid out line

DP_L = (f_L_L *(L_fitting_L+L_liquid)/D_PIPE+1.5)*(rho_mix_2*
Vsl_mix_2^2/2)/100000;

% PIPE-SEP Equilibrium Liquid Level

L_l1_new= ((P_UF_KOV-P_HI_SEP)*100000+DP_L*100000 -
DP_G*100000- rho_mix_2*g*(Z_1-Z_3-L_p)- rho_mix_1 *g *(Z_1-
Z_2-L_r)-
f_G_G*(L_g1+L_inlet)*rho_mix_1*Vsg_est_PIPE_SEP^2/D_PIPE_SE
P/2)/(g*(rho_L+rho_G_PIPE_SEP)-
```

% Liquid Reynolds number in PIPE-SEP;
% Liquid Reynolds number in PIPE-SEP liquid out line;

% Liquid friction factor in PIPE-SEP;
% Liquid friction factor in PIPE-SEP liquid out line;

% Pressure loss in PIPE-SEP liquid out line, (bar);

```
f_L*rho_mix_2*Vsl_PIPE_SEP^2/2/D_PIPE_SEP-
f_G_G*rho_mix_1*Vsg_est_PIPE_SEP^2/D_PIPE_SEP/2);

delta= (L_l1_new-L_l1);

if L_l1_new <= 0.085
   disp('GB')
end

if L_l1_new > 0.085
   L_l1=L_l1_new;

Q_GCU = 5;                                          % Gas carry under (Sm^3/h)

GCU_PIPE_SEP=Q_GCU/Q_G_S;

% Swirled flow to gas blow by model

% Calculate film thickness:
Reno_G_C=
(Vsg_PIPE_SEP*rho_G_PIPE_SEP*D_PIPE_SEP_e)/mu_G;
N_L = (g*D_PIPE_SEP_e^3*rho_L*(rho_L-
rho_G_PIPE_SEP)/mu_L^2)^0.5;                        % Two phase Grashoff number;
Theta_B = 140*N_L^0.433*Reno_G_C^(-1.35)*D_PIPE_SEP; % Swirled film thickness, (m);

% Calculate film height

Frn = Vmix^2/(g* D_PIPE_SEP);                       % The Froude number;

C = 2.35;
n = 0.022;                                          % Constant C and the power n

H_film = C *(Frn) ^0.5*(Reno_inlet)^n *(1+f_inlet)^(-0.25) *
A_PIPE^0.5;                                         % Swirled film height, (m);
```

```
% Liquid split ratio

S_R = pi*D_PIPE_SEP*H_film*Theta_B*1000/Q_L
Vsl_film = S_R *Q_L/1000/(pi/4*(D_PIPE_SEP^2-(D_PIPE_SEP-
Theta_B)^2));                                          % Swirled film velocity, (m/s);

% Entrainment fraction

N_uf = mu_L/(rho_L*sur_tension*(sur_tension/g/(rho_L-
rho_G_PIPE_SEP))^0.5);
Reno_film = rho_L*Vsl_film*Theta_B/mu_L;
Reno_f_film = 250*log(Reno_film)-1265;
a = 2.31e-04 * Reno_film^(-0.35);
E_max = 1-Reno_f_film/Reno_film;

V=0.1;

% Liquid carry over

LCO_PIPE_SEP =S_R*E_max*V;

%%=============================================

Q_LCO = LCO_PIPE_SEP *Q_L;                             % Liquid carry over flowrate, (l/s);
Q_GCU = GCU_PIPE_SEP *Q_G_S;                           % Gas carry under flowrate, (Sm^3/h);
eta_Liquid = (1-LCO_PIPE_SEP)*100;                     % Liquid separation efficiency, (%)
eta_Gas = (1-GCU_PIPE_SEP)*100;                        % Gas separation efficiency, (%)


disp ( ['Inlet Temperature (degree)             ', num2str(T_inlet)] );
disp ( ['Inlet Pressure (bara)                ', num2str( P_inlet)] );
disp ( ['PIPE-SEP Inside Pressure (bara)        ', num2str( P_PIPE_SEP)] );
disp ( ['HI-SEP Inside Pressure (bara)          ', num2str( P_HI_SEP)] );
disp ( ['UF KOV Pressure (bara)                 ', num2str( P_UF_KOV)] );
disp ( ['Liquid Flowrate (l/s)                ', num2str( Q_L)] );
```

```
disp ( ['Standard Gas Flowrate (Sm^3/h)           ', num2str(Q_G_S  )] );
disp ( ['Superficial Gas Velocity (m/s)          ', num2str(Vsg)] );
disp ( ['Superficial Liquid Velocity (m/s)       ', num2str(Vsl)] );
disp ( ['Mix Velocity (m/s)                    ', num2str(Vmix)] );
disp ( ['Inlet GVF (%)                         ', num2str(GVF_inlet )] );
disp ( ['Gas Velocity in PIPE-SEP (m/s)          ', num2str(Vsg_PIPE_SEP)] );
disp ( ['Gas Velocity in HI-SEP (m/s)            ', num2str(Vsg_HI_SEP)] );
disp ( ['Liquid Velocity in PIPE-SEP (m/s)       ', num2str(Vsl_PIPE_SEP)] );
disp ( ['Liquid Velocity in HI-SEP (m/s)         ', num2str(Vsl_HI_SEP)] );
disp ( ['Liquid level in PIPE-SEP (mm)           ', num2str(L_l1_new)] );
disp ( ['Pressure loss along gas leg(bar)        ', num2str( DP_G)] );
disp ( ['Pressure loss along liquid leg(bar)     ', num2str(DP_L)] );
disp ( ['Liquid carry over                     ', num2str(LCO_PIPE_SEP)] );
disp ( ['Gas carry under                       ', num2str(GCU_PIPE_SEP)] );
disp ( [' Liquid carry over(l/s)                ', num2str(Q_LCO)] );
disp ( ['Gas carry under(Sm^3/hr)              ', num2str(Q_GCU)] );
disp ( ['Liquid separation efficiency(%)         ', num2str(eta_Liquid )] );
disp ( ['Gas separation efficiency(%)            ', num2str(eta_Gas )] );
disp ( ['Churned flow boundary                 ', num2str(CM )] );
```

Appendix E: Pipe-Hi-SEP Optimal Design Model

```
% PIPE-HI-SEP optimal design model (SI Units)
% Developed by Yinghui Zhou--------March 2012

%%=========================================
```

PIPEHIcost

```
function f=PIPEHIcost(x,d)

D_HI_SEP = x(1);H_C2 = x(2);H_F2 = x(3);H_LIN2 = x(4);H_S2 = x(5);H_H2 = x(6);H_LLL2 = x(7);H_LLLL2 = x(8);
D_NOZ1 = x(9); D_NOZ2 = x(10); D_NOZ3 = x(11); tcs_HI_SEP = x(12);D_PIPE_SEP = x(13);H_C1= x(14);H_F1= x(15);H_LIN1 = x(16);H_S1 =
x(17);H_H1= x(18);H_LLL1 = x(19);H_LLLL1 = x(20);tcs_PIPE_SEP = x(21);

%%=========================================
f =
(tcs_HI_SEP/1000*pi*D_HI_SEP*(H_C2+H_F2+H_LIN2+H_S2+H_H2+H_LLL2+H_LLLL2)+tcs_PIPE_SEP/1000*pi*D_PIPE_SEP*(H_C1+H_F1+H_LIN1
+H_S1+H_H1+H_LLL1+H_LLLL1))*7850;
```

PIPEHIconstrain

```
function [c,ceq]=PIPEHIconstrain(x,d)

% Variables

D_HI_SEP = x(1);H_C2 = x(2);H_F2 = x(3);H_LIN2 = x(4);H_S2 = x(5);H_H2 = x(6);H_LLL2 = x(7);H_LLLL2 = x(8);
D_NOZ1 = x(9); D_NOZ2 = x(10); D_NOZ3 = x(11); tcs_HI_SEP = x(12);D_PIPE_SEP = x(13);H_C1= x(14);H_F1= x(15);H_LIN1 = x(16);H_S1 =
x(17);H_H1= x(18);H_LLL1 = x(19);H_LLLL1 = x(20);tcs_PIPE_SEP = x(21);

% Given parameters

Q_L = d(1);Q_G_S = d(2); P_inlet = d(3); T_inlet = d(4); T_LLL2 = d(5);T_H2 = d(6);T_S2 = d(7); LCO=d(8);  D_m2=d(9); D_m1=d(10);
```

```
d=[13.24,   11800,   68.94,    15.55,   180,    30,   30,  0.01, 3.41e-05, 300];

% Constants

rho_L = 824.9; mu_L = 3e-03; sur_tension = 0.07; mu_G = 1.03e-05; g = 9.8;

% Calculat PIPE-SEP inlet flow properties:

Q_G_A = Q_G_S/P_inlet;                          % Actual inlet gas flow rate, (Am^3/hr);
Q_M = Q_L+Q_G_A;                                % Inlet mixture flow rate, m^3/hr
GVF_inlet = Q_G_A /Q_M;                         % Inlet gas void fraction, GVF;
LVF_inlet = Q_L/Q_M;                            % Inlet liquid void fraction, LVF;

% Calculated Gas Density at PIPE-SEP inlet:

%rho_G = ( P_inlet *101330*28.96 )/ (8314 * (273 + T_inlet ));
rho_G = 59.42;                                  % Gas density at inlet pipe, (kg/m^3);

% Calculate Inlet mixture properties:

rho_mix = rho_L*(1-GVF_inlet)+ rho_G * GVF_inlet;
mu_mix = mu_L*(1-GVF_inlet)+ mu_G * GVF_inlet;

                                                % Mixture density, (Kg/m^3);

                                                % Mixture viscosity, (pa.s);
% Inlet pipe constrains:

c(1) = -
D_NOZ1+(4*(Q_M/101.94)/(pi*60/(rho_mix/16.018)^0.5))^0.5*0.3048
;
A_NOZl = pi/4*D_NOZ1^2;

%PIPE-SEP inlet velocity

Vsl_inlet = Q_L/3600 / A_NOZl;                  % Superficial inlet liquid velocity,(m/s);
Vsg_inlet =  Q_G_A/3600 /A_NOZl;                % Superficial inlet gas velocity, (m/s);
```

```
V_mix=Q_M/3600/A_NOZl;                          % Mixture inlet velocity, (m/s);
Reno_inlet = rho_mix * D_NOZ1 * V_mix /mu_mix;  % Reynolds number at inlet;
f_inlet = Q_G_A / Q_L;                          % Inlet gas to liquid volumetric ratio ;

% Calculat the intermiddle gas inlet flow properties:

Q_gas_inlet_M = Q_L*LCO+Q_G_A;                  % Gas inlet mixture flow rate, m^3/hr
GVF_gas_inlet = Q_G_A /Q_gas_inlet_M;           % Gas inlet gas void fraction, GVF;
LVF_gas_inlet = Q_L*LCO/Q_gas_inlet_M;          % Gas inlet liquid void fraction, LVF;

% Calculate the intermiddle gas inlet  mixture properties:

rho_mix_gas_inlet = rho_L*(1-GVF_gas_inlet)+ rho_G *
GVF_gas_inlet;                                  % Mixture density, (Kg/m^3);
mu_mix_gas_inlet = mu_L*(1-GVF_gas_inlet)+ mu_G *
GVF_gas_inlet;                                  % Mixture viscosity, (pa.s);

% Inter-middle pipe constrains

c(2) = -
D_NOZ2+(4*(Q_gas_inlet_M/101.94)/(pi*60/(rho_mix_gas_inlet/16.01
8)^0.5))^0.5*0.3048;
c(3) = -D_NOZ3+(4*(Q_L*(1-
LCO)/101.94)/(pi*60/(rho_L/16.018)^0.5))^0.5*0.3048;
D_NOZ = max(D_NOZ2,D_NOZ3);
A_NOZ = pi/4*D_NOZ^2;

%%=========================================

% HI-SEP gas inlet flow properties

Vsl_gas_inlet = Q_L*LCO/3600 / A_NOZ;           % Superficial inlet liquid velocity,(m/s);
Vsg_gas_inlet = Q_G_A/3600 /A_NOZ;              % Superficial inlet gas velocity, (m/s);
V_mix_gas_inlet = Vsl_gas_inlet + Vsg_gas_inlet;% Mixture inlet velocity, (m/s);
Reno_gas_inlet = rho_mix_gas_inlet * D_NOZ * V_mix_gas_inlet
                                                % Reynolds number at inlet;
```

```
/mu_mix_gas_inlet;              f_gas_inlet = Q_G_A / (Q_L*LCO);
                                                                    % Inlet gas to liquid volumetric ratio ;


% HI-SEP g force constrain

c(4) =10-(Q_gas_inlet_M/3600/A_NOZ)^2/D_HI_SEP/g;
c(5)=-200+(Q_gas_inlet_M/3600/A_NOZ)^2/D_HI_SEP/g;

% Calculate HI-SEP terminal velocity:                              % Terminal velocity, m/sec

V_t_HI_SEP_1 = 0.75*2.38*( sur_tension /rho_L)^0.25*((rho_L-
rho_G)/rho_G)^0.5*0.3048;

% HI-SEP liquid film re-entrainment constrains:

Re_film=Q_L*LCO/3600*rho_L/(pi*D_HI_SEP*mu_L);
Vtang=((-3.1*0.2+4.72)*Vsg_gas_inlet-
1.38)*(0.15/D_HI_SEP)^0.3/(D_HI_SEP/2)^(-1);
Vaixal=((-19*0.2+15.38)*Vsg_gas_inlet+17.4*0.2-
9.98)*(0.15/D_HI_SEP)^2/(D_HI_SEP/2)^(-1);
%a=(Q_gas_inlet_M/3600/A_NOZ*0.4)^2/D_HI_SEP;
a=Vtang/2;

Nu_film=mu_L/(rho_L*sur_tension*(sur_tension/(a*(rho_L-
rho_G)))^0.5)^0.5;

if Re_film<160
V_t_HI_SEP_2=0.4572*(sur_tension/mu_L)*(rho_L/rho_G)^0.5*Nu_fi
lm^(-0.5);
end

if Re_film<=1635  &  Re_film>=160 & Nu_film <=1/15
V_t_HI_SEP_2=3.5905*(sur_tension/mu_L)*(rho_L/rho_G)^0.5*Nu_fi
lm^0.8* Re_film^(-1/3);
```

```
end

if Re_film<=1635 & Re_film>=160 & Nu_film >1/15
V_t_HI_SEP_2=0.4115*(sur_tension/mu_L)*(rho_L/rho_G)^0.5*
Re_film^(-1/3);
end

if Re_film>1635   & Nu_film <=1/15
V_t_HI_SEP_2=0.3048*(sur_tension/mu_L)*(rho_L/rho_G)^0.5*
Re_film^0.8;
end

if Re_film>1635   & Nu_film >1/15
V_t_HI_SEP_2=0.03493*(sur_tension/mu_L)*(rho_L/rho_G)^0.5;
end

c(6)=Vaixal-V_t_HI_SEP_2;
V_t_HI_SEP=V_t_HI_SEP_1;

% HI-SEP Gas capacity

c(6) = (Q_G_A/3600/((pi/4)*(D_HI_SEP^2-D_NOZ^2))) -
0.75*V_t_HI_SEP;                                        % Vessel diameter, inch,1 meter = 39.370 078 74 inch
D_HI_SEP_INCH = D_HI_SEP*39.37 ;
c(7) =-D_HI_SEP+2*D_NOZ;

% H_C2

H_E=0.2;
H_T2=2*D_NOZ;
c(8)=-H_C2+(H_T2+2*D_NOZ+H_E);

% H_F2

FN_gas_inlet = V_mix_gas_inlet^2/g/D_HI_SEP;
```

```
H_F2_1=
( A_NOZ^0.5*2.35*Reno_gas_inlet^0.022*FN_gas_inlet^0.5*(1+f_gas     %Swirled film height , m
_inlet)^(-0.25));

% HI-SEP separation performance constrain

d32 =
0.79*(sur_tension/rho_G)^0.6*(1/Vsg_gas_inlet)^1.2*D_NOZ^0.4;
H_F2_2 =
(9*D_NOZ*mu_G*D_HI_SEP/(D_m2^2*V_mix_gas_inlet*(rho_L-
rho_G)));

H_F2= max(H_F2_1, H_F2_2);

% H_LIN2

c(9)=-H_LIN2+ max(0.3+1/2*D_NOZ,0.2+H_LIN1);

% H_H2

V_H2 = T_H2*Q_L/3600;
 ceq(2)=-H_H2+(V_H2/(pi/4*(D_HI_SEP^2)));
                                                    % The holdup volume, m^3;
% H_S2

V_S2 = T_S2*Q_L/3600;
ceq(3)=-H_S2+( V_S2/(pi/4*(D_HI_SEP^2)));           % The surge volume, m^3;

% H_LLL2

ceq(4)=-H_LLL2+( T_LLL2*Q_L/3600/(pi/4*(D_HI_SEP^2-
D_NOZ^2)));

% H_LLLL2
```

```
if P_inlet<20
ceq(5)=H_LLLL2-15*0.0254;
else
ceq(5)=H_LLLL2-6*0.0254;
end

% Ratio_HI_SEP

H_HI_SEP_G = H_F2+H_C2;                                   % HI-SEP gas section length, m;
H_HI_SEP_L = H_LLLL2+H_LLL2+H_H2+H_S2+H_LIN2;             % HI-SEP liquid section length, m;
H_HI_SEP = H_HI_SEP_G + H_HI_SEP_L;                       % HI-SEP total length, m;
Ratio_HI_SEP = H_HI_SEP/D_HI_SEP;
c(10)=Ratio_HI_SEP-15;
c(11)=-Ratio_HI_SEP+2;

%%=============================================

% Calculate superficial velocity in PIPE-SEP:

A_PIPE_SEP = ( pi * D_PIPE_SEP ^ 2 ) / 4;                 % Cross-sectional area of the PIPE-SEP, (m^2);
A_G_PIPE = ( pi * D_NOZ ^ 2 ) / 4;                        % Cross-sectional area of the PIPE-SEP gas outline, (m^2);
A_PIPE_SEP_R = A_PIPE_SEP - A_G_PIPE;                     % Restricted cross-sectional area of the PIPE-SEP, (m^2);
D_PIPE_SEP_e = (4*A_PIPE_SEP_R/pi)^0.5;                   % PIPE-SEP equivalent diameter, (m);
Vsg_PIPE_SEP = ( Q_G_A/3600 ) /A_PIPE_SEP_R ;             % Superficial gas velocity in PIPE-SEP, (m/s);
Vsl_PIPE_SEP = Q_L/3600 /A_PIPE_SEP_R;                    % Superficial liquid velocity in PIPE-SEP, (m/s);

% PIPE-SEP g force

c(12)=5-(Q_M/3600/(pi*D_NOZ1^2/4))^2/D_PIPE_SEP/g;
c(13)=(Q_M/3600/(pi*D_NOZ1^2/4))^2/D_PIPE_SEP/g-200;
% Stoke's law
if D_m1<100
V_t_PIPE_SEP_1=(1488*g*(D_m1*0.000001*3.28)^2*((rho_L-
rho_G)*16.018)/(18*mu_G*1000))*0.3048;
End
```

```
% Intermediate law
if D_m1>=100 & D_m1<1000
V_t_PIPE_SEP_1=(3.49*g^0.71*(D_m1*0.000001*3.28)^1.14*((rho_L
-
rho_G)*16.018)^0.71/((mu_G*1000)^0.43*(rho_G*16.018)^0.29))*0.3
048;
end

% Calculate film thickness
Reno_G_C= (Vsg_PIPE_SEP*rho_G*D_PIPE_SEP_e)/mu_G;          % Reno number of gas phase in PIPE-SEP;
N_L = (g*D_PIPE_SEP_e^3*rho_L*(rho_L-rho_G)/mu_L^2)^0.5;
Theta_B = 140*N_L^0.433*Reno_G_C^(-1.35)*D_PIPE_SEP ;      % Two phase Grashoff number;

                                                           % Swirled film thickness, (m);


% H_F1

FN = V_mix^2/g/D_PIPE_SEP;
H_F1 = ( A_NOZl^0.5*2.35*Reno_inlet^0.022*FN^0.5*(1+f_inlet)^(-
0.25));                                                    % Swirled film height , m;
V_t_PIPE_SEP=V_t_PIPE_SEP_1;

% PIPE-SEP gas capacity

c(14)=(Q_G_A/3600/((pi/4)*(D_PIPE_SEP^2-D_NOZ^2))) -
0.75*V_t_PIPE_SEP;                                         % Vessel diameter, inch,1 meter = 39.370 078 74 inch
D_PIPE_SEP_INCH = D_PIPE_SEP*39.37 ;
c(15) = -D_PIPE_SEP+2*D_NOZ;

% H_C1

H_T1=2*D_NOZ;
c(16) =-H_C1+(H_T1+D_PIPE_SEP/2+2*D_NOZ) ;

% H_LIN1
```

```
c(17) = -H_LIN1+(0.3+1/2*D_NOZ1);

% Geometrical constrains1   H_H1,H_S1,H_LIN1
ceq(6)=H_H1-H_H2;
ceq(7)=H_S1-H_S2;

% H_LLL1

if P_inlet<20
ceq(8)=H_LLL1-15*0.0254;
else
ceq(8)=H_LLL1-6*0.0254;
end

% H_LLL1

c(18)=-H_LLLL1+2*D_NOZ;

H_PIPE_SEP_G = H_F1+H_C1;
H_PIPE_SEP_L = H_LLLL1+H_LLL1+H_H1+H_S1+H_LIN1;
H_PIPE_SEP = H_PIPE_SEP_G + H_PIPE_SEP_L;
Ratio_PIPE_SEP = H_PIPE_SEP/D_PIPE_SEP;
c(19)=Ratio_PIPE_SEP-15;

c(20)=2-Ratio_PIPE_SEP;

% Geometrical constrains2

c(21)= D_PIPE_SEP-D_HI_SEP;
c(22)=H_PIPE_SEP-H_HI_SEP;
c(23)=-D_HI_SEP;
c(24)=-H_C2;
c(25)=-H_F2+1;
c(26)=-H_LIN2;
```

```
c(27)=-H_S2;
c(28)=-H_H2;
c(29)=-H_LLL2;
c(30)=-H_LLLL2;
c(31)=-D_NOZ1;
c(32)=-D_NOZ2;
c(33)=-D_NOZ3;
c(34)=-D_PIPE_SEP;
c(35)=-H_C1;
c(36)=-H_F1;
c(37)=-H_LIN1;
c(38)=-H_LLL1;
c(39)=-H_LLLL1;

%Wall thickness

c(40)=-tcs_HI_SEP+( (1.1* P_inlet*D_HI_SEP)/(2*950*0.8-
1.2*1.1*P_inlet)*1000+3.2);
c(41)=-tcs_PIPE_SEP+( (1.1* P_inlet*D_PIPE_SEP)/(2*950*0.8-
1.2*1.1*P_inlet)*1000+3.2);
```

PIPEHIOptimial

```
d=[13.24, 11800, 68.94, 15.55, 180, 30, 30, 0.01, 3.41e-05,
300];

f=@(x)PIPEHIcost(x,d);
g=@(x)PIPEHIconstrain(x,d);
x0=[0.5, 0.6, 1, 0.4, 0.3, 0.3, 1.7, 0.2, 0.11, 0.09, 0.02,
32,0.2,0.1,0.1,0.5,0.3,0.2,0.2,0.1,20];

xL=zeros(1,21);
xU=inf(1,21);

options = optimset('Algorithm','active-set', 'display', 'iter');
[x,area]=fmincon(f,x0,[],[],[],[],xL,xU,g,options);
```